Optimizing Wide-Field Illumination and Single-Molecule Photoswitching for Localization Microscopy

A Thesis submitted to the
University of Strathclyde for the degree of

Doctor of Philosophy

By
Lucas Herdly

Photophysics Research Group
Department of Physics
University of Strathclyde
Glasgow

2025

This thesis is the result of the author's original research. It has been composed by the author and has not been previously submitted for examination which has led to the award of a degree.

The copyright of this thesis belongs to the author under the terms of the United Kingdom Copyright Acts as qualified by University of Strathclyde Regulation 3.50. Due acknowledgement must always be made of the use of any material contained in, or derived from, this thesis.

Abstract

Nanometre-scale molecules such as proteins and DNA constitute the building blocks of biological structures responsible for every function of life. Conventional light microscopy allows to study cells but it meets a lateral resolution limit of 250 nm as described by Ernst Abbe in 1873. Abbe's limit remained unbroken until the end of the twentieth century when E. Betzig, W. E. Moerner and S. Hell developed super-resolution microscopy.

Our work concentrates on direct STochastic Optical Reconstruction Microscopy (dSTORM), a single molecule localisation microscopy (SMLM) technique, that consists of the photoswitching of fluorescent molecules and their localisation with nanometre precision followed by the reconstruction of a super-resolution image from the localisation information. However, the quality of results using dSTORM depend strongly on the careful tuning of many parameters from the microscopy hardware to sample preparation and data analysis.

This work addresses several avenues of optimisation of the dSTORM process through four themes. First, improvements to hardware and data analysis for optimizing 3D-SMLM are described in the context of building a versatile dSTORM-focused microscopy platform. The careful characterisation of our setup allowed the identification and investigation of several improvement paths. Second, a Forster Resonance Energy Transfer (FRET) -based method was explored to enable multi-channel dSTORM without chromatic aberrations. While the concept could be demonstrated in ensemble spectroscopy, single molecule imaging did not show proper channel separation which lead us to explore two aspects of dSTORM imaging to improve the channel separation, illumination across the field of view and the influence of the buffer on photoswitching. Third, we evaluated how a single Micro Electro Mechanical System (MEMS) mirror could produce a uniform illumination across a large field of view and compared it to a recognized optical beam-shaping device, the piShaper. Our approach matched the pishaper performance with an improved

tuneability to produce other illumination schemes. We also presented our comparison method that can be applied to other illumination schemes. Finally, we systematically studied the influence of pH and Thiol concentration on photoswitching and on the quality of dSTORM imaging with Alex Fluor 647. We concluded that the thiolate concentration rather than pH or the total thiol concentration alone is the relevant parameter influencing photoswitching and the quality of results and observed a degradation in resolution for sub-optimal buffer conditions when we imaged the glucose transporter GLUT-4 in the plasma membrane of adipocytes. We also proposed a framework to optimise the switching buffer for dSTORM.

Overall, this work explored several approaches to improve the quality of dSTORM and proposes several methods to achieve better results in dSTORM experiments through hardware, sample preparation and data analysis optimisation.

Acknowledgements

First, I would like to thank Sebastian van de Linde for supervising my work throughout my PhD project. Our discussions allowed me to acquire knowledge about super-resolution microscopy and skills in conducting research. I would like to thank Gail McConnell for her support and fruitful questions about the project. I would like to thank Yves Mély for introducing me to the fascinating field of advanced microscopy and sparking my interest in research that led me to continue my education with a PhD.

Thank you to the photophysics group for providing a friendly and helpful environment. Thank you to David, Olaf, Yu, Brian for always asking the right questions to open new research paths.

I thank Brian, Ross, Alan and Iain for their motivation that made my task of supervising their projects easy.

Thank you to Paul, Ralf, Peter, Angeline, Holly and Gwyn for their contribution to my work during this PhD project.

Thank you to Alastair, Ben, Chloe, Gillian, Hajar, Hazel, Milan, Rhona, Yok, you made each day in the lab fun and fruitful.

To my family, my parents, my grandmothers, my brother and sister, thank you for your never-ending support during this project, I would not have finished it without you. And to Irina, you helped me find motivation when I needed it and I look forward to seeing what is yet to come.

Table of Contents

Abbreviations

Contributing authors	
AK	Alan Keenan
BJ	Brian Jordan
IJH	Iain James Harley
LH	Lucas Herdly
PJ	Paul Janin
PWT	Peter William Tinning
RB	Ralf Bauer
RP	Ross Phillips
SvdL	Sebastian van de Linde

Abbreviations	
ADC	Analog-Digital Counts
AF	Alexa Fluor
BME	β-MercaptoEthanol
BSA	Bovine Serum Albumin
DNA PAINT	DNA Point Accumulation in Nanoscale Topography
dSTORM	direct STochastic Optical Reconstruction Microscopy
EMCCD	Electron-multiplying Charge-Coupled Device
FIJI	Fiji Is Just ImageJ
FOV	Field Of View
FRC	Fourier Ring Correlation
FRET	Fluorescence Resonance Energy Transfer
FT	Fourier Transform
FWHM	Full width at half maximum
GGC	Glucose/Glucose oxydase/Catalase system
GLUT-4	GLUcose Transporter 4
GUI	Graphical user interface
HILO	Highly Inclined Laminated Optical sheet
IJM	the ImageJ Macro language
IRF	Instrument Response Function
ISC	InterSystem Crossing
MAD	Median Absolute Deviation
MEA	β-Mercaptoethylamine = Cysteamine

MEMS	Micro ElectroMechanical System
MINFLUX	Minimal fluorescence photon fluxes microscopy
NA	Numerical Aperture
PAINT	Point Accumulation In Nanoscale Topography
PALM	PhotoActivated Localisation Microscopy
PBS	Phosphate Buffered Saline
PET	Photoinduced Electron Transfer
PMT	PhotoMultiplier Tube
PSF	Point Spread Function
RMS	Root Mean Square
ROI	Region Of Interest
RS$^-$	Thiolate
SD	Standard Deviation
SIM	Structured Illumination Microscopy
smFRET	single molecule Fluorescence Resonance Energy Transfer
SMLM	Single Molecule Localisation Microscopy
SMS	Single Molecule Surface
SMS	Single-Molecul Surface
SNR	Signal to Noise Ratio
SOFI	Super resolution Optical Fluctuation Imaging
SPAD	Single-Photon Avalanche Diode
SRRF	Super-Resolution Radial Fluctuations
STED	STimulated Emission Depletion
STORM	STochastic Optical Reconstruction Microscopy
TAC	Time-to-Amplitude Converter
TCSPC	Time Correlated Single Photon Counting
TIRF	Total internal reflection fluorescence
TRABI	Temporal, Radial-Aperture Based Intensity estimation

Research outputs

Peer-reviewed articles

L. Herdly, P. Janin, R. Bauer, and S. van de Linde, "Tunable Wide-Field Illumination and Single-Molecule Photoswitching with a Single MEMS Mirror," ACS Photonics, vol. 8, no. 9, pp. 2728–2736, 2021, doi: 10.1021/acsphotonics.1c00843. (Herdly et al. 2021b) (An early version of this work was published as a preprint on bioRxiv (Herdly et al. 2021a))

C. Franke et al., "Approach to map nanotopography of cell surface receptors," Commun. Biol., vol. 5, no. 1, pp. 1–16, 2022, doi: 10.1038/s42003-022-03152-y. (Franke et al. 2022)

L. Herdly, P. W. Tinning, A. Geiser, H. Taylor, G. W. Gould, and S. van de Linde, "Benchmarking Thiolate-Driven Photoswitching of Cyanine Dyes," J. Phys. Chem. B, 2022, doi: 10.1021/acs.jpcb.2c06872. (Herdly et al. 2023)(An early version of this work was published as a preprint on bioRxiv (Herdly et al. 2022))

Conference presentations: poster, flash talks and oral presentations

Scottish Universities Physics Alliance Annual Gathering, 2018, Poster, "Characterisation and calibration of a 3D super-resolution microscopy system"

Frontiers of Bioimaging, Glasgow, 2018, Poster, "Characterisation and calibration of a 3D super-resolution microscopy system" (updated poster)

Glasgow imaging Network symposium, Glasgow, 2018, oral presentation, "Characterisation and calibration of a 3D super-resolution microscopy system"

Doctoral Multidisciplinary Symposium, University of Strathclyde, Glasgow, 2019, oral presentation, "3D super-resolution microscopy without axial scanning: comparison of methods"

Picoquant single-molecule workshop, Berlin, 2019, Poster and flash-talk presentation, "Tuneable photoswitches for chromatic aberrations-free multi-channel super-resolution imaging"

Chapter 1. General Introduction

In 2014, the Nobel Prize in Chemistry was awarded to Eric Betzig, Stephan W. Hell and William E. Moerner "for the development of super-resolved fluorescence microscopy " ('The Nobel Prize in Chemistry 2014. NobelPrize.Org' 2024). This award recognized the development of a new field of microscopy that circumvented a physical limit that was thought definitive for more than a century. Super-resolution microscopy methods became widely used and allowed the studying of molecular processes in the cells at the single molecule level, which was a great improvement compared to the ensemble measurements restricted by the resolution limit of conventional microscopy (Moerner 2012, 2015).

This new field of super-resolution fluorescence microscopy (abbreviated super-resolution or super-resolution microscopy later in this work) rests on fluorescence, microscopy and the diffraction limit as stated by Ernst Abbe in the second half of the 19th century (Ernst Abbe 1874).

In this general introduction, we will discuss fluorescence, microscopy, the diffraction limit and the development of super-resolution microscopy.

1.1 Fluorescence

Luminescence describes the emission of light, a photon, by a molecule or atom after receiving energy by a process other than heat. When heat is involved, it is called incandescence (Valeur and Berberan-Santos 2011).

In fluorescence, the molecule or atom absorbs an incoming photon and one of its electrons is transferred to another energy level e.g. excited to a higher singlet energy level. It quickly relaxes to the lowest vibrational energy state of the excited singlet state before relaxing to

any of the vibrational energy levels of the ground state, a process that can be accompanied by the emission of a fluorescence photon(Lakowicz 2006). Singlet energy levels conserve the opposed spin signs with the electron staying on the ground state. The excited electron can be transferred to a triplet excited state by changing its spin, a process called intersystem crossing (ISC). In this case, the transition back to the ground state is forbidden according to the Pauli Exclusion principle. The relaxation by emission of a photon from the triplet state is called phosphorescence and has lower emission rates meaning that the phosphorescence lifetimes $(10^{-6} - 10^{0}\ s)$ are much longer than fluorescence $(10^{-10} - 10^{-8}\ s)$.

1.1.1. Jablonsky Diagrams

Introduced by Alexander Jablonsky in 1933 (Jablonski 1933), the Jablonski diagram is used to represent electronic energy levels of atoms and molecules and the processes that involve the transitions of electrons form one level to another (Figure 1).

The Jablonsky diagram represents electronic and vibrational energy levels with lower energy levels on the bottom of the diagram (Figure 1 (a)).

S_0 is the singlet ground state. This corresponds to the lowest energy level of the molecule. S_{1-3} can be populated upon excitation of the molecule by the absorbance of a photon for example. T_1 is a triplet state where the spin of the electron is parallel to the spin of the electron staying on level S_0. Vibrational sublevels divide each electronic level. Upon absorbance of a photon (Figure 1 (b)), an electron populates one of the vibrational levels of a higher electronic level. The energy of the absorbed photon is equal to the difference of energy levels corresponding to the transition. Electrons can quickly relax to lower vibrational levels (Figure 1 (c) green) by internal conversion and then emit a fluorescence photon to relax to the ground state S_0 (Figure 1 (c) red).
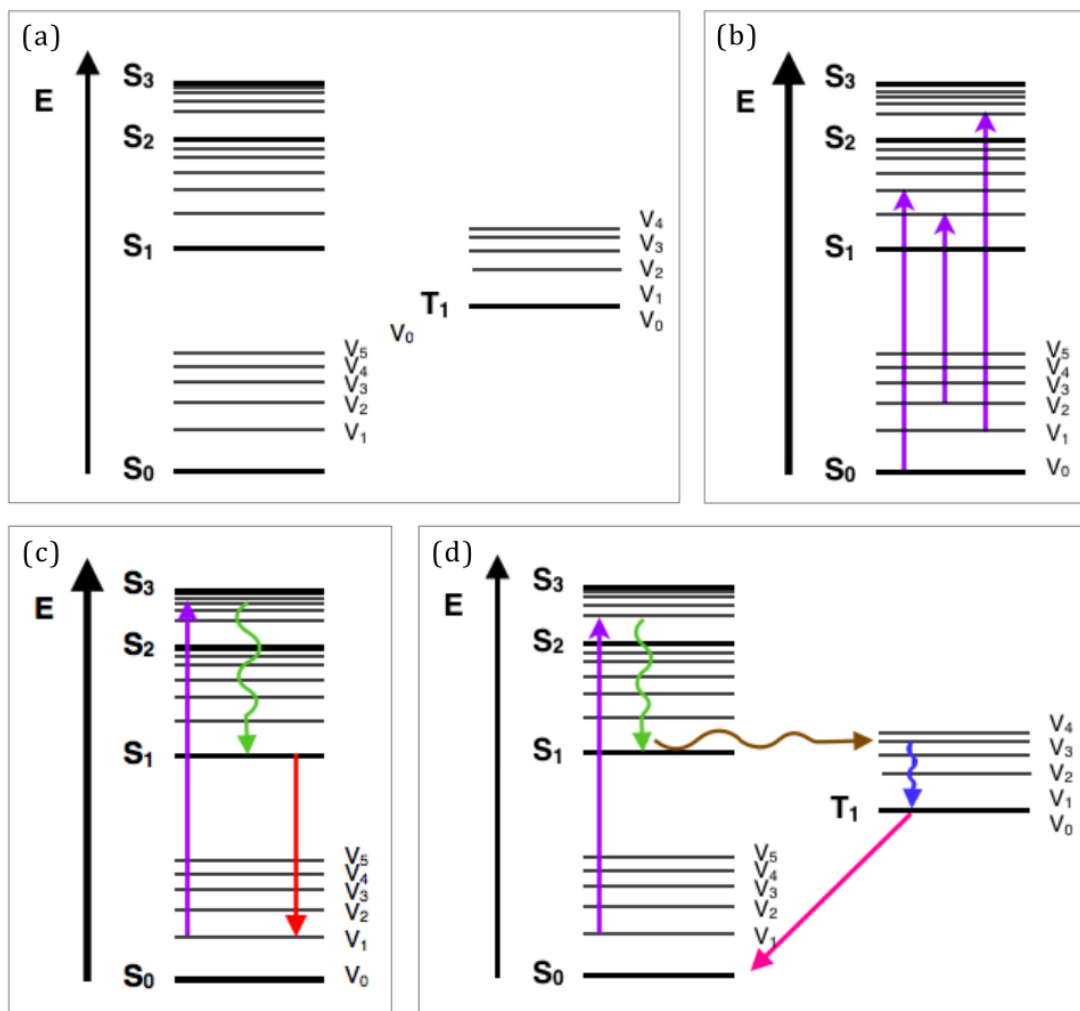
Figure 1 Jablonsky diagrams : (a) Electronic energy levels are represented as well as vibrational energy levels, (b) A molecule can absorb photons of energy corresponding to a transition between two energy levels, (c) non-radiative (wavy arrows) and radiative (straight arrows) transitions can occur, (d) transitions between singlet and triplet energy levels are called intersystem crossing. Reproduced and adapted with permission from (Jordan McEwen 2024)

Another transition of the excited state electron can occur by InterSystem Crossing (ISC) when an excited electron transfers from S_1 to an excited triplet state T_1 (Figure 1 (d) brown). The electron can then finally relax to the singlet ground state by emitting a fluorescence photon (Figure 1 (d) pink)

1.1.2. Stokes shift

Internal conversions to the lowest vibrational state of the excited singlet state are much faster ($10^{-12}\,s$) than radiative relaxation to S_0 ground state ($10^{-9}\,s$). This means that the vast majority of fluorescence emission is the result of transitions from the lowest energy level of the excited state S_1. It follows that the fluorescence emission is shifted to longer wavelengths that correspond to smaller energy differences compared to the absorbance electronic transitions (Figure 2). That is called the Stokes' shift (Lakowicz 2006).

1.1.3. Absorbance and emission spectra

Molecules composed of several atoms have several electronic levels, each divided in multiple vibrational levels. Transitions between any two levels are characterised by the energy difference between the levels. This energy can be related to the energy of photons that corresponds to $E = h\nu = hc/\lambda$ where h is the Planck constant ($h \approx 6.63 \times 10^{-34}\,\text{J}\cdot\text{s}$), ν is the frequency of the electromagnetic wave associated to the photon, c is the speed of light and λ is the wavelength of the electromagnetic wave associated to the photon. The absorbance of a photon transfers an electron from one electronic level to another, and the energy of the photon must correspond to the energy difference between the two levels. We can measure the absorbance of light by a molecule at each wavelength. The molecule will absorb photons that correspond to each transition between any two energy levels. By measuring the absorbance of a molecule at a range of wavelengths we can build an absorbance spectrum that is specific to the molecule and is the sum of all the possible transitions between its energy levels. Because of the limited precision of absorbance measurements and solvent relaxation, absorbance spectra look continuous whereas they should in theory be a series of minute peaks corresponding to each transition (Figure 2).
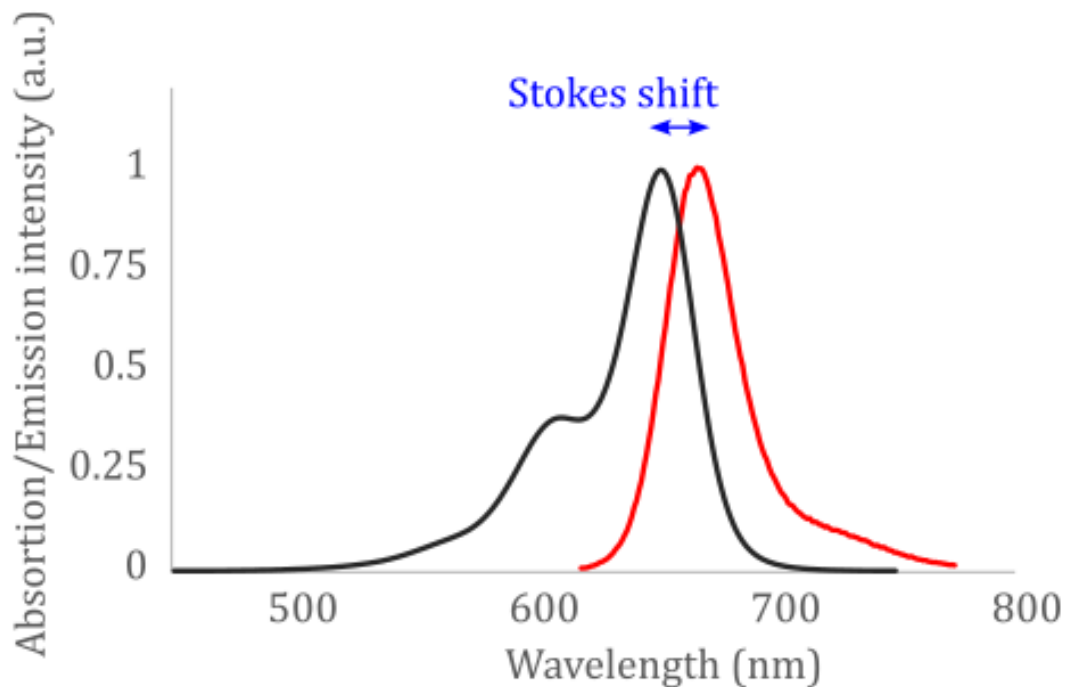
Figure 2 Alexa Fluor 647 absorbance (black) and emission (red) spectra. They are specific to each molecular species as they translate the electronic transitions happening upon absorption and emission of photons.

A similar spectrum can be plotted by measuring the fluorescence emission of a molecule in response to the absorbance of light of a chosen wavelength (Figure 2).

Atomic absorbance and fluorescence emission spectra are composed of well separated peaks that correspond to the transitions between electronic levels because there are no molecular bonds with other atoms and the rotational and vibrational levels do not exist.

1.1.4. Quantum yield

An electron on a higher energy level can relax to the ground state by radiative or non-radiative transitions. Non radiative transitions are not associated with the emission of a photon and the excess energy is dissipated in the form of heat or mechanical energy to the

surroundings. The quantum yield of a molecular species is the ratio of the number of emitted photons to the number of absorbed photons (Lakowicz 2006). It can be defined as a ratio of radiative and non-radiative processes:

$$\Phi(\lambda) = \frac{k_r}{k_r + k_{nr}} \tag{1}$$

Where k_r is the rate of fluorescence emission (s^{-1}) and k_{nr} is the rate of all non-radiative relaxation (s^{-1}).

1.1.5. Fluorescence lifetime

The excited state lifetime describes the average time that the fluorophore stays in the excited state before leaving it (Lakowicz 2006). It can be defined as:

$$\tau = \frac{1}{k_r + k_{nr}} \tag{2}$$

In the absence of competing non radiative processes, the intrinsic fluorescence lifetime is $1/k_r$. Usually non radiative processes exist but we measure only radiative relaxation rates (fluorescence). It follows that quantitative analysis of fluorescence lifetimes should take into account non radiative relaxation processes that can influence the results. For example, if a fast non-radiative relaxation process is present in a sample, the fluorescence lifetime measured by observing the time delay between absorption and emission of photons can be biased towards shorter values than the actual lifetime of the fluorescence emission pathway.

1.1.6. Fluorescence spectroscopy methods

Fluorescence spectroscopy measures the fluorescence properties of fluorescent samples as a large population, We call them ensemble measurements in the following. Ensemble measurements are used to build proofs-of-concepts of a new idea or as a routine control of

sample preparation. In the present work we used absorbance spectroscopy, fluorescence emission spectroscopy and fluorescence lifetime spectroscopy (time-resolved fluorescence spectroscopy). Those three methods allow the investigation of several of the many photophysics parameters of a given molecule in a given environment (absorbance, emission, fluorescence lifetime, polarisation)

Absorbance spectroscopy

Absorbance is measured with a UV-Vis spectrometer (Perkin Elmer Lambda 25) for a range of wavelengths to build an absorbance spectrum. Each molecular species in solution presents a signature absorbance spectrum with peaks for wavelengths absorbed by the species.

The UV-Vis spectrometer consists of a light source, here two of them to cover a large wavelength range: a deuterium lamp produces light between $190 - 350 \, nm$ and a halogen lamp covers the $300 - 1100 \, nm$ range. The light is filtered to a very small wavelength range by a monochromator, is split in two equal paths that pass through the sample and a reference sample, respectively. The residual light is measured by a detector on the other side. The monochromator includes a scanning mirror that allows to scan a chosen range of wavelengths, measuring the residual light for each step to reconstruct an absorbance spectrum. The absorbance is defined as:

$$A_\lambda = \log_{10} \frac{I}{I_0} \tag{10}$$

Where A_λ is the absorbance of the sample at wavelength λ (1)

$\quad I_0$ is the light intensity received by the sample $(W \cdot m^{-2})$

$\quad I$ is the transmitted light intensity $(W \cdot m^{-2})$

Each molecule absorbs light at specific wavelengths due to its structure. An absorbance spectrum shows peaks that are a signature of the molecule present in the sample. This can

be used as an identification tool.

A UV-Vis spectrometer allows for quantitative measurements and absorbance follows Beer-Lambert's law which allows the quantification of molecules in the sample:

$$A_\lambda = \varepsilon \cdot c \cdot l \tag{11}$$

Where A_λ is the absorbance of the molecule in the sample at wavelength λ (1)

ε is the molar absorbance coefficient ($L \cdot mol^{-1} \cdot cm^{-1}$)

l is the length of the light path through the sample (cm)

c is the concentration of the molecule in the sample ($mol \cdot L^{-1}$)

Absorbance is additive so the absorbance of a mixture of species absorbing at the same wavelength is the sum of their individual absorbances.

Beer-Lambert law only applies for absorbance values below 1.0. In practise, a sample is measured and if the absorbance is measured larger than 1.0, the sample is diluted and measured again and the concentration of the original sample is extrapolated from the second measure (Thatipamala, Hill, and Rohani 1993).

Fluorescence emission spectroscopy

A fluorescence emission spectrometer (Horiba Fluorolog) has a similar structure to the absorbance spectrometer. A wide wavelength excitation lamp produces broadband light that is selected by a scanning monochromator and shun on a sample. Fluorescence emission light is collected at a 90° angle of the excitation light path to minimise parasitic light from the excitation beam to be detected. The collected fluorescent light passes through another scanning monochromator and is recorded by a detector.

The fluorescence emission spectrometer allows scanning both excitation and emission wavelengths. This allows the characterisation of molecular species in a sample.

Fluorescence emission and absorbance spectroscopy are often combined to investigate the

composition or photophysical properties of a sample.

Fluorescence lifetime spectroscopy

Time-resolved fluorescence spectroscopy focuses on measuring the fluorescence lifetime of fluorescent molecules and the changes of the fluorescent lifetime in response to the environment in the sample. Typical fluorescent lifetimes last a fraction to a few nanoseconds. Fluorescent lifetime is a reliable signature of a given fluorophore in a given environment. Highly sensitive to the environment, fluorescent lifetime is a good marker to probe the environment and interactions of a fluorescent molecule with a sample.

In this work, we used the Time Correlated Single Photon Counting (TCSPC) method (Wahl 2014).

TCSPC consist of shining a pulsed laser on a sample while starting a stopwatch, waiting for the sample to emit a photon to stop the stopwatch when the photon is detected.

In more details, a high frequency pulsed laser is focused on a sample. For each pulse of laser, a start signal is sent to the time measuring device, a time-to-amplitude converter (TAC) that converts elapsed time to a measurable voltage by building the voltage in a capacitor between the start and stop signal. The fluorescent photon emitted by the sample is detected by a Photomultiplier Tube (PMT) that sends the stop signal to the TAC. A PMT is an amplification instrument that transforms the detection of a single photon into a measurable electrical current pulse involving millions of electrons (Wahl 2014). The electrical current generated is proportional to the rate of single photon detection so a PMT can be used to count single photons emitted by a fluorescent sample. PMT are also fast, which allows them to report millions of single photon detections per second (Wahl 2014). A PMT relies on a light sensitive photocathode that produces an electron when it absorbs a photon. The electron then passes through a charged electrode, the dynode. The collision

between the electron and the dynode releases additional electrons. The newly produced electrons are directed to another dynode and trigger more electrons to move. The cascade effect after several dynodes in line results in an electrical current of millions of electrons at the anode of the PMT.

When the stop signal arrives at the TAC, the voltage of the capacitor is measured and recorded in a histogram of recorded lifetimes. One time value is measured for each cycle of the pulsed laser. Acquisition parameters are adjusted so that on average one or two photon are detected for each hundred cycles of measurement. This avoids biases in measurements towards shorter lifetimes. Accurate records also require considering photons that are detected after being scattered by the sample or reflected by the instrument instead of following the absorbance/emission pathways. This is called the Instrument Response Function (IRF) or prompt. Typical times for the IRF are shorter than fluorescent lifetimes and it can be "subtracted" from the raw data during data analysis.

After hundreds of thousands cycles, typically when the highest bin count reaches 10000, the experiment is stopped and the histogram of lifetimes is analysed.

Fluorescent lifetimes follow an exponential decay probability curve that can be analysed by fitting single or multi-exponential decay functions following this equation:

$$f(t) = A * \sum_i A_i e^{\frac{-t}{\tau_i}} \tag{12}$$

In this project we used two programs to perform the exponential decay fitting, Horiba DAS-6 (Horiba Scientific, n.d.) and Pulse 6 by J-C Brochon (Brochon 1999).

1.1.7. Forster Resonance Energy Transfer (FRET)

Forster Resonance Energy Transfer (FRET) describes an energy transfer that happens between two fluorophore molecules when they are close to each other (Th. Förster 1948;

Theodor Förster 2012). FRET is observed when the two molecules are less than 10 nm apart as this energy transfer scales with the inverse sixth power of the distance between the partners (Figure 3(b)).

$$E = \frac{1}{1 + \left(\frac{r}{R_0}\right)^6} \tag{13}$$

Where E is the FRET efficiency, r is the distance between the donor and the acceptor and R_0 is the distance between the donor and the acceptor for which the efficiency is 50%.
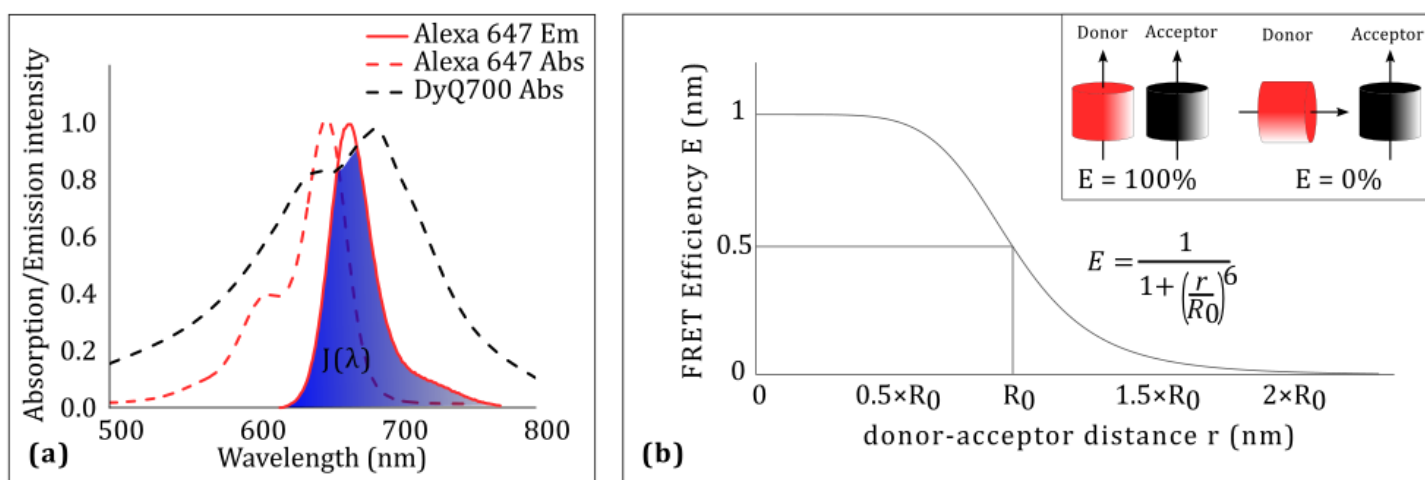
Figure 3 Fluorescence resonance energy transfer (FRET) can happen between a donor and acceptor molecule. (a) FRET requires an overlap of the donor emission and the acceptor absorbance spectra. (b) FRET efficiency is highly dependent on the donor-acceptor distance and the relative orientation of their respective dipoles (insert). R0 is the distance for which the FRET efficiency is 50%. The FRET efficiency is maximum when the donor and acceptor dipoles are aligned and minimum when they are orthogonal.

FRET occurs when the donor molecule of the pair becomes excited and relaxes in a non-radiative manner by transferring the excess energy to the acceptor molecule. This energy transfer happens through a coupling of the dipole moments (Valeur and Berberan-Santos 2011). FRET has been used to monitor conformational changes in proteins (Hong and Maret 2003) or study protein-protein interactions (Truong and Ikure 2001). The energy transfer induces several changes to the photophysical behaviour of the two fluorescent

molecules. The donor is quenched, its fluorescence emission intensity is decreased. Its fluorescence lifetime is also shortened. The fluorescence emission intensity of the acceptor molecule is increased.

Apart from the distance between the donor and acceptor molecule, the relative orientation of their dipole moments (Figure 3(b, insert)) and the overlap of their emission and absorbance spectra, respectively, influence the efficiency of FRET (Figure 3(a)). The Förster distance, usually named R_0 corresponds to the distance between FRET partners where the FRET efficiency is 50%. That is to say where 50% of excitation events result in a resonance energy transfer (Figure 3(b)).

Previous work also showed that FRET is compatible with single molecule microscopy measurements (Holden et al. 2010; Roy, Hohng, and Ha 2008) and can be demonstrated for switchable dyes such as Cy5 (Uphoff et al. 2010).

Switchable dyes bring another level of complexity. If both donor and acceptors are fluorescent and switchable, four pair populations are observed as follows: donor ON - acceptor ON, donor ON - acceptor OFF, donor OFF - acceptor ON, donor OFF - acceptor OFF. Each population will have a different emission profile.

Dark quenchers

At first, FRET was applied to donor acceptor pairs where both partners were fluorescent molecules. Both emitted fluorescent light with different but possibly overlapping wavelength and the FRET process influenced the fluorescence of both fluorophores. A dark quencher is a molecule that can transfer one of its electrons to a higher energy level and become excited by the absorbance of a photon but relaxes mostly by non-radiative processes, it does not emit fluorescence. They can act as an acceptor in a FRET pair (Le Reste et al. 2012). Le Reste et al. showed that dark quenchers are suitable as single

molecule FRET acceptors for single molecule imaging by TIRF microscopy. A limitation the authors pointed out is the bleaching of dark quenchers that can occur. When they are bleached dark quenchers lose their quenching ability as their dipole moment is perturbed and consequently, they do not meet FRET requirements of spectral overlap. One could extrapolate that dark quencher might be subject to photoswitching in the thiol-containing reducing environment used in dSTORM. If that was to be confirmed, it would increase the noise in the quenched probes intensity and blur the separation between quenched and unquenched probes.

1.2 Microscopy

In the second half of the 17th century, Antoni van Leewenhoek was one of the early developers of microscopes and is generally recognized as the first to observe single cells with a microscope. Early microscopes were rare and of varying quality. The 18th century saw the development of more reliable microscopes.

Microscopes are widely used tools that allowed many advances in biology and medical science. They lead to the understanding that cells are the basic units of life, from unicellular organisms to multicellular organism in all three domains of life, Archaea, Bacteria and Eukarya.

Optical microscopy is used to observe structures and processes in cells in the presence or absence of dyes that improve contrasts. The low contrast of cells and thin tissues under the microscope can be mitigated by the use of dyes that target specific compartments or structures of the cell including absorbing dyes and fluorescent dyes.

The targeting of specific structures can be obtained by the dye itself that associates directly with the target structure, for example ethidium bromide is a DNA intercalator that inserts

between nucleic acids of the DNA. Alternatively, non-specific dyes can be attached to a targeting molecule, for example an antibody or a toxin that specifically interacts with a structure of the cell.

At the end of the 19th century, Ernst Abbe introduced the limit of resolution due to diffraction (Ernst Abbe 1874) and by doing so, he created the foundation to produce microscopes with steady quality. In this article, Abbe presented the optical principles of the limits of resolution of microscopes and how they apply to the manufacturing of microscopes. He wanted to describe the theoretical equations governing the physics of image formation in a microscope so that microscope construction could rely on theory rather than empirical trial and error to optimise the microscope performance. The use of these equations aimed at allowing microscopes manufacturers to design instruments of calculated performance before building them instead of measuring the performance of empirically built microscopes after the fact. He also presented methods to standardise the evaluation of existing microscopes to estimate their performance. Finally, he presented the limits of performance expected for an idealised given microscope considering a perfect manufacturing without error.

1.3 Super-resolution microscopy

1.3.1. The diffraction barrier

Optical microscopy is based on photons that are emitted by a sample to form an enlarged image of the sample. To understand the limit of diffraction, we consider the sample as a series of infinitely small point emitters. If we first imagine a single emitter, the image of this point emitter on the camera of the microscope is not infinitely small. Because of the

diffraction of light at the objective pupil, a point emitter is imaged as a spot of finite size determined by the optical properties of the imaging setup that is commonly called point spread function (PSF). The main factors influencing the PSF are the numerical aperture of the microscope and the wavelength of the emitted light.

The image of a sample is an overlap of all the images of individual point-like emitters. The image is blurred, and the limit of resolution is defined as the minimum distance between two objects that we can discriminate.

Ernst Abbe described the minimum Full Width at Half Maximum (FWHM) of the PSF according to the diffraction of light at the objective pupil to be about half the wavelength of the detected light.

In 1903, Lord Rayleigh described what is now known as the Rayleigh criterion. It states that the minimum distance between two PSFs that are distinguishable is the distance that makes the maximum of one PSF coincide with the first minimum of the other PSF (Rayleigh 1903). This distance can be used as the limit of achievable resolution imposed by diffraction in microscopes. It can be written as:

$$d_{Rayleigh} = 0.61 \frac{\lambda}{NA} \tag{3}$$

Where λ is the wavelength of the observed light and NA is the numerical aperture of the microscope objective.

1.3.2. Circumventing the resolution limit

Cellular biology processes happen at nanometre scales inaccessible to conventional optical microscopy. Even cell organelles are poorly resolved in conventional optical microscopy. Considering the Rayleigh distance, only two parameters can be changed, the wavelength of the "messenger particle", photons or electrons and the numerical aperture of the

microscope.

Electron microscopy was the first method to surpass the resolution limit of conventional optical microscopy by using accelerated electrons with shorter wavelengths (Schermelleh et al. 2019). This allowed to improve drastically the achievable resolution with the drawbacks of limited targeting of specific structures and large and complicated instruments. But the main limitation of electron microscopy for biology studies is the intensive sample preparation including fixation, drying and coating of samples that forbid live cell observation.

At the end of the 20th century, several methods were developed to circumvent the resolution barrier in light microscopy. Each super-resolution method has its own advantages and limitations that can drive the choice of one method over another for a research project. The main differing parameters are the resolution improvement achieved, the speed of acquisition, the amount of data analysis required after acquisition and the level of hardware modifications needed compared to a conventional microscope (Schermelleh et al. 2019).

1.3.3. Super-resolution microscopy methods

The main super-resolution microscopy methods can be grouped by the strategies through which they improve the achievable resolution in optical microscopy. STED microscopy uses lasers and phase masks to deplete fluorescence sparing a very small area, SIM uses patterned illumination and mathematical reconstruction, SOFI and SRRF analyse the fluctuations of fluorescence intensity and SMLM methods use temporal separation and localization of photoswichable emitters (Vangindertael et al. 2018).

STimulated Emission Depletion (STED) microscopy

STED microscopy uses a modified confocal microscope setup that allows a second laser in addition to the standard fluorescence excitation laser (Klar et al. 2000). A donut shaped laser transfers fluorophores into a non-fluorescent dark state, sparing a small region in the "hole" of the donut. A second laser excites fluorescent molecules in a large area but only fluorophores in the spared central region emit fluorescent light that is collected by the confocal microscope and an image is built by scanning the sample. As fluorescence can only be emitted by the non-depleted central region, the resolution of the reconstructed images is improved to 50-60 nm lateral resolutions routinely (Schermelleh et al. 2019; Wegel et al. 2016; Sahl, Hell, and Jakobs 2017).

Structured Illumination Microscopy (SIM)

SIM uses patterned illumination in widefield (Gustafsson et al., 2008; Schermelleh et al., 2008)) and more recently through a scanning confocal microscope (Schulz et al. 2013). SIM relies on Moiré fringes that can be described as the patterns emerging from the superimposition of two or more repeating patterns. An important feature of Moiré patterns is that their frequency is smaller than the frequencies of the individual superimposed patterns. As an optical microscope acts as a filter of higher frequencies in the Fourier space, the resolution of the final image is improved compared to conventional microscopy (Vangindertael et al. 2018). The resolution improvement is obtained by mathematical reconstruction from several images recorded with different illumination patterns. SIM does not require any special sample preparation, and it works in thicker samples than other methods but it requires precise alignment and calibration of the microscopy setup (Schermelleh et al. 2019).

Fluctuation-based super-resolution microscopy

Super resolution Optical Fluctuation Imaging (SOFI) (Dertinger et al. 2009) and Super-Resolution Radial Fluctuations (SRRF) (Culley, Tosheva, et al. 2018) are two super resolution methods that improve the resolution by analysing the fluorescence intensity of blinking fluorophores in confocal or widefield microscopy images.

This thesis concentrates on the last group of methods that will be described in the next section, Single Molecule Localisation Microscopy (SMLM).

1.4 Single-Molecule Localisation Microscopy (SMLM)

Single Molecule Localisation Microscopy (SMLM) is a group of super-resolution microscopy methods that rely on the precise localisation of single molecules that are separated in time by blinking (Figure 4 (a)) and are observed individually in separate camera frames (Van De Linde and Sauer 2014; Rust, Bates, and Zhuang 2006; Heilemann et al. 2009; Betzig et al. 2006; Hess, Girirajan, and Mason 2006; Sharonov and Hochstrasser 2006). In SMLM, most fluorophores are in a dark state at the beginning of the recording. A small subset of fluorophores is activated and imaged. The size of the subset is controlled by chemical and laser intensity parameters, and it is chosen so that statistically, the probability is low that two fluorophores closer than the diffraction limit are activated at the same time. The fluorophores are imaged and photobleached or they switch back to the dark state. Another subset of fluorophores is activated and imaged. These few steps are repeated over tens of thousands of camera frames. The single molecules are then precisely localised (Figure 4 (b)) in each frame and a pointillistic image (Figure 4 (e)) is reconstructed with the

coordinates of all localised emitters. Routinely, resolutions of 20-50 nm are obtained, and expert laboratories can reach 10 nm resolutions (Lelek et al. 2021). The main difference between SMLM methods is how the fluorophores are switched ON and OFF.
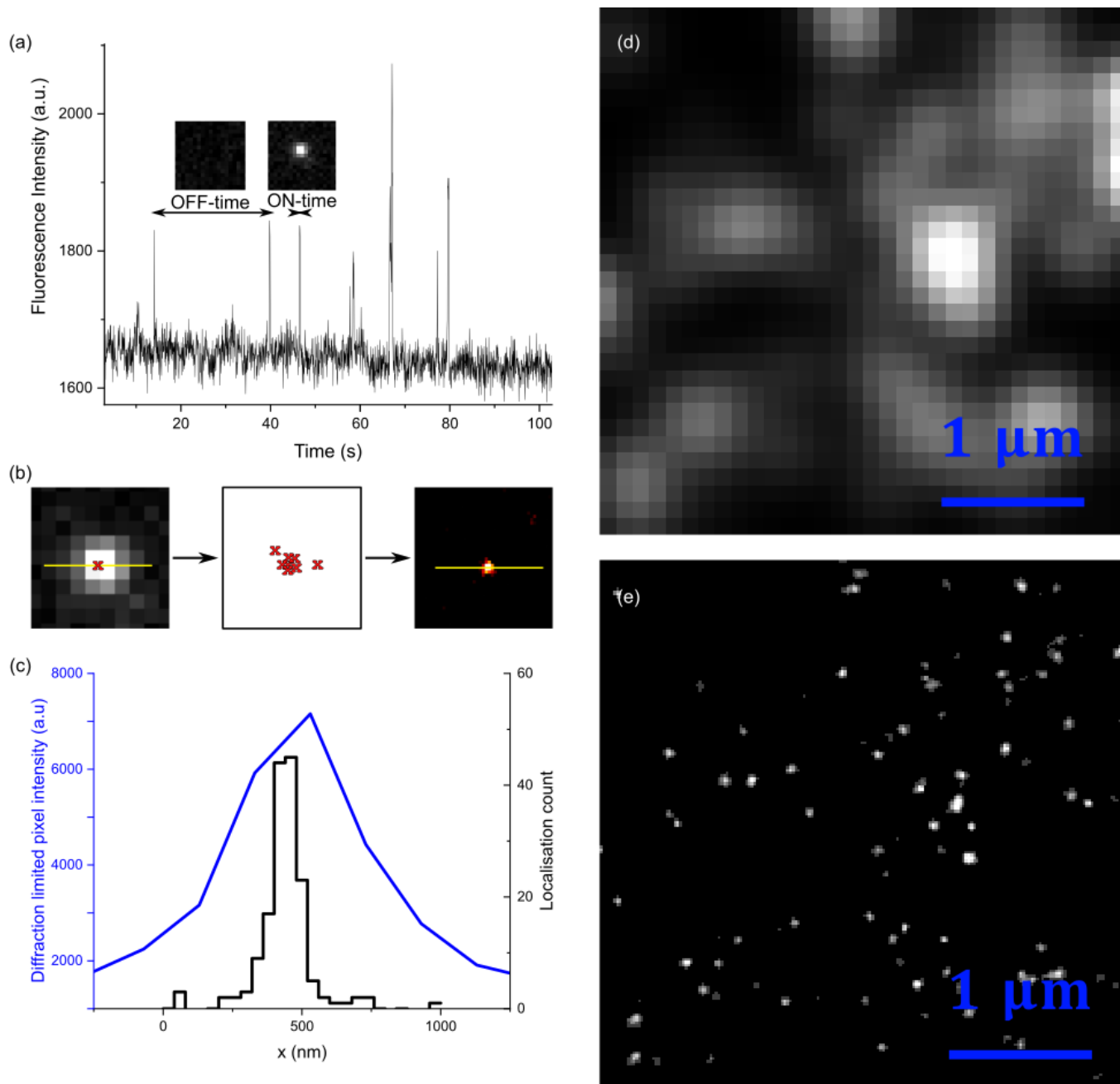

Figure 4 Single molecule localisation microscopy image reconstruction: (a) SMLM relies on the photoswitching of fluorescent molecules between a fluorescent form (ON-time) and a non-fluorescent form (OFF-time). (b)The centre of the PSF of each fluorescent molecule in each frame is localised precisely (b, left). All fluorescence events are localised (b, centre) and an

image is reconstructed as a 2D histogram where each pixel intensity value corresponds to the number of localisations in the corresponding area (b, right). (c) When we compare cross sections (yellow line in b) of the diffraction limited (blue) and super-resolution reconstructed (black) images, we observe that a point emitter's image is smaller in the reconstructed image which shows a better resolution. Single molecule localisation microscopy drastically improves the resolution by localising individually in separate camera frames emitters that are too close to be resolved in conventional microscopy. While a diffraction limited microscopy image (d) lacks fine details, the reconstructed super-resolution image (e) reveals fine structures (here, we observed glucose transporters GLUT-4 at the plasma membrane of adipocytes cells, more details are discussed in chapter 5 of this work).

1.4.1. SMLM experimental considerations

SMLM methods usually use a widefield microscopy setup. The quality of results of an SMLM experiment relies on several factors. The labelling should be sufficient to report the target structure without impacting the structure or function of the target. Thus, the physical size of the fluorophore should be kept to a minimum. A good spatial separation of emitters is obtained by a good separation of their individual emission in time. Then, each fluorophore should be active in a few frames every thousands of frames so that, statistically, they are not fluorescent simultaneously with their closest neighbours.

A high signal to noise ratio promises a better localisation precision and a better resolution in the reconstructed image. The SNR can be improved by reducing the background, e.g. with cooled cameras and TIRF (total internal reflection fluorescence) illumination. It can also be done by increasing the signal by increasing the number of photons emitted by the fluorophore in the frame. That will be achieved through camera settings (longer exposure time) or by changing the buffer conditions (Herdly et al. 2023). The imaged sample is immersed in a water-based solution containing a pH buffer system that controls the pH, thiols that are involved in the photoswitching of cyanine dyes and an enzymatic system to control the concentration of dissolved oxygen.

Typical SMLM image stacks contain tens of thousands images and are recorded in a dozen

minutes to an hour depending on the fluorescence intensity, camera sensitivity and number of recorded frames. This prevents the use of SMLM for observing fast biological processes. The localisation analysis takes a few seconds to several minutes depending on the choice of software package and the complexity of the analysis. Some efforts are made to allow close to live analysis during image recording.

1.4.2. Separation of emitters and cyanine photoswitching

SMLM methods rely on the sequential imaging of nearby emitters in different frames so that their precise localisation is not impacted by the overlap of their PSF in the recorded image. Emitters are separated in time before their localisation separates them in space.

To separate emitters so that their PSF do not overlap, SMLM typically requires the recording of tens of thousands images of the same field of view of the sample while the majority of emitters are non-fluorescent and a small subset of emitters is fluorescent in each frame (Lelek et al. 2021).

The ON and OFF switching of fluorophores is stochastic for an individual molecule but it can be statistically controlled for populations of fluorophores. The switching between states can be driven by chemical or photochemical processes. Switching fluorophores are recorded in conditions that ensure that on average, two active fluorophores will be well separated in space to avoid overlap of their emission patterns.

Point Accumulation In Nanoscale Topography (PAINT) is a method in which fluorophore are not switched ON and OFF but they are freely moving in the imaging buffer and transiently attach to the target for a short time before moving freely in the buffer again (Lelek et al. 2021; Sharonov and Hochstrasser 2006; Schnitzbauer et al. 2017). The time

they spend immobilized on the target allows their precise localisation. This method suffers from a high background from freely diffusing fluorophores, but this can be mitigated by TIRF imaging for example. DNA-PAINT is a prominent variant of PAINT, where the fluorophore is bound to a short DNA oligo strand whereas the target holds the complementary DNA strand. By varying the sequence and length of the DNA strands, the immobilization time can be tuned.

(fluorescence) PhotoActivated Localisation Microscopy ((f)PALM) approaches were initially presented by Betzig et al (Betzig et al. 2006) and Hess et al (Hess, Girirajan, and Mason 2006) in 2006. ((f)PALM uses fluorescent proteins that can be activated upon illumination by UV light. In PALM, fluorophores can irreversibly switch from an OFF to an ON state by activation by UV light or spontaneously. Each subset of activated fluorophores is photobleached with longer wavelengths before the next subset is activated. In fPALM, fluorescent proteins (for example Eos and Dendra 2) can be switched from one fluorescent state to another irreversibly. In their initial "green" state, they absorb around 488 nm but upon irradiation by UV light at 405 nm they switch to a "red" state where they absorb at 561 and 520 nm respectively (Turkowyd, Virant, and Endesfelder 2016). Again the "red" fluorescent protein needs to be photobleached before the next subset is activated.

Fluorescent proteins can be encoded directly in model organisms to attach the fluorophore to the target protein (Shcherbakova et al. 2014).

In 2005, Bates et al (Bates, Blosser, and Zhuang 2005) and Heilemann et al (Heilemann et al. 2005) demonstrated that carbocyanine dyes can be switched between a dark and a fluorescent state. This led to the development of STochastic Optical Reconstructiuon Microscopy (STORM) (Rust, Bates, and Zhuang 2006) and directSTORM (dSTORM) (Heilemann, Van De Linde, et al. 2008; Van De Linde et al. 2011; Heilemann et al. 2009).

In STORM, a pair of reporter and activator dyes, Cy5 and Cy3, respectively, are associated

on a DNA scaffold in close proximity. Cy5 can be switched to a dark state by red light and it can be switched back ON with green light. The recovery rate of Cy5 depends strongly on the presence of Cy3 in close proximity (Bates, Blosser, and Zhuang 2005; Rust, Bates, and Zhuang 2006).

dSTORM uses the same property of Cy5 and other carbocyanine dye such as Alexa Fluor 647 (later named Alex 647 or A647) to switch between a dark and a fluorescent state but it was demonstrated that Cy5 could be photoswitched directly without the need for an activator dye, thus simplifying target labelling (Heilemann, Van De Linde, et al. 2008).
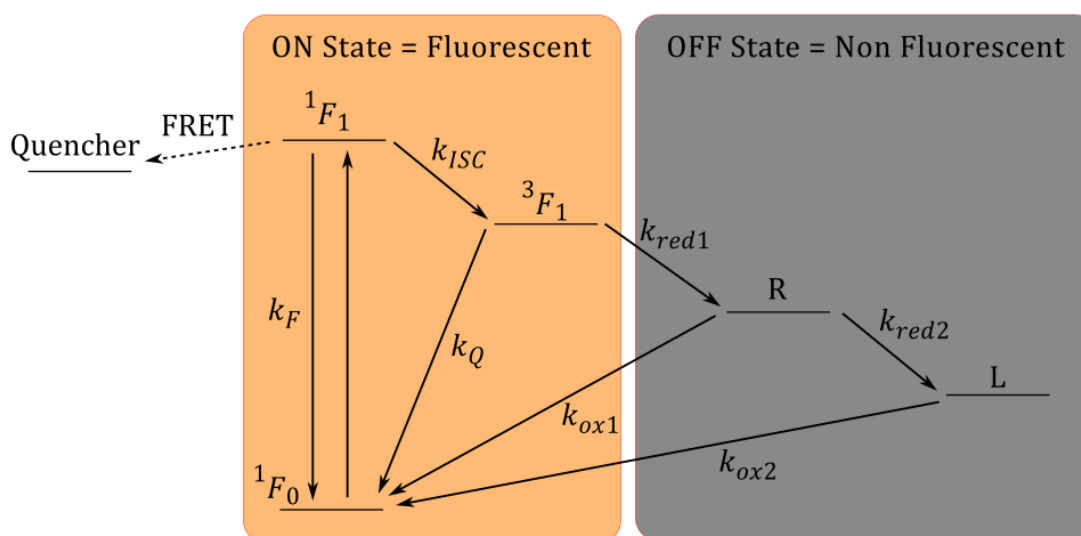
Figure 5 Photoswitching of carbocyanine dyes in dSTORM. Cyanine dyes emit fluorescence photons by cycling between singlet ground and excited states ($^1F_0$ and $^1F_1$, respectively). Unfrequently, they can undergo intersystem crossing to populate a triplet excited state $^3F_1$ and return to the singlet ground state $^1F_0$ by emitting a phosphorescence photon. The triplet excited state $^3F_1$ can also react with reducing agents to switch to a non fluorescent reduced state R that can in turn be further reduced to a leucoform L. Both R and L states can react with oxidating agents to return to the singlet ground state $^1F_0$ without emitting photons and resume the fluorescence cycle. Each state transition happens at a rate k_i that is influenced by the properties of the dye and environmental influences. The tuning of those rates allows to control the photoswitching rate and emission rate of fluorophores. The presence of a FRET partner adds another energy relaxation path that influences the behaviour of the fluorophore and the corresponding fluorescence emission.

This thesis focuses on dSTORM and the details of the underlying photoswitching

mechanism will be described in the following (Figure 5). In dSTORM, the underlying mechanism of the photoswitching of Alexa 647 and some other carbocyanine, rhodamine and oxazine dyes has been demonstrated (Van De Linde and Sauer 2014). A fluorophore can absorb a photon in its absorbance wavelengths and transition from a singlet ground state $^1F_0$ to a singlet excited state $^1F_1$. It can then relax by emitting a photon and going back to the ground state with a fluorescence emission rate k_F. But another route available from the singlet excited state $^1F_1$ is the conversion to a triplet state $^3F_1$ by InterSystem Crossing (ISC) at a rate k_{ISC}. Because $k_{ISC} \ll k_F$, the population of the triplet state is much less likely than the emission of a photon so on average the fluorophore will go through thousands of fluorescence cycles before populating the triplet state.

From the triplet state, the fluorophore can be quenched back to the ground state $^1F_0$ by a potent triplet state quencher such as molecular oxygen without the emission of a photon with a rate k_Q, in which case it can resume the fluorescence cycle. Another route available from the triplet state $^3F_1$ is the interaction with reducing agents (e.g; thiols) that disrupt the conjugated electrons chain to form a non-fluorescent reduced fluorophore radical R with a rate k_{red1}. Because $k_{red1} \ll k_Q$, it is more likely that the fluorophore will get back to the ground state $^1F_0$ than switching to the OFF-state R, which means that on average, the fluorophore will go through many cycles through the triplet states $^3F_1$ before being switched OFF.

Some fluorophores can further be reduced to a leucoform L with a rate k_{red2}. Both the R and L forms of the fluorophore can be oxidized back to the singlet ground state $^1F_0$ with rates k_{ox1} and k_{ox2}. The photoswitching buffer contains two controllers to manipulate the rates involved. An oxygen scavenger system removes oxygen from the buffer and reduces the oxidation rates k_Q, k_{ox1} and k_{ox2}. Thiols are also present in the buffer and promote the

transition to the OFF-state R and also the relaxation to the ground state through back electron transfer (Holzmeister, Gietl, and Tinnefeld 2014; Gidi et al. 2020). Moreover, their concentration controls the reducing rates k_{red1} and k_{red2}.

If we consider that $k_{red1} \ll k_Q \ll k_F$ and that we can at the same time remove oxygen to reduce k_{ox1} and k_{ox2}, after a few seconds in the fluorescence cycle, most fluorophores in a sample will populate the dark state and reactivate stochastically after long times. This describes the blinking of molecules in dSTORM. They emit thousands of photons on average during an ON time shorter than a second in dSTORM experiments before switching to a dark state where they reside for a few minutes before switching back to the ON state and showing again thousands of cycles of fluorescence.

We can describe the photoswitching in terms of number of cycles need on average to make a transition. For example, on average, the ISC transition $^{13}F_1/{}^3F_1$ will require thousands of fluorescence cycles to occur and the $^3F_1/R$ transition will require hundreds of ISC cycles, equating to hundred thousands of fluorescence cycles.

When we introduce the acceptor for FRET in the shape of a dark quencher, there will be an energy transfer (FRET) by the interaction of the acceptor with the singlet excited state $^1F_1$. Because of this energy transfer, the fluorophore repopulates the singlet ground state $^1F_0$ and can resume the fluorescence cycle. Because the FRET interaction happens with the singlet excited state $^1F_1$ it competes with the rate k_{ISC} but does not change k_{red1}. It means that there will be fewer photons emitted each second i.e. lower emission intensities and it will take more time on average for the fluorophore to switch OFF because it will take more $^1F_0/{}^1F_1$ cycles to generate enough ISC cycles for the reduction transition to occur.

1.4.3. Single Molecule Localisation

Data analysis is key in SMLM. The precise and accurate localisation of hundreds of thousands of single molecules allows the reconstruction of the super resolution image. SMLM emerges from the idea that individual molecules can be precisely localised if their PSF do not overlap. This stems from the idea that the centre of a pattern can be determined with a precision smaller than the pattern width. When the microscopy setup is designed to spread the PSF of individual emitters over a few camera pixels, sub pixel differences in the coordinates of an emitter can be resolved by localising precisely the centre of the PSF as the PSF is symmetrical around the true position of the emitter.

The main steps of a localisation software are the detection of single-molecule candidates, the validation and precise localisation of single molecules and the export of results, usually with a reconstructed image and a localisations list.

The first step aims at detecting possible single molecule emissions, to define starting coordinates for the 2D Gaussian fitting. The preprocessing of the image can involve noise reducing algorithms such as wavelet filtering (Ovesný et al. 2014). Detection of candidates is then allowed by extracting local maximas or thresholding the pre-processed image. The list of candidates is then used to fit a 2D Gaussian or more complex PSF models to the region of each candidate and extract sub pixel coordinates. More complex PSF models include experimentally measured PSF functions that correspond to the microscopy setup. Experimentally measured PSF are more precise than idealised PSF function such as 2D gaussian but require an additional calibration step (Sage et al. 2019).

The 2D Gaussian function is a good approximation of the true PSF pattern (or Airy pattern). It is used by many localisation algorithms as it is easier to fit and fitting parameters (equation (4)) directly provide a good approximation of the PSF width (σ_x and σ_y),

amplitude (A) and the coordinates of its centre (x_0 and y_0).

$$f(x,y) = A exp\left(-\left(\frac{(x-x_0)^2}{2\sigma_x^2} + \frac{(y-y_0)^2}{2\sigma_y^2}\right)\right) + B \qquad (4)$$

The most accurate algorithms are based on maximum likelihood estimation (Sage et al. 2019; Ober, Ram, and Ward 2004).

Localisations can be filtered in post-processing by applying filters to their parameters. For example, out of focus localisations can be rejected by applying boundaries to the PSF FWHM allowed.

1.4.4. Results

The filtered list of localisations is usually exported as a text file and a super-resolution image is created. Usually they consist of two-dimension histograms counting the number of localisation and/or their respective intensity in bins smaller than the diffraction limit, 5-50 nm usually. The color code of reconstructed images can reflect the number of localisation or intensity but it can also use any other parameter of the localisation list. As an example, color-coding by the frame number can show drift during the experiment when repeated localisations of an emitter change coordinates over time. Quantitative analysis can be performed on the localisations list by grouping the repeated localisations of each emitter using cluster analysis.

A pointillistic image is then reconstructed by plotting a 2D histogram of the coordinates of all the localisations in the entire image stack. Again, the image color code can show the number of localisations at each coordinate but also other parameters.

1.5 3D SMLM

1.5.1. 3D visualisation in the human eye and in super-resolution microscopy

A microscope works as a camera for small objects. In an image, a 3-dimensional scene is depicted on a surface. The information from the third dimension can leave traces in the 2D image. In an image (Figure 6 (a)), some parts are blurred, others are sharp. The latter constitute the focal plane. Similarly, we observe the world with our eyes that convert the 3D world into 2D images forming on the retina that are then interpreted by the brain. Human 3D perception is currently investigated by brain imaging to decipher the computation performed by the brain in the visual cortex (Welchman 2016). This review also describes how the eye-brain system uses depth cues to interpret the 3D scene observed.

We combine depth cues that provide complementary information to interpret a scene (Figure 6 (c)). Depth cues include(Welchman 2016):

- Disparity: Because the two eyes record images from different positions in space, the recorded images are slightly different and objects at different depths in the scene will be affected differently in their positions in the two formed images.

- Shadows: Projected shadows can give hints of objects positions in space

- Size: size comparison of familiar object in a scene gives a sense of their relative position in the scene

- Occlusion. An object obstructing the vision of another one must be closer to the observer. Whether the obstruction happens for both eyes gives additional

information.

- Texture: repeating structure on an object or a part of the scene can be a good reference for size comparison. For example, the repeating pattern on a carpet will look smaller at the distal end relative to the observer. If the object is familiar then the observer knows that the texture/carpet pattern has the same size over the carpet surface, hence this is a cue to the depth.

- Blur: Objects at the focal plane of the eye will produce a sharp image on the retina whereas objects away from the focal plane (grey box, Figure 6 (b)) will be blurred.

- Shading: The variation of light and shadow over the surface of an object gives clues to its curvature and shape as surfaces that are perpendicular or parallel to the direction of light illuminating the scene will reflect different amounts of light.

- Perspective: parallel lines in a scene will appear to converge on a point when observed by the eye. Using this fact on lines that we know to be parallel in a scene gives hints of their relative position in space.

The visual system first needs to create a correspondence between the images from two eyes (Welchman 2016). This matching step is also an important step in biplane 3D SMLM (see section 1.5.2). In this case, we measure coordinates shifts between the two planes recorded on the same camera chip and choose a search radius to account for the noise that might blur the position of emitters. Current research suggests that the human brain interprets the various depths signals in quasi-independent modules and combines the results of the quasi-independent analysis to form an interpretation of the 3D scene (Welchman 2016).

A microscope has limitations and cannot use all the methods that the human eye-brain system has evolved to perform.
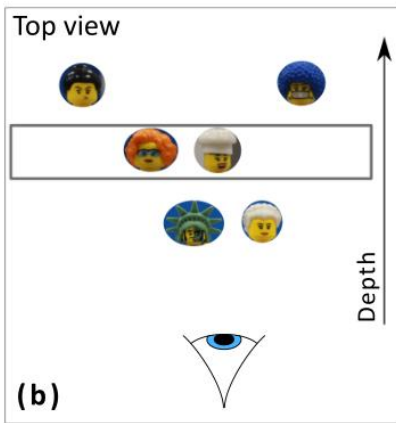
Figure 6 How the human eye-brain system reconstructs 3D scenes: (a) Humans can reconstruct the positions of objects in a 3D scene from a 2D image. (c) The eye-brain system uses a combination of depth cues to interpret the 3D arrangement of objects in the scene that is observed. We often combine several cues to elucidate the position of objects.

Stereopsis and convergence are not possible with a single microscope objective and microscopy samples such as thin tissue samples or single cell layers are transparent which forbids the use of occlusion. Hence the occultation is not useful. The relative sizes of objects are too similar to extract any relevant axial information. Finally, we can change the focus and it is often the method of choice in microscopy. This is done by scanning a sample perpendicular to the focal plane and reconstructing a 3D image or a stack of 2D images.

In this project, we want to avoid the very long acquisition time of axial scanning 3D microscopy. Particularly, SMLM already requires the recording of several thousand frames for each focal plane. This would lead to many issues such as very long data acquisition and analysis, photobleaching, and sample stability issues.

An alternative to scanning 3D microscopy is to extract the axial information from 2D images themselves. This could be done with a very simple algorithm: In focus = in the focal plane, out of focus = in front or behind the focal plane, more blurred = farther from the focal plane.
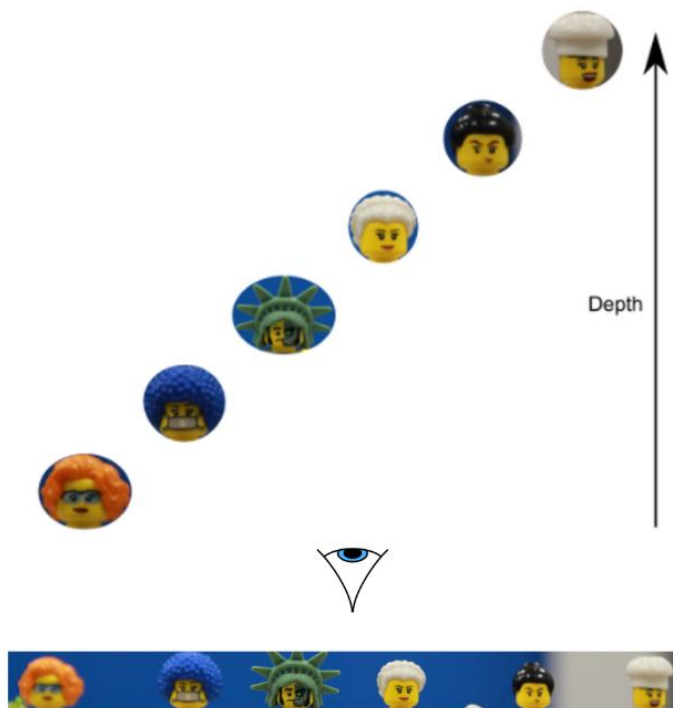
Figure 7 When we forbid occultation, relative size and other human eye methods for 3D reconstruction, it is harder to determine whether the figure with glasses or the one with a chef's hat are in front or behind the focal plane.

When the only available information is the blurriness, we cannot discriminate objects in front or behind the focal plane (Figure 7). 3D SMLM methods aim at resolving this issue and quantifying the blurriness to extract relevant axial information from 2D images. SMLM

has an advantage compared to conventional microscopy in that we record images of spatially separated subsets of emitters, and we can encode information in the shape of these images.

1.5.2. 3D SMLM

The most common methods for 3D SMLM can be classified in three categories, multiplane imaging, including biplane imaging, point-spread function engineering and interferometry (Sage et al. 2019). In multiple plane imaging, images of two (Figure 8 (a) left) or more focal planes are analysed to extract the axial position of each fluorophore (Huang et al. 2008; Juette et al. 2008). In PSF engineering, an optical aberration is voluntarily introduced in the system (Pavani et al. 2009). This aberration is designed to show a change depending on the axial position of the emitter (Figure 8 (a), right). The angle, position, shape or size of the aberration encodes the axial position of the emitter (Proppert 2014).

Finally, interferometry uses two opposing objectives to generate photon interference that can be decoded to obtain axial information (Shtengel et al. 2009). Interferometry will not be described in more detail as it was not studied in this work.
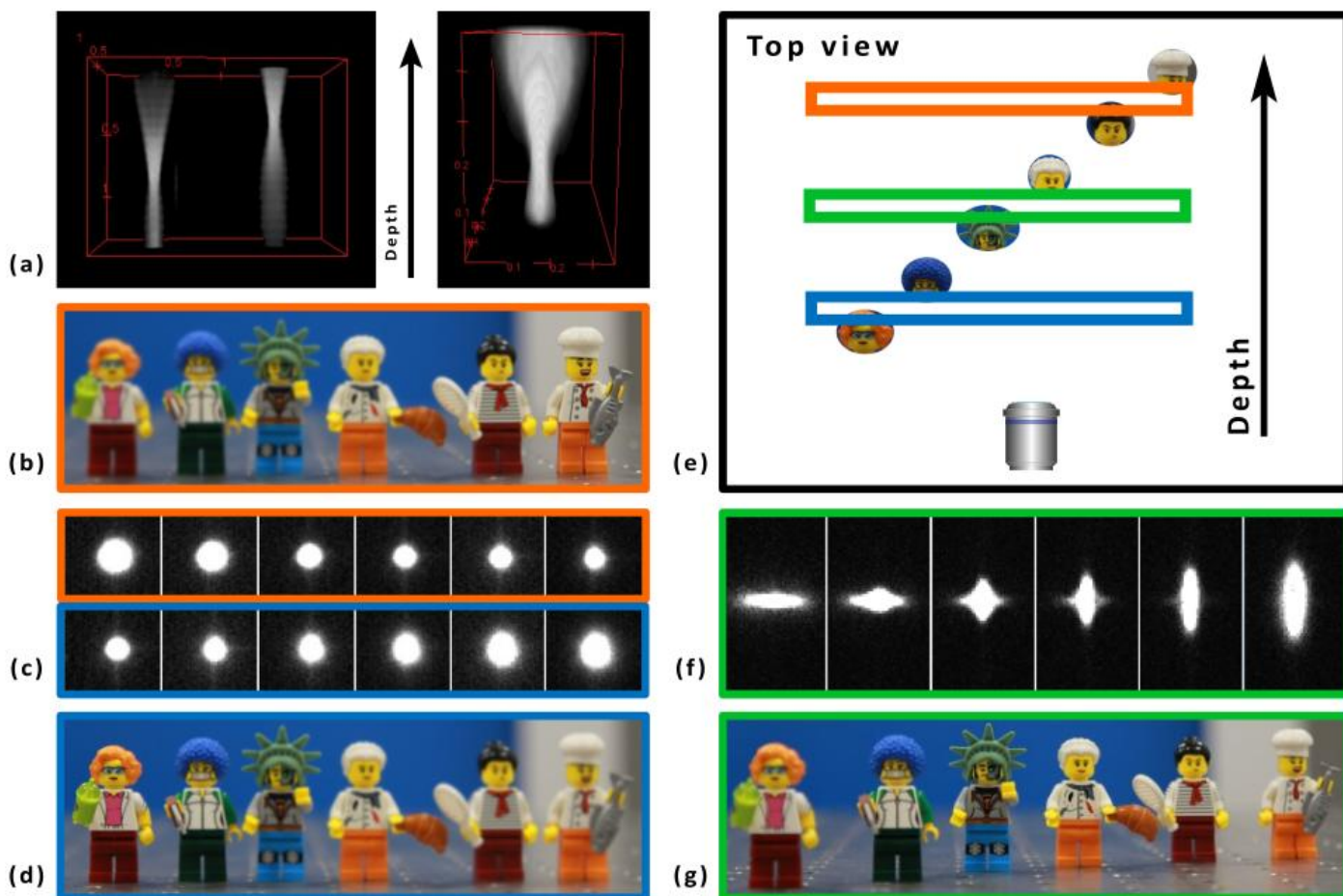
Figure 8 3D-SMLM (a) 3D reconstruction of the PSF in biplane(left) and astigmatism (right) 3D-SMLM. The depth of an emitter relative to the focal plane is encoded in the shape and size of the PSF. (b-d) In biplane, two images of the sample are recorded. The focal planes of the two images are shifted along the axial direction. Each emitter has a different image size on each image corresponding to a different degree of "blurriness". By comparing the relative image sizes in both images and using a calibration reference, we can determine the axial position of each emitter in the sample. (e) Top view of the scene showing the position of both focal planes in biplane and the position of the focal plane in astigmatism. (f-g) in astigmatism, the PSF is distorted in orthogonal directions above and below the focal plane. The direction encodes on which side of the focal plane the emitter is located and the size of the PSF encodes the distance from the focal plane.

1.6 SMLM applications

The development of super resolution microscopy has allowed biologists to study sub cellular structures such as the nucleus and organelles with improved resolution. Macromolecules were studied and their protein subunits were observed by SMLM (Löschberger et al. 2012). A few applications are presented here as examples among many other uses of SMLM to answer biology questions.

SMLM and particle averaging lead to the discovery of the subunits organization of the nuclear pore complex (Schlichthaerle et al. 2019; Szymborska et al. 2013; Broeken et al. 2015; Löschberger et al. 2012). Nuclear pore complexes have also been used as reference structures to compare different methods developments in SMLM (Thevathasan et al. 2019). The cytoskeleton in axons and dendrites of rat hippocampal neurons was better understood after SMLM resolved its ultrastructure (Xu, Zhong, and Zhuang 2013). The structure of herpes simplex virus was also studied by SMLM (Laine et al. 2015). By using SMLM and particle averaging, Laine et al showed that proteins organise in concentric shells in the HSV-1 viral envelope.

The Glucose transporter 4(GLUT-4) dispersal in reaction to insulin was studied by Koester et al using dSTORM (Koester, Geiser, Bowman, et al. 2022).

In this study, the authors showed that the dispersal of the glucose transporter 4 (GLUT-4) at the plasma membrane is stimulated by insulin. Further, they show that this effect is specific to GLUT 4 in several cell types and that this mechanism could be related to insulin resistance observed in diabetes (Koester, Geiser, Laidlaw, et al. 2022; Gao et al. 2017). This study shows that SMLM can be used to advance the understanding of human diseases and contribute to the effort to address a world-wide health issue.

1.7 Recent developments and outlook

Recent developments of SMLM methods aim at addressing the remaining limitations of SMLM and widen the applications of SMLM methods. Some research groups also focus on the development of new fluorescent dyes (Grimm et al. 2016, 2015) or the use of fluorescent nanoparticles for SMLM (W. Li et al. 2022).

SMLM can be combined with other imaging methods to obtain complementary information about a single sample by combining methods that have different advantages and limitations. For example, correlative light and electron microscopy combines SMLM and electron microscopy. In this association, electron microscopy allows a better resolution but lacks target specificity while SMLM allows imaging of a specific biological structure (Sochacki et al. 2014).

SMLM can be combined with light sheets to improve the performance of SMLM in thick samples (Cella Zanacchi et al. 2011).

Another recent development is MINFLUX that aims at reducing the local laser illumination intensity to reduce sample damages that have been reported for high laser intensities. MINFLUX combines the donut shaped laser illumination of STED and the photoswitching of single molecules of SMLM and applies a three-point localisation method to precisely localise fluorescent emitters with very good resolution and lower photon counts than other SMLM methods(Balzarotti et al. 2017).

Recently, two teams combined structure illumination and SMLM methods to gain a two-fold improvement of the resolution compared to the SMLM alone (Gu et al. 2019; Cnossen et al. 2020).

1.8 Thesis summary

This thesis presents the development of a multi-purpose imaging platform focused on dSTORM. The following chapters each present one aspect of the optimisation of dSTORM imaging to optimise the quality of results for future projects in the laboratory.

In chapter 2, we present the microscopy setup that was used during this PhD project. We discuss the importance of data analysis and how developing custom data analysis routines helps the work in SMLM. We also describe how a 3D SMLM setup can be implemented with minimal hardware changes and some additional data analysis and calibration.

In chapter 3, we present a FRET-based method for multi-channel SMLM. We describe ensemble absorbance, fluorescence emission and time-correlated fluorescence spectroscopy experiments that provide a proof-of-concept of the multi-channel method in ensemble measurements. FRET efficiencies of 60-80% are measured. Single molecule experiments showed a limited separation of two channels that overlap strongly on their intensity. A better understanding and control of Alexa 647 photoswitching was necessary and led to the work in the next chapters.

In chapter 4, we demonstrate that a MEMS mirror can be used to transform a Gaussian illumination into a homogeneous illumination, with comparable performance to a commercially available refraction based flat illumination device, the piShaper, but with the additional tuneability. We investigate the effect of different illumination schemes on the photoswitching of Alexa 647 and the consequences for the quality of SMLM images using several metrics to evaluate the quality of the illumination. We also present a protocol to evaluate competing illumination schemes and propose a method to optimise the choice of the recording frame rate. Our MEMS device also shows several advantages over the piShaper such as the low electric control requirements, as a simple sinus sum electrical

signal was used, a small footprint in the setup and the opportunity to use different parameters to produce an illumination gradient for studying photoswitching.

In chapter 5, we study 14 combinations of pH and MEA concentrations to investigate their respective impact on the photoswitching of Alexa 647 and consequently on the image quality. Their impact appears to be summarised by the thiolate concentration as a one-dimension parameter that is dependent on the two other parameters.

We demonstrate that small changes to thiolate concentration can strongly penalize the resolution of SMLM. We propose a method to find the best range of thiolate concentration the use of a range of thiolate concentrations of 1.5-15.6 mM for which we observe >90% of the resolution improvement. Within this range of thiolate concentrations, the MEA concentration and pH can be varied to accommodate other requirements of experiments such as the combination of cyanine dyes with other pH sensitive dyes or pH sensitive samples.

Chapter 2. Multi-purpose microscopy setup building, characterisation and software development towards 3D super-resolution microscopy

2.1 Abstract

A reliable and well-understood microscope system is paramount to achieve the best increase in resolution permitted by dSTORM. The characterisation, calibration and optimisation of our system consist of several steps that will be developed in this chapter. This will include the limitations found in any optical system and enable us to develop correction strategies to reduce their impact on the quality of future experiments. This chapter describes most of the instruments and software that was used throughout the project. Instruments or software that were used only in some parts of the project will be detailed in the relevant chapters.

Setting up instruments and designing protocols for experiments or data analysis was an important part of this PhD project. The first months of the work were focused on building and characterising the setup. All along this PhD project, protocols were developed to use new setup features that improved the SMLM results quality. Further improvements are described in chapter 4 to obtain flat-field illumination and chapter 5 to study the photoswitching of cyanine dyes. Several developments of the SMLM setup discussed in this

chapter are not used for experiments in the following chapters because the work presented in this thesis is part of a wider project in the laboratory which aims at building a multi-purpose microscopy platform that will benefit from those setup developments in the future.

The third spatial dimension can be explored on a dSTORM system by altering the emission path. This method consists in "decoding the third dimension" as Sven Proppert described it in his thesis (Proppert 2014). His thesis describes in great details the theoretical and practical details of 3D localisation microscopy. 3D dSTORM had been used before the present work by many super-resolution research groups. Our work on 3D-dSTORM focused on optimising well-established methods for our setup.

In this chapter, we present the characterisation of our dSTORM system on reference structures, fluorescent beads and single molecule surfaces. We further describe and compare several methods to perform 3D localisation microscopy in order to optimize the hardware and data analysis. Furthermore, we discuss how computer simulations can be used to compare data analysis methods to improve localisation accuracy in SMLM experiments.

2.2 Introduction

SMLM setups are composed of one illumination side with at least one laser, followed by one objective and a sample holder, i.e. a microscope body, and an imaging path with at least one camera (Cabriel et al. 2019; Huang et al. 2008; Szalai et al. 2021; Zhou et al. 2019).

Our work focuses on dSTORM (direct STochastic Optical Reconstruction Microscopy), a single molecule localisation microscopy (SMLM) method that consists of the

photoswitching of fluorescent molecules and their localisation with nanometre precision (Heilemann et al. 2009; Van De Linde et al. 2011). In this work, we present the characterisation of our dSTORM system on fluorescent beads and single molecule surfaces. This assessment of our system will allow us to improve the limitations of the first design of the SMLM setup. The three-dimensional calibration will allow us to easily extract more information from the modification of the PSF (Astigmatism) or by comparing two different emission paths (Biplane) and a supplementary data analysis step.
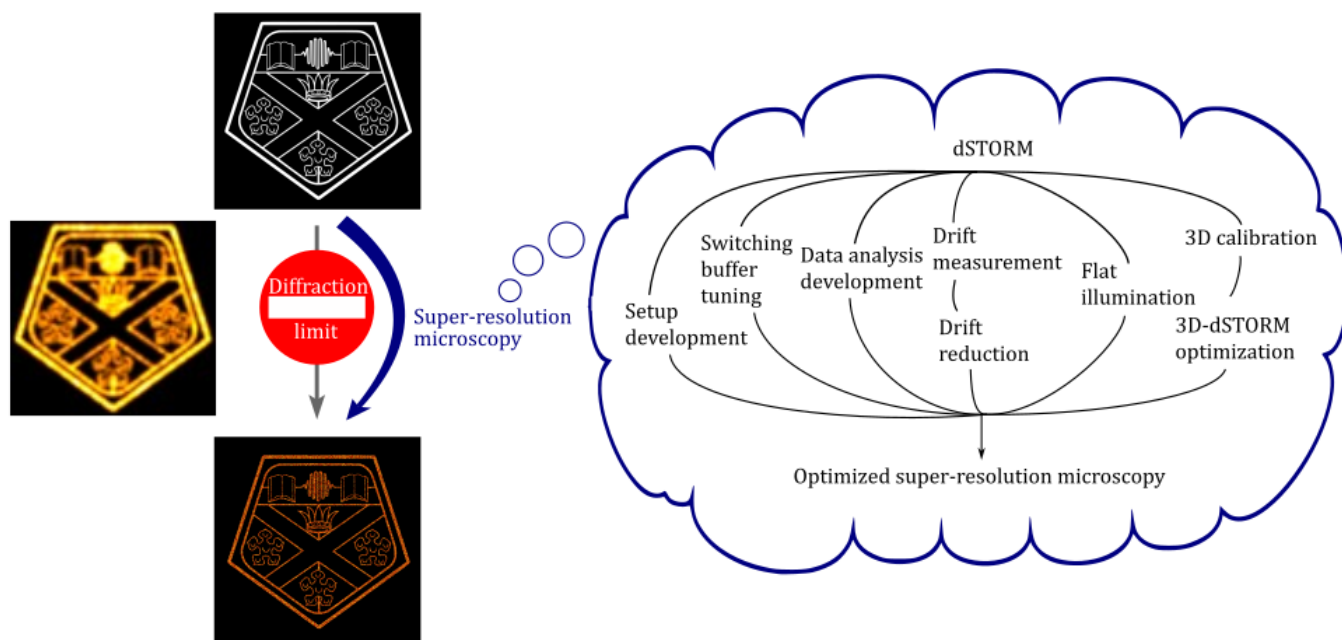
Figure 9 dSTORM is more than turning a switch on. Super resolution microscopy is a powerful tool that allows circumventing the diffraction limit of resolution of conventional microscopy. A sample with details smaller than the diffraction limit (top image) will produce an image lacking details in conventional microscopy (left image) but super-resolution methods can recover fine details (bottom image) but require additional work. As an example in dSTORM, one needs to choose a microscopy setup that includes a fast and sensitive camera as well as a powerful laser illumination. Data recording and analysis is more complex and time consuming to obtain a single super resolution image than simply recording a conventional microscopy image.

The improvement of spatial resolution in all three dimensions is achieved by the fine tuning of several parameters as well as the calibration and characterisation of the

microscopy system and the development of correcting measures (Figure 9).

2.3 A Single Molecule Localisation Microscopy (SMLM) setup

This section addresses various aspects of the design, assembly and characterisation of a Single Molecule Localisation Microscopy (SMLM) setup. First, we describe the parts required for a minimal setup (including in brackets the parts that we used as examples). It should be noted that the setup described here is only one possible setup for SMLM. Later, we describe optional devices that can be added to improve SMLM performance or user friendliness. For each piece of the setup, details are given about the required assembly, characterisation, or calibration. All parts were bought from Thorlabs unless otherwise stated.

The minimal setup (Figure 10) for SMLM must contain:

- The illumination side

- The microscope body

- The imaging side

2.3.1. Minimal setup for SMLM

Illumination side

Usually, the illumination source is a laser (Toptica iBeam smart 640SHP 14195) that provides light of high intensity, well collimated and with a narrow wavelength bandwidth, further cleaned by a narrowband filter (Chroma ZET635/20x). Several lenses adjust the laser width to the required beam size and focus it on the back focal plane of the objective

with the help of several mirrors.
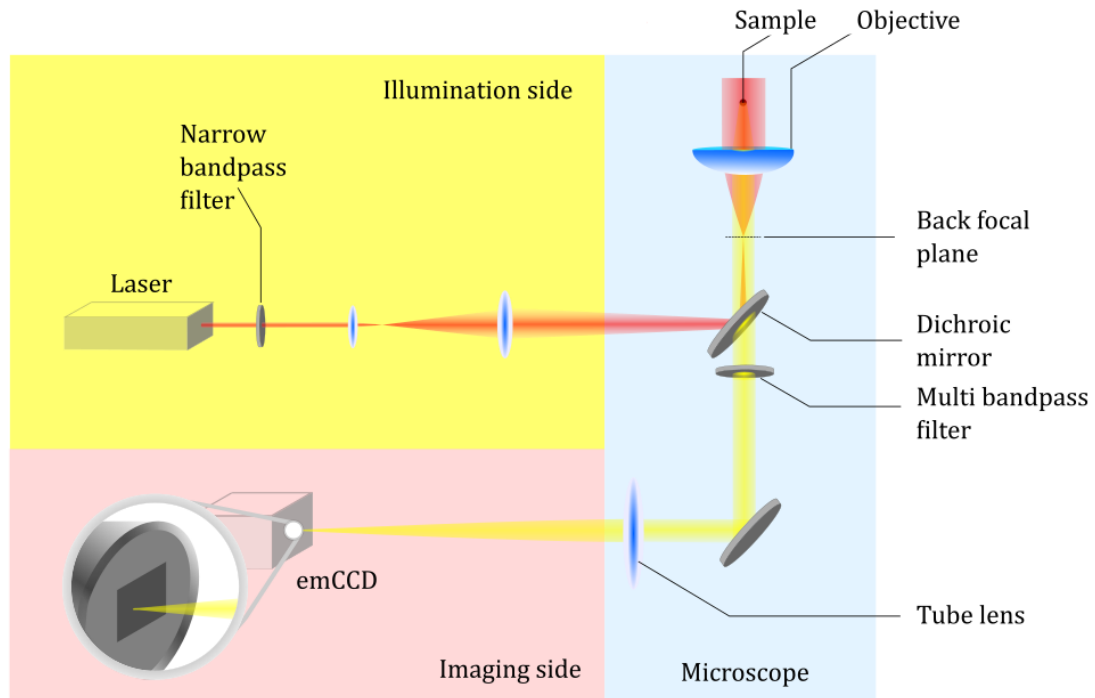
Figure 10 Minimal setup for single molecule localisation microscopy: the illumination side allows the excitation of fluorophores by using a light source (usually a laser), mirrors and lenses. The microscope body provides a structure to hold the sample, the objective and dichroic mirror. Their role is to bring the illumination to the sample and collect the emitted fluorescence light and transmit it to the imaging side. The imaging side collects the emitted fluorescence light, scales and forms the image on a camera sensor to record images of the sample's fluorescence emission.

The laser output was measured to be stable and linear above 50mW (Figure 14 (a)).

For single colour dSTORM one laser can be enough if an appropriate fluorophore is used.

More lasers can be used for multi colour SMLM or to aid controlling the photoswitching of some fluorophores.

Microscope body

Usually a commercially available microscope body (Olympus IX-73) is used to hold and arrange the dichroic mirror and filter(s), the objective, the sample and the tube lens (Figure 10). The laser enters the microscope body, is reflected by the dichroic mirror and

focused on the back focal plane of the objective (Olympus PlanApo N60XO SC2 oil NA1.40 or APON60XOTIRF NA 1.49 for chapters 4 and 5). Collimated light leaves the objective to illuminate the sample. The fluorescence light emitted by the sample fluorophores is collected and collimated by the same objective. The dichroic mirror (Chroma zt532/640rdc) as well as a multi bandpass filter (ChromaZET532/640), will allow the fluorescent light to pass while rejecting any reflected laser light. The tube forms an image of the fluorescent emitters on the camera sensor.

The dichroic mirror and filter are chosen to prevent the reflected and scattered laser light from reaching the camera sensor as it would affect the signal-to-noise ratio. At the same time, the fluorescence light collected by the objective should be transmitted to reach the sensor and produce an image. Dichroic mirrors and filters are chosen accordingly to match the fluorescence properties of the chosen fluorophore(s). Several combinations of mirror/filter can be assembled in the filter cube of the microscope body and changed from one experiment to the next. For example, for Alexa 647, the dichroic mirror and filter used here will have matching wavelengths as seen in Figure 11 (b).

Imaging side

For SMLM, a very sensitive and fast camera (Andor iXon Life 888) is required for detecting single molecules that emit a few hundred to a few thousand photons in 50-500 ms. The camera chip records images at a chosen rate (≈10-20 Hz) for most applications in this work). This rate includes the exposure time (50 or 100 ms) and the image transfer time (4.5 ms). EMCCD and sCMOS cameras are available today to reach those requirements, each with their advantages and drawbacks (Lelek et al. 2021; H. Li and Vaughan 2018). To collect as many photons as possible, the microscope objective should have a high numerical aperture, 1.4 or 1.49 here. Using two objectives on opposite sides of the sample

to collect almost twice as many photons is possible, this is known as 4pi microscopy (Hell and Stelzer 1992).

Another paramount condition for SMLM is the accurate localisation of single molecules. This is done by fitting a PSF model or approximation (2D-Gaussian function) to the recorded images. Accurate fitting requires an oversampling of the PSF on the camera sensor. Camera physical pixel sizes range from 5 to 16 μm (13 μm for our camera) (Mullan, n.d.). An efficient sampling requires a pixel size after magnification typically smaller than the PSF standard deviation (*SD*) or 144 nm in visible light. This value can be calculated from the PSF full width at half-maximum (*FWHM*) for a normal distribution: $FWHM \approx 2.355 \times SD$.

It follows that the magnification of the microscope objective and optional post-magnification devices should be around 50-150× and chosen according to the camera characteristics. Here, we used a 60× oil objective (Olympus PlanApo N60XO SC2 oil NA1.40 or APON60XOTIRF NA 1.49 for chapters 4 and 5) and a post-magnification device (Cairn research Optosplit II) described later in this chapter. The pixel size after magnification was measured at 122nm/pixel (Figure 11 (a)), with a total magnification of 107×. The Optosplit II provides a 107/60 = 1.78× magnification, close to the announced 1.7× (OptoSplit II, n.d.). The magnification is measured by comparing the physical size of a micrometer ruler (Agar scientific L4202), 100 μm with 2 μm steps here, and the size of the image on the camera chip. Figure 11 (a) shows that 100 μm in the sample corresponds to 822 pixels, so each pixel gathers light from an area of 122×122 nm^2 in the sample. Images recorded by our camera use analog-to-digital converter units or counts (ADC) as a unit. The quantum efficiency of the sensor in the 650-700 nm range is 90%. The camera sensitivity measured by the manufacturer was 19.3 electrons per count with the amplification parameters used throughout this thesis work. The EM gain was always set at 300 to reduce the readout

noise to the minimum (Andor, n.d.). Following, we can calculate a conversion factor:

$300/19.3 = 15.5$ counts (ADC) correspond to one photon detected on the camera sensor.
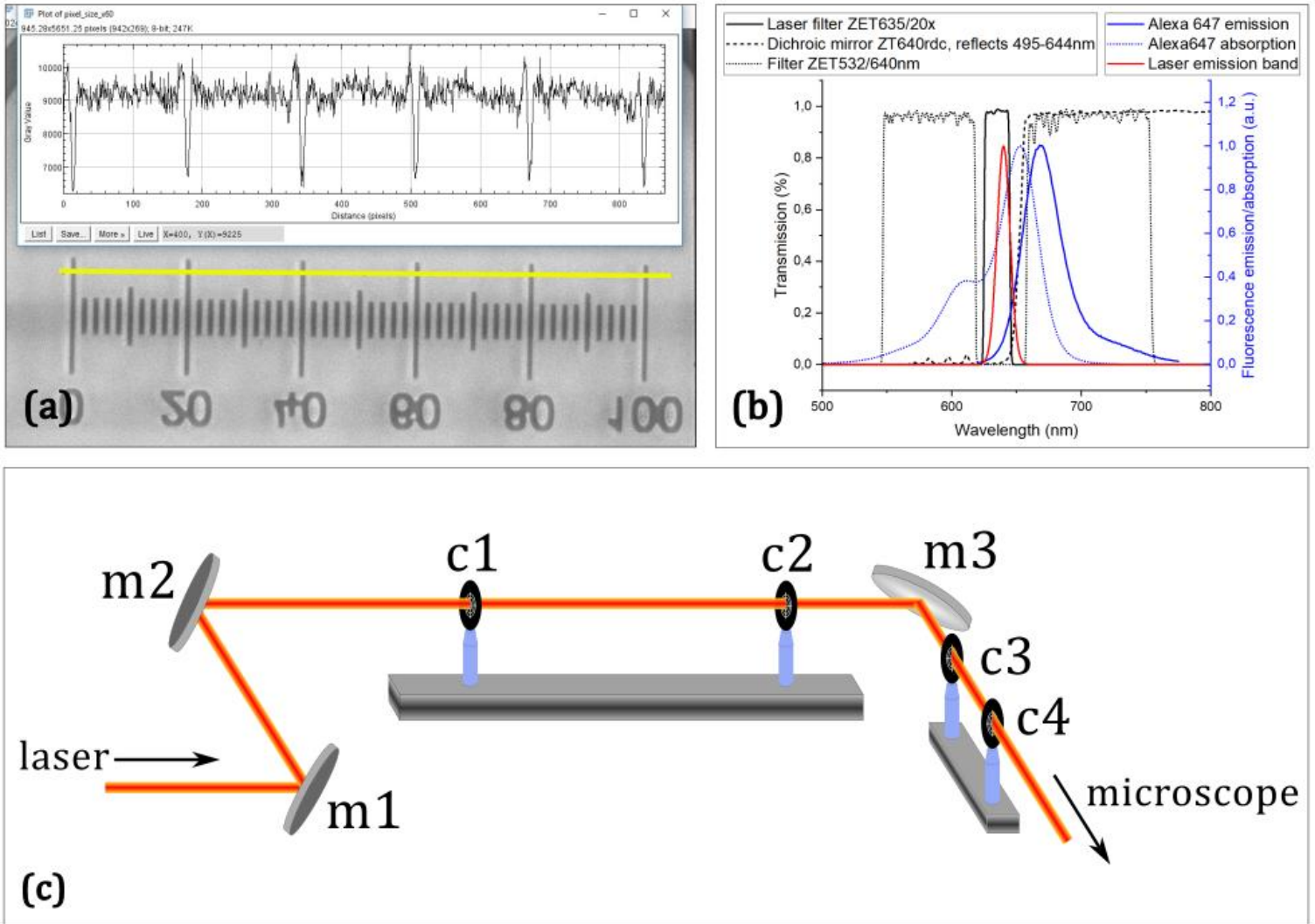
Figure 11 Alignment and characterisation of the microscopy setup (a) The pixel size after optical magnification is calculated from an image of a micrometre ruler. The micrometre ruler has a physical length of 100 μm. It is set on the sample stage, and an image is recorded. It allows determining the width the area corresponding to each pixel in the sample (here 122 μm) (b) Transmission, absorbance, fluorescence and laser emission spectra. The laser filter blocks all light outside of the target band of laser emission. The laser emission targets the absorbance of Alexa647. The dichroic mirror reflects the laser wavelength. The emission filter blocks the laser wavelength band but transmits the fluorescence emission wavelengths. Transmission, fluorescence emission and absorbance data were downloaded from ('Spectra Viewer - Chroma Technology Corp', n.d.). The laser emission spectrum is shown as a Gaussian peak of centre and width as stated by the laser manufacturer. (c) Laser alignment procedure. Several mirrors and centring targets allow aligning the laser path to lenses and the objective

2.3.2. Laser alignment procedure

When building the microscopy setup, mirrors and lenses are used to direct and shape the laser to the required beam size and focusing. The centre of both mirrors and lenses is preferred to reflect or transmit the laser beam as aberrations are smallest. Hence, the alignment of mirrors, lenses and laser is an important step for any single-molecule sensitive widefield microscope. The protocol for such an alignment can be performed as follows.

To avoid any risk to the eyes and skin, the laser alignment procedures were always performed with the laser at its lowest power, 0.5 mW. First, mirrors are placed to bring the laser to the sample position. We want the laser to enter the microscope horizontally, at the right height to match the microscope body entry and perpendicular to the back entrance of the microscope. The laser must also be aligned to the dovetail optical rails that will hold lenses later. This alignment to the optical rails will allow the repositioning of lenses to adjust the laser focus while conserving the laser alignment.

First, mirrors are placed one after the other from the laser exit to the microscope body (Figure 11 (c)). At each step, the mirror is placed so that the laser reflects in the centre of the mirror and roughly positioned to target the position of the next mirror. Once two mirrors are placed, the laser can be aligned parallel to the table at the height of the microscope laser entrance and along the optical rails.

For each step, two mirrors, one more upstream, $m1$, one more downstream, $m2$, are used to align the laser beam to the required path using two targets (Thorlabs LMR1AP) along the path, one close $c1$, one far $c2$ (Figure 11 (c)). First, we align the laser parallel to the table and at the right height using vertical rulers (Thorlabs BHM3, BHM4) in place of targets $c1$ and $c2$. When the laser is parallel to the table, we add targets $c1$ and $c2$ and adjust their

height to centre the laser on target along the vertical axis. Next, we use mirror *m1* to centre the laser beam on target *c1* and mirror *m2* to centre the laser on target *c2*. We alternately adjust mirrors *m1* and *m2* until the alignment is satisfactory. Then, we can add mirror *m3*, adjust its height and position to centre the laser beam, adjust *m3* so that the reflected laser is parallel to the table. We then add targets *c3* and *c4* and adjust their height to that of the laser. We can repeat all steps described for *m1* and *m2* with mirrors *m2* and *m3* to align the laser to targets *c3* and *c4*, respectively. This is repeated for each mirror until the microscope body. To align the last two mirrors, we printed targets that were placed at the microscope body laser entrance, on the objective turret and on the ceiling directly above the objective position using a plumb line. Again, the laser is aligned to the targets sequentially as described before. Finally, the objective is set in place, and a fluorescent sample is added on the sample holder. The final alignment is done by centring the laser on the camera live image and the ceiling target.

When all mirrors are added, lenses are added one after the other using the same protocol but the lens closest to the microscope body is added first. During this part mirrors should not be moved, the alignment should be performed by only moving lenses. A lens is added, at its approximate position along its dovetail rail and the fine-tuning screws of the holder are used to centre the laser beam on the targets downstream as described before. Finally, each lens is moved along the dovetail rail to expand or focus the laser beam as required. The last step is to focus the laser onto the back focal plane of the microscope objective while ensuring that the laser enters the objective along the optical axis. This can be achieved by minimizing the size of the laser spot on the ceiling target, which corresponds to a collimated beam out of the objective.

The proper alignment of the laser beam is an important step of setting up the microscopy system and should be done carefully. It must be done precisely and should not require

frequent corrections when using stable components, for example the optomechanical components from Thorlabs used in this project.

2.3.1. Optional add-ons

To complete the minimal setup presented above, several devices can be added to the microscopy system. We will now present those that we used. The sample stage of the microscope was raised a few millimetres to allow the use of the nosepiece and the piezoscanner described in this section.

Optical table

The microscopy system was built on an optical table (Newport RS4000). The optical table acts as a rigid platform to reduce the misalignment of optical components over time. Furthermore, the table feet include an air cushion provided by an air compressor that helps damping vibrations to improve the stability of the system. Common sources of vibrations that can impact the quality of data in super resolution microscopy include building movements, nearby foot traffic or street traffic and mechanical devices such as air conditioning.

MEMS tilting mirror

The MicroElectroMechanicalSystem (MEMS) consists of a fast-oscillating mirror that we used to improve the illumination uniformity of our samples. This will be discussed in detail in chapter 4.

Cairn Research Optosplit II

The Optosplit allows splitting the fluorescent light collected by the objective according to the desired property of light, wavelength, polarization or equally with a beamsplitting mirror into two separate paths. Each path can include additional lenses or filters and they

are both focused on the camera sensor to obtain two images using the same sensor (Figure 12 (c)).
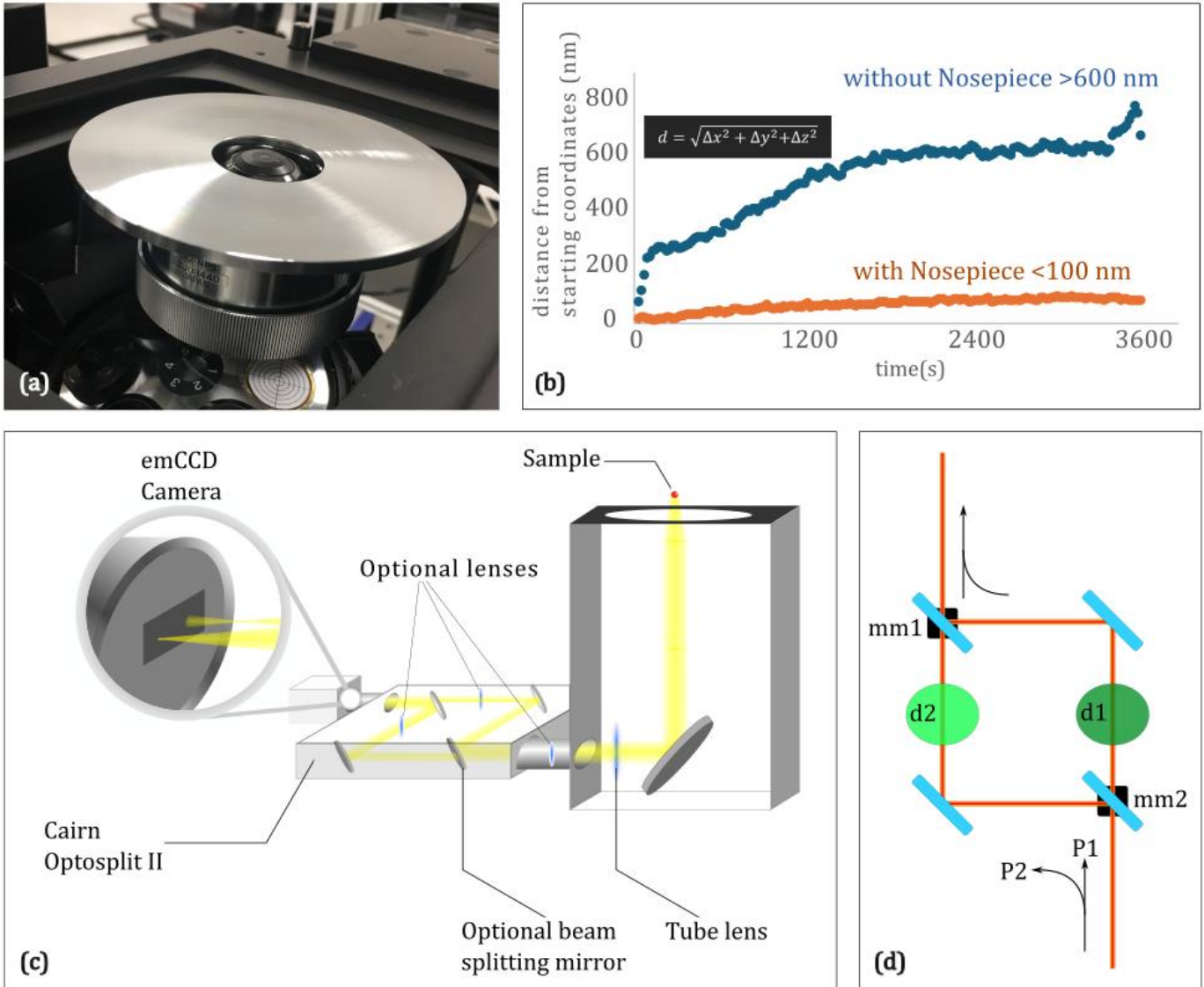
Figure 12 Advanced SMLM setup (a) Nosepiece Olympus ix2-nps Nosepiece stage. (b) Drift is reduced with the nosepiece. The total drift distance in an hour is less than 100 nm with the nosepiece and 600 nm without the nosepiece. (c) The optosplit device allows the addition of optional lenses or filters in three locations. This feature will be used for biplane and astigmatism 3D-SMLM (see section 2.5) (d) switching between illumination schemes is achieved by adding mirrors mm1 or mm2. Both mirrors are mounted on magnetic bases that ensure repeatable placement when switching from one path (P1) to the other (P2).

This has the advantage of not requiring the synchronization of data between two cameras.

Furthermore, the field of view corresponding to half the camera chip (512×512 px = 62×62 μm^2) matches the image produced by the optical setup within the limits of acceptable optical aberrations.

Even though this is an optional element of a SMLM setup, we used it in all versions of our setup as it provides the post magnification required for a good sampling of the PSF. Apart from the additional magnification, this device also allows biplane and astigmatism 3D SMLM that will be describe in section **Erreur ! Source du renvoi introuvable.**. Finally, it could be used to perform spectral demixing multi colour SMLM with one camera (Andronov et al. 2022) or study polarization with SMLM (Rimoli et al. 2022).

Total Internal Reflection Fluorescence (TIRF) and Highly Inclined Laminated Optical (HILO) sheet stage

The TIRF motorised stage (Thorlabs Z825B) is controlled by the Thorlabs Kinesis software via a Thorlabs K/Cube DC Motor controller. The motorised stage holds the last mirror before the microscope laser entrance. By moving laterally, the stage allows to shift the laser beam to the side of the objective allowing various illumination modes (Figure 13) such as widefield, Highly Inclined Laminated Optical sheet, also referred to as HILO (Tokunaga, Imamoto, and Sakata-Sogawa 2008), or Total Internal Reflection Fluorescence (TIRF) (Funatsu et al. 1995). The computer control allows an accurate positioning of the stage at previously defined distances from the centre of the objective (Figure 13 x_1 or x_2). This allows switching between illumination modes during an experiment with good reproducibility. The computer control allows switching between illumination modes without accessing physically the back of the microscope that would require removing laser guards and of course lowering the laser power. HILO illumination allows generating a thin inclined sheet of excitation light. This produces optical sectioning of the sample that
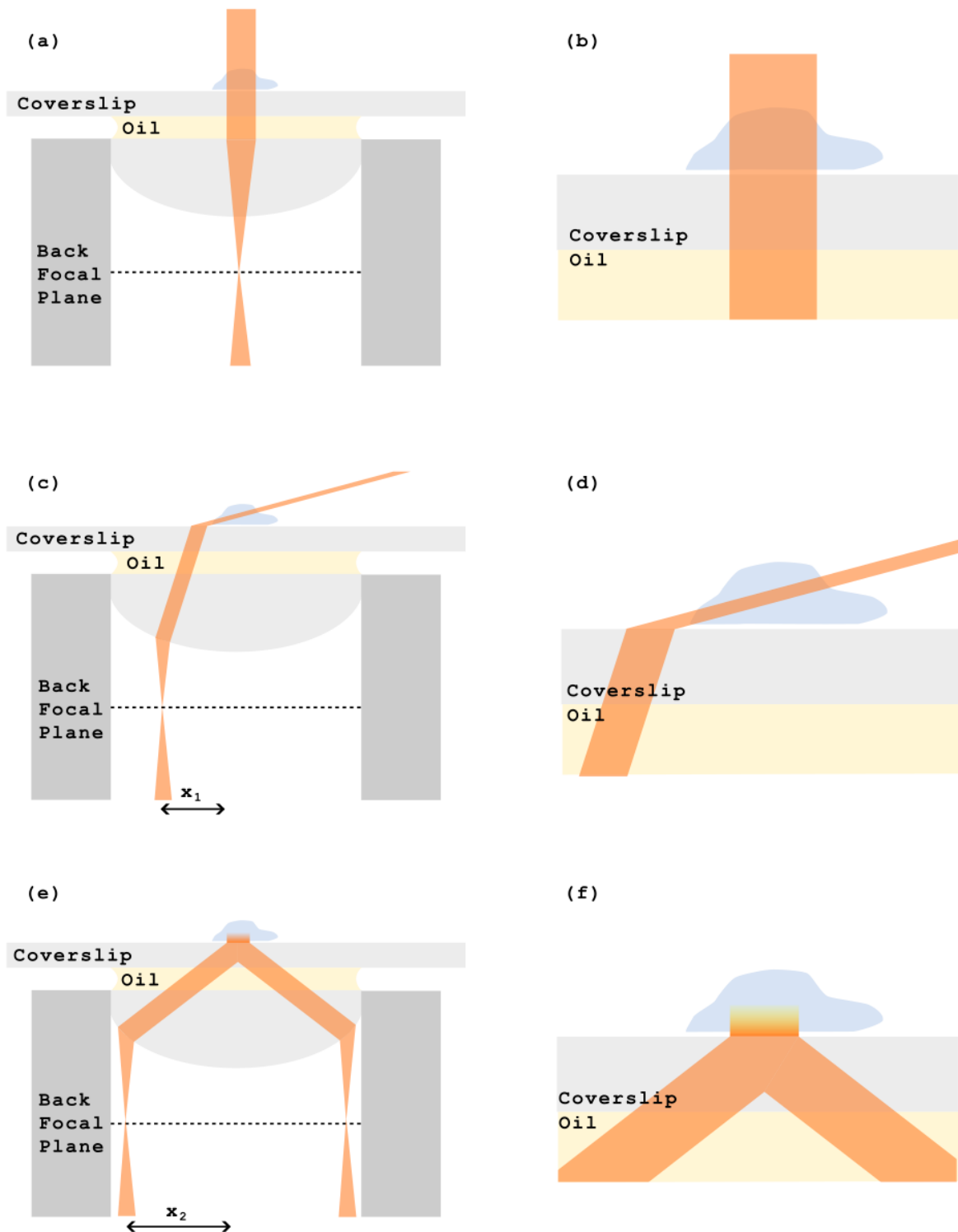
Figure 13 Illumination modes. (a, b) In widefield illumination, the sample is illuminated as well as the background leading to poor signal to background ratios in biological samples. (c, d) In highly inclined laminated optical microscopy (HILO), the laser beam is translated to the side of the objective. The beam is refracted and produces a light sheet that only illuminates a thin inclined slice of the sample, thus reducing the background signal (from fluorescence, reflection, scattering...). (e, f) in TIRF mode, the laser is further translated so that the incident angle at the glass/sample interface θ is larger than the critical angle $\theta_c = sin^{-1}(n_2/n_1)$ with n_1 and n_2 the refractive indices of the objective lens glass and the sample, respectively. In this situation, an evanescent wave appears at the glass/Sample interface. The illumination intensity drops exponentially with the distance from the glass interface. This strongly decreases background signal but only allows imaging of a section of the sample close to the glass surface (typically a few hundred nm)

reduces background fluorescence and improves the signal to background ratio while allowing to observe the sample at different depth. In TIRF, total internal reflection is achieved by overcoming the critical angle of the glass/sample interface, which generates an evanescent wave that only illuminates a thin layer of the sample at the interface. It greatly reduces the background fluorescence as the illumination intensity of the evanescent wave decreases exponentially with the distance from the interface.

Nosepiece

SMLM requires the recording of several thousands of images that will be analysed later to combine the information in one reconstructed super-resolution image. The acquisition takes from several minutes to several hours. During this time, the sample stage drifts in all three dimensions. Although drift can be corrected during data analysis (Cnossen et al. 2021; Fazekas et al. 2021; Tang et al. 2014), we chose to reduce it in the raw data. We used a passive device to reduce the stage drift (Olympus Nosepiece IX2-NPS). It consists of a robust metal cylinder that holds the microscope objective as well as the sample metal plate (Figure 12(a)). The conventional focusing ability of the microscope body is lost and replaced by a helicoid on the Nosepiece that is more precise and less sensitive to drift. We compared the drift with and without the nosepiece as depicted in Figure 12(b). Without nosepiece, lateral drifts were measured at several hundred nm and the focus was completely lost after one hour, which corresponds to an axial drift of more than 500 nm. With the nosepiece, the lateral drift was less than 50 nm and the axial drift was less than 100 nm after three hours, thus maintaining focus for a prolonged time. To optimise the stability of the nosepiece the focus is set in the sample the day before the experiment is performed and adjusted on the day of the experiment to allow mechanical relaxation to avoid focus hysteresis.

Piezo scanner

The piezo scanner (Piezoscanner P721CDQ, Physik Instrumente) is used to create calibration curves for 3D SMLM. This will be described in more detail in section 2.5. The piezo scanner is set instead of the nosepiece between the objective turret and the objective. It allows scanning a sample axially while recording images with a good control of position and speed of scanning. This enables the camera to record images of fluorescent beads or single fluorescent molecules while scanning them axially with nanometric movement per frame.

Filter wheel

A computer-controlled filter wheel (Thorlabs FW102C) is placed in the laser beam path to control the laser power in rough steps. The wheel holds five neutral density filters (of optical density 0.5, 1, 2, 3, 4) and an empty position. As it is computer controlled, it can be used to change the laser power reaching the sample while the laser delivers high power requiring the laser guards to stay in place. The big limitation in our setup for the use of the filter wheel is the empty position that is used when the maximal laser intensity is required. The laser alignment is very precise, and a small change will strongly affect the illumination quality as discussed in chapter 4. The filter wheel is placed at an angle slightly different than perpendicular to the laser beam to avoid back reflection and damaging of the laser device. This small angle introduces a small displacement of the laser beam when a filter with two air/glass interfaces is present. To solve this issue, we used the lowest optical density filter as a standard.

Variable polarising beam splitter to control laser power

The laser provides linearly polarized light. We can use this property to our advantage to control the illumination power of the sample. By introducing a half-wave plate (Thorlabs

AHWP05M-600) in the laser beam, we can rotate the plane of polarisation by an angle twice the angle between the incident laser plane of polarisation and the half-wave plate fast axis (Figure 14(c)). Placing the half wave plate in a stepper motor rotation mount (Thorlabs K10CR1/M) gives control of the angle the polarisation plane is rotated.
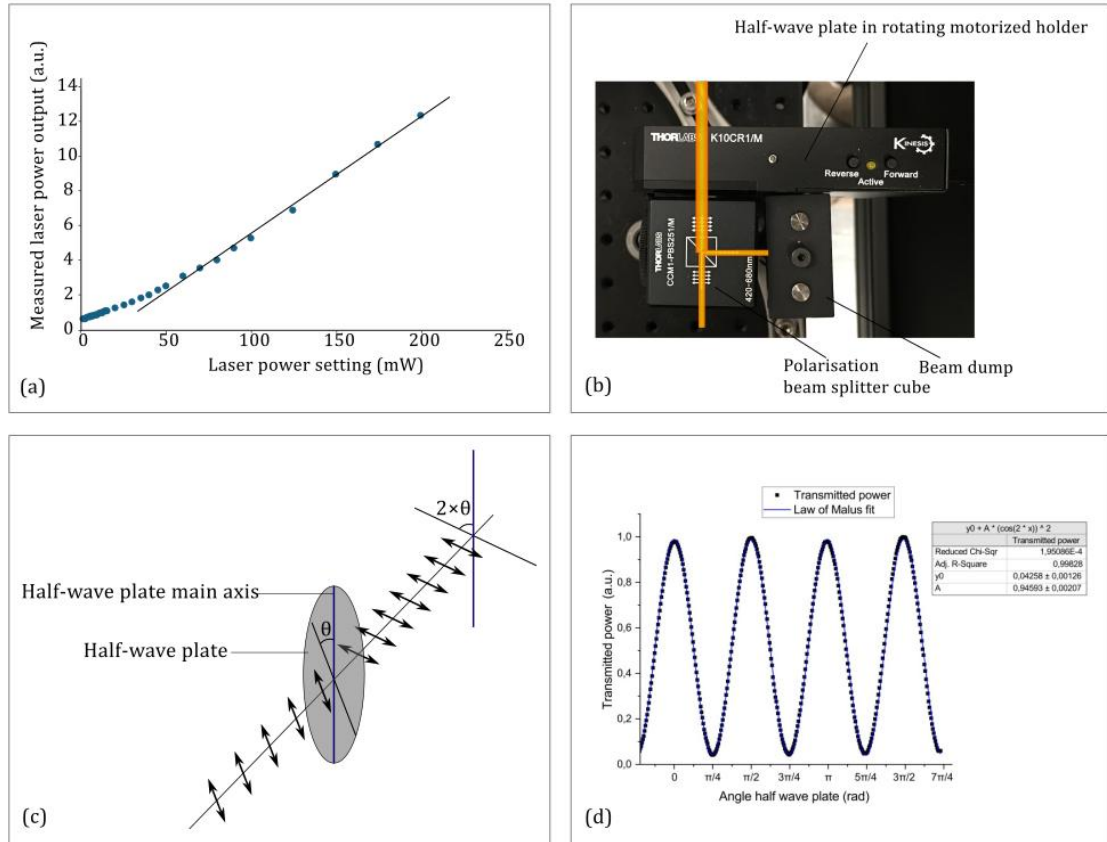
Figure 14 (a) The measured output laser power is linear for settings above 50 mW. (b) Laser power is controlled by a half-wave plate that can be rotated and a polarization beamsplitter. The beamsplitter cube reflects the s-component of the incoming laser and allows the p-polarized light to pass. (c) The half-wave plate changes the angle of polarization of the laser. It doubles the angle between the polarization axis of the laser and the half-wave plate main axis. (d) The measured output power at the exit of the polarisation beam splitter follows theory accurately. Rotating the halfwave plate rotates the polarization axis of the laser beam and changes the proportion of light that can pass through the polarizing mirror according to the Law of Malus.

By combining this with a polarizing beam splitter (Thorlabs CCM1-PBS251/M) we obtain a variable attenuator (Meadowlark Optics 2003; Stehr, Schwille, and Jungmann 2019). The setup is shown in Figure 14(b). The polarizing beam splitter reflects s-polarised light and

transmits p-polarised light ('Broadband Polarizing Beamsplitter Cubes in 30 Mm Cage Cubes', n.d.). The beam splitter is placed in order to transmit the maximum of the laser light when the half-wave plate is not present. The addition of the half-wave plate allows rotating the laser polarisation plane by 0-90° when the half-wave plate rotates 0-45°. When the polarisation plane of the laser is rotated 90°, the transmission is minimum and the reflection is maximum on the beamsplitter. The transmitted component continues in our illumination arm of the setup while the reflected component is absorbed by a beam block (Thorlabs LB1/M).

We measured the power of the laser transmitted by the beamsplitter with a powermeter (Coherent FieldMax II TO with an OP-Vis sensor).

When the half-wave plate main axis is parallel to the laser polarisation plane, the polarisation is unchanged, and the maximum transmission is observed (Figure 14(d)). When the half wave plate is rotated 45° or $\pi/4$ rad the polarisation plane of the laser is rotated 90° and the minimum transmission is observed. According to the Law of Malus, the transmitted intensity follows:

$$I = I_0 \times cos^2(\theta) \tag{4}$$

Where I the transmitted intensity, I_0 the incoming intensity and θ the angle between the polarisation axis of the beam splitter and the polarisation axis of the incoming light(Malus 1809).

This is confirmed in (Figure 14(d)) with a very good function fit.

Magnetic stands

Magnetic mirror stands (KB25/M) allow the use of another important optional device to achieve homogeneous illumination of the sample that will be discussed in chapter 4. They are composed of two magnetic plates that align accurately to allow placing and removing

optical parts from the setup easily while conserving a good alignment. The repeatability of placement is claimed to be within a few μrad by Thorlabs and we have observed no loss of alignment when switching between illumination modes in our experiments. By placing either magnetic mirror mm1 or mm2 (Figure 12(d)), we can select path P1 or P2 that goes through devices d1 and d2 respectively. This is useful to compare instruments in the illumination path on a unique sample and obtain accurate comparisons, for example between a Gaussian or a flat-field illumination (see chapter 4).

After discussing the hardware, we will discuss the software used in our project.

2.4 Data analysis and computer simulations, towards Iain James Harley's work

2.4.1. Introduction

In SMLM, data analysis was developed as open source by a large community of researchers that shared software packages and algorithms. New analysis methods are still developed in parallel to hardware and methods developments to extract more information from microscope images.

Super resolution SMLM requires efficient and reliable software to localise millions of fluorescent emitters in tens of thousands of frames. It should ideally be reliable, customizable and fast to approach live analysis of the recorded data (Sage et al. 2019). The development of localisation algorithms has brought better spatial resolution as well as

shorter analysis time and in some cases the analysis is close to real-time during acquisition. Each software caters to the priorities of the team that developed it and is usually a trade-off between computation time, accuracy, sensitivity, ability to analyse 3D data or high-density samples. Some research teams also worked at developing tools to evaluate the performance of localisation software in controlled conditions (Wolter et al. 2011).

A wide comparison of available software was conducted by the SMLM community driven by D. Sage, T-A. Pham and S. Holden (Sage et al. 2019). They used recorded data as well as realistic simulations that allowed calculation of the real error of each software by comparing the analysis results with the ground truth of simulations. This is an example of how computer simulations can help develop data analysis in SMLM.

This study helps researchers to make an educated choice of software for their needs.

Localisation data is then further processed to extract more information. This is usually done by writing custom routines that might be shared and used by the super-resolution community in the form of macros or plugins for ImageJ for example. Many researchers also use simulations to develop their data analysis tools.

2.4.2. Data analysis

Data analysis includes the refinement of raw data by correcting imaging artefacts (optical aberrations, drift), the extraction of relevant information from the raw data, the quantification and analysis of several photophysical parameters including the photoswitching parameters and finally the visualisation of results in reconstructed images, data plots and tables of numerical values.

The automatization of data analysis answers several limitations of manual data analysis. Users that repeat the same analysis on various datasets will make errors at one point, they

will skip an analysis step or use wrong analysis parameters. A well-written analysis routine will avoid those user errors. Moreover, a computer program can work at night for a more resource demanding analysis and free some time for the researcher to focus on other tasks. In our experience, analysis automatization can be time-consuming, but it was relevant for repeated experiments. In this section, we will discuss localisation software programs developed outside of our team that we used, data visualisation and analysis macros written by Sebastian van de Linde in ImageJ and Python Jupyter notebook (Kluyver et al. 2016) routines written by me for the analysis of flat illumination data discussed in chapter 4.

Localisation software

Localisations programs aim to find the sub-diffraction coordinates of single fluorescent emitters in the sample by fitting a 2D Gaussian function such as:

$$f(x,y) = A exp\left(-\left(\frac{(x-x_0)^2}{2\sigma_x^2} + \frac{(y-y_0)^2}{2\sigma_y^2}\right)\right) + B \qquad (5)$$

Where A is the amplitude, x_0 and y_0 are the coordinates of the emitter, σ_x and σ_y are the widths of the Gaussian function along the x- and y-axis (standard deviation of the Gaussian function) and B is the offset that corresponds to the background.

Other approaches include more complex fitting functions such as a PSF model extracted from experimental data (Y. Li et al. 2018) or different approaches such as the centre of mass algorithm in QuickPALM (Henriques et al. 2010).

Localisations packages usually provide pre- and post-localisation tools (Sage et al. 2019) to clean the data, reduce the noise and select localisation candidates before the actual localisation process. A list of localisations with fitting and photophysics information (residue of fitting, localisation intensities...) and an image or a stack of images to visualise the result of the localisation are usually exported as text and image files.

Most localisation software packages enable the analysis of 3D SMLM data including astigmatism, biplane and PSF engineering methods.

Filters can be applied on fitting parameters to keep only localisations that pass the filter. The right choice of filters is important to optimise the quality of the output. If filters are too lax, a lot of false positive localisations might pollute data whereas overly harsh filters will discard actual data and might lead to biases in the results. In this project, we mostly filtered data by the intensity and PSF width in x and y parameters.

In this project, we used mostly rapidSTORM (Wolter, Löschberger, Holm, Aufmkolk, Dabauvalle, Van De Linde, et al. 2012) and ThunderSTORM (Ovesný et al. 2014).

rapidSTORM (Wolter, Löschberger, Holm, Aufmkolk, Dabauvalle, van de Linde, et al. 2012) was developed with the aim to be an open-source, fast and accurate localisation software (Wolter, Löschberger, Holm, Aufmkolk, Dabauvalle, van de Linde, et al. 2012). It can handle 2D as well as 3D localisation (astigmatism or biplane data) and multi-channel data with a localisation accuracy comparable to alternatives at the time it was released but with an improved speed in comparison. It includes a Graphical User Interface that makes adjusting the analysis parameters easy. Particularly the filter based on any of the output parameters helps by cleaning the data early in the data analysis process. rapidStorm was used by Ross Philips (RP) in his BSc project and by me for this thesis work.

ThunderSTORM (Ovesný et al. 2014) is an ImageJ plugin for localisation. It is open-source, and it allows batch processing and can be integrated in additional ImageJ programming to customise the pre- or post-processing in ImageJ. ThunderSTORM was used by IJH and BJ in their Master projects.

ImageJ macros for data analysis

ImageJ had a big impact on the development of image data analysis, especially as a tool for

custom analysis routine development for all researchers to develop and share (Van De Linde 2019). Automated analysis and macro programming allow us to automatise analysis of large amounts of data even with minimal knowledge of programming. Fiji also includes a Graphical User Interface (GUI) to be included in the macro, so that a well-established analysis routine can be easily used by researchers with no knowledge of programming. The GUI permits choosing analysis parameters without the need to modify the code directly.

Macros can be written in the ImageJ Macro Language (IJM), hence allowing for automatic analysis of data sets. Via the IJM, data analysis can be further expanded beyond localisation and visualisation of fluorophores, such as registration of chromatic aberrant datasets, cluster analysis, time-correlated photophysics analysis, and 3D decoding.

The FIJI (Fiji Is Just ImageJ) packaging of ImageJ includes many tools, plugins and other functions related to the analysis of biological images (van de Linde 2019; Schindelin et al. 2012), hence, it was chosen as the main platform for image data analysis for this project.

Sebastian van de Linde developed several macros in ImageJ to help visualising and analysing 2D and 3D SMLM data. I will briefly summarise their function here as they were used extensively throughout this project. The development of these macros accompanied by a commentary on the use of ImageJ for SMLM data analysis was published by SvdL in 2019 (Van De Linde 2019).

LocFileVisualizer

LocFileVisualizer can import a localisation file that was output by a localisation software. LocFileVisualizer can produce customizable visual representations (super-resolution images) of the localisation data using several filters to improve the visualisation quality. The super-resolution image consists of a 2D histogram counting localisations with the choice of pixel size. The intensity of pixels is usually non-linear in relation with localisation

74

counts or additional filters are applied to help visualization, but LocFileVisualizer can also generate quantitative images where each pixel counts localisations in the corresponding area for further quantitative analysis. LocFileVisualizer allows to circle localisations on the raw data image stack. This permits a visual evaluation of the performance of the localisation parameters. The user can determine whether the localisation software misses dim emitters or finds false positive localisations in the background noise.

ExtractLocalisations

This macro is meant to be used after the LocFileVisualizer. In ImageJ, the user can define Regions Of Interest (ROI). The ExtractLocalisations macro will create new localisations files for each ROI or a single file grouping localisations from all selected ROIs. This is useful to study single emitters as they blink along the recording session.

Loc_tracker

Loc_tracker tracks emitters on localisation files. It opens a localisation file from TRABI, rapidSTORM or ThunderSTORM, finds emitters that are present in several sequential frames and exports a list of those tracks with average coordinates, first frame number, number of frames, total and average spot intensity and a list of individual intensities. This macro can be used to study the photophysics of emitters in samples.

GenerateCalibration3DBP

This macro needs biplane or astigmatism calibration data. This is provided by loading a sorted localisation file with the LocFileVisualizer. The sorted localisation file contains localisations recorded during an axial scan of a reference sample in a biplane or astigmatism 3D SMLM setup. The macro takes the calibration data as well as several parameters from the calibration experiment and creates a calibration curve following a chosen z-function (see section 2.5) and plots the calibration curve. Finally, it exports the

calibration curve to a file to be used in the assignment macro.

Assignment3DBP

This macro uses a calibration file produced by the GenerateCalibration3DBP macro to assign an axial position to localisations recorded in the same 3D setup as the calibration data. It works for Astigmatism, FWHM biplane and intensity biplane data.

ImageJ plugins

Plugins are more complex and more integrated programs compared to macros and can add new functionalities that are not readily accessible in ImageJ (Van De Linde 2019). In the present project, we used a few plugins that were developed by other research groups among the super-resolution community.

FRC (Fourier Ring Correlation) maps from NanoJ-SQUIRREL

Within the NanoJ-SQUIRREL plugin developed by Culley et al (Culley, Albrecht, et al. 2018a) we used the FRC map tool to evaluate the resolution performance in our flat-field illumination (Chapter 4) and thiolate benchmarking projects (Chapter 5). NanoJ-SQUIRREL is a plugin that groups several methods to evaluate the quality of localisation data analysis including error mapping tools and FRC (Fourier Ring Correlation) maps.

Resolution is often used as a quality evaluator in super-resolution imaging. In SQUIRREL, the resolution is measured as the FRC resolution as defined by Banterle et al. and Nieuwenhuizen et al (Nieuwenhuizen et al. 2013; Banterle et al. 2013).

Fourier Ring Correlation (FRC) (Nieuwenhuizen et al. 2013) compares two images generated from two statistically independent subsets of the analysed dataset. A Fourier transform (FT) of each image is produced and FTs are compared. Starting from the centre of the FT, circles of increasing diameters are drawn. For each circle, a correlation is calculated between pixels on the perimeter of the circle on both FT images. A correlation

equal to 1 denotes a perfect identity whereas a correlation value of zero shows full independence of values between the compared subsets. A correlation plot shows the decay of correlation with spatial frequency (linked to the circle diameter). The FRC resolution is defined as the inverse of the spatial frequency corresponding to a drop of correlation below 1/7 ~0.143.

We used the FRC map tool to compute the local resolution of a sample and used the resulting map as a marker of overall super-resolution quality. FRC maps are generated as follows (Culley, Albrecht, et al. 2018a):

We used the LocFileVisualizer to split the localisations in two equivalent groups by separating localisations in odd and even frames. Independent super resolution images are reconstructed from each localisation file and exported by the LocFileVisualizer.

The two images are then loaded to SQUIRREL. Both images are split in blocks following a grid pattern. FRC is performed on each block to calculate a FRC resolution value. A heatmap is then generated showing the results of the FRC analysis in each block. Missing or insufficient correlations are replaced by interpolation of adjacent blocks.

TRABI

Temporal, Radial-aperture-based Intensity estimation (TRABI) is an ImageJ plugin for intensity analysis of SMLM datasets (Franke, Sauer, and van de Linde 2017). This plugin uses a photometric method to generate a z-dependent photometric parameter. It compares photon numbers in different areas of the emission pattern (PSF) to extract information about the axial position of emitters from a 2D image. TRABI was inspired by Aperture Photometry, a method used in astronomy to quantify the brightness of stars. It uses two circular apertures around the centre of a localisation spot and calculates P, the ratio of photon numbers between the central circle and the corona between the two circles. Given

the redistribution of photons in the PSF with defocusing, the ratio P is dependent on the axial position. One limitation of this method resides in the symmetry of P around the focal plane making localisations at equal distances on each side of the focal plane indistinguishable. This can be avoided by placing the focal plane at the sample/glass interface so that the sample will reside only on one side of the focal plane. With this method, the axial working range of TRABI is reported to be 600 nm.

TRABI was used in RP's project (Chapter 3).

Origin Pro and Python/Jupyter notebooks

At the beginning of this project, data was analysed mostly with OriginPro ('Https://Www.Originlab.Com/Origin', n.d.). Later data analysis and visualisation was performed using custom-written Python routine (Granger and Perez 2021) on Jupyter notebooks (Granger and Perez 2021). Python and Jupyter notebooks are a good alternative to commercial software packages. They are open-source, they perform as well as commercial alternatives and are fully customisable.

JupyterLab is an open-source notebook application that allows interactive computing.

Jupyter notebooks allow integration in a single file of data analysis code, plots and comments. The document can then be shared and run by others. Details of the data analysis routines that we developed for specific applications will be discussed in chapters 4 and 5.

The effort put in data analysis development had two main motivations, standardizing data analysis and developing tailored routines for our needs. The standardization was motivated by the observation of errors in repeated manual data analysis at the beginning of this project. Comparable data sets were analysed with dissimilar routines that led to uninterpretable results. The main issue here was determined to be human error in the

copying of data or in the application of data analysis steps that were sometimes forgotten or applied with different parameters. The development of tailored analysis was motivated by me not finding an easy way to apply the data analysis that I wanted to apply in OriginPro.

To tackle those two issues, I first developed a few macros for batch processing of several datasets in Origin Pro to make the data analysis reproducible for various datasets and then moved to JupyterLab and Python to add the custom analysis and open-source to the standardization.

The development of data analysis software or routines can also rely on computer simulations.

2.4.3. Computer simulations

Presenting background knowledge of one's research project is important for the audience to understand the fundamentals and can benefit from clear and concise visual aids. As an example, in this thesis, the core of the research involves dSTORM as the main method. Initially, to explain this method to various audiences, images were modified with an illustration software (Inkscape) but they did not really resemble actual data (Figure 15(A)). Later, a basic simulation program was developed to produce more accurate representations of real datasets (Figure 15(B)).

Computer simulations are used widely in physics. Here, our first use of dataset simulations was to produce a dataset mimicking the University of Strathclyde logo to explain the concept of dSTORM in slide presentations.

Other applications of simulations include teaching (Jimoyiannis and Komis 2001; Spodniakova Pfefferova 2015), exploring the evolution of a system as it follows a set of hypotheses, which can be confirmed or rejected by performing an experiment "in real life".

Simulations are also used to develop data analysis and explore the artefacts of data analysis. We used simulations to that end in chapter 4 and 5.
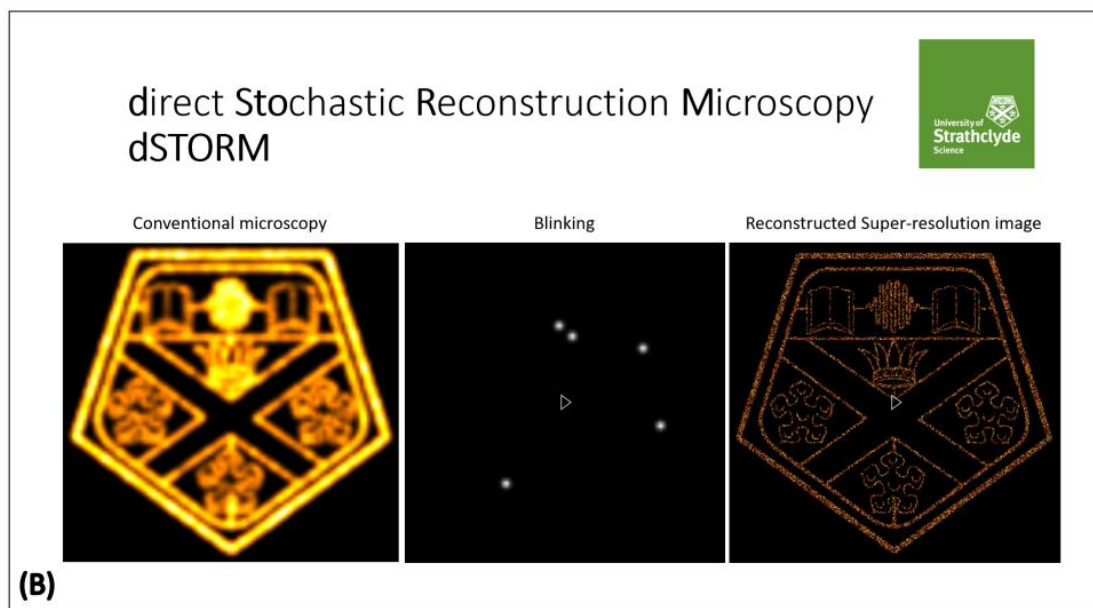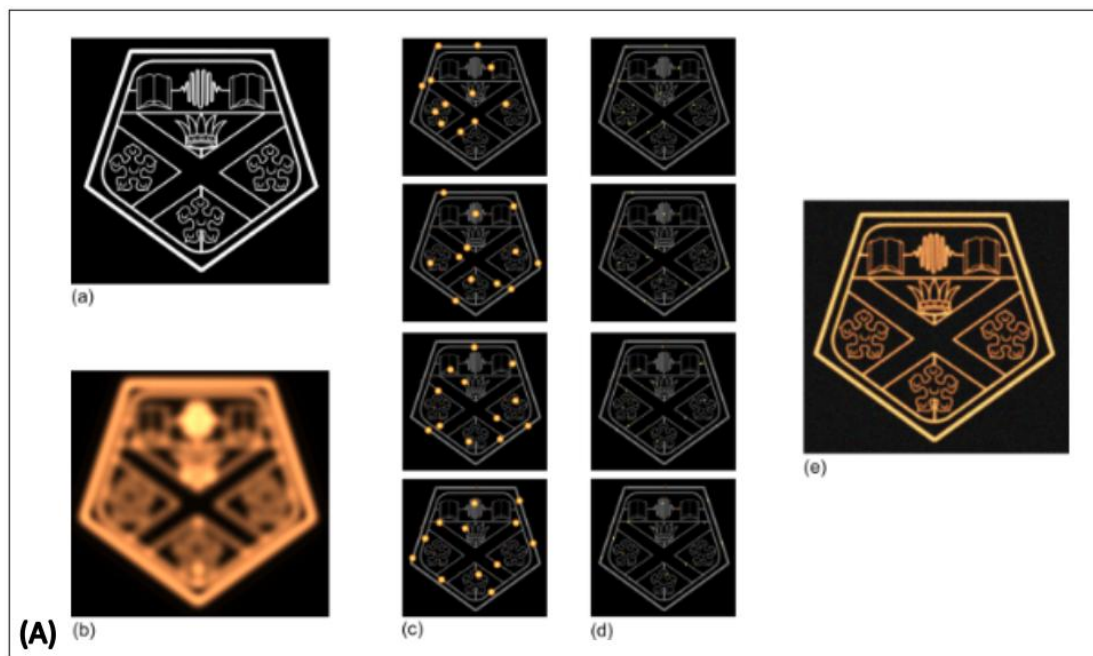
Figure 15 (A) Early presentation of the concept of dSTORM using an illustration software. (B) An improved presentation using dSTORM_Generator to generate simulated data frames that better approximate real-world SMLM data. Additionally we used the simulated data frames to produce a video of the blinking and reconstruction of the simulated data.

The simulation code (dSTORM_Generator) works as follows (Figure 16). As an input, one

or several high-resolution images are used as the ground truth of the imaged structures. Here we will prefer using images with high contrast. For each channel/image, an intensity mask is applied on the image to generate a binary image. Among the white pixels of the binary image, a random set of coordinates is selected and stored as a list of emitters in a text file as the ground truth for future comparison. A stack of high-resolution images is created with pixels coloured white according to the emitter positions in the ground truth data. To generate a dataset mimicking diffraction limited microscopy, a Gaussian blur filter is applied to the previous image stack, then noise is added before the image resolution is reduced by binning pixels. The resulting image stack is saved for each channel. Finally, for multichannel, all channel stacks are merged as one stack. For now, the simulation allows variation of parameters such as the number of frames, the number of channels and for each channel the number of emitters per frame, the intensity of emitters, and the length of the ON-time of fluorophores (in frame number). This simple code allows generation of datasets that are simplified compared to the actual behaviour of fluorophores in dSTORM. A more advanced simulation software written by SvdL was used in the chapter 4 on flat-illumination to develop the data analysis. Future development of this simulation code would include reworking the ON-OFF switching to be more realistic according to what is known for fluorophores such as Alexa647 (Ha and Tinnefeld 2012; H. Li and Vaughan 2018; Stennett, Ciuba, and Levitus 2014; Van De Linde and Sauer 2014). This would include ON and OFF times to not be synchronized with image frames, neither in length nor in phase. The emission intensity of fluorescent molecules follows an exponential distribution and the simulation would be more realistic with intensities distributed accordingly. An efficient comparison tool should be developed to compare localisations obtained through the localisation software rapidSTORM (Wolter, Löschberger, Holm, Aufmkolk, Dabauvalle, van de Linde, et al. 2012) or ThunderSTORM (Ovesný et al. 2014)

to the ground truth data. This would allow evaluating the performance of the localisation algorithms and to optimize localisation parameters. Furthermore, a more efficient control of noise level and signal-to-noise ratio would be beneficial.
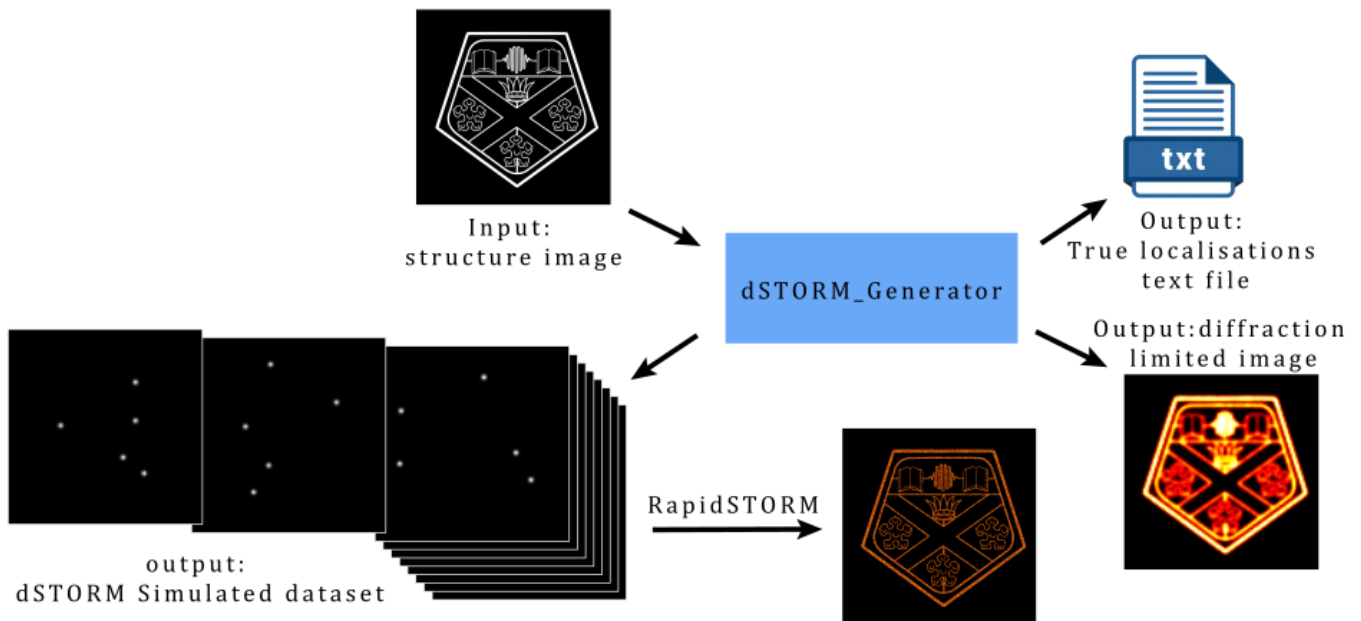
Figure 16 dSTORM_Generator. The program takes a reference image as an input and produces a stack of images, a list of true localisations and a "diffraction limited image" that is a projection of the image stack on a single image. Several parameters allow controlling the PSF an pixel size and the switching parameters.

Finally, this being one of my first programming projects, there is a lot of optimisation to apply to make the code more efficient.

Another use of simulated datasets to improve data analysis is the work of Iain James Harley that I helped supervise in our group.

Iain James Harley's project on Optimisation of Single-Molecule Localisation Microscopy (Harley 2020)

Iain James Harley (IJH) worked on analysing the effects of different data analysis methods for SMLM. On the same dataset of simulated SMLM data, he compared combining frames to

increase the signal to noise ratio before localising emitters to averaging the localisation coordinates found separately in different frames of a fluorophore's ON event.

One noticeable point was raised that will help improving SMLM accuracy. Localisation precision benefits more from recording a number of photons in a single frame compared to the merging of several frames recording the same total number of photons.

The main result of this project showed that in most cases, it was more advantageous to localise emitters in individual frames and then calculate the average of localisations coordinates instead of merging sequential frames and then localise the emitter once.

Combining image frames before localisation was more efficient when the emission in each frame was dim and when the signal to noise ratio was low. The recent interest of SPAD arrays for single molecule imaging led to the development of smart aggregation methods that combine frames more efficiently (Gyongy et al. 2016, 2018).

To conclude, this project showed that averaging localisation coordinates was the best method to improve localisation accuracy when fluorophores ON time was significantly longer than the exposure time of the camera unless a very low signal to noise ratio led to many missed localisations.

2.5 3D SMLM setup and calibration

2.5.1. Introduction

A more detailed description of 3D super-resolution microscopy can be found in the general introduction of this thesis.

3D SMLM aims at extracting 3D information from the 2D image produced by a camera and microscope. The length of acquisition prevents using conventional methods for exploring

the third dimension of samples. For example, axially scanning a sample to record 100 slices would be very time-consuming, would require intensive data analysis to correct for drift and might even be completely unfeasible because of the photobleaching induced by the high laser power routinely used in SMLM. The super-resolution community has developed several methods to encode the 3D information in the shape and size of the PSF recorded for each emitter. These methods bring a drawback for the x and y precision as they usually involve splitting the number of photons by half (biplane) or spreading them on a larger surface (astigmatism). But this drawback is manageable in comparison with the additional information that these methods bring. In this section, we will describe the characterisation and calibration of a 3D SMLM setup using two methods, biplane and astigmatism.

Here, we will discuss material and methods development for 3D SMLM before describing the calibration step and performance of two 3D SMLM methods, biplane and astigmatism, i.e. multiplane and PSF engineering, respectively.

2.5.1. Material and methods development

3D SMLM setup

Biplane

In biplane SMLM, we record two axially shifted images of the sample on a single camera to simplify the data analysis. The fluorescent light emitted by the sample and collected by the objective is separated in two equal parts by a beam splitting mirror in the Optosplit device. We introduce a focal shift in one path by adding a defocusing lens (Figure 17(a)) and record both images on a single camera.

Astigmatism

For astigmatism, the fluorescence light is not split. A cylindrical lens is introduced in the
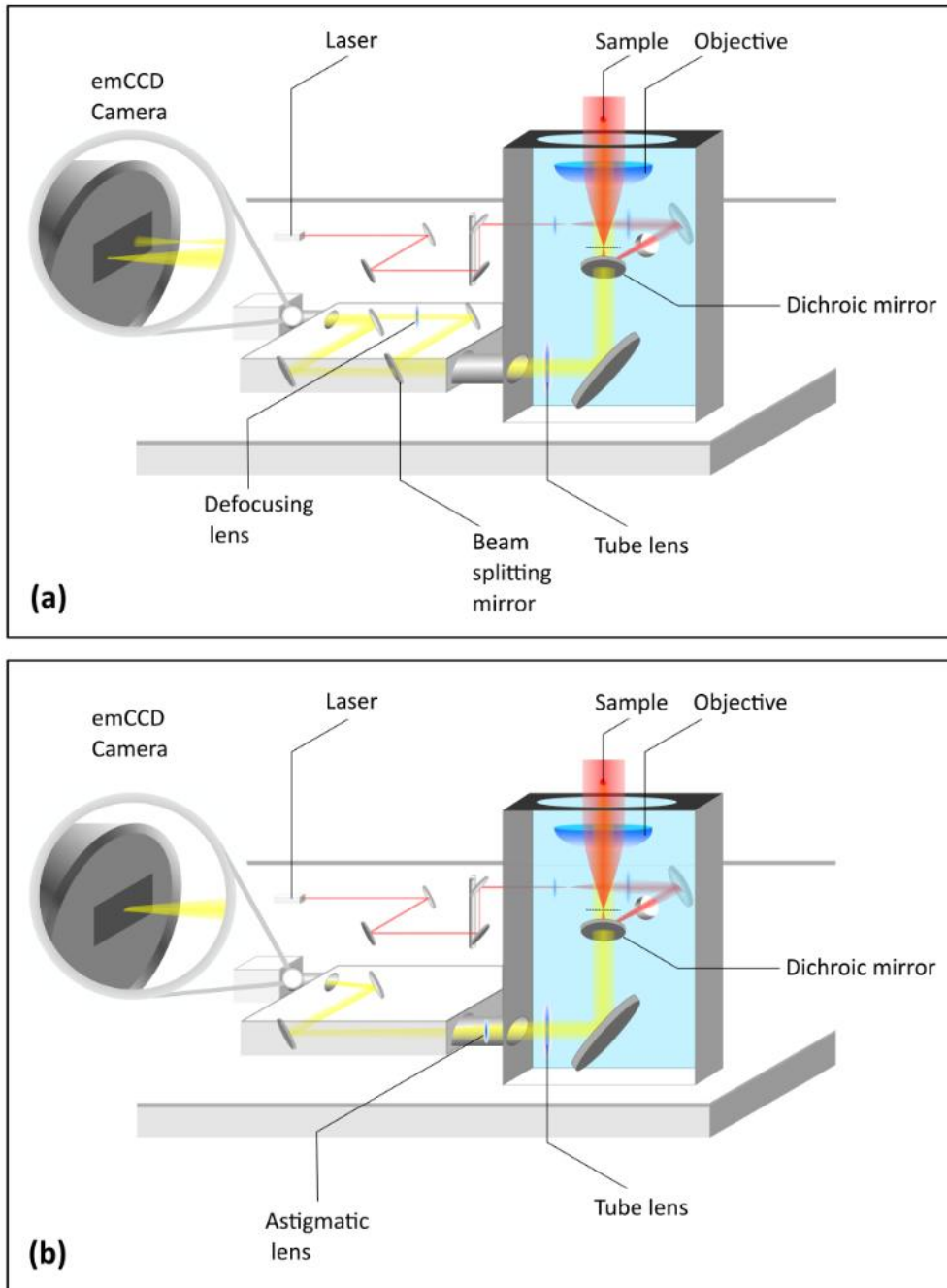
Figure 17 3D SMLM setups. (a) Biplane SMLM setup. (b) Astigmatism SMLM setup.both setup contain a laser that is guided and shaped by mirrors and lenses to the proper size and focused on the back focal plane of the objective. The sample fluorescence light is collected by the same objective, and either split into two path and submitted to a focus shift in only one path or modified by an astigmatism lens. The fluorescence light is focused on the camera sensor to form an image that can be recorded.

light path and adds an optical aberration that encodes the axial position of the emitter in the PSF shape and size (Figure 17(b)). The PSF elongates in orthogonal directions x and y for emitters above and below the focal plane, respectively.

Fluorescent samples: fluorescent beads, single molecule surfaces (SMS) and DNA Nanorulers sample

Early experiments used fluorescent beads (Tetraspeck T14792) for their brightness and stability over time. This allowed recording PSFs with high photons counts even with limited illumination powers. This reference standard sample consists of microspheres labelled with four fluorescent dyes of different colours. We used the samples with beads of sizes 100, 200 and 500 nm. Because the size of beads is comparable to the PSF size and each bead holds multiple dye molecules, this sample was used to demonstrate that our system allows 3D SMLM. But it is not directly translatable to single molecule samples. We then prepared single molecule surfaces (SMS) (Figure 18) for more accurate calibration and further experiments, according to protocols published before (Heilemann, van de Linde, et al. 2008). A Labtek Chamber is cleaned as follows:

- Sonification in Decon 90 3%, 30°C, 30 min
- Wash 3 times with sterile-filtered H2O
- Sonification in sterile water, 30°C, 30 min
- Wash 3 times with sterile-filtered H2O
- Moistening with 99% ethanol
- Wash 3 times with sterile-filtered H2O
- Sonification in KOH 1M, 30°C, 60 min
- Wash 3 times with sterile-filtered H2O
- Rinse with 99% ethanol
- Dry with N_2

In the clean Labtek chamber, we incubated sequentially, washing three times with PBS between each treatment, with:

- A mixture of Bovine Serum Albumin (BSA) and biotinylated-BSA
- Neutravidin

- Biotinylated double-strand DNA labelled with a fluorophore, here Alexa647

By adjusting the concentration for biotinylated BSA and labelled DNA, we can produce a reference sample of spatially separated single fluorescent molecules randomly distributed in the plane just above the chamber surface.

This sample can be used for different purposes, such as illumination characterisation (chapter 4), 3D calibration, localisation precision and resolution determination and fluorescence kinetics studies (chapter 5)
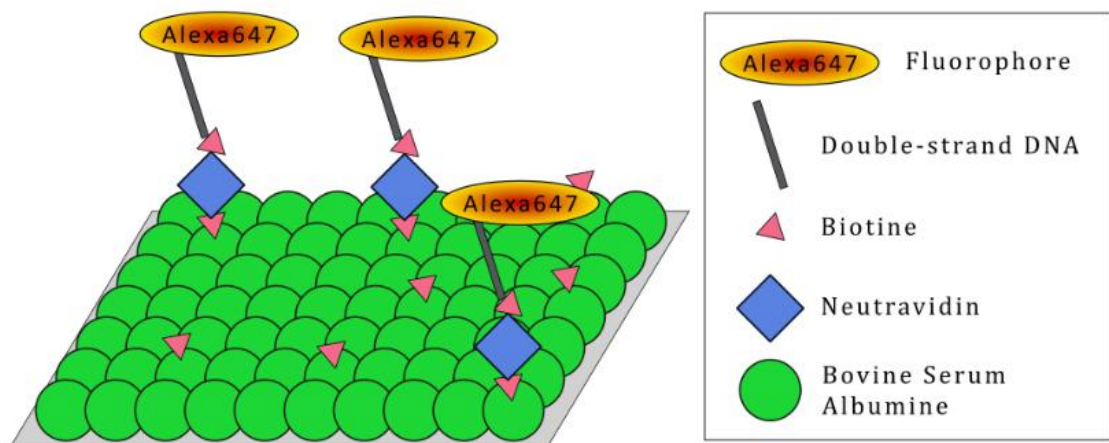
Figure 18 Single molecule surfaces are prepared by sequential treatment with Biotinylated BSA, Neutravidin and dsDNA fluorescent probes. After each step, careful washing removes non-specific binding.

A DNA Nanoruler (Gattaquant) sample is a commercially available sample used for the characterisation of 3D-SMLM setups (Schmied et al. 2013). It uses the DNA-PAINT methodology (See General Introduction) and consists of a DNA origami construct that holds two fluorophores at a fixed distance of $80.6 \pm 20.5\ nm\ (mean \pm standard\ deviation)$ according to the manufacturer. DNA nanorulers were used to characterise our 3D SMLM setup (section 2.5).

3D calibration

3D SMLM requires an initial calibration experiment. A reference sample, here a single

molecule surface (SMS), is scanned axially while an image stack is recorded. This allows the production of a reference table that allows a correlation between the axial position of an emitter and the shape and size of its image(s) on the camera. Alternatively, a formula can be deduced from the calibration data to directly link the PSF shape and size to the axial position.

This calibration step requires the axial scanning of the reference sample. We used a piezo scanner (Physik Instrument P721CDQ) to move the microscope objective axially.

By applying an electrical tension to a piezo electric material, it is distorted in a reproducible manner. This effect is used to produce nanometre-precise movements of the objective. We used a triangle function movement for our calibration step. This means that the objective oscillates up and down at a constant speed and temporal frame information can be related to an axial position, i.e. the axial distance between two acquired frames.

The piezo scanner software allows to choose the amplitude A of the triangle function and its frequency v. We can then deduce the scanning speed s:

$$s = 2Av \qquad (6)$$

Similarly, the camera software provides the camera cycle time (T_0) that corresponds to the time between two frames. Hence, the distance travelled by the camera objective between two recorded frames is:

$$d = sT_0 \qquad (7)$$

Figure 19 shows an example of calibration curve for biplane (a-c) and astigmatism (d-f) 3D-SMLM. For biplane, the average size of the PSF in x and y is calculated in both planes. We observe a similar behaviour in both planes with an axial shift introduced by the defocusing lens in one optical path. The minimum PSF size corresponds to the fluorescent emitter being in the focal plane. For astigmatism, we plot the PSF size in x and y directions. They change in opposite ways along the axial scanning as expected for a cylindrical lens.
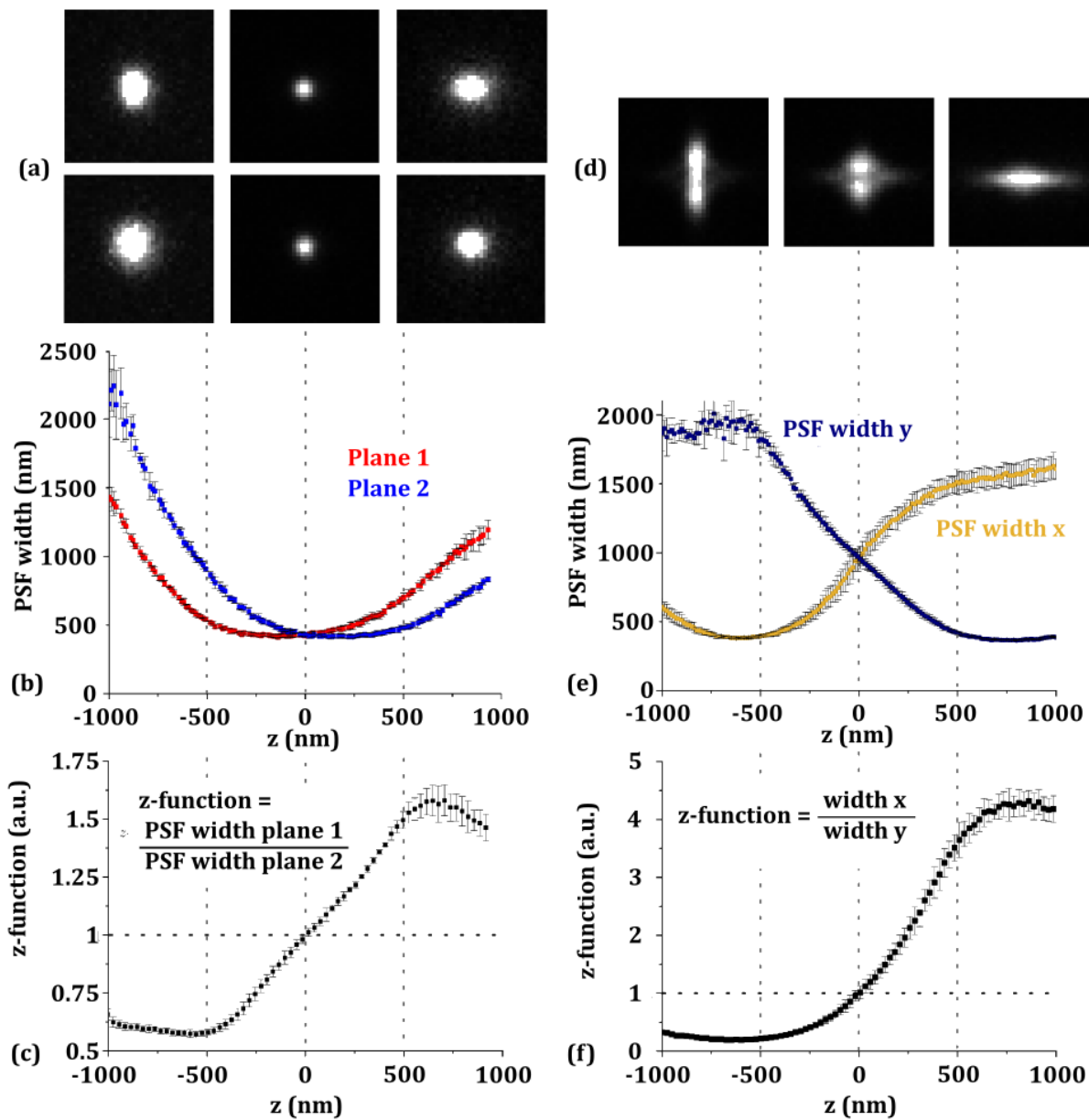
Figure 19 3D calibration and z-function (a,d) Sample images of emitter below, in and above the focal plane for biplane(a) and astigmatism (d)3D-SMLM.(b,e) PSF size in both planes or in x and y are recorded as a function of the axial position. (c,f) z-function are calculated from values in (b,e). The z-function alows to assign a single axial position to each emitter in an unknown sample after a calibration step.

We arbitrarily fix $z = 0$ as the axial position where the z-function equals 1 in both methods.

This position corresponds to the middle of the useable range of 3D-SMLM. In Figure 19 (c)

and (f) we plot the z-function that summarises the information from the two curves in

Figure 19 (b) and (d) respectively. Here, we used a simple ratio of the two curves to create a function that associates each axial position to a single value and vice versa. This circumvents the issue of only using the PSF size in one plane that did not allow discriminating emitters above and below the focal plane. To assign an axial position to emitters in an unknown sample we can build a look up table linking z function values and axial positions in the calibration plot or we can invert x and y axis in calibration plots (Figure 19 (c,f)) and fit a high order polynomial function. This function can then be applied to the z-function value of emitters in the unknown sample to assign an axial position.

Data analysis

The data analysis macros used in this section were written by SvdL and are described in section 2.4. Shortly, they allowed automation of the calibration and assignment steps described above.

Data visualisation can be a 2D image color-coded with the calculated axial position or a 3D reconstruction of the volume using for example the 3D Viewer plugin in ImageJ.

Tilted slide control

After the 3D-SMLM setup was built and calibration was performed for astigmatism we built a control experiment to demonstrate the capability of our system to perform 3D-SMLM. A reference slide holding fluorescent beads attached to the glass slide was set on the sample holder at an angle by adding two coverslips under the glass slide on one end. The tilt was aligned with the x-direction of the camera. The thickness t of the two coverslips and length l of the sample slide was measured using callipers. The angle α of the sample was calculated from those two measurements with $\sin(\alpha) = t/l$.

After data was recorded and localisation was performed, the axial position a was calculated from x_i the x-axis distance of fluorescent beads from the coordinates of

90

fluorescent beads in the focal plane and the angle α calculated above:

$$a = x_0 \tan \alpha \qquad (8)$$

(a)

(b)
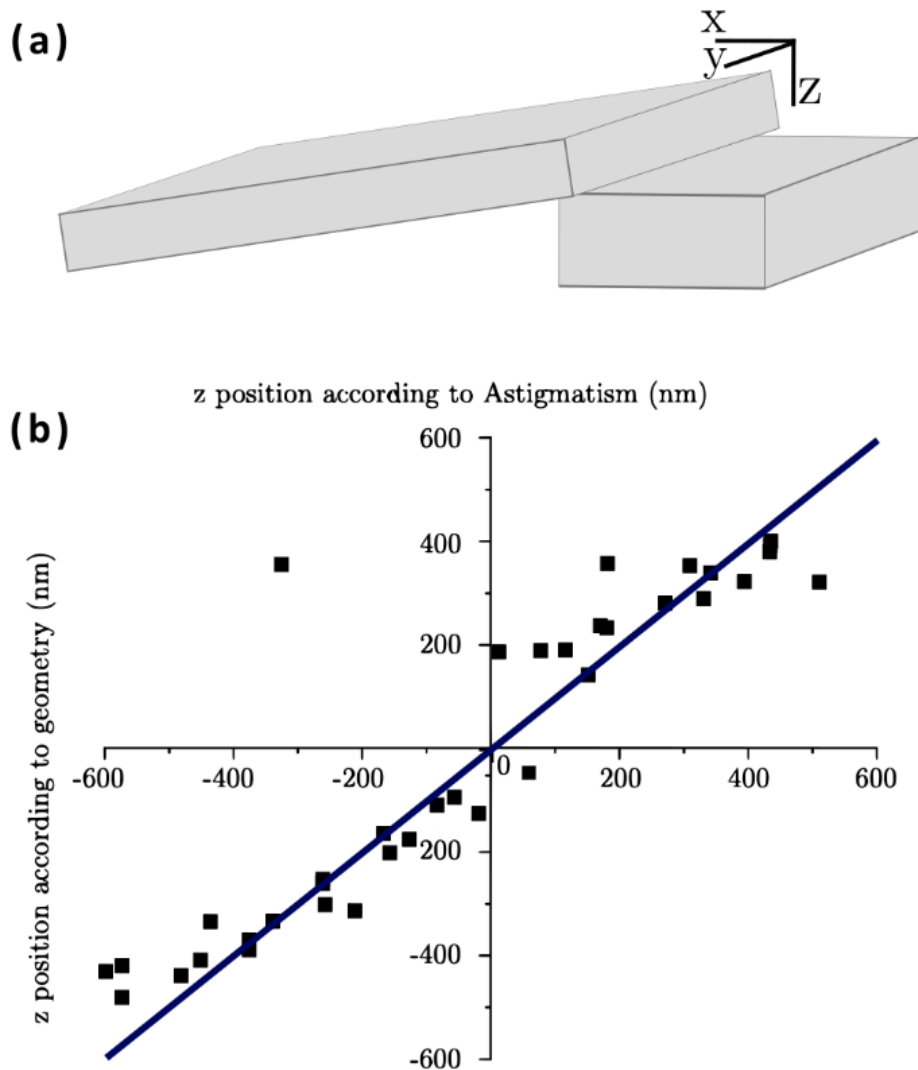
Figure 20 Validation of the calibration curve for astigmatism. (a) A tilted slide at a known angle is imaged and 3D SMLM astigmatism data analysis is applied. (b) The axial position is retrieved from the PSF according to the calibration curve and compared to the value calculated from geometry. The blue line represents the perfect match between astigmatism and geometry.

Separately, an axial position was assigned according to the astigmatism calibration z-

function. The axial positions obtained by both methods are compared in Figure 20 (b). We conclude that 3D-SMLM can be performed on our microscopy setup with a range of 1000 nm with the cylindrical lens used in this experiment.

2.5.2. Further optimisation of 3D-SMLM

Once we demonstrated our capability to perform 3D-SMLM in our setup, we investigated several avenues to improve its performance. This work was later continued by two master students (Jordan 2018; Phillips 2019). We compared different focal lengths for the added defocusing or cylindrical lenses and we compared different formulas for the z-function.

Biplane focal length

In this experiment, we axially scanned a sample of fluorescent beads of diameter 0.1 μm (Tetraspeck T14792) while recording images. Fluorescent beads were localised with rapidSTORM using a free PSF width parameter and the z position was calculated as described before. Z = 0 was arbitrarily set where the PSF size was the same in both planes. The localisation software can detect emitters that are within 1000 nm on either side of the focal plane with a satisfactory accuracy. By varying the focal length of the defocusing lens, we modify the focal shift between two planes and the shift between the PSF width minima in the two planes. An accurate z-function relies on a trade-off between a good overlap of the regions where the localisation software can accurately detect emitters and a sufficient difference in the size of PSFs between the two plane images. A very small defocus (Figure 21, 10m lens) gives a maximum range of use but negatively impacts the axial resolution. A larger defocus reduces the overlap of usable PSF localisation but allows better axial resolution.
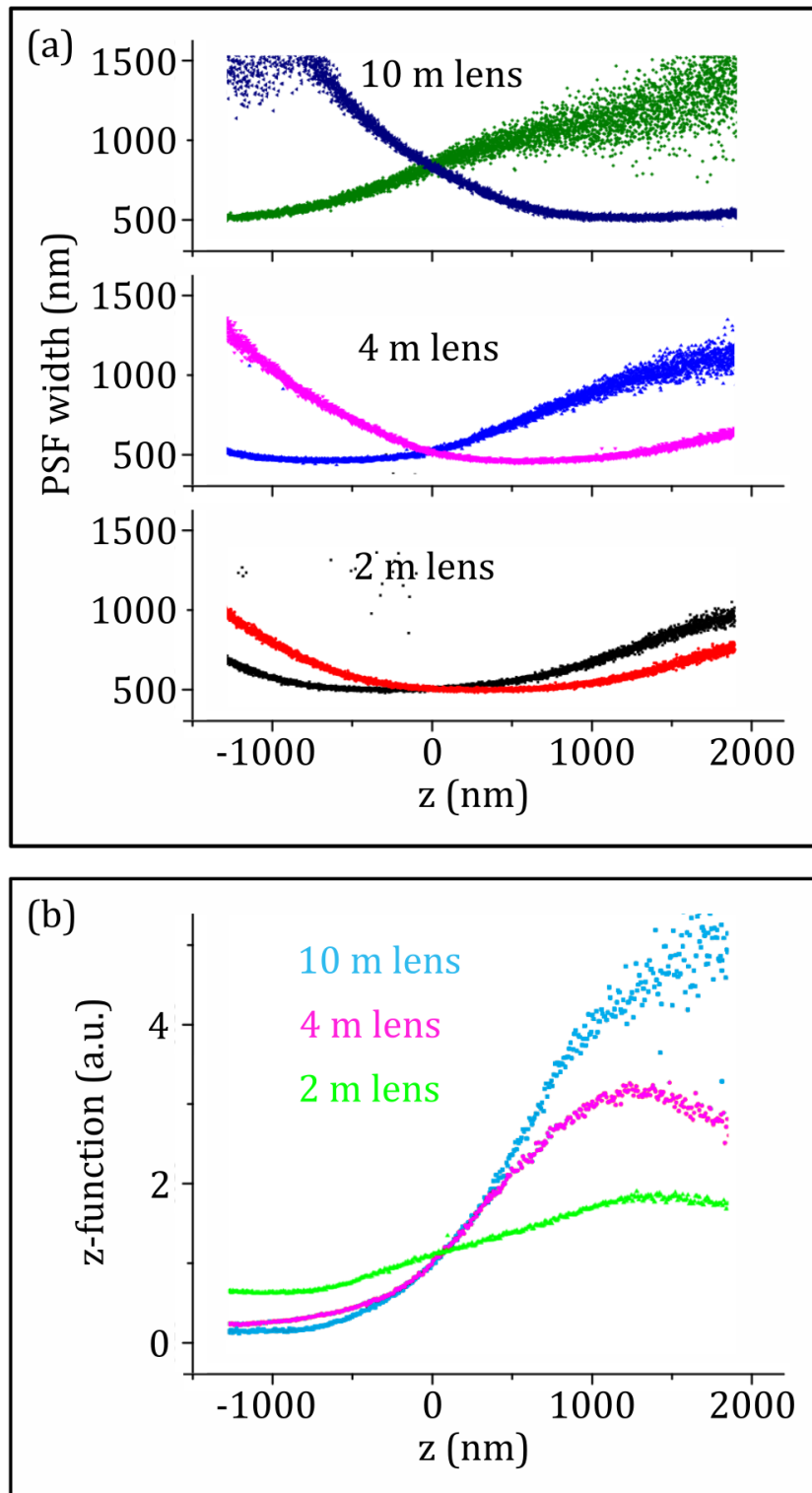
Figure 21 Biplane lens focal length: (a) The average PSF width of fluorescent beads in plane 1 (Green, blue, black) and 2 (Navy, pink, red) is shown for three defocusing lenses of focal length 2, 4 and 10 m. (b) The corresponding z-functions (ratio of PSF width in plane 1 and 2) are calculated for all three conditions. The choice of the focal length for the biplane defocusing

lens influences the focal shift between planes (a), the axial range of use and the axial accuracy of the axial localisation (b). A steeper z-function allows for a more precise axial localisation but reduces the range of use.

A more detailed investigation of focal lengths was done by Brian Jordan and Ross Phillips (see section 2.5.3 below)

Z-function development

The z function allows us to summarize the characteristics in different planes or in x and y directions of the PSF of one emitter with a single number. This number describes the shape and size variation of the PSF along the axial range. Another point of the z-function is to discriminate whether emitters are above or below the focal plane. Finally, the z-function should assign a value to only one axial position.

Ratio vs normalized difference

Initially we used a simple ratio a/b of PSF width in x and y for astigmatism and in plane 1 and 2 for biplane (Figure 22). The ratio of PSF sizes follows the prerequisites stated above but it has some limitations. The shape is not symmetrical with respect to the focal plane, the noise seems proportional to the value of the z-function which makes it less accurate for one side of the focal plane compared to the other.

Later we decided to use a different z-function to resolve these limitations:

$$\frac{a - b}{a + b} \tag{9}$$

Here, we obtain a symmetrical function around the focal plane (Figure 22). The value for this z-function is 0 at the focal plane and increases with the distance from the focal plane. Further, we observe a constant level of noise on either side of the focal plane.

New photometric biplane methodology

Biplane relies on the localisation software fitting a 2D Gaussian function to the recorded

images. The Gaussian fitting function has three main free parameters, namely Full Width at Half Maximum (FWHM) in x- and y-directions and the intensity that is a function of the amplitude of the fitted Gaussian function. Having three parameters can make the analysis of large datasets long, even with a dedicated software aimed at a fast localisation such as rapidSTORM (Wolter, Löschberger, Holm, Aufmkolk, Dabauvalle, Van De Linde, et al. 2012).
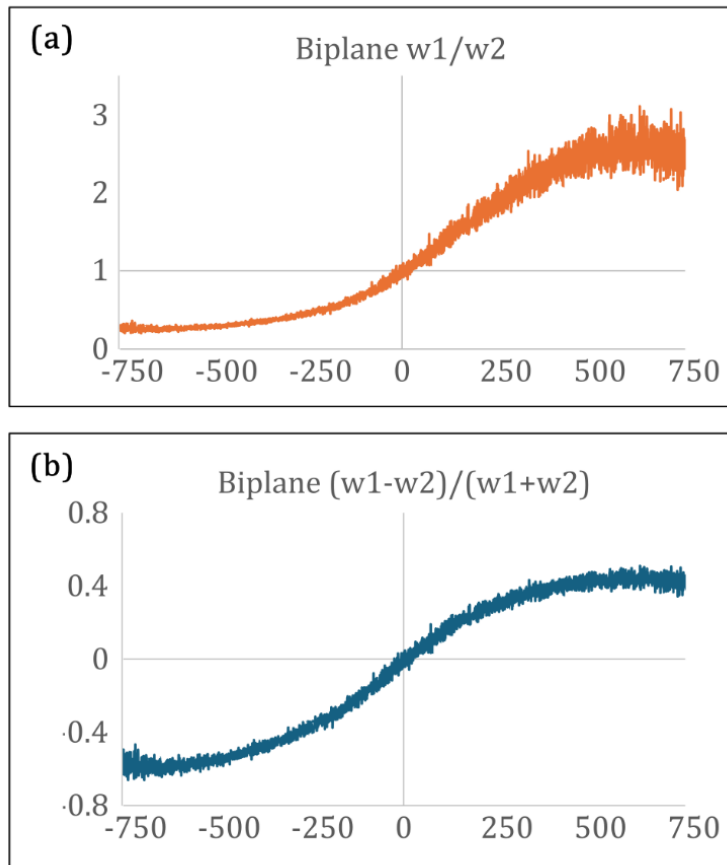
Figure 22 Comparison of biplane calibration curves with two z-functions. (a) simple ratio of PSF widths, (b) normalized difference of widths

During our experiments on 3D-SMLM optimisation, we wanted to accelerate the data analysis in conditions that did not immediately require a very good localisation accuracy but rather a general trend to assess the quality of the recorded data. To do so, we tried to use rapidSTORM with a fixed Gaussian width (FWHM = 500 nm). Here the Gaussian fitting only has one variable parameter, the amplitude. It resulted in a much faster analysis and

we realised that this method was similar to photometry methods used in astronomy as well as methods developed by SvdL et al with TRABI (Franke, Sauer, and De Linde 2017) that was already derived from astronomical photometry. We also realised that the amplitude in each plane obtained with this method could be used as a parameter for biplane 3D-SMLM.

DNA Nanoruler control

As a final evaluation of our ability to perform 3D-SMLM in our setup, we imaged a reference sample of DNA Nanoruler and found a distance between the two fluorophores to be $88.2 \pm 17.1\,nm\,(mean \pm standard\,deviation)$ comparable to the manufacturer's results $(80.6 \pm 20.5\,nm)$.

Convinced that our 3D setup was usable, I helped supervise the work of two students that spent several months in the lab to investigate further optimisation of 3D-SMLM.

2.5.3. Master students' projects

Continuing the work presented above, two master students studied 3D-SMLM in the lab after this project. Below is a short summary of their projects that show the next steps of the research on this subject.

Brian Jordan (PH450 project report) *(Jordan 2018):*

Brian Jordan first investigated how, in biplane SMLM, the focal shift could influence the working range and the rate of change of the z-function. Those parameters are markers of the usable axial range of biplane SMLM and the axial accuracy. He studied how various artificial shifts between the imaging planes influence those parameters and concluded that smaller focal shifts increase the working range despite a poor axial resolution whereas a large focal shift give a better axial resolution over a shorter working range. The optimal

focal shift trade-off is determined to be 330 nm. To translate the focal shift into a lens focal length, Brian Jordan measured the focal shift introduced by planoconvex lenses of four focal lengths from 2 to 10 m. He demonstrates that by interpolation the ideal focal length is 7.68 m. The closest focal length available at the time was 5 m and he pursued his experiment with this lens. Brian Jordan then showed the influence of the fluorescent beads sizes on the quality of calibration curves. Finally, he performed the tilted sample slide experiment as described above for biplane and concluded in a good correspondence between geometry and biplane axial positions. All of his work was performed with fluorescent beads.

Ross Phillips (PH450 project report)(Phillips 2019):

Ross Phillips continued the evaluation of focal length for biplane and then also for astigmatism. He reproduced the experiments that were done earlier by Brian Jordan and developed a metric to determine a region of high accuracy around the focal plane and an extended working range with limited axial precision. He then investigated three focal lengths for the cylindrical lens in astigmatism.

After using fluorescent beads, Ross Phillips prepared Single Molecule Surfaces (SMS) to obtain more accurate calibration curves with single molecule emitters instead of large beads. A good density of fluorescent molecules still allowed for good statistics. Astigmatism, FWHM biplane and intensity biplane calibration curves were produced and their performances were evaluated on Gattaquant DNA nanorulers.

He concluded that, for the available lenses that he could test, FWHM biplane performs better than astigmatism and intensity biplane had the best results of the three.

2.5.4. Conclusion and outlook

In this section, we described how the third dimension can be investigated by 3D SMLM methods including biplane and astigmatism. We described the 3D microscopy setup, the reference samples used and the calibration steps required. Then we evaluated the performance of our setup before supervising students on optimisation projects. We showed that adding 3D capability to a 2D SMLM setup is cheap and only requires little calibration work.

The intensity biplane method was used as an analysis tool in a paper by Franke et al (Franke et al. 2022).

Further investigation could be made to improve performance. We discussed the idea of expanding the axial working range of 3D SMLM by combining astigmatism and biplane. An astigmatic lens would be used to encode the axial position of emitters before the light beam is divided in two equal parts. One light path includes an additional defocusing lens as in biplane. The defocusing lens should be chosen so that a slice of the sample is imaged with the astigmatism method on plane 1 and a shifted slice of the sample is imaged with astigmatism as well on plane 2. A small overlap of slices would allow alignment of both slices to reconstruct a volume twice as thick as for simple astigmatism. A limitation could come from the separation of the beam of light for biplane on top of the spreading of the PSF due to astigmatism. This would result in fewer photons in each PSF, making the Gaussian fit less accurate and potentially leading to more missed localisations.

2.6 Chapter conclusion and outlook

In this chapter, we have presented the microscopy setup that was used during this PhD project. We discussed the importance of data analysis in SMLM and how developing

custom data analysis routines helps the work in SMLM. We discussed the use of simulations for the purpose of presentation as well as scientific research. Finally, we described how a 3D SMLM setup can be implemented with minimal hardware changes and some additional data analysis and calibration. At the end, we also shortly summarized how this project was continued by others in the lab.

Further improvement of SMLM performance will be discussed in depth in dedicated chapters (see chapter 4 and 5).

Chapter 3. Intensity-based multi-channel dSTORM

3.1 Introduction

3.1.1. Multi-channel super-resolution microscopy

SMLM with its improved resolution promised to open the field of biological research to a molecular level that was barely accessible before, as most biological processes happen at a scale that will always be unreachable to conventional microscopy. Quantitative methods for SMLM were developed to study protein distribution (Coltharp, Yang, and Xiao 2014). The natural next step was to expand the methods to the study of several targets in the same sample.

Like with conventional microscopy, SMLM users often study the interaction of molecules in biological systems, and they need methods to obtain super resolution images that discriminate and, even better, allow the quantification of different biological targets in one sample. Hence, the need for multi-channel SMLM drove the super-resolution microscopy community to develop several multi-channel SMLM methods.

The main methods previously described include:

a) Several activators (Bates et al. 2007; Dani et al. 2010): The STORM method of SMLM uses an activator and reporter pair of dyes placed in close proximity. The activation of the activator dye by an activation laser triggers an energy transfer to the reporter dye that relaxes by emitting a photon. The multi-channel version of

STORM relies on a different dye pair for each target structure where only the activator changes. Because the reporter dye is always the same, this method avoids chromatic aberrations but still require a long acquisition time as each channel is recorded individually by shining the corresponding activation laser.

b) Sequential imaging (Löschberger et al. 2012; Laine et al. 2015): In sequential imaging, the different targets are labelled prior to the imaging with dyes that absorb and emit in different spectral regions. Images for different channels are then acquired sequentially, each with the relevant excitation laser and buffer adjustments if necessary.

c) Spectral demixing (Bossi et al. 2008; Lampe, Tadeus, and Schmoranzer 2015; Lampe et al. 2012): Similar to the previous method, two targets are labelled with spectrally partially separated fluorophores. The collected fluorescent light is split based on the light wavelength. Each fluorophore has a signature ratio of intensity on the two images.

d) Sequential staining (Valley et al. 2015; Tam et al. 2014): Each target in a sample is imaged independently, usually using the same dye to avoid chromatic aberrations. Between each target imaging, the previous labels are removed by washing or bleached before a new set of labels is added on the next target that is then imaged. Long acquisition times are often needed for this method.

Limitations come with each of these methods. Synchronizing camera acquisitions with lasers of several colours can be time-consuming and still require extra data analysis steps to handle cross talk between channels. The chemical composition of the switching buffer is a trade-off between different requirements when several dyes are present in the sample at the same time. Chromatic aberrations, sample drift due to long acquisition times or washing steps require corrections during the data analysis. Long

acquisition times with various high-power lasers can affect the integrity of samples as well as repeated washing steps for sequential methods.

Tools have been developed to perform the registration that corrects chromatic aberrations such as the imageJ plugin bUnwarpJ (Arganda-Carreras et al. 2006) but they require fiducials to be added to the sample, in practice, multi fluorescent beads are used. Registration errors are reported around 10 nm (Löschberger et al. 2012), which is close to the resolution that can be achieved in optimal SMLM resolution.

3.1.2. dSTORM and photoswitchable probes

dSTORM is presented in detail in the general introduction of this thesis. dSTORM is a super-resolution microscopy method that belongs to the SMLM family. It relies on the switching of dyes between a fluorescent and a non-fluorescent state. The switching is reversible and can be controlled to promote one population or the other by changing the buffer conditions. Thiol containing reducing agents can interrupt the chain of conjugated electrons that is responsible for the molecule's fluorescence. The removal of the thiol part in the presence of oxygen restores the fluorescence of the molecule. Thiol derivatives concentration, pH and oxygen concentration can be adjusted to control the population in each state (Van De Linde and Sauer 2014; Van De Linde, Wolter, and Sauer 2011). dSTORM is compatible with Fluorescence Resonance Energy Transfer (FRET) as demonstrated before (Uphoff et al. 2010; Holden et al. 2010).

3.2 A FRET-based multi-channel SMLM method

3.2.1. Novel blinking probes

By using the properties of dark quenchers and other common tools of SMLM, we worked on the development of new imaging probes for dSTORM. The new probes, also named tuneable photoswitches, are aimed at multi-channel dSTORM with fewer limitations than previously presented methods. The tuneable photoswitches are based on Cy5/Alexa647, some of the best performing dyes for dSTORM (Dempsey et al. 2011) in the presence or absence of a dark quencher (Figure 23 top right corner). A DNA double helix serves as a scaffold for the fluorophore, the dark quencher and the labelling tool that targets a chosen structure (antibody, toxin). DNA provides a finely adjustable distance between FRET partners that has already been used in this manner (Le Reste et al. 2012).

Probes that label different targets and represent different channels will be imaged at the same time and will be separated during data analysis by their intensity and activated state time, the ON time. For two channels, one probe will have a dark quencher in FRET distance from the carbocyanine fluorophore that will have a reduced emission intensity and an extended ON-time. The other probe will only hold the carbocyanine, fluorescing at higher emission rates for a shorter time. The total number of photons is expected to be the same over a complete ON event for both channels (Figure 23).
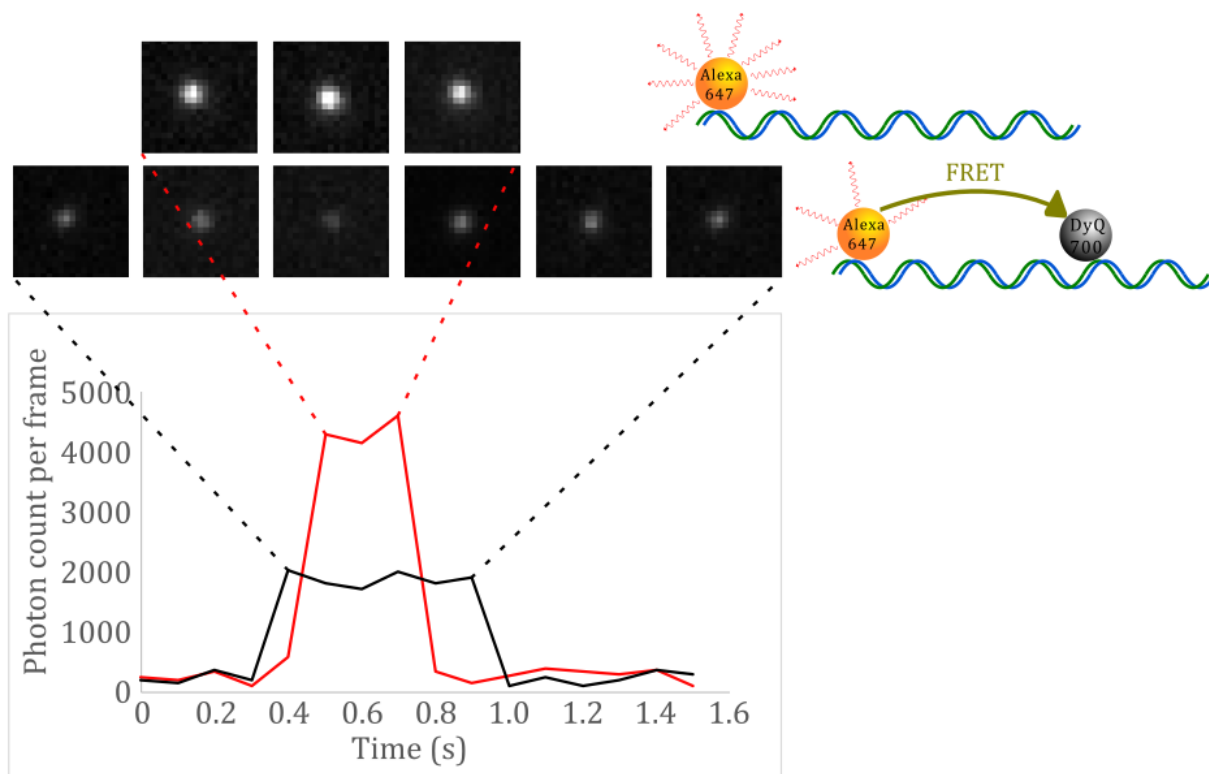
Figure 23 Novel Probes for Multi-channel SMLM. The probes we present in this section are composed of a double strand DNA scaffold holding Alexa 647 as well as an optional FRET partner (here DyQ700) at a chosen distance. In the presence of a FRET partner, Alexa 647 emits fluorescence at a lower rate leading to a lower photon count per frame and takes longer to switch OFF. Expected time traces of Alexa 647 in the presence (black) or absence (red) of a FRET partner show the influence of FRET on the fluorescence emission of Alexa 647. These were generated with the simulation chapter described in the previous chapter. Parameters that control the fluorescence emission intensity and the duration of emission before switching OFF were chosen to reflect the expected behaviour of our probes.

This can be explained when we consider the photoswitching (Van De Linde et al. 2013) and FRET mechanisms (Lakowicz 2006) described in the general introduction (Section 1.4.2.). Because the FRET interaction happens with the singlet excited state $^1F_1$ it competes with the rate k_{ISC} but does not change k_{red1}. It means that there will be fewer photons emitted each second i.e. lower emission intensities and it will take more time on average for the fluorophore to switch OFF because it will take more $^1F_0 / \, ^1F_1$ cycles to generate enough ISC cycles for the reduction transition to occur.

Probes design

The design of probes was done by SvdL before this PhD project started. It required to associate a fluorophore compatible with dSTORM, a dark quencher compatible with the fluorophore for FRET and a scaffold to hold them at a controllable distance. Alexa 647 was chosen for its prominent use in dSTORM, it is recognized as one of the best fluorophore for SMLM, it is very bright and it has reliable switching behaviour under controlled buffer conditions. The red excitation wavelength of Alexa 647 is also beneficial to reduce autofluorescence in biological samples. The dark quencher DyQ700 was chosen for the proof-of-concept based on its FRET compatibility with Alexa 647 (spectral overlap and calculated R_0 distance compatible with DNA, see section 3.2.2 below). Finally, dsDNA has been used before for single molecule FRET (Clegg et al. 1993; Le Reste et al. 2012; Holden et al. 2010; Uphoff et al. 2010) and is a versatile platform that allows some control over the distances and is compatible with biology applications.

The oligonucleotide sequences were chosen to minimize the probability of loop and hairpin formation to maximize the proper hybridisation of the dsDNA. The sequence was also chosen with Thymine on places that were considered for internal strand labelling. The labelling consists of a modified Thymine that holds the fluorophore or the quencher on a 6-carbon chain. The labelling spots were chosen to offer several distances close to the Förster distance calculated for the pair Alexa 647 – DyQ 700.

It was chosen to label the sense strand with Alexa647 and the antisense strand with the quencher and a biotin on the 5' end. Having the fluorophore and the quencher on different DNA strands allows combination of strands to vary the donor-acceptor distance. Biotin is used to attach probes to a neutravidin coated surface for single molecule microscopy experiments. It is placed on the quencher strand to ensure that all fluorophore that are supposed to be associated with a quencher are. Finally, labelling a single DNA strand with

three modifications is more chemically complex and more expensive.

3.2.2. Single molecule FRET on dsDNA probes

dsDNA probes are a well-established platform for single molecule FRET studies (Clegg et al. 1993; Le Reste et al. 2012; Holden et al. 2010; Uphoff et al. 2010). They come with the need for a few calculation tools for accurate FRET measurements. Here, we discuss geometry to calculate distances on DNA, the difference between terminal and internal labelling of DNA and a common mistake in estimating FRET efficiency from fluorescence lifetimes.

Förster distance of the Alexa 647 - DyQ700 dye pair

The theoretical FRET half distance R_0, or Förster distance, can be derived from the properties of the donor and acceptor, respectively Alexa647 and DyQ700 for this project. The general equation is:

$$R_0^6 = \frac{9000 \cdot (ln10) \cdot \kappa^2 \cdot Q_D}{128 \cdot \pi^5 \cdot N \cdot n^4} \cdot J(\lambda)$$

(14)

Where:

κ^2 describes the relative orientations of the donor dipole and the acceptor dipole. We fix it to 2/3, the value for freely rotating donor and acceptor.

Q_D is the donor's quantum yield in absence of an acceptor.

N is Avogadro's number, $6.022 \cdot 10^{23} \ mol^{-1}$

n is the refractive index of the solution.

$J(\lambda)$ is the spectral overlap integral ($M^{-1} \cdot cm^{-1} \cdot nm^4$) described by:

$$J(\lambda) = \frac{\int_0^\infty F_D(\lambda) \cdot \varepsilon_A(\lambda) \cdot \lambda^4 \cdot d\lambda}{\int_0^\infty F_D(\lambda) \cdot d\lambda}$$

(15)

Where:

$F_D(\lambda)$ is the fluorescence intensity of the donor in the range λ to $\lambda + \Delta\lambda$

$\varepsilon_A(\lambda)$ is the extinction coefficient of the acceptor at λ ($M^{-1} \cdot cm^{-1}$)

λ is the wavelength (nm).

The denominator acts as a normalisation factor for the donor fluorescence intensity.

The Förster distance for Alexa 647 and DyQ 700 that we used in this work was calculated in the preliminary work of this project by Dominic Helmerich (Dominic 2017):

$$R_0(Alexa647 - DyQ700) = 5.79nm \tag{16}$$

FRET efficiency from lifetime experiments

It has been reported that using the average lifetime from a multi exponential decay can be biased when analysing quenched probes (Becker and Bergmann 2023). If a substantial part of fluorophores is not quenched properly in the quenched probe population, their contribution to the average lifetime can skew down the FRET efficiency calculated from the average lifetime. Becker et al advise to use the short lifetime value of the two exponential decay fit in the calculation of FRET efficiency, especially when trying to relate FRET efficiency values to donor-acceptor distances (Becker and Bergmann 2023). We compared the two methods to calculate the FRET efficiency, and we observed a large underestimation of FRET efficiency when using the average lifetime compared to theoretical calculations. In Figure 24 (d), dark/light blue dots show FRET efficiency calculated with the average lifetime while red/orange dots show FRET efficiencies calculated with the short lifetime. Average lifetime leads to smaller FRET efficiencies that further deviate from theoretical values calculated from the geometrical model discussed above. Considering this, we will use the short lifetime component of the quenched sample to calculate FRET efficiencies in the results section below.

Calculating FRET distances on dsDNA

The distance of two FRET partners attached to a double strand DNA can be approximated by using a cylindrical model for the DNA double helix DNA first described by Clegg et al (Clegg et al. 1993). The donor-acceptor distance is then calculated as (Uphoff et al. 2010; Clegg et al. 1993):

$$R = \sqrt{(\Delta * n + L)^2 + d^2 + a^2 - 2da * cos(\theta * n + \Phi)} \tag{17}$$

Where $\Delta \approx 0.34\ nm$ is the axial distance between two base pairs, n is the number of base pairs between the donor and acceptor anchors, $\theta \approx 36°$ is the rotation angle between two adjacent base pairs, L is an additional axis distance to account for the linker when one fluorophore is attached to the end of the DNA strand ($L = 0.4\ nm$ for terminal labelling, $L = 0\ nm$ for internal labelling), d and a are the distances between the DNA axis and the donor and acceptor respectively ($d = a = 1.8\ nm$ for amino-C6-dT labelling, $\Phi \approx 228°$ represents the angle between a donor and acceptor that are attached to opposite DNA strands on adjacent base pairs.

Terminal vs internal labelling

In this chapter we used four quenched probes, M2-16-Q, M3-8-Q, M3-10-Q and M3-12-Q. M2 and M3 refer to the design generation and 8,10,12 and 16 are the positions of the Alexa 647 labelling on the DNA sequence counted from the 5' end. 5' and 3' ends refer to extremities of a DNA strand. Their names refer to the position on the sugar cycle that form the backbone of DNA. Detailed sequences are shown in Appendix. Alexa 647 is attached to DNA by using a modified deoxyribothymine (amino-c6-dT) molecule that binds to Alexa 647 with a 6 carbon long spacer. Probes from generation M2 had an internal labelling of both the fluorophore and the quencher. This means that the quencher and fluorophore were attached to the side of the dsDNA and were positioned away from the dsDNA axis.
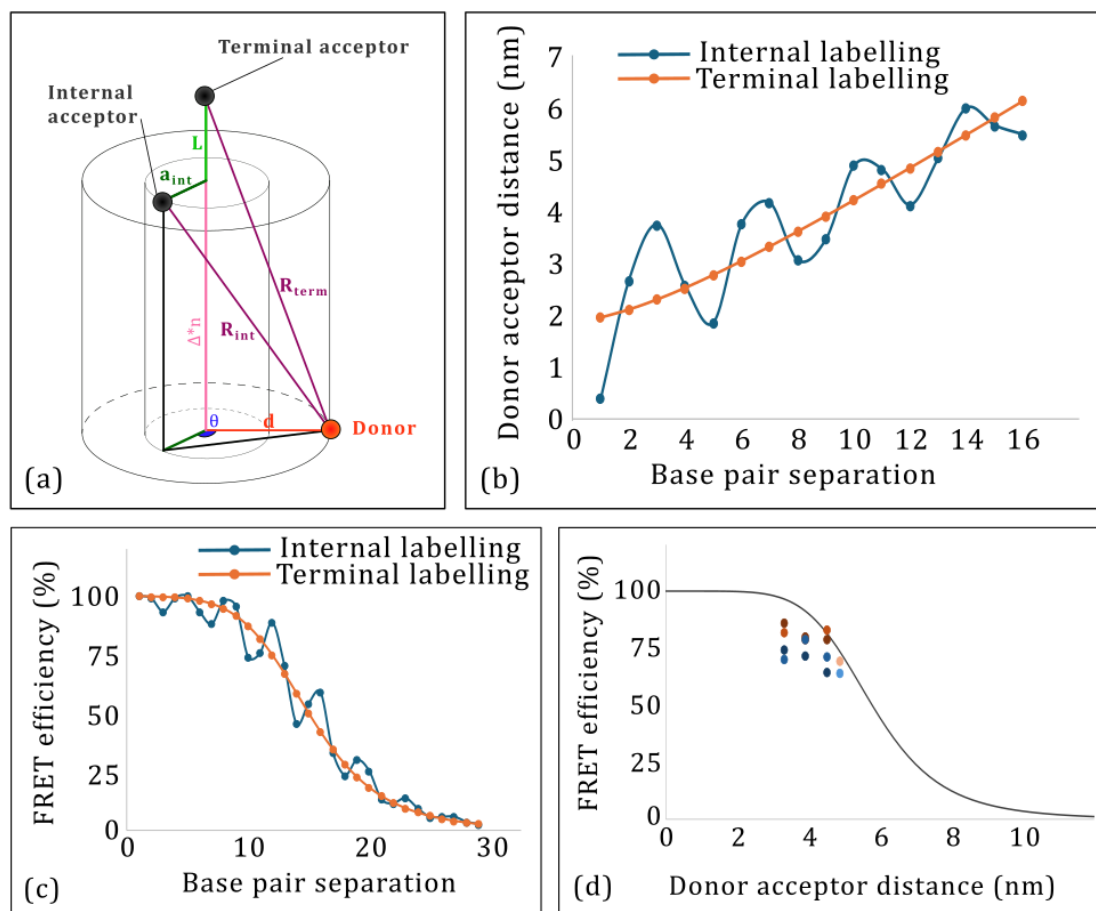
Figure 24 Single molecule FRET on DNA probes. (a) Geometrical model of dsDNA labelled by a FRET donor and a FRET acceptor. In this simplified model' the double strand DNA is considered as a rigid cylinder with donors and acceptor attached axial or orthogonally with rigid linkers. The simplified model allows a first approximation of donor acceptor distances but does not consider the flexibility of DNA and linkers in real life. Additionally, the model does not account for the relative orientation of donors and acceptors. (b) When both FRET partners are internally labelled, the distance is not directly proportional to their base pair separation. (c) A consequence of (b) is that FRET efficiency is not directly proportional to the base pair separation. (d) Experimental FRET efficiencies are lower than theoretical values calculated from the geometrical model. This shows the limits of the simplified cylindrical model. Probes used in this experiment are listed in Table 1 and detailed sequences are shown in Appendix.

Whereas for M3 generation, the fluorophore was internally labelled and the quencher was terminally labelled on the 3' end. The quencher was attached to the last nucleotide in the sequence and was positioned in the prolongation of the dsDNA axis. This difference has implications for the donor-acceptor distance (D-A distance) calculations. For terminal

quencher labelling, the D-A distance increases with the number of base pairs between the

donor and acceptor anchor nucleotides. But when both are internally labelled, the distance

is not directly proportional to the base pair separation (Figure 24 (b)). It follows that the

expected FRET efficiency oscillates in a similar manner for internally labelled probes

(Figure 24(c)) whereas it decreases regularly with the base pair separation in terminal

quencher probes. For generation M3, we used terminal labelling of the quencher to

simplify the distances in probes that we wanted to compare. Table 1 shows the D-A

distances for the four probes used in this chapter.

Table 1 Calculated theoretical distances between donors and acceptors for probes studied in this chapter using equation (17). The distance values are calculated with equation 17 using the manufacturer's specifications for the linker length. As expected from the model, M2 distances are larger because of the internal labelling.

Probe name	Donor-acceptor distance R (nm)	Base pair distance n
M2-16-Q	4.86	10
M3-8-Q	3.31	7
M3-10-Q	3.90	9
M3-12-Q	4.51	11

3.2.3. Tackling limitations of previous multi-channel SMLM methods

Colour cross-talk is observed when different dyes are used for different channels in SMLM.

There are two types of cross talk:

-   When the two channels are imaged simultaneously (spectral demixing) with two
    cameras where the two images are separated by a dichroic mirror, some photons
    from one channel may still pass through the dichroic mirror or be reflected when
    they should not and contribute to the image of the wrong channel

-   When the two channels are imaged sequentially (sequential imaging) with two

excitation wavelengths, fluorophores assigned to one channel might still have a limited ability to absorb the wavelength used to image the other channel and contribute to the other channel.

These two methods also require a registration step during the analysis to compensate for the distortion between channels due to chromatic aberrations. Chromatic aberration is non-linear across the field of view and requires initial calibration or the use of fiducials in the sample to be corrected. Additionally, the remaining error from chromatic aberrations correction is reported to be around 15-20 nm (Hebisch et al. 2017) or 10 nm (Löschberger et al. 2012). That is close to the optimal lateral resolution obtained in SMLM and it might become the limiting factor against improvement of resolution in these methods.

The use of different fluorophore also implies that the buffer is a trade-off between optimal conditions for each fluorophore(Löschberger et al. 2012). As we will see in chapter 5 the buffer conditions can strongly influence the photophysics of switching fluorophores leading to reduced super-resolution performances when the buffer is sub-optimal. A sub optimal buffer can reduce the total number of photons emitted by a fluorophore during an ON event, leading to a loss of localisation precision and resolution. A sub-optimal buffer can lead to photoswitches to stay activated for long times, increasing the risk of PSF overlap and errors in the localisation which led to a loss of resolution.

Recording all channels at the same time allows a shorter recording time to ensure a smaller drift that does not need correction. A single recording also avoids an extra data analysis step to align several datasets recorded sequentially.

Finally, deep samples are subject to autofluorescence when illuminated at wavelength shorter than 600 nm. The autofluorescence reduces the signal to noise ratio, impacting in turn the localisation precision and the resolution. Here, we used fluorophores that absorb in the red region of the light spectrum above 600 nm. This should reduce the

autofluorescence and bring a better tissue penetration when imaging deeper in a sample.

3.2.4. Data analysis

Absorbance and fluorescence intensity spectra corrections

Absorbance data was corrected by measuring the absorbance of a blank cuvette containing the same buffer as the sample measured. The blank absorption spectrum was subtracted from the sample spectrum. Additionally, the instrument also corrected the absorption values for the non-constant intensity of the light source across wavelengths. Finally, absorbance is generally shown to scale linearly with concentrations for values of absorbance below 1. To avoid additional corrections, if a sample showed a peak of absorption above 0.75, it was diluted in the same buffer and the measurement was reproduced. The dilution was taken into account to analyse data later.

The non-linearity of absorbance with the sample concentration for values above 1 is generally described as a deviation from the Beer-Lambert law (equation (18)) that describes ideal conditions. In practise, highly concentrated samples lead to scattering, molecule aggregation and energy transfers between close absorbing molecules and other effects altering the linearity of absorbance measurements. Additionally, we can consider that in high concentration samples, light will encounter several absorbing molecules while following one path across the cuvette. This also contributes to the non-linear relation between absorption and sample concentration.

Fluorescence normalisation by the absorbance

Obtaining comparable values for fluorescence emission to quantify FRET requires to normalize the measured emission intensity by the concentration of fluorophore (Alexa647) in the sample cuvette. Absorbance at 647 nm is a good marker of Alexa647's concentration

because it is directly proportional to the concentration:

$$A_\lambda(Alexa647) = \varepsilon_\lambda(Alexa647) \cdot c(Alexa647) \cdot l \qquad (18)$$

Unfortunately, DyQ700, the quencher we use in our probes also absorbs at the same wavelength. A correction step is required to extract the concentration of Alexa647 from the total absorbance for a quenched probe sample.

Absorbance spectra can be measured for individual DNA strands. We measured an absorbance spectrum for the sense strand labelled with Alexa647 and the antisense strand labelled with DyQ700 separately (Figure 25, red dots and green dashes). A control of both unlabelled DNA strands did not show any absorbance in the 350-800 nm wavelength range (not shown). We can observe that the maximum peak for Alexa647 is 647 nm and that DyQ700 also absorbs significatively at the same wavelength. DyQ700 also shows a peak at 400 nm where Alexa647 has no significant absorbance. The blue line in Figure 25 shows the absorbance spectrum for a mixture of complementary DNA strands. The mixture spectrum is a combination of the individual strands spectra.
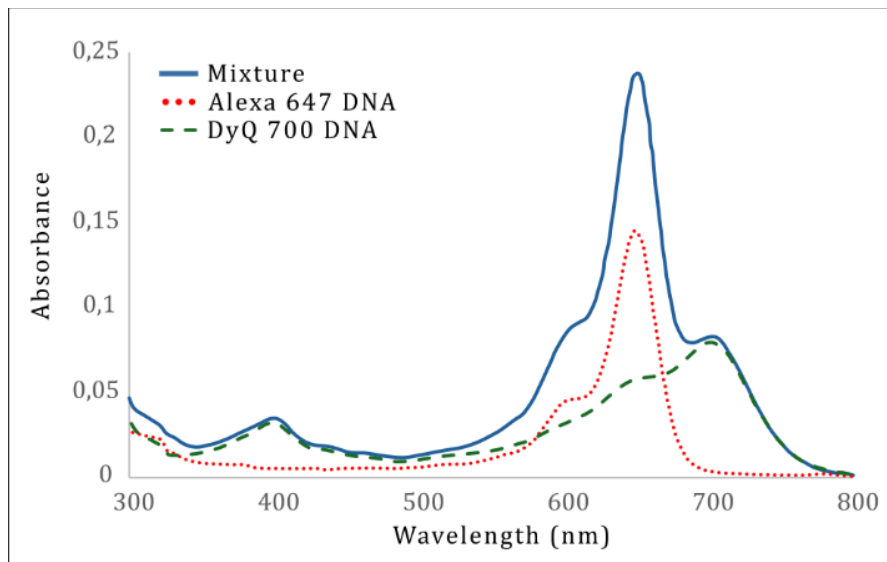

Figure 25 Absorbance correction. Both Alexa647 and DYQ700 absorb light between 600 and 700 nm but only DYQ700 absorbs at 400 nm. This allows calculating a correction factor for fluorescence emission that normalise for the quantity of Alexa647 in the sample. The correction factor is calculated from the absorption at 647 and 400 nm.

Absorbance is additive, the absorbance of a mixture is the sum of the absorbance of its components (Lakowicz 2006):

$$A_\lambda(mixture) = A_\lambda(Alexa647) + A_\lambda(DyQ700)$$

Absorbance is linear for values below 1 and the ratio of peak heights in an absorbance spectrum is constant for a given molecule. If α is the ratio of absorbance at 647 and 400 nm for DyQ700, then:

$$\alpha = \frac{A_{647}(DyQ700)}{A_{400}(DyQ700)} \tag{19}$$

$$A_{650}(Alexa647) = A_{647}(mixture) - A_{647}(DyQ700) \tag{20}$$

$$A_{650}(Alexa647) = A_{647}(mixture) - \alpha \cdot A_{400}(mixture) \tag{21}$$

α was calculated to be 1.78 from DyQ700 alone absorbance spectrum.

The absorbance of Alexa 647 at 647 nm calculated by this method will be used as the normalizing factor for Fluorescence emission for all spectroscopy experiments. When using a non-quenched probe, we directly use the absorbance at 647 nm.

SMLM data analysis

Microscopy data was localised using rapidSTORM with a filter on the relative intensity of localisations compared to the local background. As described before (Franke, Sauer, and De Linde 2017), the intensity is underestimated by rapidSTORM but as we use a single molecule surface, all emitters are attached to the plane coverglass and the underestimation will be the same for all. This issue must be considered for quantitative analysis and was accounted for in Ross Phillips' work where he used TRABI(Franke, Sauer, and van de Linde 2017) to correct intensities (see section 2.5.3). The output localisation files were used to track localisations in sequential frames with an ImageJ macro written by SvdL and described in more details in chapter 4 of this thesis and (Herdly et al. 2021b).

The tracking macro uses the list of localisations to reconstruct a super-resolution image of

the sample. Graphical cluster analysis is then used to extract localisations that correspond to the same emitter. If the cluster meets geometrical conditions, single-molecule time traces are drawn and the ON time is determined for each ON event.

An output file of individual ON events with their ON-time length, their average and individual frame intensities and their localisation coordinates is created and can be used for the channel separation.

3.3 Results and discussion

Absorbance, fluorescence emission and lifetime spectroscopy were performed on single strand DNA and double strand DNA probes to control the labelling, monitor the hybridisation of DNA and observe FRET in quenched probes. Then, SMLM experiments were conducted to study single molecule fluorescence traces.

3.3.1. Ensemble measurements

Single strand characterisation

After receiving the single strand DNAs labelled with Alexa 647 or DyQ700, we measured the absorbance of each DNA strand to control the presence of the fluorophore and the quencher. A large peak is observed at 260 nm that corresponds to DNA absorbance in all samples (Figure 25). Alexa 647 single strand showed the expected absorbance peaks between 600-700 nm. The DyQ700 single strand also showed an absorbance spectrum consistent with the specifications from the manufacturer. The fluorescence emission spectrum (Figure 25) of the Alexa 647 strand was also recorded and matched the expected profile. The DyQ700 strand fluorescence spectrum was measured as well and did not show any measurable fluorescence in the 500-800 nm region (not shown). We then mixed

Alexa647 and DyQ complementary DNA strands in a hybridisation buffer containing SSC buffer, 10 % dextran sulfate, 50% formamide in water and let the hybridisation take place at room temperature overnight.

An absorbance spectrum of this sample showed a superposition of both Alexa 647 and DyQ 700 peaks and a large peak at 260 nm that corresponds to DNA that was less than the sum of individual strands absorbances as expected from the lower extinction coefficient of dsDNA compared to single strand DNA. This was an argument in favour of DNA hybridisation but we proceeded with denaturation experiments to measure the melting temperature of our DNA samples.

DNA hybridisation and melting temperature

dsDNA separates into its two single strand DNA when the temperature is increased. The proportion of single and double strand DNA in a mixture of complementary strands follows a sigmoidal function (ThermoFisher Scientific 2022) with increasing temperature and can be fitted with a Boltzmann function (Figure 26 (a)). The melting temperature T_m is defined as the temperature at which 50% of the DNA is hybridised in a sample. It can be theoretically calculated by considering the nucleotide sequence (Markham and Zuker 2005). For M2-16-N and M2-16-Q, the theoretical melting temperature of 72.3°C was calculated with the DINAMelt server tool (Markham and Zuker 2005).

We investigated the melting temperature of our DNA probe M2-16-Q by absorbance and fluorescence emission spectroscopy (Figure 26 (b-d)).
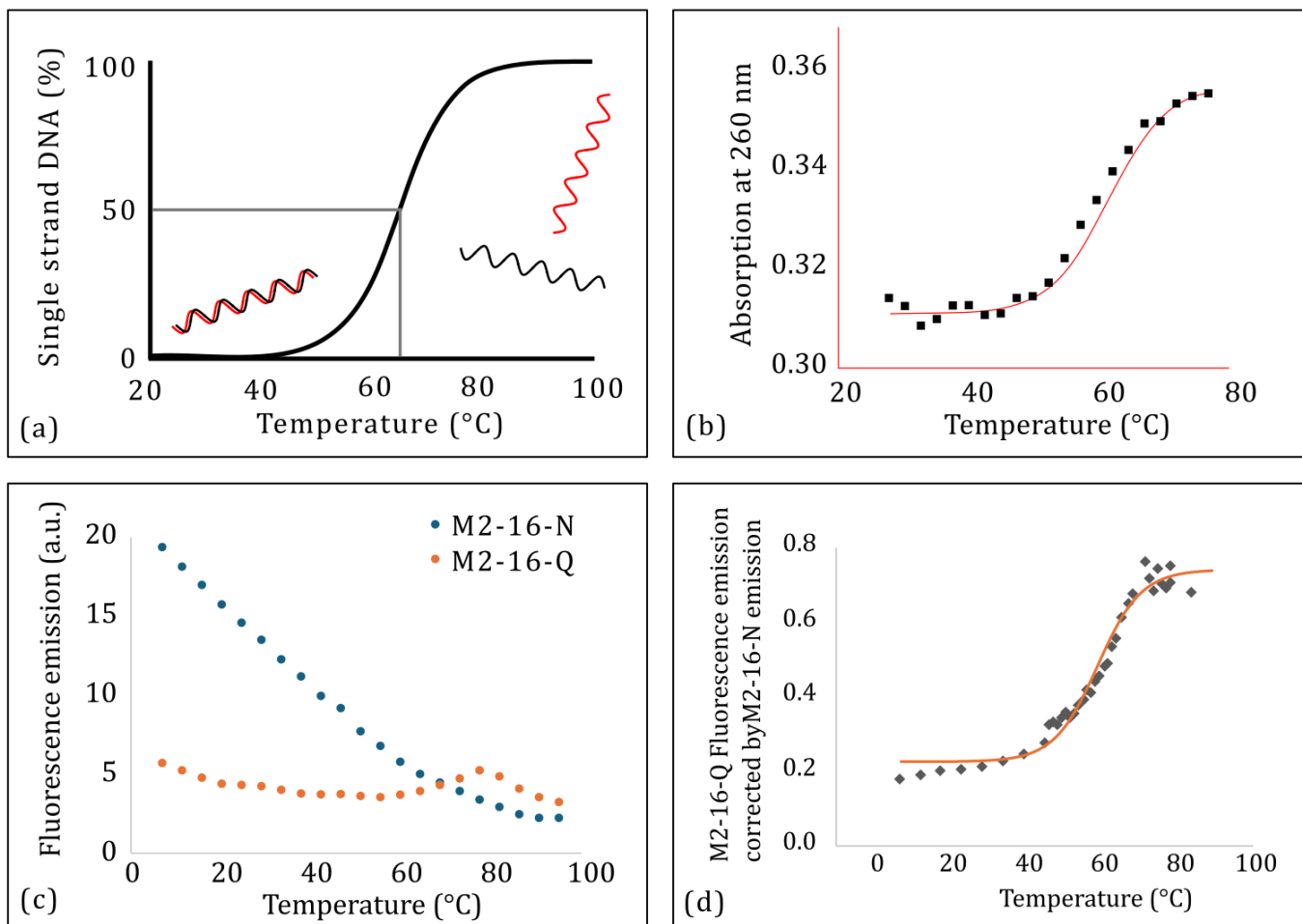
Figure 26 DNA denaturation experiments: (a) Complementary strands of DNA combine to form double strand DNA at lower temperatures and separate into single strands at higher temperatures. This is a theoretical visualisation of the DNA strands association/separation (b) Experimental observation of DNA denaturation by the change of Absorbance at 260 nm with increasing temperatures. The extinction coefficient of double strand DNA is lower than that of single strand DNA for the same sequence. (c) Fluorescence intensity of Alexa647 strongly decreases with increasing temperatures and a correction must be applied to the quenched probe to (d) monitor the separation of the DNA strand by fluorescence emission. At higher temperature, the separation of DNA strands increases the donor-acceptor distances, which decreases the FRET efficiency and increases the corrected fluorescence emission. The curves shown in b and d are sigmoid functions fits to the data

ssDNA and dsDNA have different extinction coefficients for a given nucleotide sequence. For ssDNA, the absorbance is approximately 30 % higher than dsDNA for the same nucleotide concentration and sequence (Nwokeoji et al. 2017). This allows the monitoring of DNA denaturation and hybridisation with increasing and decreasing temperatures,

respectively. In Figure 26 (b), we see that when the temperature increases, the absorbance at 260 nm increases, denoting the single strand separating. The highest temperature that the instrument reached in this experiment was 78°C. The lack of clear plateau at higher temperature decreases our confidence in the function fitting. The reported melting temperature of the fitting is 61.5°C, lower than the theoretical value calculated with the DINAMelt server tool.

The fluorescence emission of Alexa 647 in absence of the quencher, in probe NQ16, decreases with increasing temperature (Figure 26 (c)). As Jiang et al showed (Jiang et al. 2019), it can be explained by the higher collision rates that come with higher temperature that promote non-radiative relaxation (collisional quenching) and reduce the fluorescence emission rates, that is to say the fluorescence emission intensity.

For the quenched probe Q16, we observe a lower fluorescence intensity at room temperature when most DNA is in the double strand form and Alexa 647 is quenched by DyQ 700. When the temperature increases, the probe denatures, Alexa 647 is no longer quenched by DyQ700 and the fluorescence intensity gets closer to that of the unquenched probe NQ16. We correct the fluorescence emission of probe Q16 for the effect of temperature on Alexa 647 emission by dividing the fluorescence intensity of Q16 by the fluorescence intensity of NQ16 at the same concentration (Figure 26(d)).

After correction, we observe the familiar denaturation sigmoidal curve and we can fit the data to obtain a melting temperature of 62.5 °C. This value differs from the theoretical value calculated in DINAmelt. Importantly, DINAmelt only considers the blank DNA without linker and modifications such as dyes and quenchers that might modify the melting temperature by their steric hindrance and electrostatic or hydrogen bonds they might form with one or the other DNA strand. This explains the deviation from the calculated value on DINAmelt.

Demonstrating FRET in our M2-16 probes

To demonstrate FRET in our quenched probes, we compared two probes, M2-16-Q and M2-16-N.

Table 2 DNA sequences of probes M2-16-N and M2-16-Q

Name	Sequence
M2-16-N	5' GAT TGA CCC TAG ACC XTG ATT CGC ATT GAC TAC 3'
	3' CTA ACT GGG ATC TGG AAC TAA GCG TAA CTG ATG - Biotin 5'
M2-16-Q	5' GAT TGA CCC TAG ACC XTG ATT CGC ATT GAC TAC 3'
	3' CTA ACX GGG ATC TGG AAC TAA GCG TAA CTG ATG – Biotin 5'

X = AF647 on a modified deoxyThymine, X = DyQ700 on a modified deoxyThymine

M2-16-N is a double strand oligonucleotide of 33bp (Table 2) labelled with Alexa 647 on position 16 of the sense strand and Biotin on the 5' end of the antisense strand.

M2-16-Q is a double strand oligonucleotide of 33bp (Table 2) labelled with Alexa 647 on position 16 of the sense strand and Biotin on the 5' end and DyQ 700 on the position 28 of the antisense strand.

M2-16-N and M2-16-Q absorbance and fluorescence emission spectra were recorded and the absorbance correction was applied to the fluorescence emission spectrum (Figure 27 (a,b)).

The FRET efficiency was calculated as before:

$$E = 1 - \frac{I_{647}(\text{M2} - 16 - \text{Q})}{I_{647}(\text{M2} - 16 - \text{N})} \tag{22}$$

With I_{647}, the peak intensity at 647 nm after correction.

The FRET efficiency was calculated at 68.2%, lower but close to the calculated theoretical value of 73.9% calculated with the donor acceptor distance on DNA and FRET efficiency equations described earlier.
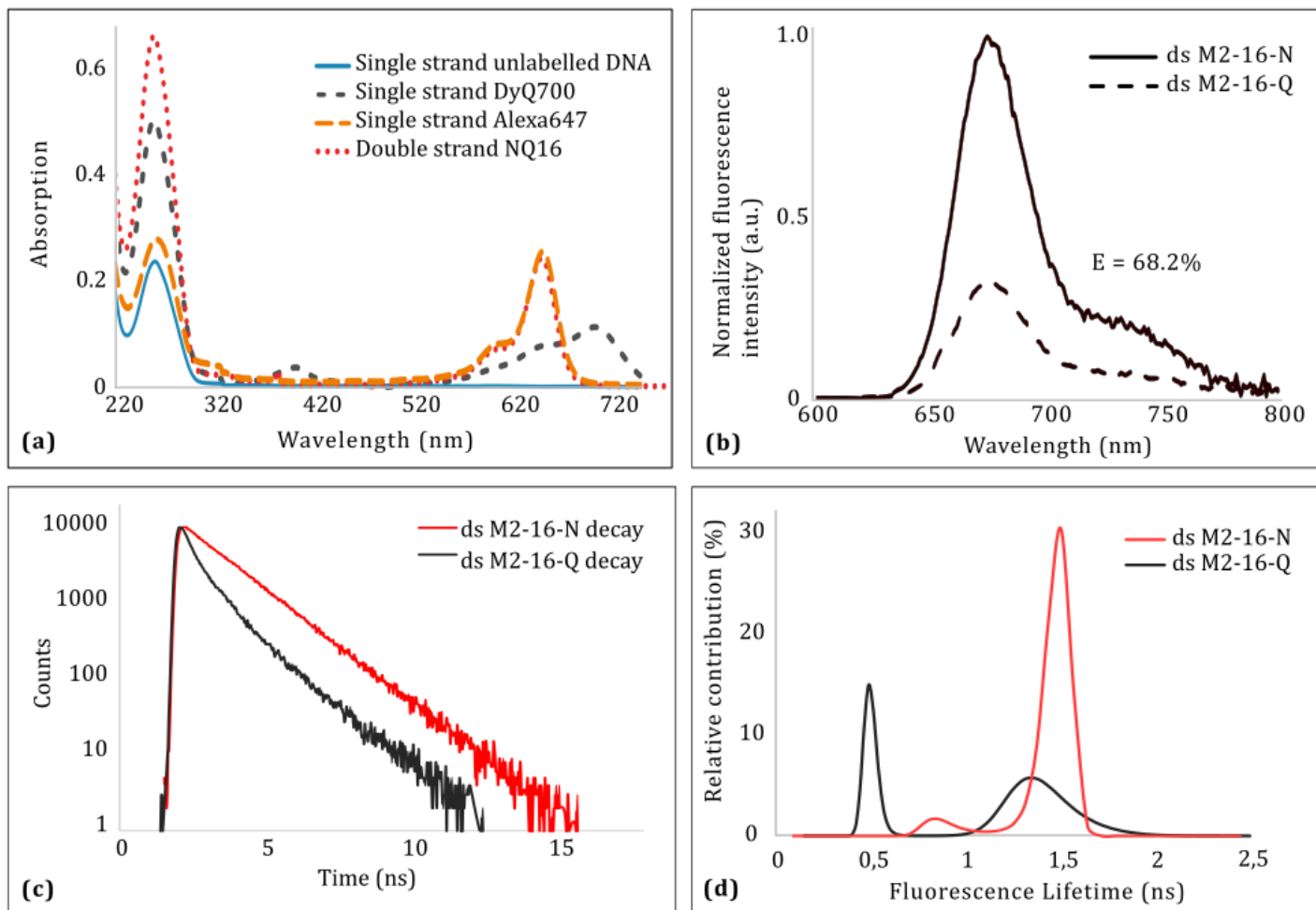
Figure 27 Results for probe M2-16-Q and M2-16-N. (a) Absorbance confirms the labelling of DNA strands. (b) Fluorescence emission of Alexa 647 is decreased in Q16 probe. The FRET efficiency is evaluated at E=68.2%. (c) The effect of FRET quenching is also observed in fluorescence lifetimes. (d) In NQ16 probes, most fluorophores show a long fluorescence lifetime whereas in Q16, a short lifetime population is detected.

Finally, we measured the fluorescence lifetimes of our two probes (Figure 27 (c)) and fitted the decay with two different softwares, Horiba DAS and Pulse 6 by J-C Brochon (Table 3 and Table 4).

The Pulse 6 software provides a distribution of lifetimes (Figure 27 (d)) that shows that in M2-16-N most fluorophores have a long lifetime while in the M2-16-Q probe, a significant part of the fluorophores has a shortened lifetime, indicative of FRET. A similar description of events is described by the amplitude changes for the short and long lifetimes in the

Horiba DAS software results.

Table 3

Horiba DAS	A_1	τ_1 (ns)	A_2	τ_2 (ns)	Reduced χ^2
M2-16-N	8.10%	0.743	91.90%	1.460	0.983
M2-16-Q	60.30%	0.474	39.70%	1.367	0.935

Table 4

Brochon Pulse 6	A_1	Width (ns)	τ_1 (ns)	A_2	Width (ns)	τ_2 (ns)	Reduced χ^2
M2-16-N	11.03%	0.095	0.881	88.97%	0.082	1.474	1.077
M2-16-Q	61.01%	0.037	0.501	38.99%	0.17	1.388	1.086

Table 5

Method	Weighted average Lifetime		τ short / τ long	
Software	Horiba DAS	Brochon Pulse 6	Horiba DAS	Brochon Pulse 6
FRET efficiency	46%	47%	65%	64%

In Table 5, we compare two methods to calculate the FRET efficiency from lifetimes. The weighted average methods was reported to underestimate the FRET efficiency and our results corroborate this statement.

FRET efficiencies calculated from the lifetimes with the ratio of lifetimes method were consistent with the fluorescence emission spectroscopy results but still not reaching the theoretical values.

Still, these experiments demonstrate that our quenched probe M2-16-Q exhibits quenching due to FRET.

Differences between model derived and experimentally measured values of FRET efficiency can be explained by the simplicity of the model that does not take all parameters into account. An important parameter for FRET efficiency is the relative orientation of the dipole moments of the donor and acceptor. The theoretical model used here fixes the value

of κ^2 in equation (14) at 2/3. This value translates the average relative orientation of a donor and acceptor moving freely in space. In our samples, both the donor and acceptor are attached to the DNA strand. Steric restriction and resistance to bending of their linker to the DNA strands hinder their free rotation leading to the relative orientation of their respective dipole moments being restricted. This explains some of the deviation of the experimental data from the model. In the future, a more accurate analysis of the relative orientation of the donor and acceptor considering the physical restrictions of the DNA structure and linkers would be beneficial to refine the cylindrical model.

Benchmarking donor-acceptor distances with 7, 9 and 11 bp separation

A new set of probes was designed for the next round of experiments. Probes M3-8, M3-10 and M3-12 are labelled with Alexa647 on either position 8, 10 or 12 of the sense strand, respectively, and are terminally labelled on the 3' end with DyQ 700 and on the 5' end with a biotin on the antisense strand. The choice of terminal labelling was a consequence of the distances calculations described in the section 3.2 of this chapter. With a terminal quencher, the donor acceptor distance is proportional to the base pairs separation whereas for internal labelling, distances can be counterintuitive (see section 3.2.2).

Our probes are designed with a donor-acceptor distance of 3.31, 3.90 and 4.51 nm respectively. Theoretical FRET efficiencies were calculated to be 96.6, 91.4 and 81.7%. Like for M2-16, the fluorescence intensity spectra are corrected for the concentration of Alexa 647 in the sample with the corrected absorbance at 650 nm, as described earlier in this chapter.

Fluorescence emission spectroscopy gave FRET efficiencies for M3-8-Q, M3-10-Q and M3-12-Q, of 87.7%, 80.8% and 81.6% respectively. These results are smaller than the theoretical values of FRET efficiency and the probes 10 and 12 are very close. This could be

explained by the donor-acceptor distance being too short in the three probes to observe a strong variability of FRET efficiency between them.
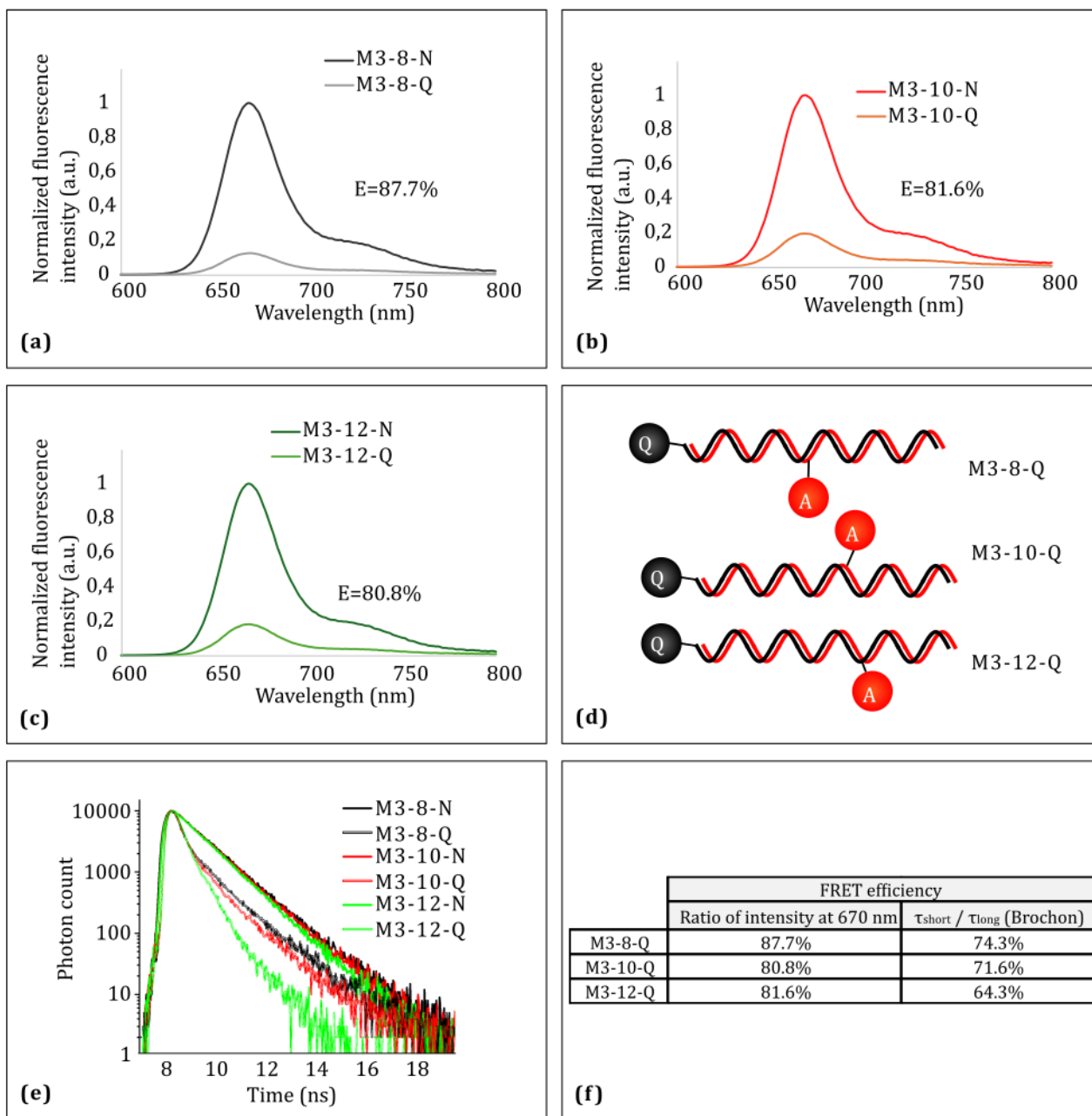
Figure 28 Results M3 probes: (a-c) Fluorescence spectroscopy of (d) three probes terminally labelled with DyQ700 and labelled on base pair 8, 10 or 12 with Alexa 647. (e) Fluorescence lifetimes decay are measured with TCSPC. (f) FRET efficiencies are lower than theoretical values calculated with the cylinder model for fluorescence intensity spectroscopy and time-correlated spectroscopy. Lifetime based FRET efficiencies follow the order of donor acceptor distances.

The underestimation was already observed for M2-16-Q.

3.3.2. Single molecule microscopy

Finally, we prepared single molecule surfaces according to the protocol described in the section 2.6.2 of this thesis with M2-16-N and M2-16-Q probes.

Switching buffer was added to both samples and data stacks of 15000 frames were recorded with each frame lasting 100 ms. Localisation and tracking of fluorescence traces were applied to the data and the frequencies of fluorescence intensities were calculated and plot as a histogram (Figure 29).
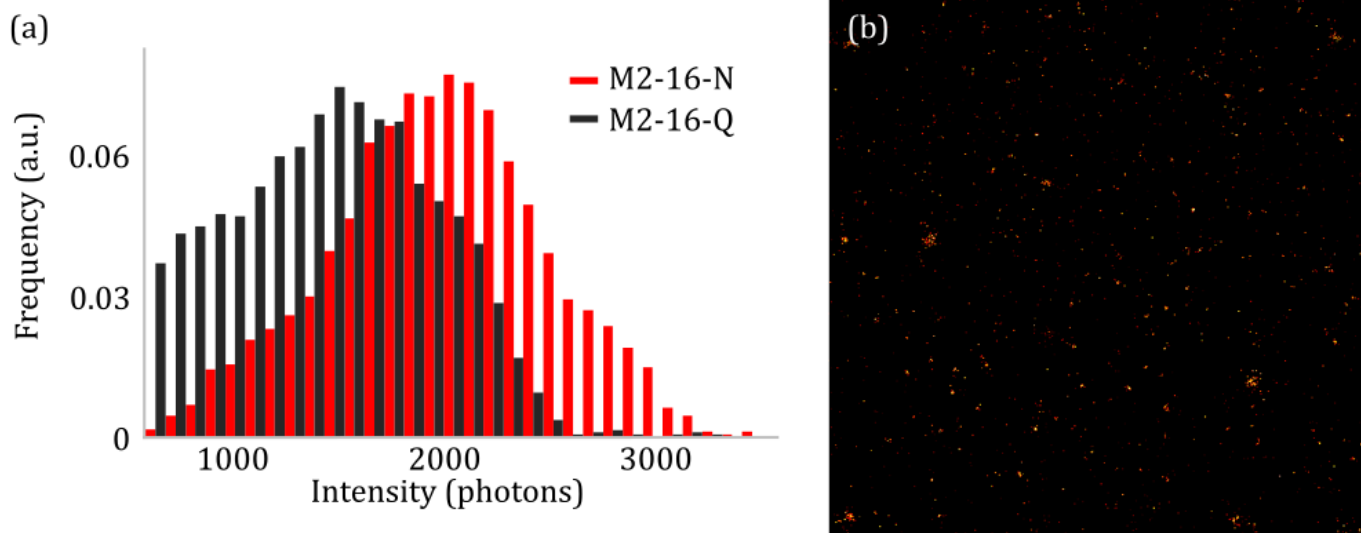
Figure 29 Single molecule surfaces experiments: (a) Localisation intensity distributions for M2-16-N and M2-16-Q single molecule surfaces imaged separately. Distributions for the quenched and unquenched probes strongly overlap, which forbids choosing a clear threshold to separate the two populations. (b) Reconstructed image of a single molecule surface of a mixture of M2-16-N and M2-16-Q probes. The colour code (red to yellow) represents the photon budget of each localisation event. The two probes emission intensities are not separated enough to show a clear difference between the two probes populations.

We see a large overlap of intensities between the quenched probe, M2-16-Q, and the non-quenched probe, M2-16-N. The FRET efficiency could be measured by the average intensity of localisations in each sample and we would obtain only 25.2% efficiency. This shows that

more investigations are needed before we can use the quenching based multichannel SMLM method.

Time was too short at the end of this PhD project to investigate the Probes with Alexa647 in positions 8, 10 and 12 in SMLM.

Several ideas have been discussed to answer the question why the difference was so low between the measured intensities of M2-16-N and M2-16-Q.

The relations between the exposure time of the camera and the length of an ON event of the probes is a factor to consider if we want to improve the separation of channels. If the exposure time is of the same order as the ON time, the two probes will have a similar intensity on each frame because even though the photon rate of the unquenched probe is higher, the total number of photons during one ON event is expected to be the same as explained earlier.

We used Gaussian illumination in this experiment and the non-uniform illumination of the field of view lead to a broadening of the intensity distribution of fluorophores across the field of view, leading to more overlap in the presented histogram. The working principle of FRET-based multi-channel SMLM could be demonstrated but the separation of channels was negatively impacted by the non-uniform illumination. We concentrated on the flat-illumination in chapter 4.

Finally, the bleaching or photoswitching of the quencher has been reported previously. The switching buffer that controls the photoswitching of Alexa 647 for SMLM could interfere with the quencher capability as a FRET acceptor. The thiol reducing agents could react with DyQ 700 and change its absorbance properties by changing the dipole moment of the molecule and thus affecting FRET efficiency. This would also broaden the intensity distribution of M2-16-Q towards higher intensities.

3.3.3. Master students' projects

After this part of the PhD project was paused to proceed with the work of chapters 4 and 5, two master students, Ross Phillips and Alan Keenan worked on their own projects (Keenan 2019; Phillips 2020) that were related to this one. Here is a short summary of their respective work.

Alan Keenan:

AK reproduced the melting curve experiments for M2-16-Q and another probe with a different dark quencher. He performed the experiments with absorbance, fluorescence emission and lifetime spectroscopy and obtained similar results to those presented here for FRET efficiencies and melting temperatures.

Ross Phillips:

RP investigated the relation between the exposure time of the camera and the length of ON events and the consequences on measured ON times and intensity for quenched and unquenched probes. RP also included three additional dark quencher candidates, BBQ, BHQ and DyQ 3. He showed that long exposure times alter the separation of quenched and unquenched probes according to their intensity and ON time. The additional dark quencher candidates were rejected as FRET efficiencies were not as good as with DyQ700. Finally, RP showed that a 2D mapping of intensity and ON time of single molecule traces allowed distinguishing between two distributions that could be used to separate two channels. Because of a significant overlap of the two distributions, a lot of localisations needed to be rejected.

3.4 Conclusion

In this chapter, we presented a quencher-based method for multi-channel SMLM. We

described ensemble absorbance, fluorescence emission and time-correlated fluorescence spectroscopy experiments that provide a proof-of-concept of the multi-channel method in ensemble measurements. FRET efficiencies of 60-80% could be measured and were 20% smaller than the theoretical values calculated by the DINAmelt tool.

Single molecule experiments did show a reduced separation of two channels that overlap strongly on their intensity. More optimisation needs to be conducted to efficiently separate channels.

A better understanding and control of Alexa 647 photoswitching would positively contribute to this project and will be discussed in chapter 5. Uniform illumination would remove one degree of freedom to the intensity variability of our probes and thus improve the separation of quenched and unquenched probes. The flat illumination and its effect on the emitter intensities distributions are discussed in the chapter 4.

Bleaching or switching of dark quenchers in thiol-containing reducing buffer used for SMLM experiments could further explain the difficulty to discriminate between quenched and unquenched probes in SMLM experiments compared to ensemble experiments. One option to limit these effects would be to benchmark dark quenchers to find those that are less likely to bleach or blink, for example if the conjugated electron chain were less sensitive to thiol reduction because of a bulky protecting moiety on the molecule. This project would require more experiments that we did not perform in the present PhD project.

Chapter 4. Flat illumination with a MEMS tilting mirror

4.1 Abstract

One challenge common to all fields of microscopy is the uniform illumination of the sample across the field of view. It is particularly important for quantitative microscopy, for example in dSTORM super resolution images. The switching behaviour of carbocyanine dyes that are widely used in dSTORM depends on the local illumination intensity. Importantly, the performance of super resolution imaging is not only influenced by emitter brightness, but also by the switching kinetics of the imaged fluorophores.

This leads to a variation of performance (achieved resolution, inaccurate quantitative analysis, missed structures) across the field of view when the illumination is not uniform, for example when an unmodified Gaussian laser beam is used.

Several methods have been developed to solve those limitations and some of them are commercially available.

In this chapter, we study a new approach to obtain a homogeneous illumination, also referred to as flat-illumination, of a large field of view $(62.5 \ \mu m)^2$ and compare it to a commercially available device (piShaper) that has been used in published works in the past (Ibrahim, Mahecic, and Manley 2020). Our illumination scheme is built around a MicroElectroMecanical Systems (MEMS) device, a small, very fast oscillating mirror.

This study also led us to develop a solid analysis routine for the analysis of switching kinetics of carbocyanine dyes. This routine could be used later to evaluate other

illumination schemes or study other factors that influence photoswitching kinetics. The next chapter uses the same analysis routine to compare various switching buffer conditions.

The MEMS device provides a homogeneous illumination comparable to the piShaper, although with a lower average illumination intensity in the sample but with the opportunity to obtain different illumination schemes easily apart from the flat illumination. The controlled illumination scheme allowed by the MEMS device will be used in the next chapter to study the photophysical properties and buffer chemistry of carbocyanine switching.

4.2 Authors contributions

Paul Janin (PJ) and Ralf Bauer (RB) developed, built and characterised the MEMS tilting mirror.

LH integrated the MEMS in the microscopy setup and tested various setup designs to allow parallel comparison of MEMS and other illumination schemes.

LH acquired all data.

LH and SvdL developed the data analysis and discussed the results

4.3 Introduction

In dSTORM, photoswitching rates are strongly influenced by the local illumination intensity. The switching rates impact the resolution improvement as they are linked to the density of simultaneously activated emitters, the brightness of emitters and the number of activations of each emitter during acquisition (Bates, Blosser, and Zhuang 2005; Heilemann, Van De Linde, et al. 2008). In this work, another motivation for flat-

illumination was the limited separation between intensity-based channels observed in the chapter 3. We expect the channel separation to benefit from the narrowing of emitters intensity and ON time distributions in each channel under a more homogeneous illumination.

A uniform illumination of the sample is then required to produce uniform image quality across the field of view (FOV). Furthermore, with the development of quantitative methods for SMLM (Ehmann et al. 2014; Jungmann et al. 2016; Endesfelder et al. 2013; Nicovich, Owen, and Gaus 2017; Marenda et al. 2021), the illumination must be homogeneous for the quantification to be consistent across the field of view.

Conventional wide field microscopy often uses a Gaussian laser beam to illuminate the sample. The illumination is then more intense in the middle of the FOV compared to the sides and corners. The intensity disparity can be reduced by spreading the laser beam with a telescope. This leads to more homogeneous illumination at the cost of a strong decrease of the average intensity due to the spreading of the laser beam (Figure 30)

SMLM methods often require relatively intense laser illumination although some efforts are being made to decrease the needed laser intensity following the demonstration of adverse effects of powerful lasers on samples (Waldchen et al. 2015). SMLM typically uses laser intensities of $0.1 - 1\ kW \cdot cm^{-2}$ (Waldchen et al. 2015).

This led several research teams to develop flat-illumination schemes using various approaches. Multi-mode fibres (Deschamps, Rowald, and Ries 2016; Zhao et al. 2017), microlens arrays (Douglass et al. 2016), refractive beam-shaping elements (Khaw et al. 2018; Rowlands et al. 2018; Stehr, Schwille, and Jungmann 2019), spatial light modulators (S.-Y. Chen et al. 2018) are some of the approaches described before.

At a similar time as this work was done, a system using two fast scanning mirrors called ASTER was reported to produce a flat-illumination (Mau et al. 2021).
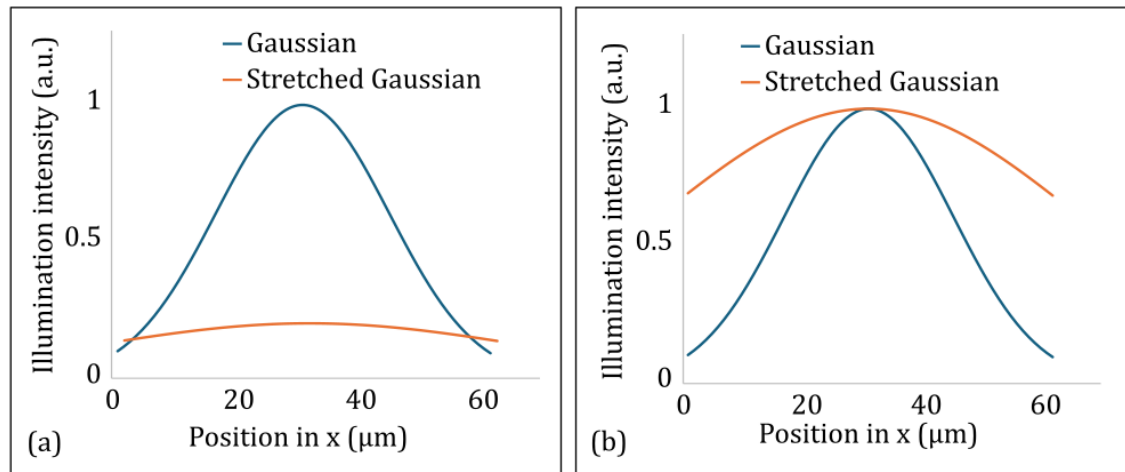
Figure 30 Standard and spread gaussian illumination. (a) Absolute and (b) normalised excitation intensity across the field of view for standard (blue) and stretched (orange) Gaussian illumination. Those plots illustrate the method of enlarging a gaussian laser beam to flatten the illumination inside the microscope field of view. They were generated using the equation for the gaussian distribution $f(x) = a \cdot exp\left(-\frac{(x-b)^2}{2c^2}\right)$ and varying parameters a, b and c.

We propose an approach that uses a single optical micro electromechanical systems (MEMS) mirror to create a homogeneous illumination for SMLM.

MEMS are used in the biomedical research for a wide range of applications including optical scanners to deliver light in a controlled manner (Qiu and Piyawattanametha 2019), optical biosensors (Ren et al. 2020) and signal acquisition in photoacoustic microscopy (S. L. Chen et al. 2013). One application of MEMS to microscopy is the use of MEMS digital micromirror devices to modulate the PSF (S. Li et al. 2018) with very high responsiveness. The PSF pattern can be updated at rates of 32 kHz.

We decided to use a simpler and smaller device to easily implement it in the microscopy setup. Using a single MEMS mirror that allows 2D scanning requires less space and demands simpler electrical controls. They are easier to integrate, are highly reliable and do not scatter light in all directions. MEMS have already been used for 1D or 2D illumination

scanning in light-sheet microscopy (Bakas et al. 2021; Landry, Hamann, and Solgaard 2020).

In this chapter, we compared the new MEMS approach to conventional Gaussian illumination and the piShaper, a refractive device that has been demonstrated to produce flat illumination in wide-field microscopy (Stehr, Schwille, and Jungmann 2019; Mahecic et al. 2020).

We also developed a method to compare illumination schemes based on a number of photoswitching metrics that can be related to the final quality of super resolution images. Finally, we demonstrate another MEMS setting that allows for studying single-molecule photoswitching, which will be utilised in the next chapter as well.

4.4 Materials and methods

4.4.1. Microscopy Setup

A microscope body (Olympus IX3) serves as the centre of the setup, holding a 60X oil immersion objective of NA 1.49 (Olympus APON60XOTIRF). On the illumination side, a diode laser (Andor Toptica iBeam Smart 641 nm) was set on 200 mW output for all experiments. A cleanup filter (Chroma ZET635/20x) was placed at the output of the laser. Two parallel light paths are available on the setup, one includes the MEMS mirror and the other includes the refractive flat illumination device piShaper 6_6_Vis. Switching between the two paths is allowed by two mirrors on magnetic bases (see section 2.4.3.). In the MEMS path, the laser was focused on the MEMS by a 500 mm lens (Thorlabs AC508-500-A-ML). In the piShaper path, the laser is expanded and collimated by a telescope (Thorlabs LD1464-A-ML and AC-254-100-A-ML) and a Galilean beam expander (Thorlabs BE02-05-

A) to meet the input requirements of the piShaper. Then in either case the modified laser beam is focused on the back focal plane of the objective by a telescope (Thorlabs AC254-050-A-ML and AC508-180-A-ML)

On the imaging side, the fluorescence emission was filtered by a dichroic mirror (Chroma zt532/640rpc) and a fluorescence filter (Chroma ZET532/640). A post magnification device (Cairn Optosplit II) provided an extra 1.8x magnification and the image was focused on an emCCD camera (Andor Ixon Life 888).
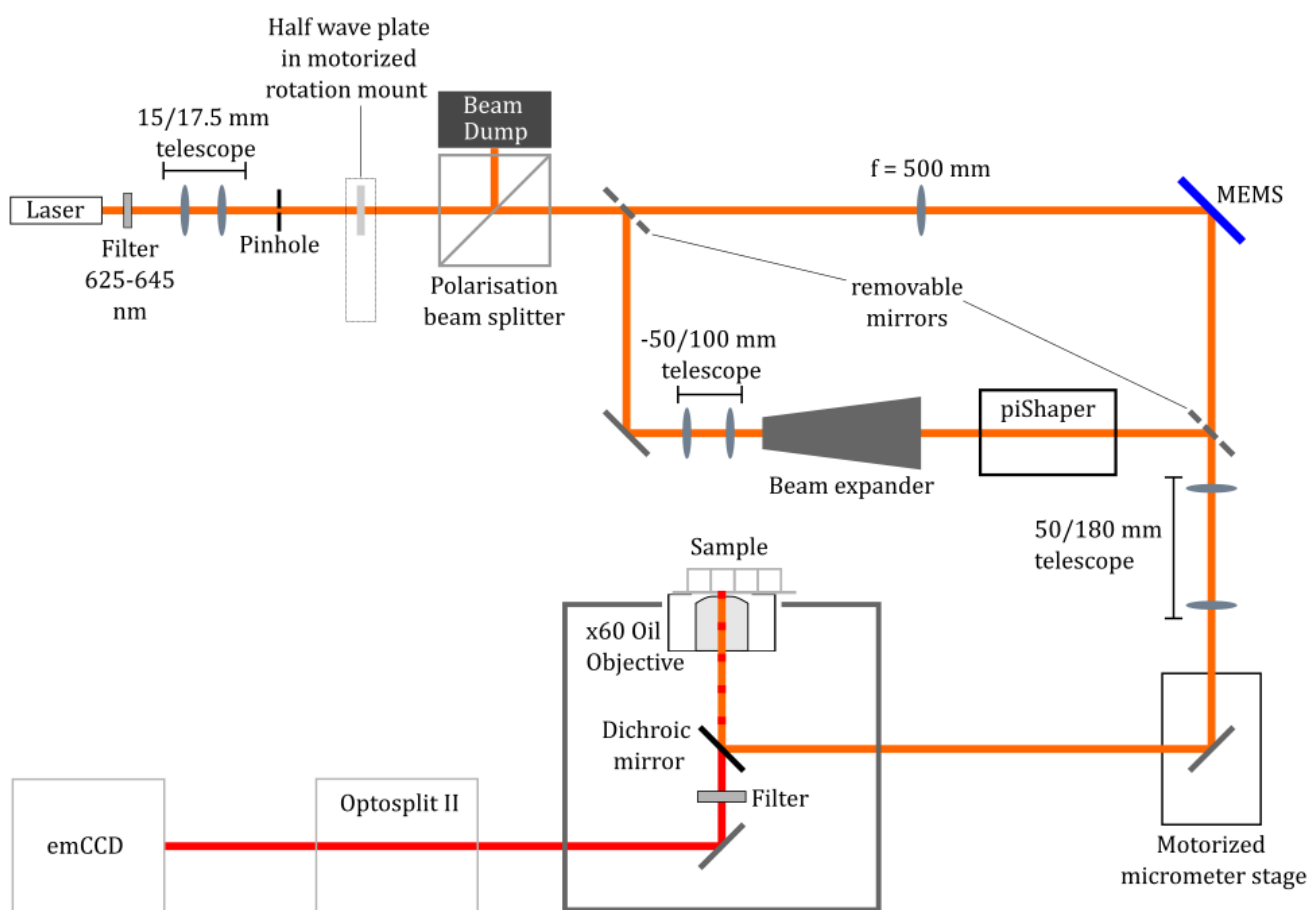

Figure 31 SMLM setup allowing to switch between several illumination schemes. Adapted and reprinted with permission (CC BY 4.0) from "Tunable Wife-Field Illumination and Single-Molecule Photoswitching with a Single MEMS Mirror", ACS Photonics 2021, 8, 2728-2736 (Herdly et al. 2021). Copyright 2021, The Authors. Published By the American Chemical Society"

4.4.2. Sample preparation

In this chapter, we used single molecule surfaces (SMS) of dsDNA Alexa647 probes M4-8-N for all illumination schemes.

The preparation of SMS is described in more detail in chapter 2. Shortly, a Nunc Lab Tek II 8-well Chamber slide sample surface is treated sequentially with a mixture of BSA and biotinylated-BSA, streptavidin and biotinylated M4-8-N probe, washing with PBS between each treatment.

4.4.3. Switching buffer

For imaging, the Lab Tek chambers were filled with photoswitching buffer and sealed with a microscopy coverglass without any headspace. The chemical composition of the photoswitching buffer was the same for all illumination schemes.

The photoswitching buffer has been described before (Schäfer et al. 2013) and is composed of 50 mM mercaptoethylamine (MEA), 5% (w/v) glucose, 10 U L^{-1} glucose oxidase and 200 U mL^{-1} catalase in PBS adjusted to pH 7.4.

4.4.4. MEMS

This section 4.4.4 is rewritten from the information provided by PJ and RB in the published article that reports this work (Herdly et al. 2021b).

We used a 2D optical scanner MEMS mirror that uses resonant piezoelectric actuators to tilt the mirror in 2 dimensions with high repetition rates. The high frequency actuation required low voltage by taking advantage of the resonance frequencies of the device. The scanning mirror has a 400 μm mirror and is cut from a single block of silicon crystal. This ensures a good reliability and tolerance to deformation (Janin et al. 2019). Figure 32(a)

shows the structure of the MEMS mirror that we used. Several MEMS devices are etched on the silicon crystal and mounted on an electronical board but we only used the 400 μm MEMS mirror in this project (Figure 32 (c)).
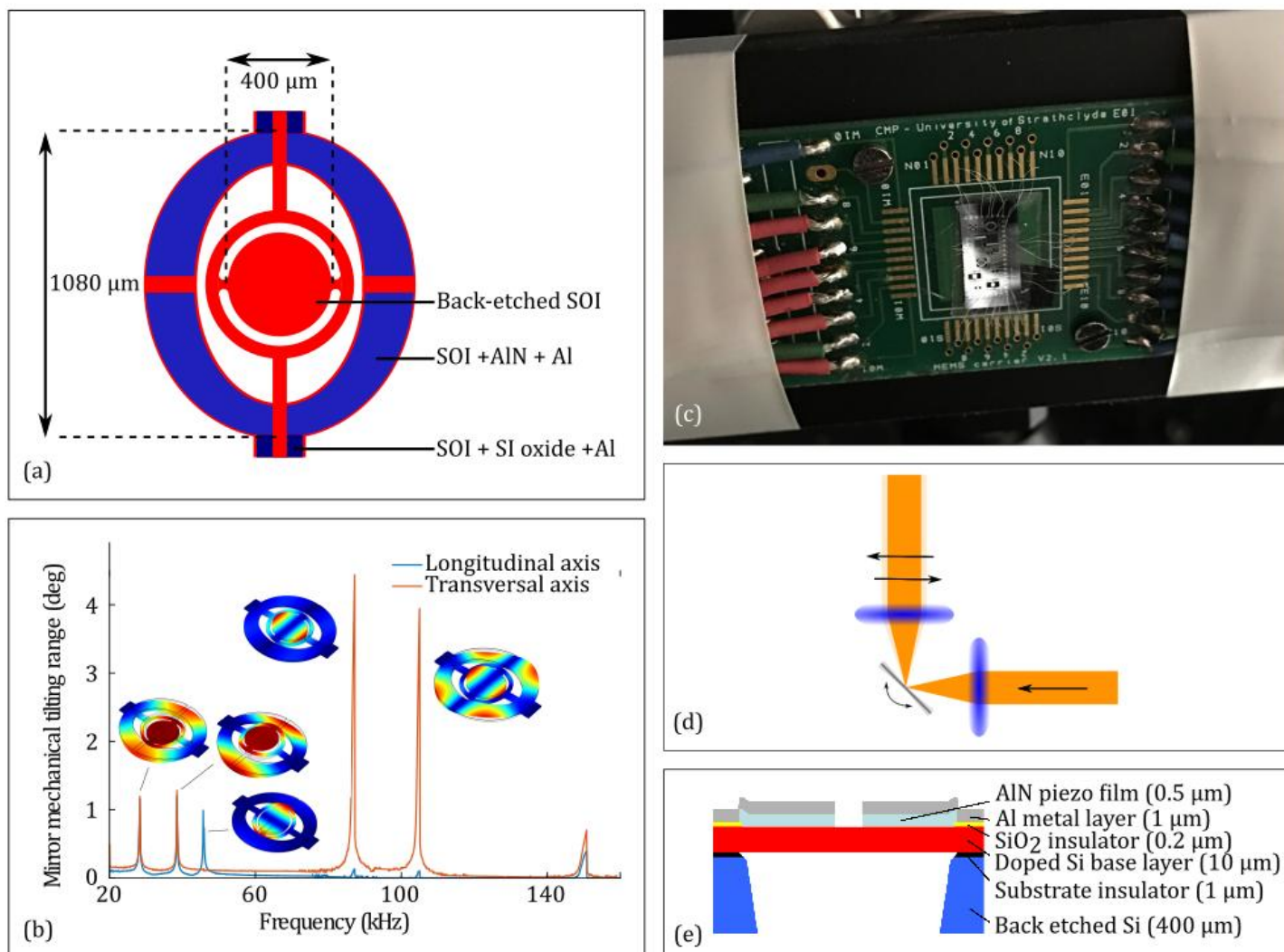
Figure 32 MEMS structure and characterisation. (a) The MEMS structure. (b) Six resonance frequencies of the MEMS were shown during characterisation. (c) The MEMS is attached to an electronic board to allow the electrical control of the MEMS. (d) The oscillating mirror drives the laser position. (e) MEMS layers structure. Adapted and reprinted with permission (CC BY 4.0) from "Tunable Wife-Field Illumination and Single-Molecule Photoswitching with a Single MEMS Mirror", ACS Photonics 2021, 8, 2728-2736

The device is designed to take advantage of the mechanical coupling to produce tip tilt rotations in *x* and *y* directions at the actuation resonance frequencies that we used, around

45.5 and 85.5 kHz (Figure 32(b)). The device was made according to the cost-effective method MEMSCAP PiezoMUMPS multiuser process as described by others (Cowen et al. 2014). The fabrication used a 10 μm silicon-on-insulator device layer for the device geometry and a 500 nm aluminium nitride piezoelectric layer. The manufacturing process left a curvature of radius 20 cm on the mirror. This is compensated by the lenses in the setup. The thin piezoelectric layer only produces small displacements when a constant voltage is applied but by applying sinusoidal currents to act on the resonance frequencies of the material, larger displacements are obtained that result in angles of up to 1°.

The device has several eigenmodes between 10 and 100 kHz (Figure 32(b)). We used the frequencies around 85.5 and 45.5 kHz to trigger the tilting in x and y directions. The tilting was driven by applying an alternating current (AC) voltage signal to one of the four actuators. The actuators were driven with only positive voltage current. The sinusoid signal was shifted toward higher positive values to avoid the depolarization of the piezoelectric layer. The prototype mirror absorbs more than 50 % of the light at 641 nm. This had two main effects on this work. The illumination intensity in the FOV was lower with the MEMS compared to the piShaper and the absorbance led to a heating of the MEMS that changed the mechanical properties of the material and shifted the resonance frequencies. This was investigated in section 4.5.2.

One advantage of the presented MEMS device is that we drove the tilting in two directions x and y by applying a single voltage signal to a single actuator. The was possible by generating a voltage signal that is the sum of two sine waves, with the frequency of each sine wave corresponding to the resonance frequency of one tilting axis. The 2D superposition of the two sine waves is called a Lissajous scan (Tanguy et al. 2020) with an effective repetition frequency equal to the greatest common denominator of the two chosen sine wave frequencies. The sum of sine waves functions is generated by a small

program that runs on LabView, sumSineRatioControl.vi (Figure 33). A GUI allows the choice of both frequencies, the ratio of amplitude between frequencies and the total amplitude. The greatest common denominator that represents the repetition rate of the Lissajous pattern is also calculated and displayed in the GUI. The program can then send the waveform to the signal generator (Agilent AG33250A).
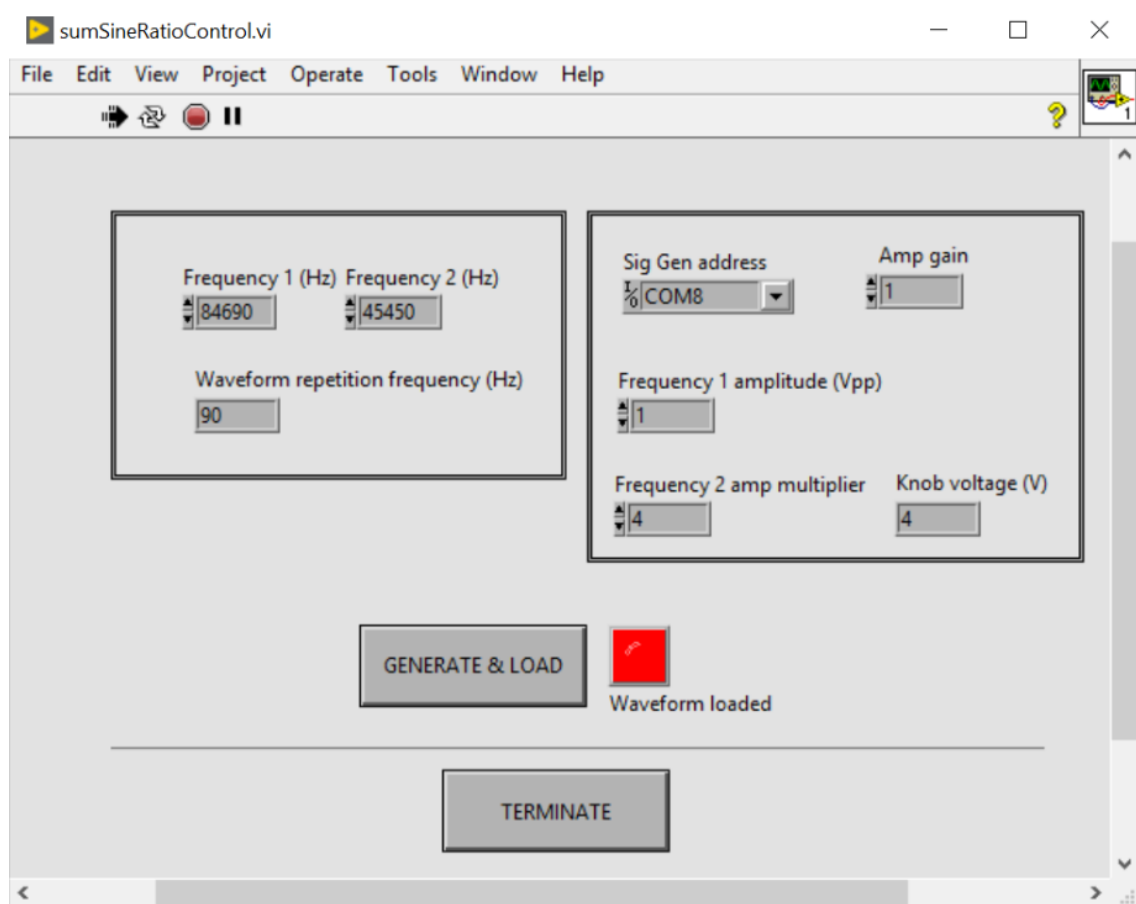

Figure 33 sumSineRatioControl.vi GUI. The graphical user interface of the sumSineRatioControl.vi software allows the user to choose the resonance frequencies, the relative amplitudes, to control the repetition frequency of the resulting pattern, generate and upload the sum of sinusoidal signals to the electrical waveform generator that drives the MEMS.

4.4.5. Data analysis

rapidSTORM localisation

Raw camera frame stacks were analysed with rapidSTORM as described before (chapter 2) to localise fluorophores and calculate their intensity as the number of detected photons, N_{Det}. A filter was applied before exporting the localisations to a text file. Localisations were rejected if the PSF full width at half maximum (FWHM) was outside of the range 250-450 nm. That is to reject fluorophores that may detach from the single molecule surface and float in the buffer. Also, localisations were rejected if their intensity was below 8 or 10 times the local background intensity (8 for the MEMS 4.2V and 10 for all other conditions). This intensity threshold was chosen to reject false localisations found by rapidSTORM in fluctuations of the background noise. This led to a loss of real localisations in the corners of the gaussian illumination especially and that is reflected in Figure 42. This shows the importance of flat illumination to reject false localisations while conserving data in the corners of the FOV.

Results visualisation

To compare different illumination schemes, we used two methods to divide the field of view in regions of interest. Each method is associated to a different data visualisation tool.

Heatmaps (Figure 34(b)) represent the median value of a metric in each square ROI of the FOV following a checkboard pattern. 15x15 ROIs were used for N_{Det}, the experimental precision and localization counts. 10x10 ROIs were used for the photoswitching metrics. The values of the photoswitching metrics for each ROI were also used in Figure 46 to study the photoswitching across the whole FOV.

Ring regions of interest (Figure 34(a)) were used to show the difference between

concentric regions at different distances from the centre of the field of view. The inner and outer radii of each ROI is calculated so that the surface of each ROI is the same if the ROI is entirely included in the FOV.
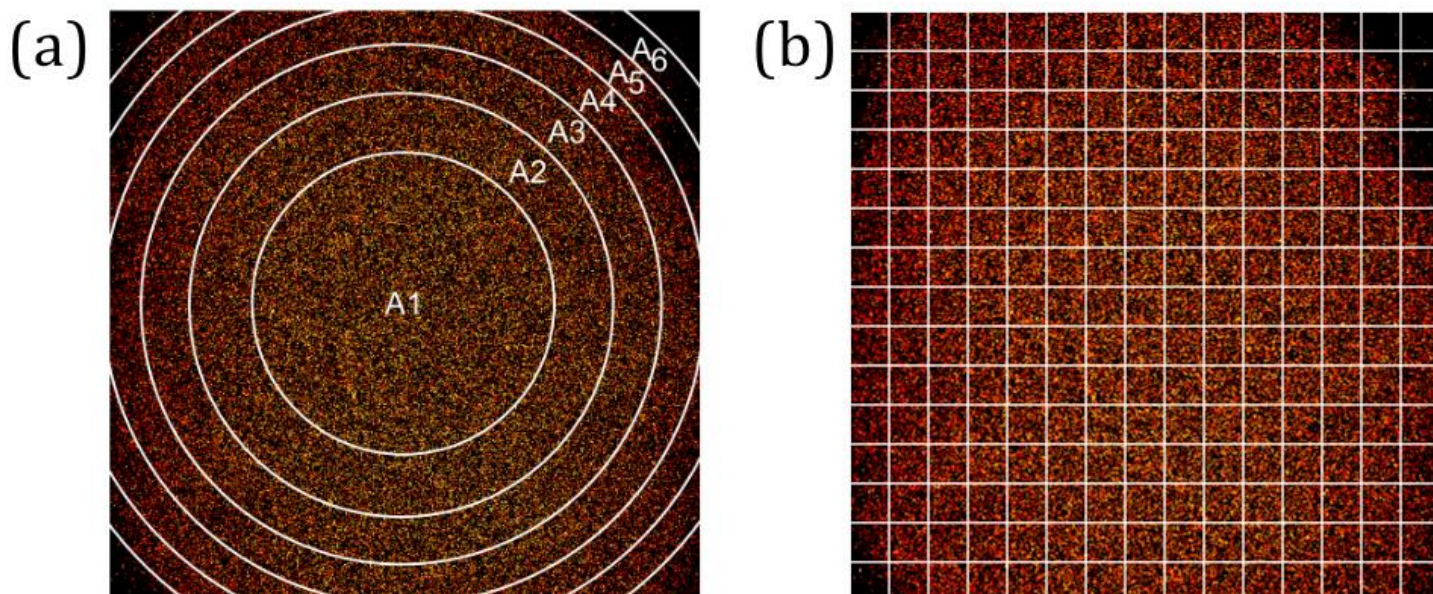
Figure 34 (a) Concentric and (b) square Regions of Interest (ROI) are used to visualise the results of analysis. Adapted and reprinted with permission (CC BY 4.0) from "Tunable Wife-Field Illumination and Single-Molecule Photoswitching with a Single MEMS Mirror", ACS Photonics 2021, 8, 2728-2736

A few ring numbers were tested and we chose this configuration as a trade-off between accurate metrics values and visible differences between illumination schemes. We used 6 ring ROIs because rings 7 and 8 that would fill the corners had too few localisations to calculate switching kinetics accurately. The value of metrics for each ring ROI was plotted as a datapoint with the outer radius as the *x* coordinate.

Clustering

Individual emitters activate several times during the recording of one data frame stack. And each activation covers several frames. To better study the effect of the local laser intensity on individual fluorophores, we applied clustering methods to associate the

localisations of a single activation event spread over several frames and associate the different activation events of each emitter across the whole frame stack.

We used two different clustering algorithms:

SvdL wrote a clustering algorithm in ImageJ Macro Language to group localisations of each emitter and calculate the switching kinetics. In this algorithm, a super resolution image is reconstructed from the list of localisations from rapidSTORM with a pixel/bin size of 10 nm. A 2D Gaussian filter with 1px standard deviation then smooths the image and the image is thresholded via applying a minimum of 0.1 localisation per pixel employing the Huang method, which produces a binary image. Masks are drawn according to the binary image and the shape and size of each cluster are analysed. Only masks of sizes 3-120px and circularity 0.9-1.0 were accepted for proceeding with the analysis. Localisations in each mask are then considered to originate from the same emitter switching ON and OFF. The switching analysis was done on each cluster of localisations (see below).

LH developed a different clustering algorithm in parallel using Python in a Jupyter notebook (Kluyver et al. 2016). The localization list from rapidSTORM was loaded in a pandas dataframe. The algorithm scanned the dataframe to group localisations with close coordinates. A cluster consisted of localisations closer than 70 nm from the cluster centre of mass. To avoid errors from nearby clusters, if localisations outside of the cluster were detected closer than 15 nm from the border of the cluster, the cluster was rejected. This filter also allowed rejection of very large clusters composed of thousands of localisations from fluorophores that do not switch OFF and are known as highlanders. This method of clustering was used to calculate N_{Det} and experimental precision metrics (see below). This clustering algorithm was an exercise to train myself as I was learning programming in Python. It was very slow and would probably benefit from some optimisation that would probably accelerate it by a few orders of magnitude. The analysis took 90 hours of

processing on a decent desktop computer for the 5 conditions reported in this chapter.

Metrics

The local laser illumination intensity influences the fluorescence emission rates and the photoswitching of Alexa 647 and thus the quality of the reconstructed super-resolution images. We measure and calculate a number of metrics, each describing some part of this influence or reporting the result quality. The metrics are the following.

Photon number, N_{Det}

N_{Det} is the number of photons detected in each frame for one localisation. It is proportional to the fluorescence emission rate of the emitter corresponding to that localisation. N_{Det} is calculated by the localisation software rapidSTORM (Wolter, Löschberger, Holm, Aufmkolk, Dabauvalle, Van De Linde, et al. 2012). It has been reported that localisation software such as rapidSTORM underestimates the number of photons (Franke, Sauer, and De Linde 2017)but as we use a single molecule layer at the glass surface of the sample chamber, the bias is the same for all illumination schemes.

Switching kinetics

τ_{ON} and τ_{OFF} are the average time the fluorophore stays in the fluorescent ON state and dark OFF state respectively. They are equal to the inverse of the switching rates: $\tau_{ON} = 1/k_{OFF}$ and $\tau_{OFF} = 1/k_{ON}$. The ratio $\tau_{OFF}/\tau_{ON} = k_{ON}/k_{OFF}$ is used to evaluate the density of active fluorophores at any time. High label densities require higher values for the ratio to reduce the occurrence of PSF overlap from two or more emitters that would lead to localisation errors.

The switching kinetics metrics are calculated by an ImageJ macro written by SvdL. Single molecule time traces of individual clusters are analysed (Figure 35).
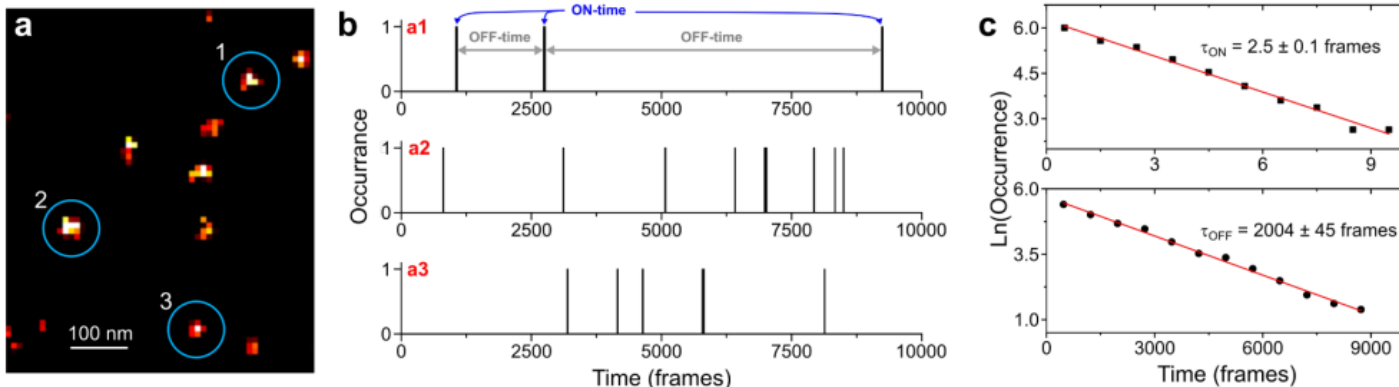
Figure 35 Tracking single molecule switching. (a) Geometrical inspection allows extracting localisations corresponding to each individual emitter. (b) Applying a threshold to intensity allows to group consecutive frames where an emitter is active to measure ON- and OFF-times for individual emitters. (c) Histogram of the distribution of ON- and OFF-times are fitted to extract τ_{ON} and τ_{OFF}. Adapted and reprinted with permission (CC BY 4.0) from "Tunable Wife-Field Illumination and Single-Molecule Photoswitching with a Single MEMS Mirror", ACS Photonics 2021, 8, 2728-2736

In the first instance, ON- and OFF-times are measured for each single-molecule trace. The ON-time is the number of consecutive frames where the fluorophore is localised, and the OFF-time is the number of frames between the last localization of one ON event and the first localization of the next ON event. All the ON-times and OFF-times of each ROI are plotted in a histogram with the ON- or OFF- time as *x*-axis, respectively, and the logarithm of the occurrence as *y*-axis. The histograms (Figure 35(c)) are then fitted with a single exponential decay function $\ln occurrence = \ln a - k \times time$, where a is the amplitude and k is the OFF and ON switching rate constant, respectively and $time$ is the ON-time or OFF-time, respectively. We can then calculate the average lifetimes in each ROI as $\tau_{ON} = 1/k_{OFF}$ and $\tau_{OFF} = 1/k_{ON}$.

Early controls of the switching analysis showed that some localisations could be missed in the middle of an ON event leading to a single ON event being counted as two shorter ones and the missed localisation being counted as an OFF time.
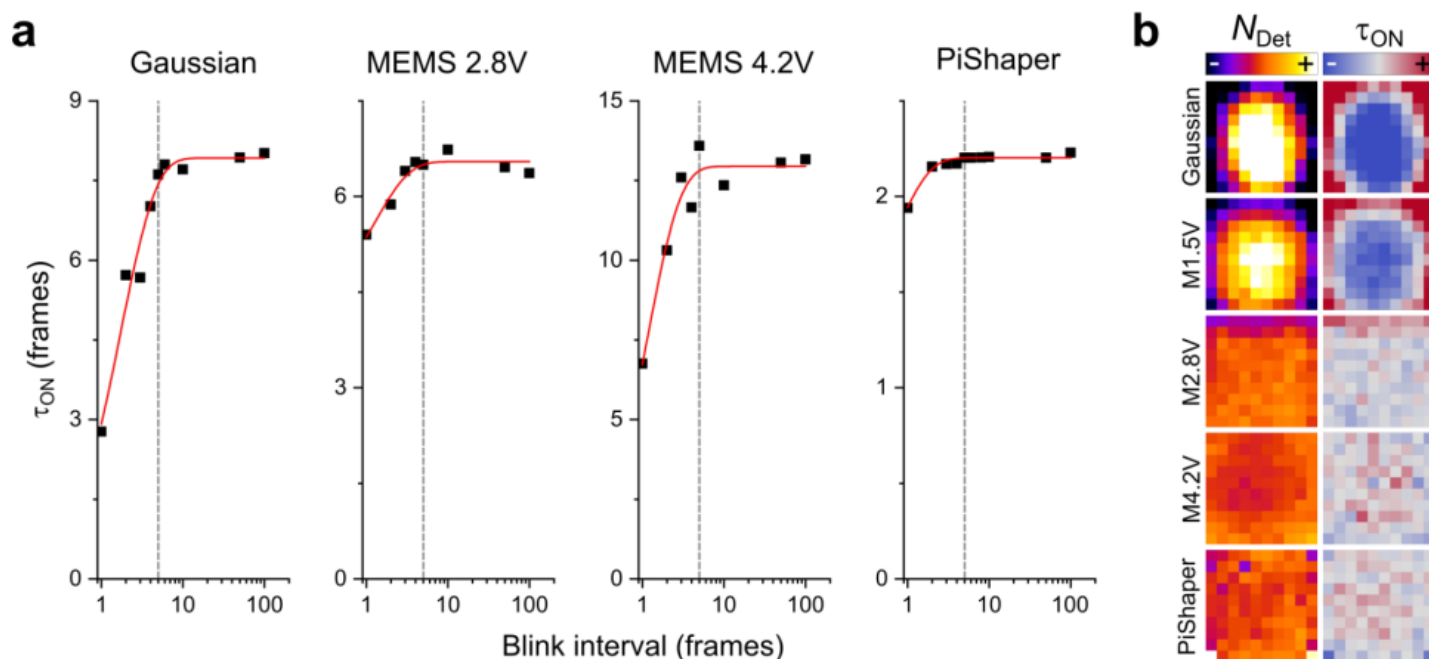
Figure 36 (a) A blink interval value of 1 means that only localisations in consecutive frames are grouped in the same ON event. Longer intervals account for missed localisations in the middle of a single ON event. Not considering missed localisations would lead to underestimated ON and OFF times. A blink interval of five frames is allowed in the analysis presented in this chapter. (b) Heatmaps of spot brightness and τ_{ON} for five illumination modes allowing blink intervals of five frames. Adapted and reprinted with permission (CC BY 4.0) from "Tunable Wife-Field Illumination and Single-Molecule Photoswitching with a Single MEMS Mirror", ACS Photonics 2021, 8, 2728-2736

This introduced some bias in the data and a blinking interval was added to the macro to account for missed localisations in the middle of an ON event. The blink interval was set as 4 missing frames allowing for non-consecutive frames to be considered part of the same ON event. The value of 4 was chosen after measuring the ON time for all illumination schemes with blink intervals of 1-100 (Figure 36). No increase of the ON time was observed for blink intervals longer than 4.

Experimental precision

In SMLM, the experimental precision is an indicator of image quality as it defines the maximum achievable resolution.

For each cluster (see above), a 2D distribution (5 nm bins) of the coordinates of all

localisations in the cluster is fitted with a 2D Gaussian function. The average of the standard deviations of the Gaussian function in x and y is used as the experimental precision for this cluster.

FRC resolution

The FRC resolution map is calculated using the ImageJ plugin NanoJ SQUIRREL (Culley, Tosheva, et al. 2018). First, we used the LocFileVisualizer macro to produce two super resolution reconstructed images using the localisations in odd and even frames. The two images are input in the SQUIRREL plugin for the FRC analysis. A Fourier transform is applied on both images and Fourier transform images are compared. Increasing radii rings are drawn on each Fourier image and a correlation value is calculated for each radius. The correlation is plotted as a function of the ring radius. The correlation function drops with increasing radius. The FRC resolution is calculated as the distance corresponding to a drop of the correlation function below 1/7 of its maximum value.

4.5 Results and discussion

4.5.1. Flat-illumination with piShaper

Irradiation intensity received by fluorophores in SMLM influences their ON- and OFF-switching rates as well as the number of photons detected for each localisation (Herdly et al. 2021b). These parameters influence the localisation precision and the resolution of the reconstructed super-resolution image. Following, a homogeneous irradiation of the sample across the field of view allows uniform resolution across the field of view. Quantitative SMLM also benefits from homogeneous illumination.

An early experiment was conducted to evaluate the rough improvement that flat

illumination could provide. A sample was prepared where a 1 μM concentrated dye solution of ATTO 655 was prepared. Then fluorescence images were recorded upon illumination by both a conventional Gaussian laser beam and the modified illumination with the piShaper. As the fluorescence intensity shows a linear response on the local illumination intensity at laser powers below $1\ kW \cdot cm^{-2}$, we can use the fluorescence emission intensity as a reporter for the local illumination intensity (Eggeling et al. 1998; Dittrich and Schwille 2001).

Figure 37 (a) and (b) shows the recorded images with a colour code for the intensity. We then analysed the distribution of the intensity value of pixels in three regions of interest (ROI) corresponding to three concentric circles (in black) centred on the centre of the Gaussian/piShaper illumination.

| (c)	standard deviation / mean (%)
Gaussian small circle	1.4
Gaussian medium circle	15.4
Gaussian large circle	33.4
piShaper small circle	3.6
piShaper medium circle	3.7
piShaper large circle	4.1
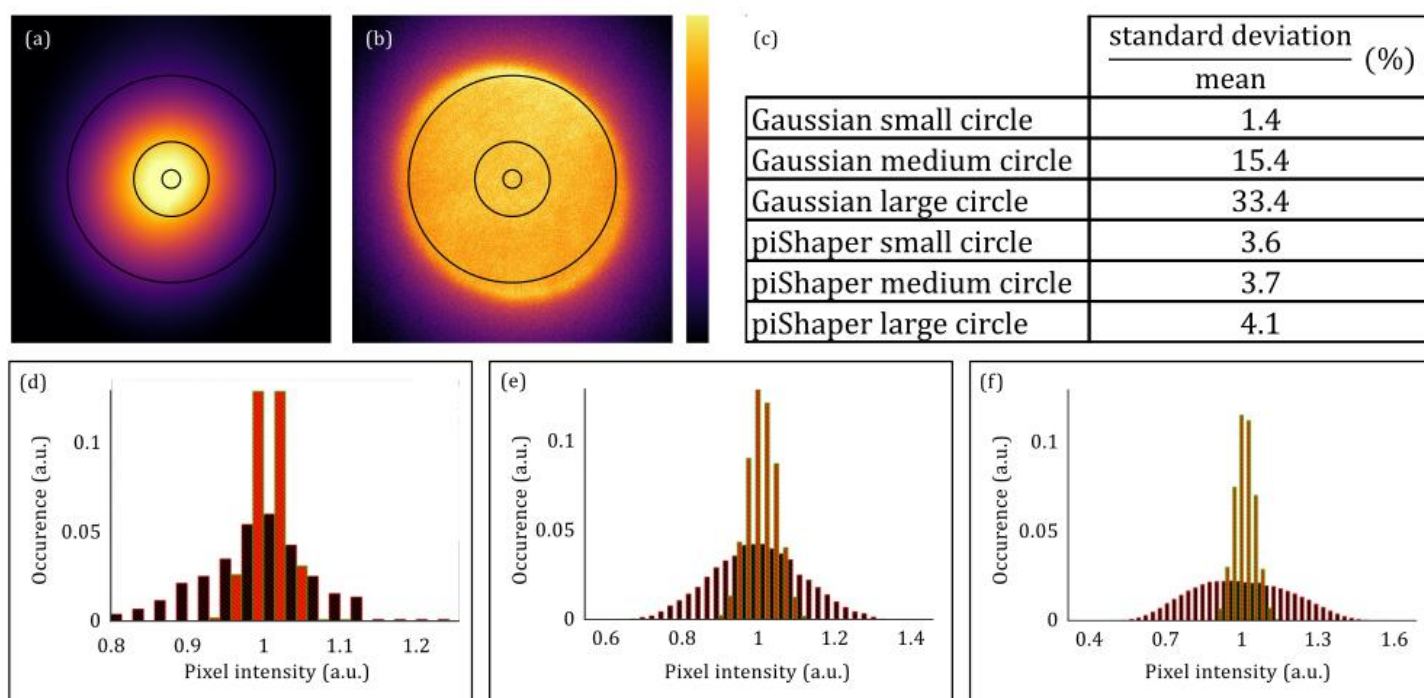
Figure 37 Images of a 1 μM ATTO 655 solution with (a) a standard Gaussian or (b) a piShaper modified illumination scheme. (c) mean and standard deviation of pixel values in concentric rings of three sizes are calculated with ImageJ and the mean value normalized standard

Intensity values are normalized by the average value in the ROI for better comparison.

We observe for the piShaper a homogeneous intensity level across all the three ROIs while for the Gaussian illumination, the average intensity decreases, and the distribution gets wider in larger circles. We also see that even for the smallest circle the distribution is wider for the Gaussian illumination than for the piShaper illumination. This shows that a widened Gaussian illumination is not as good as a dedicated flat illumination device. The piShaper has been used for SMLM before (Stehr, Schwille, and Jungmann 2019) and will serve as a reference to compare our new single-MEMS based solution for flat-illumination.

4.5.2. Characterisation of the MEMS mirror

Lissajous and MEMS simulations

Before integrating the MEMS mirror in our microscopy setup, we wanted to better understand the expected behaviour according to the theory. When an electrical signal is applied to the piezoelectric layer following a sinusoid voltage with a frequency corresponding to the tilting resonance frequencies of the MEMS, a tilting oscillation is observed. The resonance frequencies of the MEMS were measured during the characterisation of the MEMS mirror by PJ (Janin et al. 2019). The resonance frequencies for the tilting motion were measured at 45.5 and 85.5 kHz. These values are used in the simulations below. We can also apply an electric signal that is the sum of two sinusoidal curves corresponding to the two frequencies for oscillation in x and y. The corresponding pattern of motion is called a Lissajous scan (Tanguy et al. 2020) and follows the equations:

$$\begin{cases} x(t) = A_x \cdot sin(2\pi \cdot f_x \cdot t + \psi) \\ y(t) = A_y \cdot sin(2\pi \cdot f_y \cdot t) \end{cases} \tag{23}$$

Where A_x and A_y are the amplitudes of the sinusoidal curves in the x and y directions.

f_x and f_y are the frequencies of the sinusoidal curves.

ψ is the phase shift between the sinusoidal curves.

The Lissajous scan follows the path depicted in Figure 38(a, left). The path repeats at a frequency corresponding to the greatest common denominator of the two resonance frequencies. Minute changes to the frequencies can be applied to increase the repetition rate by matching frequencies to increase the greatest common denominator while losing some amplitude of oscillation.

To simulate the illumination patterns that we expect to see across the field of view (FOV) of the microscope, we used the equations above with the measured resonance frequencies of the MEMS and traced the path of the laser centre for a full Lissajous cycle (Figure 38(a)). We then transformed the path into a 2D histogram of the relative time spent in each corresponding pixel on an image of the sample. Finally, the 2D histogram image was convolved with a Gaussian beam pattern to represent the illumination of the sample during one Lissajous cycle.

By varying the amplitudes, we could simulate the effect of varying voltage of the electrical sinusoid-sum signal applied to the MEMS.

The resulting illumination for several amplitudes is depicted in Figure 38(b-c). We matched the simulations with experimental images using the MEMS at various voltages (Figure 38 (d)). We observe that with increasing voltages, the Gaussian pattern is first spread and then a square pattern of flat illumination appears and finally for an increased amplitude, a lower intensity region appears in the centre of the pattern.
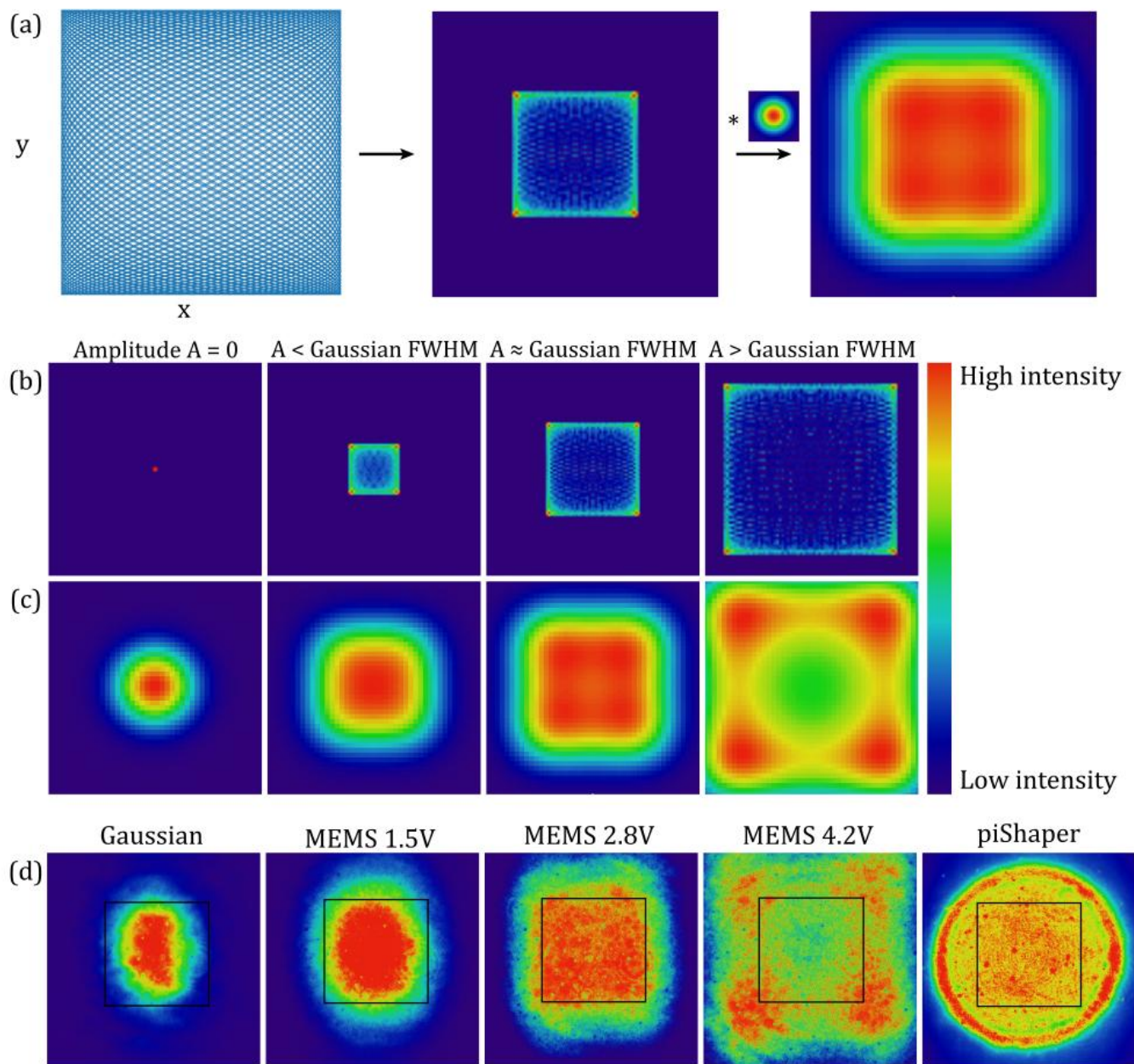
Figure 38 Lissajous and MEMS simulation: (a) The Lissajous pattern (left) is used to produce a 2D histogram (centre) of the position of the centre of the laser beam over one cycle. The convolution of the histogram and a 2D gaussian pattern results in the simulated illumination across the FOV (right). (b) Varying the amplitude of the Lissajous scan produces different behaviours of the illumination (c) across the FOV. (d) Experimental data follows the simulations, the black square represents the usual FOV used for SMLM. The illumination width was chosen to cover the FOV with the pishaper and to compare patterns of smaller, similar and larger size than the FOV for the MEMS 1.5, 2.8 and 4.2V settings, respectively. Adapted and reprinted with permission (CC BY 4.0) from "Tunable Wife-Field Illumination and Single-Molecule Photoswitching with a Single MEMS Mirror", ACS Photonics 2021, 8, 2728-2736

This can be explained by the histogram of time spent in each region of the FOV following the Lissajous scan. The laser beam spends more time at the edges of the Lissajous pattern compared to the centre. It follows that for amplitudes of scans smaller than the FWHM of the laser beam the illumination is a flattened gaussian. For amplitudes close to the FWHM of the laser beam, the illumination is a homogeneous square. For amplitudes larger than the FWHM of the laser beam, the illumination is higher in the corners of the square and lower on the sides and centre.

We observed the same behaviour in the experimental images. The tuneability of the MEMS makes it a useful tool for easy changes between different illumination schemes. In chapter 5, we use a widened Gaussian illumination to create a gradient of intensity in the field of view by simply changing the voltage applied to the MEMS. Other setups might require long and precise laser alignment and lens adjusting to change between homogeneous and other illumination schemes while we can just change the voltage setting.

Laser power and resonance frequencies

When we first received the MEMS mirror from PJ and RB, we integrated it to the microscopy setup and controlled that it behaved according to the initial characterisation (Janin et al. 2019).

First, we wanted to measure the resonance frequencies that drive the tilting in the x and y directions. We set the waveform generator that produces the oscillating electric signal on a single sinusoid function with a frequency close to the previously measured resonance frequency. We recorded images of a 1 µM ATTO 655 solution. By varying the frequency of the sinusoidal electrical signal, we saw an increase of the width of the illumination in the ATTO 655 sample. We analysed the pixel values in a region of interest covering the oscillating illumination at its maximum amplitude. By plotting the standard deviation of

pixel values normalized by the average pixel value, we observe a minimum that corresponds to the resonance frequency (Figure 39(f,g)). The experiment around 45.5 and 85.5 kHz gave us resonance frequencies of 45.67 and 86.33 kHz (± 0.01 kHz) for a laser power setting of 1 mW, which is consistent with previously measured values of 45.5 and 85.5 kHz.

We did those experiments at 1 mW laser power and then switched the laser setting to 200 mW to observe the flat illumination effect on single molecule surfaces and we could not observe any oscillation. As soon as the laser power was increased, the oscillation amplitude decreased significantly towards 0.

After controlling other factors, we realised that the laser power could influence the mechanical properties of the MEMS.

With a reflectance below 50 %, the MEMS mirror absorbs about half of the incoming laser light which leads to the heating of the MEMS material. This changes the mechanical properties of the material and shifts its resonance frequencies (Figure 39 (f,g)) We can see that effect on Figure 39 (a,b). the oscillation amplitude decreases linearly with the laser power.vWe then investigated the resonance frequency shift more precisely by reproducing the V-shaped curve in Figure 39 (f,g) for a range of laser power settings.

We then extracted the corresponding resonance frequencies (Figure 39 (c,d)) and plotted the resonance frequency shift(Figure 39(e)) that appears to be linear with laser power.

In future experiments, we used the 200 mW laser power setting and we used the corresponding resonance frequencies 45.45 and 84.69 kHz. The greatest common divisor of the two frequencies is 90 Hz, which corresponds to the repetition rate of the Lissajous pattern.
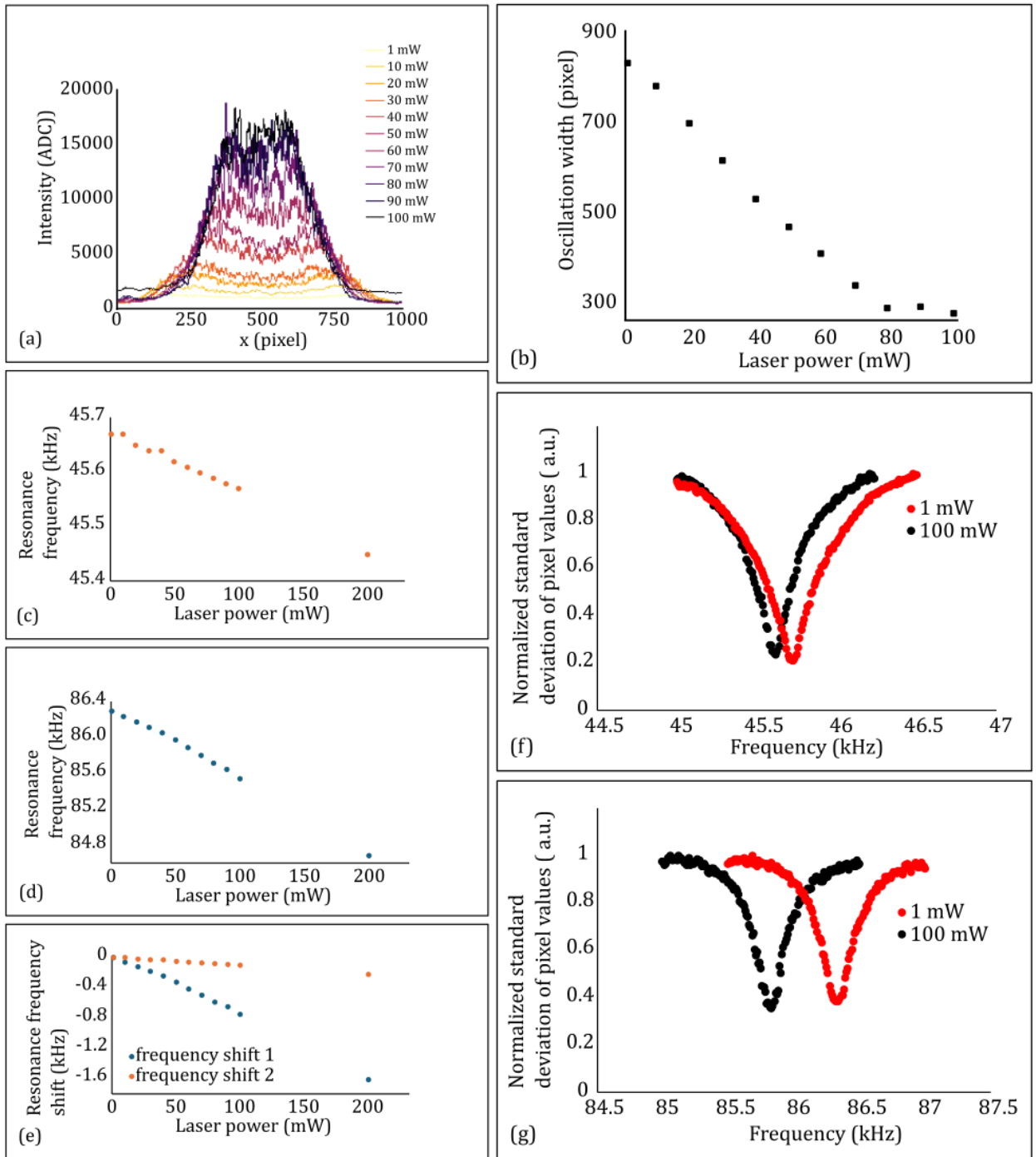
Figure 39 Laser power and resonance frequencies. The MEMS resonance frequencies depend on the illumination laser power. (a,b) Increasing the laser power decreased the width of oscillation of the MEMS mirror. (c-e) Increasing the laser power induced a linear shift of the resonance frequencies of the MEMS that were measured as the minimum of the curves in (f,g). Absorption of laser photons by the MEMS material lead to an increase of the MEMS temperature leading to a change of its mechanical properties, which in turn changed the resonance frequency of the device.

This will guarantee that the laser scans the Lissajous pattern nine times during each recorded frame (camera cycle time = 100 ms) and greatly reduce illumination biases, which would occur if the repetition rate and camera exposure time were on similar scales.

Choosing the best amplitude of oscillation for homogeneous illumination of the field of view

Once the resonance frequency/laser power issue was resolved, we set the optimal voltage amplitude of the sine-sum electrical signal that was going to drive the MEMS. The ratio of amplitude between the *x* and *y* sine waves was set at 4 to obtain a square Lissajous pattern. As we saw earlier in simulations, we want the width of the Lissajous pattern to be comparable to the FWHM of the gaussian laser to obtain a square homogeneous illumination.

We recorded images of a 1 µM ATTO 655 solution while varying the voltage amplitude of the sine-sum electrical wave (Figure 40 (a-d)).

We observe a decrease of the standard deviation of the illumination until 2.8 V and then the standard deviation increases again because of the intensity dip in the middle of the frame (Figure 40 (e)). The voltage setting 2.8 V is chosen as the flat illumination settings in the next experiments. Settings at 1.5 and 4.2 V show suboptimal settings. An advantage of the MEMS flat illumination compared to the piShaper is a better correspondence of the illumination shape to the square FOV of the camera. With the piShaper, we obtain a flat illumination by setting the circular illumination shape to cover the FOV completely and a significant portion of the illumination is lost outside of the FOV (Figure 41(d)) whereas the MEMS illumination square shape better matches the square FOV and we lose less of the illumination outside the FOV.
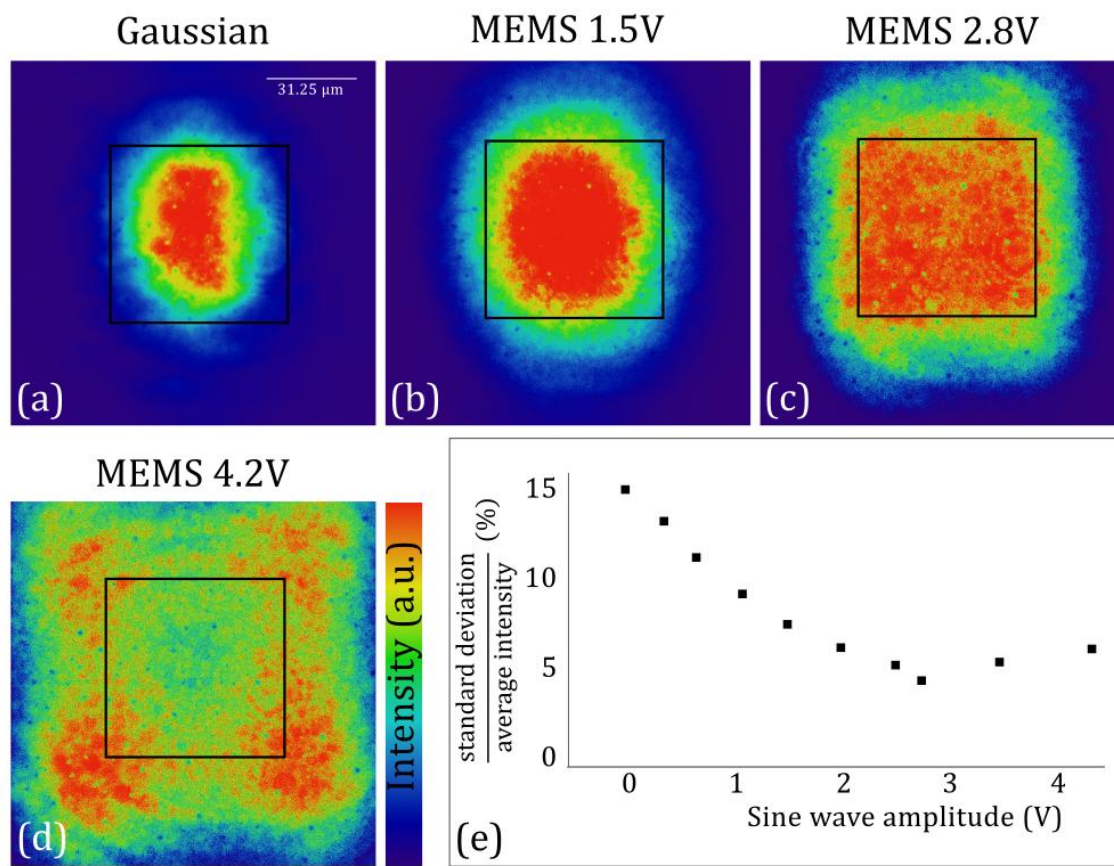
Figure 40 The choice of the sine wave amplitude (2.8 V) was motivated by the lower mean normalized standard deviation of the intensity in the 62.5 µm × 62.5 µm FOV used for SMLM experiments (black square).

4.5.3. Comparing three illumination schemes with Atto 655

We acquired a new set of images with the three illumination schemes Gaussian, piShaper and MEMS 2.8V on a 1 µM ATTO 655 solution (Figure 41) to compare them quantitatively. We use the fluorescence intensity of ATTO 655 as a reporter of the local illumination intensity as they are linearly correlated at low kW.cm-2 intensities (Dittrich and Schwille 2001). We calculated the standard deviation of pixel values in the blue field of view normalized by the average pixel intensity. We obtained 15.2, 3.2 and 5.1 % for the

153

Gaussian, piShaper and MEMS 2.8V illuminations, respectively.

(d)	Gaussian	piShaper	MEMS 2.8 V
Proportion of laser power in the 62.5×625 μm FOV (%)	36.2	25.5	36.9
Standard deviation / mean pixel value in blue FOV (%)	15.2	3.2	5.1
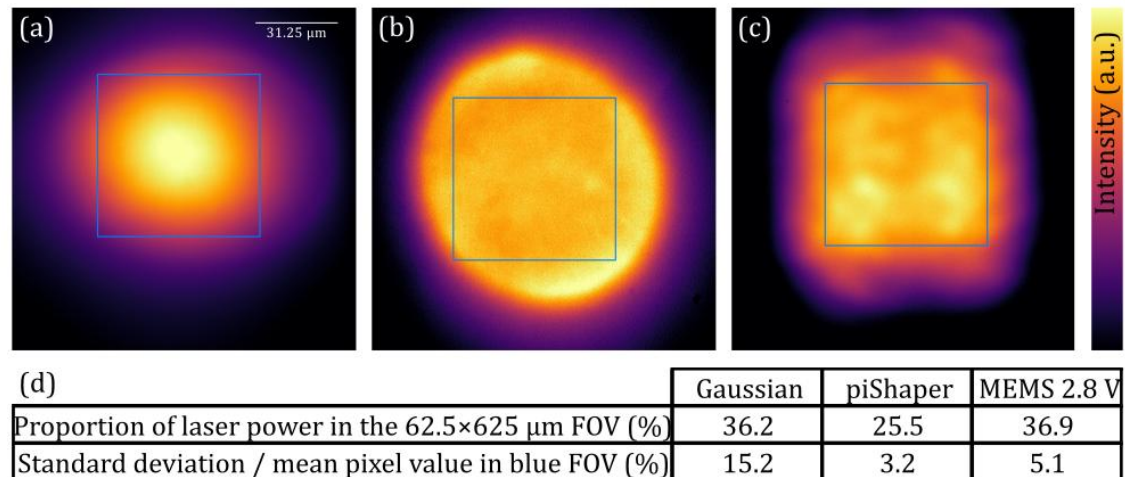
Figure 41 (a) Gaussian illumination, (b) piShaper illumination, (c) MEMS 2.8V illumination fluorescence intensity images of an ATTO 655 1 μM sample. The scale bar is 31.25 μm and applies to all three images. The blue square shows the default 512 px × 512 px = 62.5 μm × 62.5 μm field of view that we use later in this chapter for single molecule surfaces. (d) Summary of the illumination efficiency and homogeneity of the three illumination schemes.

We also calculated the proportion of each illumination scheme that fit in the single molecule experiments field of view. We measured that 36.2, 25.5 and 36.9 % of the fluorescence intensity in the large FOV was emitted in the blue FOV for Gaussian, piShaper and MEMS 2.8V, respectively.

We demonstrate here that our MEMS device provides a uniform illumination comparable to the piShaper and that it is more efficient at using most of the laser emission in the chosen FOV due to its squarish shape compared to the circular illumination of the piShaper.

Having proven the concept of our MEMS illumination and optimized the settings on concentrated dye solutions, we prepared single molecule surfaces to study the photoswitching of Alexa 647 in various illumination schemes.

4.5.4. Photoswitching of Alexa 647 in five illumination schemes

The first reason we decided to integrate flat illumination in our microscopy setup was to try to recover localisations in the corner of our FOV. For a Gaussian illumination, a lot of localisations in the corners are missed or discarded by the localisation software. This leads to dark corners in the reconstructed images and it seriously impacts any attempt to use SMLM for quantitative experiments on large FOV.

We prepared a single molecule surface and imaged it under five illumination schemes (Figure 42). We observe dark corners where emitters are not localised or their brightness is underestimated for the Gaussian and MEMS 1.5V illumination whereas the localisation numbers are homogeneous across the field of view for MEMS 2.8V, MEMS 4.2 V and piShaper illumination schemes.

The photoswitching of fluorophores has a strong influence on the quality of SMLM results and a good control of the photoswitching is paramount to obtain the best resolution improvements. We acquired 30000 frames at 10 Hz under dSTORM conditions to study the photoswitching of Alexa 647 when illuminated by Gaussian, three MEMS settings and the piShaper modes. The rapidSTORM localisation software found 0.7-1.2 million localisations for each illumination scheme. The large localisations samples allowed us to study single-molecule photoswitching accurately across the field of view.

These surfaces (Figure 43(a)) are routinely used as reference samples for SMLM development as they consist of a flat and homogeneous layer of randomly separated fluorophores attached to the glass coverslip.
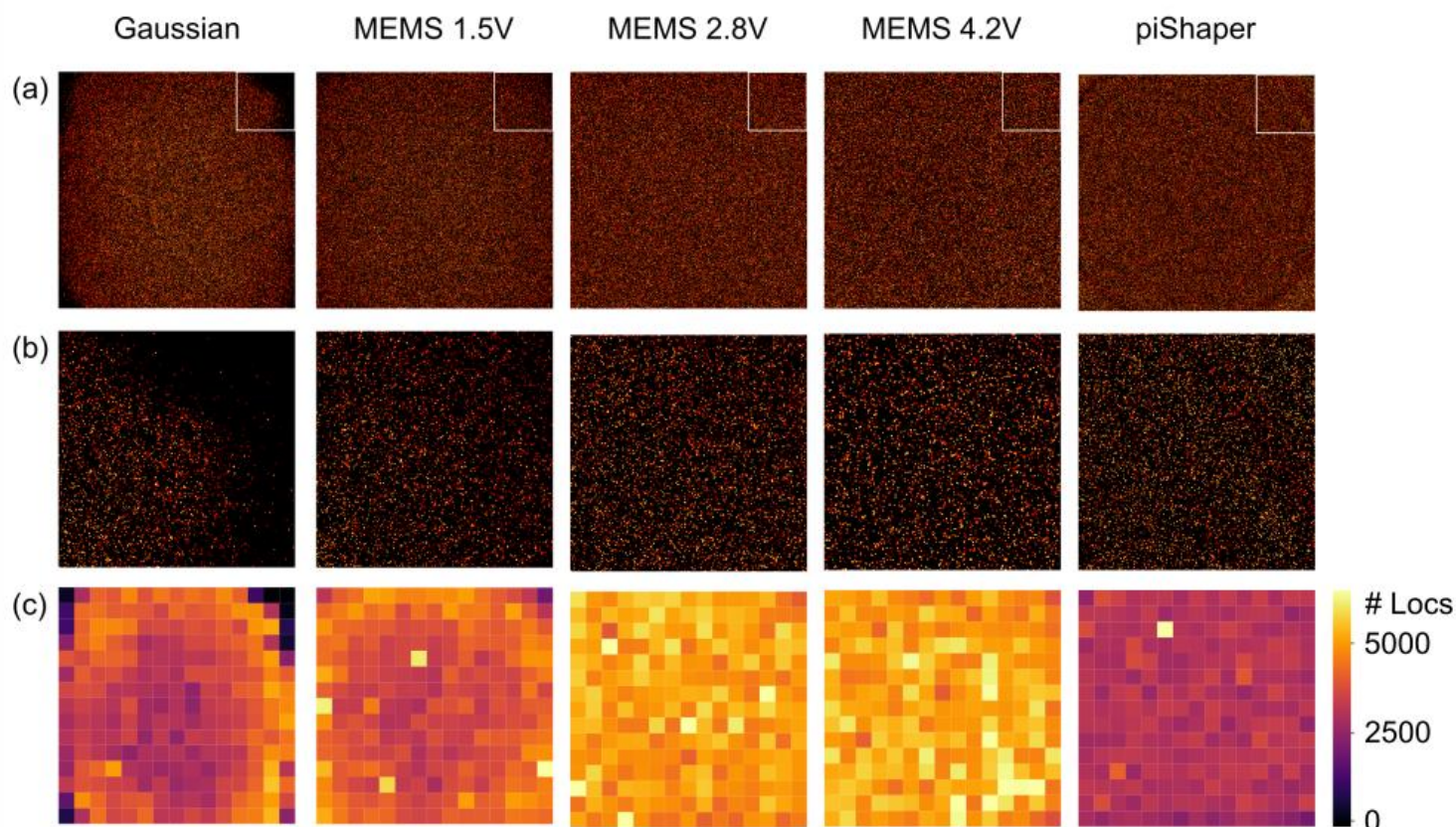
Figure 42 (a) dSTORM images (62.5 μm × 62.5 μm field of view), (b) Zoom of the square in the upper right corner and (c) Localisations counts in each square ROI for five illumination modes. Gaussian and MEMS 1.5 V illumination show a loss of localisations in corners whereas for the three other illumination modes the localisation counts are homogeneous across the field of view. Missed localisations were either discarded because their intensity was below the threshold chosen to avoid false localisations in the background noise or the goodness of fit of the 2D gaussian was too poor because of a low singal to noise ratio. Adapted and reprinted with permission (CC BY 4.0) from "Tunable Wife-Field Illumination and Single-Molecule Photoswitching with a Single MEMS Mirror", ACS Photonics 2021, 8, 2728-2736

The MEMS and piShaper improve the homogeneity of illumination, photon counts and precision across the field of view

Compared to Gaussian illumination, the MEMS 2.8V scheme showed a more homogeneous background and fluorescence emission of single molecules across the field of view (Figure 43 (b)). We then analysed concentric regions of interest (ROI) (Figure 43(c)) to show the influence of the local laser intensity on single molecule fluorescence emission. The photon count per localisation, N_{Det}, decreases when we move away from the centre in Gaussian

and MEMS 1.5 V illumination while it stays constant for the piShaper, MEMS 2.8 V and MEMS 4.2 V modes (Figure 43(d)). We observe that N_{Det} is larger for the piShaper in comparison to the MEMS mirror, which can be attributed to the low reflectivity of the MEMS mirror.
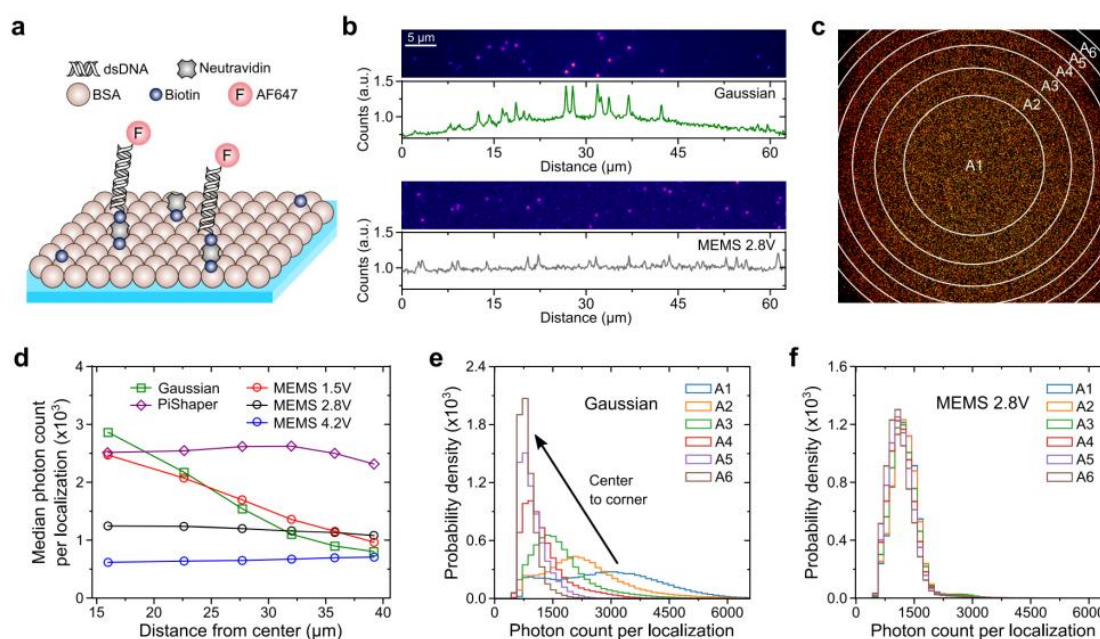
Figure 43 Single molecule brightness across the field of view. (a) Single molecule surfaces were prepared and imaged with different illumination modes. (b) 64×512 px section of a camera frame. Gaussian illumination shows inhomogeneous background and emitters intensities. (c) Concentric ring regions of interest (ROIs) are analysed. (d) ROIs farther from the centre of the image show lower median spot brightness for gaussian and MEMS 1.5 V illumination whereas other illumination modes are more homogeneous. (e,f) Photon count distributions in different ROIs are more homogeneous for MEMS 2.8V compared to Gaussian illumination. Adapted and reprinted with permission (CC BY 4.0) from "Tunable Wife-Field Illumination and Single-Molecule Photoswitching with a Single MEMS Mirror", ACS Photonics 2021, 8, 2728-2736

The average laser power was measured at 0.43 and 0.62 $kW \cdot cm^{-2}$ for MEMS 2.8 V and the piShaper respectively. We also observe that N_{Det} is constant for MEMS

4.2V but it is lower than for other schemes due to the laser beam being spread over a larger area. This supports the ideal choice of 2.8V for the electrical wave voltage.

By plotting a histogram of the photon count per localisation in the different concentric

ROIs (Figure 43 (e,f)), we see that the photon distributions remain constant across the field of view for MEMS 2.8 V in contrast to large variations observed for the Gaussian illumination.

By extending the analysis to the experimental precision including two MEMS modes deviating from the flatfield profile, we obtain further information (Figure 44). Heatmaps representing the median value of each metric in 225 square ROIs give a general view of the single molecule fluorescence emission rate and experimental precision across the field of view (Figure 44 (d,f)).

First, we note that the MEMS 1.5V mode shows a linear dependence of the spot brightness N_{Det} with increasing distances from the centre while the Gaussian illumination shows an expected non-linear relation. This intermediate mode will be used to produce a linear intensity gradient in chapter 5.

Figure 44 (b) and (c) show the radial evolution of the median localisation photon count and experimental precision. We use the median as the distributions of both metrics were skewed in several illumination schemes.

The experimental precision is inversely related to the spot brightness across the field of view as we expect from the theory of localisation (Thompson, Larson, and Webb 2002; Mortensen et al. 2010).

Heatmaps and distributions of NDet and precision show radial differences for Gaussian and MEMS 1.5 V while they show a homogeneous intensity and precision across the FOV for MEMS 2.8 V, MEMS 4.2 V and the piShaper.

The median photon count per localisation was 1249, 629 and 2514 for MEMS 2.8 V, MEMS 4.2 V and piShaper, respectively, which can be assigned to the lower local laser intensity due to poor reflectance of the MEMS and the larger laser spread for the MEMS 4.2 V setting.
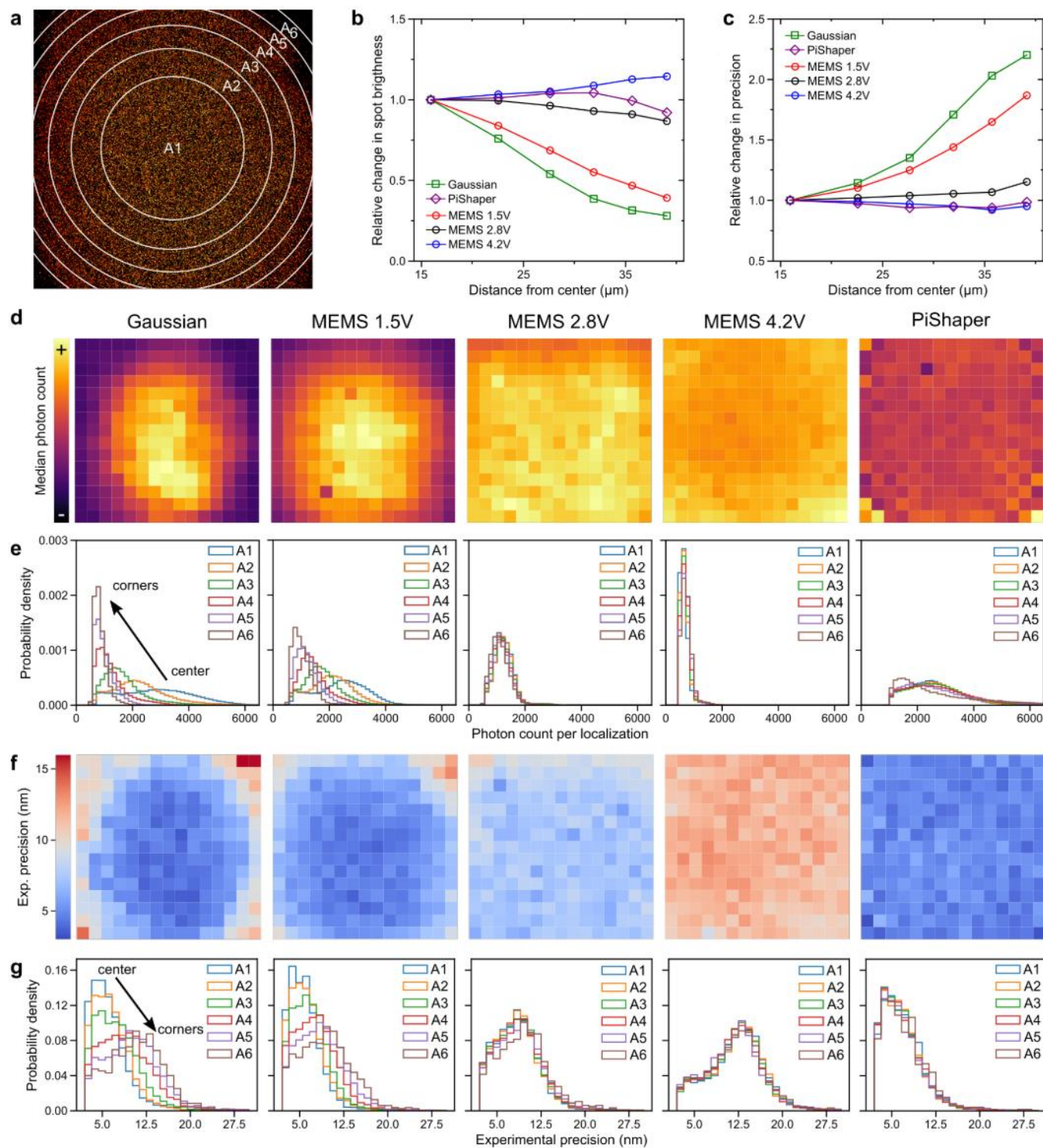
Figure 44 Intensity and precision. (a) Concentric ring regions of interest are analysed. (b,c) Spot brightness (intensity) and localisation precision as a function of ROI radii normalized by the value of the central ROI. (d,f) Heatmaps of spot brightness and experimental precision in 225 square ROIs. The median photon count or experimental precision is used for each ROI.

(e,g) Distributions of spot brightness and experimental precision for circular ROIs. Photn counts and experimental precision are shown to be uniform across the field of view for the piShaper, MEMS 2.8V and 4.2V. The shift towards lwer photon count and worse precision values in MEMS 4.2V translates the loss of local laser intensity due to spreading the laser on a larger surface area. Adapted and reprinted with permission (CC BY 4.0) from "Tunable Wife-Field Illumination and Single-Molecule Photoswitching with a Single MEMS Mirror", ACS Photonics 2021, 8, 2728-2736

The median values of the experimental precision were measured at 7.21, 12.10 and 5.03 nm for MEMS 2.8 V, MEMS 4.2 V and piShaper, respectively. This is consistent with the inverse relation described above. The Gaussian illumination and MEMS 1.5V showed some radial variability of the precision with 1.8- and 2.2-fold increase, respectively, between the centre and the corners of the FOV.

This section has demonstrated the superiority of a homogeneous illumination on the localisation intensity values that lead to a homogeneous precision across the field of view. Homogeneous emission intensities across the field of view would dispense a correction step for irradiation intensity variation in quantitative SMLM. We will now investigate the photoswitching behaviour of Alexa 647 in relation with the local illumination intensity in more detail (Figure 45).

Photoswitching of Alexa 647 in different illumination schemes

We then analysed the photoswitching of Alexa 647 under different illumination schemes. Three metrics are evaluated as well as the resolution of the reconstructed image as calculated by the FRC method (Culley, Albrecht, et al. 2018b; Laine et al. 2019). We analysed single molecule traces to extract the length of fluorescent and dark states of Alexa 647 by using a custom developed macro in ImageJ (described in the section 4.4.5).
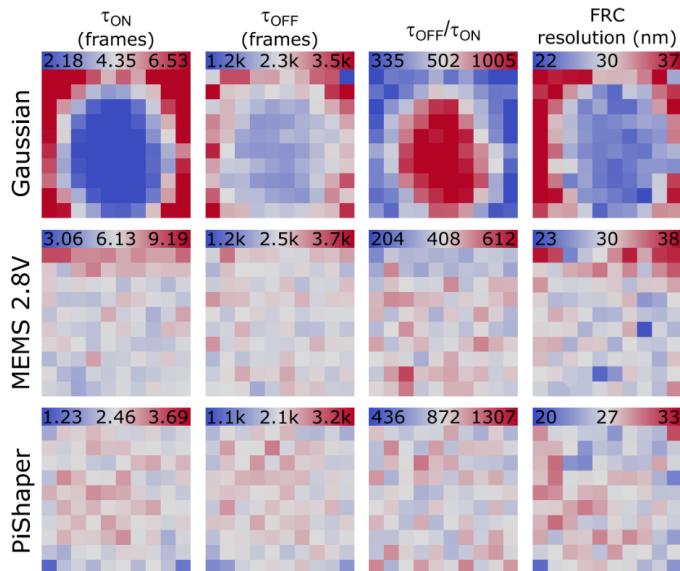
Figure 45 Photoswitching metrics and FRC resolution heatmaps. Median values of τ_{ON}, τ_{OFF}, τ_{OFF}/τ_{ON} and FRC resolution in 100 square ROIs are used to visualise the homogeneity of the photoswitching metrics across the field of view in three illumination schemes, Gaussian, MEMS 2.8 V and pishaper. While the Gaussian illumination shows a large variability of the photoswitching metrics in the centre compared to corners as expected from the difference in illumination intensity, the homogeneous illumination in MEMS 2.8 V and pishaper scheme produces homogeneous switching metrics across the field of view. The color scale corresponds to the mean of all ROIs ± 50 % for photoswitching metrics and the mean of all ROIs ± 25 % for FRC maps. Frames are 100 ms long. Adapted and reprinted with permission (CC BY 4.0) from "Tunable Wife-Field Illumination and Single-Molecule Photoswitching with a Single MEMS Mirror", ACS Photonics 2021, 8, 2728-2736

The ON-state lifetime τ_{ON} is the average time the fluorophores emit fluorescence before reversibly switching to a non-fluorescent OFF state. It is also the inverse of the OFF-switching rate k_{OFF}. The OFF-state lifetime τ_{OFF} is the average time the fluorophores reside in the dark OFF-state before being switched back to the fluorescent state. It is also the inverse of the ON switching rate k_{ON}. Both lifetimes follow exponential decay distributions (Van De Linde and Sauer 2014). $\tau_{OFF}/\tau_{ON} = k_{ON}/k_{OFF}$ is a ratio that describes the average proportion of fluorophores that are in their fluorescent ON state at a given time. It is used in SMLM(Cordes et al. 2010) as a metric to evaluate the density of emitters at a given time and predict the capacity of a localisation software to efficiently localise individual fluorophores. τ_{ON} and τ_{OFF} are influenced by the local laser intensity

across the frame (Figure 45, Gaussian). Both are reduced in higher laser intensities.

Each time Alexa 647 is excited to a higher electronic state, relaxation processes compete. On average, each relaxation pathway will happen after a number of activation cycles according to its rate *k*. At higher illumination intensity, Alexa 647 is excited more frequently and the average number of activation cycles is reached earlier, leading to an earlier switching to the dark state which corresponds to shorter τ_{ON}.

Although the reactivation is usually controlled by a laser at shorter wavelengths (Heilemann, Van De Linde, et al. 2008; Van De Linde, Wolter, and Sauer 2011), Alexa 647 in its dark state can also be reactivated by the fluorescence excitation laser at 641 nm by a photon mediated elimination of the thiolate moiety (see the general introduction for a detailed description of Alexa 647 photoswitching). This effect reduces τ_{OFF} at higher laser intensities, in the centre for the Gaussian illumination.

The FRC resolution follows a similar trend as the experimental precision in the previous section.

MEMS 2.8 V and piShaper illumination modes showed homogeneous photoswitching metrics across the field of view. The difference of the average laser intensity due to the low reflectance of the MEMS mirror explains the difference in average metrics between the MEMS 2.8 V and the piShaper. τ_{ON} is significantly longer, τ_{OFF} is slightly longer and τ_{OFF}/τ_{ON} is smaller for MEMS 2.8 V compared to the piShaper. Together with the lower photon count per localisation this explains the slightly larger FRC resolution.

We have shown that the photoswitching metrics τ_{OFF}, τ_{ON}, τ_{OFF}/τ_{ON} as well as the spot brightness N_{Det} and precision/resolution are influenced by the local illumination intensity. We will now study in more detail the linear dependence of N_{Det} with $k_{OFF} = \tau_{ON}^{-1}$.

Photon budget, sampling and frame rates

We took the values of N_{Det} and τ_{ON} for the 225 square ROIs for each condition in Figure 44 and Figure 45 and grouped them in a scatter plot as shown in Figure 46 (a). The relation is linear (Figure 46 (b,c)) when we replace τ_{ON} with $k_{OFF} = \tau_{ON}^{-1}$ up to $\tau_{ON}^{-1} = 0.35\ frame^{-1}$. We also observe that different illumination schemes have different combinations of τ_{ON}^{-1} and N_{Det} distributions but they follow the same trend. We can fit a linear function to the distribution of data points for MEMS 1.5 V up to $0.35\ frame^{-1}$ and the slope corresponds to the photon budget or the number of photons detected during an ON event. The photon budget is constant for a given detection efficiency of the setup, buffer conditions, and fluorophore used and does not depend on the local laser intensity. Here, it was measured to be 6878 ± 52 photons per ON event.
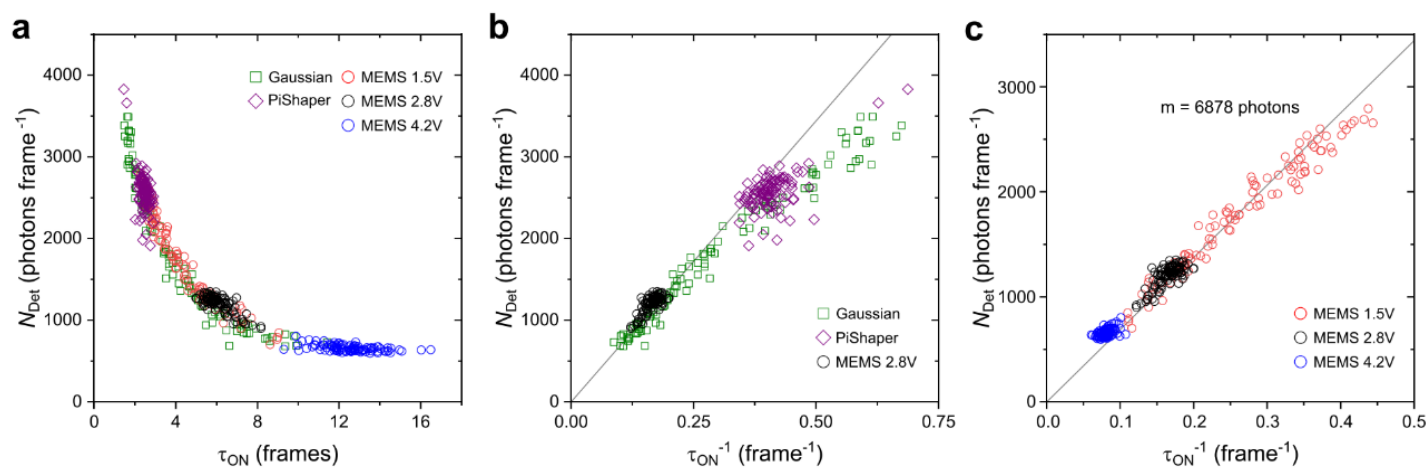
Figure 46 Photoswitching for the whole FOV. (a) Scatter plot of spot brightness as a function of τ_{ON} for the 100 square region of interest analysed in Figure 45. (b,c) Scatter plot using the inverse of τ_{ON} shows a linear relation under $0.35\ frame^{-1}$. Above $0.5\ frame^{-1}$ Photons are emitted during less than two complete frames which leads to a significant loss of detected photons. Adapted and reprinted with permission (CC BY 4.0) from "Tunable Wife-Field Illumination and Single-Molecule Photoswitching with a Single MEMS Mirror", ACS Photonics 2021, 8, 2728-2736

Above $0.35\ frame^{-1}$, the values deviate from the linear relation towards lower N_{Det} values. This corresponds to ON events limited to three frames or less. If a small fraction of

the emission time overlaps with the previous or next frame, it is unlikely that it will be detected and τ_{ON} and N_{Det} will be underestimated, which explains the deviation from the linear relation.

The Gaussian illumination, green squares, shows (Figure 46(b)) a large spread of values corresponding to the large spread of local illumination intensities. The corners of the FOV show small N_{Det} and τ_{ON}^{-1} values while the centre shows higher values. MEMS 2.8 V and piShaper show well grouped N_{Det} and τ_{ON}^{-1} values for the whole FOV with slightly higher N_{Det} and τ_{ON}^{-1} values for the piShaper due to the higher average illumination intensities. This is expected for homogeneous illumination.

We then compared the MEMS 2.8V condition to two suboptimal settings of the MEMS, 1.5 and 4.2V (Figure 46(c)). MEMS 1.5V shows a wide spread of values along the linear relation between N_{Det} and τ_{ON}^{-1} while MEMS 2.8 and 4.2V show tight groupings denoting a homogeneous illumination. MEMS 1.5V was used to fit the linear relation and obtain the photon budget value. Data points above τ_{ON}^{-1} = 0.35 $frame^{-1}$ were excluded from the fit because of the bias observed for ON events of length comparable to the exposure time of the camera. MEMS 4.2 V showed a good homogeneity but the spread of the photon emission over more than 10 frames lead to a lowered localisation precision and FRC resolution as we saw earlier in Figure 44 and Figure 45.

The asymptotic behaviour of N_{Det} and the sampling issue was investigated further by the means of numerical simulations (Herdly et al. 2021b). We demonstrated the linearity of the relation between N_{Det} and τ_{ON}^{-1} for $\tau_{ON}^{-1} < 0.5\ frame^{-1}$. For higher values of τ_{ON}^{-1}, we showed that when τ_{ON} was comparable or smaller than the exposure time of the camera, the analysis overestimated τ_{ON}, and N_{Det} saturated because all photons were detected in the same frame.

We propose that optimal results in SMLM are obtained when the ON-state lifetime of

emitters is spread on one or two frames. This promotes high localisation precision due to high numbers of detected photons. For example, in this experiment the frame rate that was set to 10 Hz for all experiments could be decreased to 2 and 3 Hz for MEMS 2.8 V and piShaper illuminations, respectively, to detect all ON events in one or two frames. Alternatively, changing the buffer conditions could change the photoswitching to better align τ_{ON} with a chosen camera exposure time. The effects of the photoswitching buffer composition will be discussed in the next chapter.

Finally, we combined the two related metrics τ_{ON} and N_{Det} into a single dimension to evaluate illumination schemes.

Single-dimension evaluation of illumination schemes

In order to evaluate the quality of SMLM results under different illumination schemes, we calculated the coefficients of variation (Standard deviation/mean) of τ_{ON} and N_{Det} for the five illumination schemes that we studied in this chapter and for centred subregions for three of them(Figure 47).

Gaussian and MEMS 1.5 V illuminations showed large coefficients of variation in both τ_{ON} and N_{Det}. We combined the two using the root mean square (RMS) of both coefficients as they are comparable in scale for all illumination schemes.

Reducing the used field of view to the central 36 and 16 % improved both coefficients of variation and their RMS for the Gaussian illumination. This can be considered similar to spreading the laser beam to obtain a more homogeneous illumination as it is done in many SMLM setups as a cheap and easy alternative.

The piShaper and MEMS 2.8 V illumination schemes still outperformed the 16 % cropped gaussian over the complete field of view (which is 6.25-fold larger than the cropped Gaussian 16 %). Cropping the MEMS 2.8 V and piShaper FOVs still improved their RMS but
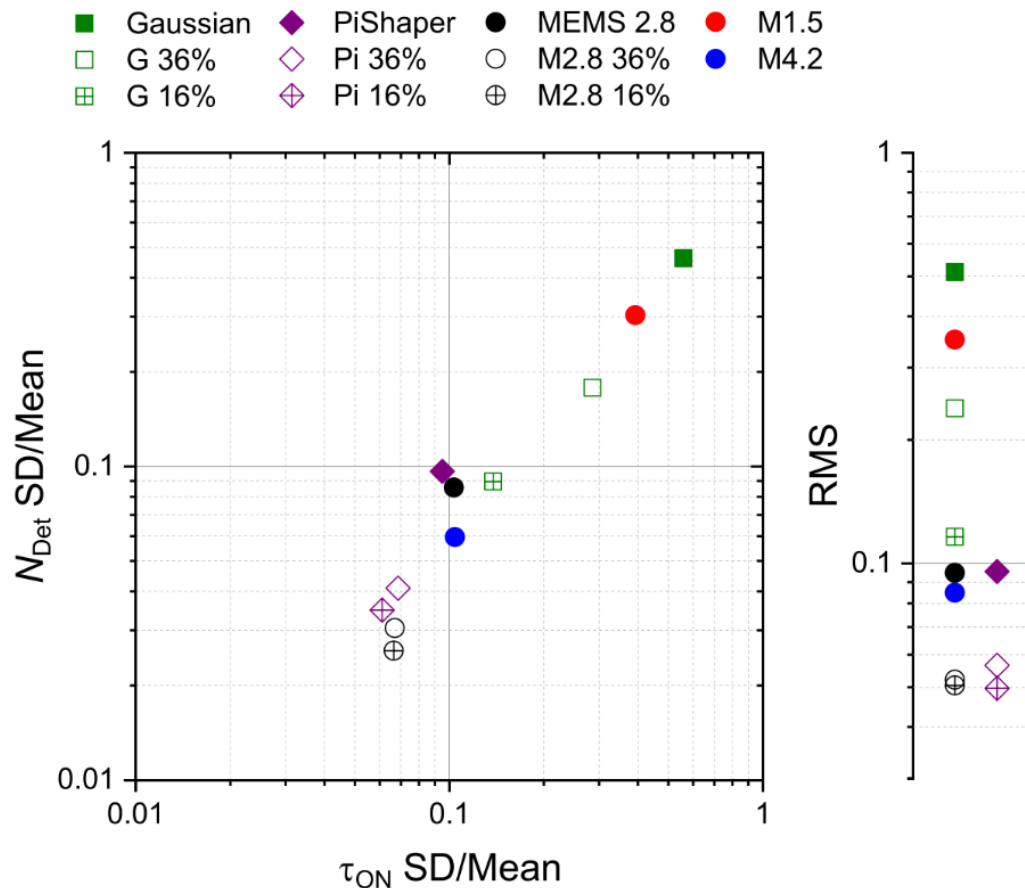
Figure 47 Single dimension evaluation metric. Coefficients of variation (left) of spot brightness and τ_{ON} can be combined by the root-mean-square value (right), Frame sizes: 100% = (62.5 μm)^2, 36% = (37.5 μm)^2, 16% = (25.0 μm)^2. This summarising plot represents the improvement of our proposed method compared to cropping the field of view for a gaussian illumination. MEMS 2.8V on the full field of view is on par with the pishaper illumination on the same field of view and just outperforms a drastic crop to just 16% of the field of view with the Gaussian illumination. Spreading the Gaussian scheme to obtain the same illumination intensity on the full field of view would require the laser power to be increased more than 6-fold, which was impossible with the laser used in this project. Adapted and reprinted with permission (CC BY 4.0) from "Tunable Wife-Field Illumination and Single-Molecule Photoswitching with a Single MEMS Mirror", ACS Photonics 2021, 8, 2728-2736

RMS values of 10 % for a large field of view $62.5 \times 62.5\ \mu m^2$ are very solid results

demonstrating that the illumination is homogeneous with both illumination schemes.

One could argue that using a telescope to spread the Gaussian laser beam over an area

much wider than the field of view and increasing the laser power would provide a similar

homogeneous illumination with sufficient local illumination intensity. This strategy comes

with other limitations as it would lead to illuminating a large area of the sample outside the field of view leading to potential photobleaching. It would also waste a large part of the laser output outside of the field of view. Additionally, this would require using high powered lasers that require additional safety measures and can lead to lenses and mirrors heating which can affect their optical performances and modify the illumination scheme quality.

We have shown that investing a little time and money to integrate a flat illumination scheme, either refractive or MEMS based is well worth the investment compared to the spreading of a Gaussian laser beam.

4.5.5. Conclusion and outlook

In this chapter, we have demonstrated that a MEMS mirror can be used to transform a Gaussian illumination into a homogeneous illumination, which is comparable to a commercially available refraction based flat illumination device, the piShaper, but with the additional tuneability. We have investigated the effect of different illumination schemes on the photoswitching of Alexa 647 and the consequences for the quality of SMLM images using several metrics to evaluate the quality of the illumination.

We have also presented a protocol to evaluate competing illumination schemes and proposed a method to optimise the choice of the recording frame rate.

Our MEMS device has several advantages such as the low electric control requirements, as a simple sinus sum electrical signal is used. It is highly reliable and takes little room in a microscopy setup. This is possible because a single mirror generates oscillations in two orthogonal directions.

The main future improvement of our prototype would be to address the low ~ 40-50 % reflectance by covering the mirror surface with metallic or dielectric coating that have

been demonstrated recently for other applications (Bauer et al. 2015).

The MEMS could also be used to obtain more exotic illumination schemes by synchronising the oscillations of the MEMS mirror with a pulsed laser to modify the laser profile in each region of interest. The synchronisation has been recently demonstrated for another application (Janin et al. 2019).

We confirmed again that the switching kinetics of carbocyanine dyes depend on the local laser intensity (van de Linde, Sauer, and Heilemann 2008). We now have a better understanding of the MEMS behaviour. In the next chapter, the effects of buffer composition on the switching of fluorophores are studied by creating a controllable laser intensity gradient within the field of view by using the tuneability of the MEMS device.

Chapter 5. Thiolates control the photoswitching of cyanine dyes

5.1 Abstract

Cyanines are widely used in SMLM as they are photoswitchable dyes with high molecular brightness. Their photoswitching is controlled by chemical and physical parameters that depend on the chemical composition of the switching buffer and the illumination intensity. In this chapter, we use the MEMS tilting mirror described in the previous chapter to create an illumination intensity gradient across the field of view of the camera and study the influence of different buffer conditions on photoswitching metrics that are known to impact the obtainable resolution. We vary the pH and mercaptoethylamine (MEA) concentration of the buffer and investigate their impact on the photoswitching of Alexa 647. We demonstrate that pH and MEA concentration can be combined in a single parameter, the thiolate concentration. We propose an optimal range of thiolate concentration of 1.5-16 mM that is a trade-off between positive and negative influences of high and low thiolate concentrations on different photoswitching metrics that in turn influence the obtainable resolution. We then evaluate the impact of acidification of the buffer by the glucose/glucose oxidase/catalase oxygen scavenger system on single-molecule photoswitching. We show that sealing the sample chamber with a coverglass greatly limits the renewing of oxygen in the buffer through exchanges with the atmosphere and reduces the acidification of the buffer by an order of magnitude. Finally, we demonstrate the impact of a suboptimal switching buffer on the resolution obtained on a

biological sample by imaging the glucose transporter protein 4 on the plasma membrane of adipocytes.

5.2 Introduction

The previous chapter explained how varying illumination power across a sample can change the photoswitching performance of Alexa 647 and how it influences the quality of SMLM images. In this chapter, we will investigate the role of the switching buffer on the photoswitching and SMLM performance. Controlling the photoswitching is the at the core of quality results in dSTORM. SMLM methods have become widely used (Vangindertael et al. 2018; Sauer and Heilemann 2017; Valli et al. 2021) and better understanding the effects of switching buffers will allow more informed adjustments of switching buffers to optimize SMLM experiments.

Several research teams have investigated and demonstrated the underlying chemical and photophysical mechanisms of cyanines switching (Ha and Tinnefeld 2012; Van De Linde and Sauer 2014; Stennett, Ciuba, and Levitus 2014; H. Li and Vaughan 2018).

Carbocyanine dyes absorbing in the red wavelengths were the first used for dSTORM and they are still the most used because of their brightness and photophysical properties (Heilemann et al. 2005). Some alternatives exist, e.g. AF 488, Cy3B or AF 588, but this work focuses on studying Alexa 647. To control the photoswitching behaviour of Alexa 647 we use a buffer containing a controlled balance of reductive thiols and oxidative agents controllers. Hence the switching buffer contains β-mercaptoethanol (BME) or β-mercatoethylamine (MEA), the latter is used in this work. An enzymatic system composed of glucose oxidase, glucose and catalase is responsible for the limitation of molecular oxygen in the sample. The anion form of thiols, thiolate, is responsible for the conversion of

fluorescent cyanines to reversibly non-fluorescent metastable molecules (Heilemann et al. 2009; Dempsey et al. 2009; van de Linde et al. 2011). A recent study (Gidi et al. 2020) also demonstrated the role of thiolates in stabilizing the fluorescent emission of cyanine dyes. Following this study, the scenario of photoswitching is as follows:

A cyanine fluorophore cycles between a singlet ground state and an excited singlet state upon absorbance and emission of photons. Intersystem crossing of an electron from the singlet excited state to a more stable triplet excited state is a rare event. The triplet state means that a pair of electrons have the same spin orientation which makes the transition back to the ground state very improbable and the triplet state more stable. Thiolates can switch back the triplet cyanine to another singlet state by Photoinduced Electron Transfer (PET) that can then: either react chemically with the thiolate and form a very long-lasting dark state or OFF state of the cyanine dye; or relax to the singlet ground state and enter the fluorescence cycle again.

The first path promotes the OFF-switching of most fluorophores used in SMLM to allow resolving densely labelled structures and the second path stabilises the fluorescence emission of cyanine dyes, contributing to their stable and bright emission that is important for a good resolution.

In this chapter, we take advantage of the tuneability of the MEMS device presented in the previous chapter. By lowering the oscillation amplitude of the tilting mirror, we switch from a homogeneous illumination across the field of view to an illumination gradient that we use to study the switching kinetics of Alexa 647 while varying the concentration of MEA and the pH of the switching buffer.

In this project, we compared 14 combinations of pH and thiol concentration while monitoring evaluation metrics for SMLM, $\tau_{ON}, \tau_{OFF}, \tau_{OFF}/\tau_{ON}$ and resolution.

We showed that optimal results as indicated by the metrics follow the concentration of the

thiolate anion that can be increased by increasing the total concentration of thiols or by lowering the pH. This will allow SMLM with optimal buffer conditions with the choice of pH between 6.5 and 8.5.

Finally, we tested our results on biological samples by imaging the glucose transporter type 4 in the plasma membrane of adipocytes.

5.3 Materials and methods

5.3.1. Microscopy setup

The microscopy setup is similar to the setup described in the previous chapter and the associated article (Herdly et al. 2021b).

The central $512 \times 512 \, pixel$ region of the camera was used for recording. Each pixel represented 122 nm as measured in chapter 2, which provided a field of view of $62.5 \, \mu m \times 62.5 \, \mu m$. We recorded 30000 frames at an exposure time of 50 ms for all experiments, except for buffer acidification experiments where we recorded 15000 frames at 100 ms exposure time. Biological samples images were recorded with the piShaper light path to obtain a flat illumination over the field of view and all the other experiments used the MEMS described in the previous chapter to generate an illumination gradient across the field of view to study the contribution of light intensity to switching kinetics. We measured the average intensity of the illumination at 0.48 and 0.72 $kW \cdot cm^{-2}$ for switching experiments with the MEMS mirror and cell experiments with the piShaper, respectively.

5.3.2. Sample preparation

We prepared single molecule surfaces as reference samples for studying Alexa 647 kinetics using the complementary 30 base pairs strands M3-s-30bp-8-AF647 and M3-as-30bp-5'Bio to make the M3-8-N dsDNA probe (sequences in Appendix). The sense strand was internally modified with Alexa 647 on the position 8 and the antisense strand was 5'-terminally labelled with biotin. Single strand DNA was purchased from Eurogentec, Ltd. Hybridisation was done by incubation at room temperature of the complementary DNA strands in a concentration ratio of 1:2, sense:antisense.

Single molecule surfaces were prepared by sequential treatment with BSA and biotinylated BSA, then streptavidin and finally the DNA probe with rinsing steps after each treatment (see chapter 2). The biological samples were prepared by Gwyn Gould's team as described before (Herdly et al. 2023; Koester, Geiser, Bowman, et al. 2022). All samples were prepared in Labtek II chambers that can contain 1 mL buffer.

5.3.3. Photoswitching buffer

Fresh photoswitching buffer was prepared for each experiment with various final concentrations of MEA from 10 to 250 mM according to previously published protocols (Schäfer et al. 2013; Herdly et al. 2021b) with chemicals purchased from Sigma-Aldrich unless otherwise specified. The buffer contains an oxygen scavenging system (described in the general introduction of the thesis) composed of 5 % (w/v) glucose, $10\ U \cdot mL^{-1}$ glucose oxidase and $200\ U \cdot mL^{-1}$ catalase in the final buffer. The buffer was prepared in PBS, and pH was adjusted by the addition of 1 M HCl or KOH. The volumes of HCl/KOH needed were determined by a preliminary experiment that will be described below in section 5.4.1.

The sample chambers were completely filled with freshly prepared buffer and sealed with

a microscopy glass coverslip to avoid any gas exchange with the atmosphere during the measurement time. Samples of the open condition of the acidification experiments were left unsealed.

For the titration of MEA, 40 mL switching buffer was prepared as described above, with 5 % (w/v) glucose, 10 $U \cdot mL^{-1}$ glucose oxidase, 200 $U \cdot mL^{-1}$ catalase and 10-250 mM MEA in PBS buffer. Titration was done with 1M KOH or HCl in H_2O and the pH was measured with a pH-meter (Oakton pH 700). The solution was mixed continuously with a magnetic stirrer and stir bar.

In acidification experiments, the pH was monitored with pH indicator strips (MQuant pH 5.0-10.0, 0.5 reading steps). The buffer was freshly prepared as described above with a final concentration of 50 mM MEA and a pH adjusted to 7.4 with KOH.

The sample chamber was filled with switching buffer, the sealed sample was covered with a coverglass and the open sample was left open. For the open sample, pH was measured with the pH strip at time 0,2 and 4 h For the sealed sample, pH was measured before sealing the chamber and after the 20 h image acquisition.

5.3.4. Data analysis

Localisation with rapidSTORM

Raw image stacks were analysed with rapidSTORM 3.3 (Wolter, Löschberger, Holm, Aufmkolk, Dabauvalle, Van De Linde, et al. 2012). We filtered non-specific localisations from the background noise by applying a signal to noise ratio (SNR) threshold. This filter was kept at the minimum to avoid discarding low intensity emitters in sub optimal buffer conditions. A visual inspection of the image stack was conducted. We used the LocFileVizualiser macro written by SvdL (Van De Linde 2019) to open the raw image stack

and add markers on top of the image stacks for localisations in the rapidSTORM localisation file. We visually inspected each image stack to control that emitters were accepted by the filter and no false localisations in the background noise were accepted. We adjusted the SNR filter to each data stack.

We also applied a filter on PSF width to reject out-of-focus localisations. Non switching bright fluorophores sometimes named highlanders are sometimes observed in SMLM. The localisations corresponding to highlanders are not rejected in the rapidSTORM filter as they will be rejected by the photoswitching time analysis later based on the localisation cluster size and the length of the ON time.

Switching analysis

The single molecule photoswitching was analysed with the same protocol as in chapter 4. The filtered localisation files from rapidSTORM were analysed with custom written macros in ImageJ (Van De Linde 2019; Schindelin et al. 2012).

The localisation files were loaded in FIJI and a super resolution image was reconstructed with a 10 nm pixel size. 49 Regions Of Interest (ROI) were drawn on the reconstructed images following a 7×7 chessboard pattern. Geometrical inspection of localisation cluster was done as described in chapter 4, accepting clusters with a minimum circularity of 0.8 and a surface of 3-300 pixels. Raw localisations in accepted clusters were analysed as single-molecule traces. ON and OFF times were determined as well as photon numbers. For each ROI, ON and OFF times for all single molecule traces were aggregated in histograms and an exponential function was fitted to determine τ_{ON} and τ_{OFF}. Repeated fitting was performed with variations of the bin size to obtain the best fit with high R^2. For the analysis of ON times, missed localisation gaps in the middle of time traces of up to 4 consecutive frames was accepted.

The spot brightness (N_{Det}) for each ROI was calculated as the median value of the photon count of all localisations accepted in the ROI. The photon count was calculated from the raw localisation data from rapidSTORM that is known to be underestimated but we accepted this bias that was constant for all conditions.

Hundreds of thousands of localisations were analysed for each buffer condition after cluster selection. 167 000 to 631 000 localisations were analysed, with 800 to 20 000 localisations in each ROI.

Resolutions

Resolutions metrics were calculated by different methods and compared.

Fourier Ring Correlation (FRC) maps were generated with the imageJ plugin NanoJ SQUIRREL (Culley, Albrecht, et al. 2018b) as described in chapter 4.

The photon limited resolution was derived from the variance of the localisation uncertainty (Mortensen et al. 2010):

$$\Delta_x^2 = \frac{\sigma_a^2}{N} \cdot \left(\frac{16}{9} + \frac{8 \cdot \pi \cdot \sigma_a^2 \cdot b^2}{a^2 \cdot N} \right) \tag{24}$$

Where:

$$\sigma_a^2 = \sigma^2 + \frac{a}{12} \tag{25}$$

σ is the standard deviation of the PSF.

a is the pixel size of the camera.

b^2 is the background noise.

N is the number of photons detected.

The photon limited resolution is $2.355 \cdot \sqrt{2 \cdot \Delta_x^2}$. The factor 2 in the square root accounts for the emCCD noise (Mortensen et al. 2010).

Numerical values were set to $\sigma = 140\ nm, a = 122\ nm, b^2 = 49\ photons$ and two

conditions, i.e. $N = N_{\tau_{ON}}$ or $N = \frac{1}{2} \cdot N_{\tau_{ON}}$.

$N = N_{\tau_{ON}}$ assumes that all photons from an ON event are captured in a single frame, which is unlikely (see chapter 3) and $N = \frac{1}{2} \cdot N_{\tau_{ON}}$ gives more realistic values for the spot brightness where the ON event and camera frame are not correlated.

The two-dimensional structural resolution is derived from the Nyquist-Shannon theorem on sampling (Shroff et al. 2008). The Nyquist limited resolution is:

$$d_{2D} = \frac{2}{\sqrt{n}} \tag{26}$$

Where n is the label density.

5.4 Results and discussion

5.4.1. Switching buffer pH adjustments

This project aims at studying the effects of pH and MEA concentrations on the photoswitching of Alexa 647. The switching buffer needs to be prepared freshly before measuring and we use about 1.5 mL for each condition. The pH meter available requires a large volume of liquid, 20 mL minimum, for measuring the pH accurately. To avoid wasting 20 mL switching buffer for a single use of 1.5 mL, we decided to determine the acid or base corrections to apply to the switching buffer to reach the desired pH at 5 MEA concentrations.

We prepared 40 mL switching buffer according to the recipe described above (section 5.3.3.) for 5 MEA concentrations, i.e. 10, 25, 50, 100 and 250 mM. The probe of the pH-meter (Oakton pH700) was submerged in the switching buffer and constant mixing was ensured by a magnetic rod and magnetic stirrer.

We measured the initial pH of the switching buffer and added 20 µL aliquots of 1M HCl or KOH and measured the pH at each addition (Figure 48(a)).

The initial pH was measured at 7.04, 6.91, 6.71, 6.50, 6.14 for 10, 25, 50, 100 and 250 mM of MEA, respectively. This is expected because the MEA used is cysteamine hydrochloride and thus starts at low pH.
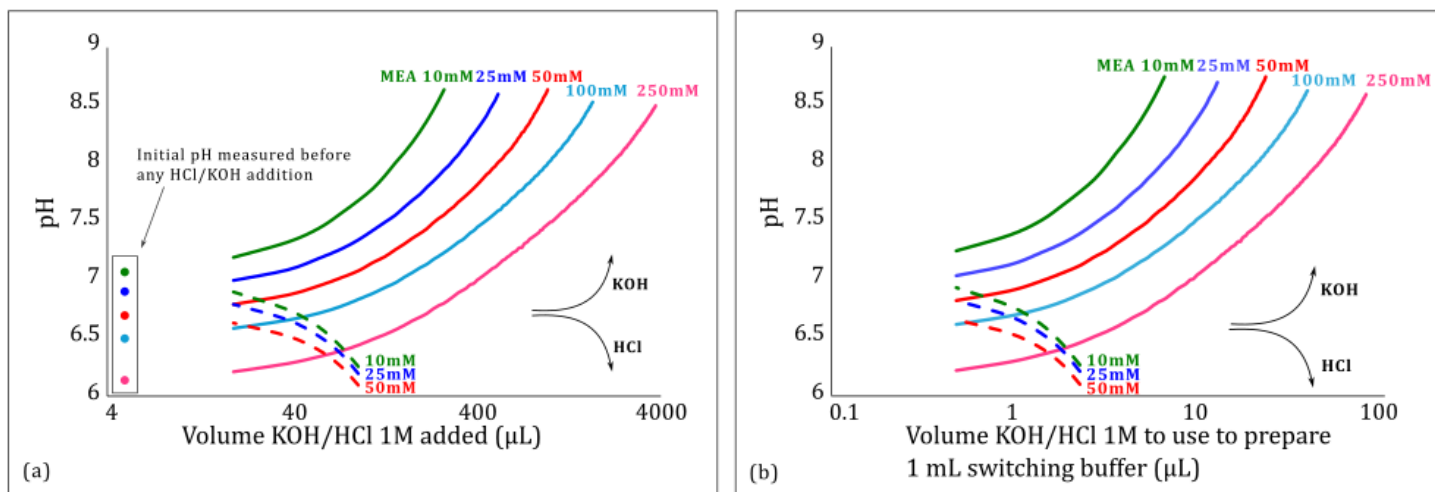
Figure 48 (a) Evolution of pH with increasing addition of 1 M HCL or KOH. (b) corrected volumes to add to 1 mL switching buffer to reach the target pH

We corrected the added volumes by dividing them by the total volume of the switching buffer at the time of the pH measurement, that is to say $40mL + n \times 20\mu L$ with n the number of 20 µL aliquots added at each time point. This resulted in Figure 48(b) that gives the volume of 1M HCl or KOH to use when preparing the switching buffer at one of the 5 concentrations at any target pH.

Table 6 shows the volumes we used to prepare the switching buffer in the experiments described below.

Table 6 Volumes used to correct the pH of 1 mL switching buffer with 1M KOH or HCl

Volumes (µL) of 1 M HCl used to correct the pH of 1mL switching buffer		pH			
		6.5	7.4	8	8.5
MEA concentration (mM)	10	1.77	0.19		
	50	1.07			
	100				
	250				

Volumes (µL) of 1 M KOH used to correct the pH of 1mL switching buffer		pH			
		6.5	7.4	8	8.5
MEA concentration (mM)	10			3.94	6.67
	50		5.47	14.62	24.86
	100	0	10.23	27.47	46.65
	250	3.11	24.38		

5.4.2. Thiol concentration and pH influence the behaviour of photoswitching fluorophores

We then prepared single molecule surfaces with the M3-8-N probe as described in section 2.5.1. Fresh switching buffer was prepared for SMLM imaging with various pH (6.5-8.5) and MEA concentrations (10-250 mM) as seen in Table 6. The datasets for 250 mM MEA and pH 8.0 and 8.5 were rejected as the switching was too bad to extract relevant data, which is in line with the findings of the study as will be shown later.

The SMLM parameters were the same for all buffer conditions (illumination, exposure time, frame number). The MEMS mirror mediated gradient of illumination was set with its power maximum in the centre of the FOV and its minimum in the corners (Herdly et al. 2021b). This allowed us to study the photoswitching kinetics of Alexa 647 at different

illumination powers in a single acquisition. The number of detected photons per frame (N_{Det}) is proportional to the illumination power when saturation is not reached at low kW·cm^{-2} illuminations (Dittrich and Schwille 2001; Eggeling et al. 1998). We used the photon number in each frame as a reporter for the illumination power across the FOV. Additionally, recent investigations of the effect of high lasers on samples encourages a reduction of laser powers in SMLM experiments (Diekmann et al. 2020; Chung et al. 2021). 49 regions of interest were analysed across the FOV for τ_{ON}, τ_{OFF}, τ_{OFF}/τ_{ON} and N_{Det}. Coloured heatmaps for three buffer conditions are shown in Figure 49.
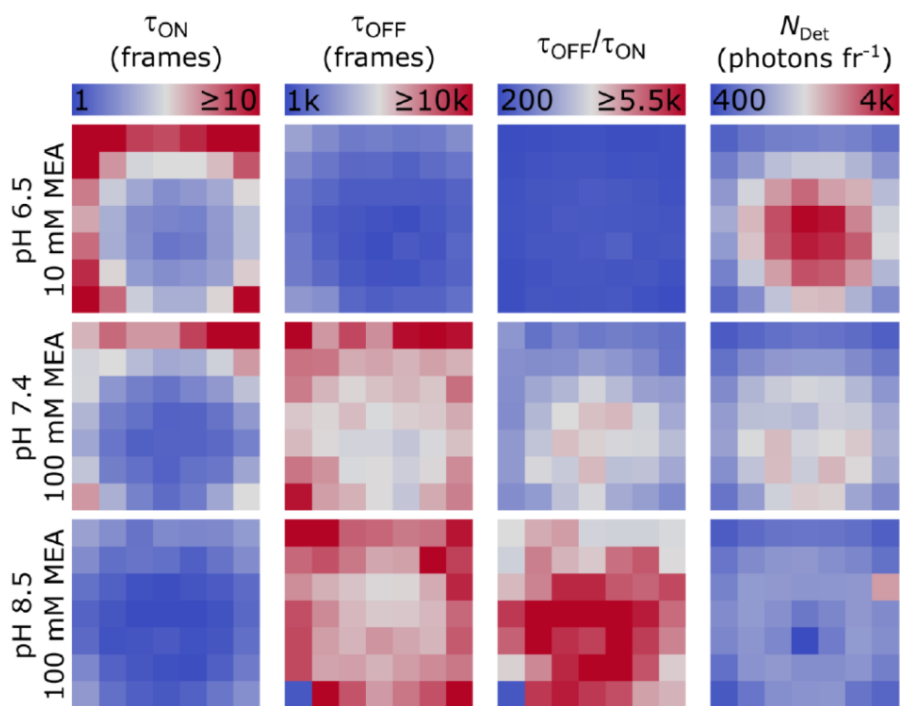
Figure 49 Heatmaps representing the variability of the switching metrics across the field of view following the MEMS induced illumination gradient for three buffer conditions, pH 6.5 10 mM MEA, pH 7.4 100 mM MEA and pH 8.5 100 mM MEA. Other buffer parameters are the same in all conditions. 49 (7x7) square ROIs were analysed across the field of view. Frames were 50 ms long. Scales apply to all images of the column to show the influence of the buffer composition on photoswitching metrics. τ_{ON} and N_{Det} increase with increasing pH and MEA concentration while τ_{OFF} and τ_{OFF}/τ_{ON} decrease. Reprinted with permission (CC BY 4.0) from "Benchmarking Thiolate-Driven Photoswitching of Cyanine Dyes", J. Phys. Chem. B 2023, 127, 732-741". Copyright 2021, The Authors. Published By the American Chemical Society" (Herdly et al., 2023)

First, we observed an influence of the illumination intensity across the field of view with lower values for τ_{ON}, τ_{OFF} and τ_{OFF}/τ_{ON} and higher values for N_{Det} in the centre (higher illumination intensity) compared to the corners. This reinforces the importance of homogeneous illumination when imaging biological samples outside of microscopy development experiments to ensure homogeneous switching conditions and subsequent homogeneous image quality across the field of view.

 Second, we observe an influence of the buffer conditions. In general, we observe an increase of τ_{OFF} and τ_{OFF}/τ_{ON} and a decrease of τ_{ON} and N_{Det} with increasing pH and MEA concentrations. Considering that the main metrics that have been linked with high quality SMLM data are large τ_{OFF}/τ_{ON} and N_{Det} values, confirm once more that the optimal buffer composition will probably be a trade-off between high photon numbers and a good emitter spatial separation guaranteed by a high τ_{OFF}/τ_{ON}.

Next, we calculated the switching rates for the transitions of Alexa 647 from the dark to the fluorescent state ($k_{ON}=1/\ \tau_{OFF}$) and from the fluorescent to the dark state ($k_{OFF}=1/\ \tau_{ON}$) and plotted them as a function of N_{Det} (Figure 50). A linear response can be seen for all conditions), which was then analysed by linear approximation (Figure 50 and Appendix). Metrics can be extracted from the fit parameters and from ROI values that provide information on the photoswitching performance in various buffer conditions.

The photon budget, $N_{\tau_{ON}}$, is calculated as the inverse of the gradient of the linear fit in Figure 50(a). It represents the total number of detected photons for an entire ON event across several sequential camera frames. Higher numbers of photons are detected during one ON event for 50 mM MEA at pH 6.5 compared to pH 7.4.

The rate of reactivation of the dark state into its fluorescent state is proportional to N_{Det}, which has been described before. The photoinduced switching of the fluorophore from the dark state to the fluorescent state occurs by elimination of the thiol adduct.
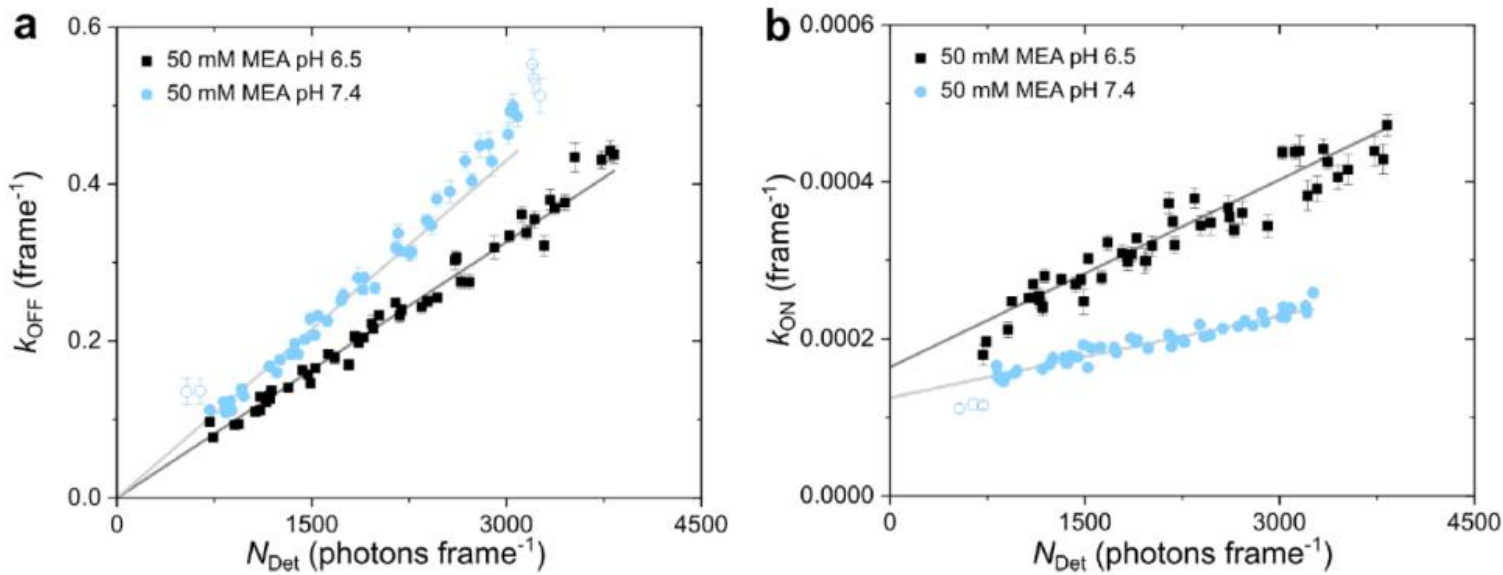
Figure 50 Examples of linear fit of k_{OFF} and k_{ON} as a function of N_{Det} for two buffer conditions, 50 mM MEA, pH 6.5 and 50 mM MEA, pH 7.4.. Fit function is shown as a line. The y-intercept was fixed to 0 for k_{OFF} but not for k_{ON}. Hollow symbols are masked data points that were ignored for the fitting. Reprinted with permission (CC BY 4.0) from "Benchmarking Thiolate-Driven Photoswitching of Cyanine Dyes", J. Phys. Chem. B 2023, 127, 732-741". Copyright 2021, The Authors. Published By the American Chemical Society" (Herdly et al., 2023)

The repopulation of the fluorophore ground state upon light absorbance has been shown with the read-out laser alone (640 nm) or with an additional shorter wavelength (405, 488 or 514 nm) that is absorbed by the dark state alone (Van De Linde et al. 2011; van de Linde, Sauer, and Heilemann 2008; Dempsey et al. 2009; Gidi et al. 2020).

Gidi et al. also showed that thiols could contribute to a repopulation of the ground state by a thermal dissociation of the fluorophore-thiol adduct. This was also described by Lars Frahm in his PhD thesis (Frahm 2016).

The thermal recovery time τ_{OFF}^0 was the inverse of the intersection of the linear fit with the axis in Figure 50(b). It describes how long it takes on average for the dark state fluorophore to switch to the fluorescent state without laser illumination.

The gradient of the same fit described the response of the activation rate k_{ON} to increasing

laser intensities as reported by N_{Det} (Figure 50)

The highest value for the ratio τ_{OFF}/τ_{ON} across the field of view was also considered.

All linear correlations are shown in appendix. For sub-optimal buffer conditions, low quality outliers were excluded from the linear fit and are indicated in hollow symbols in Figure 50 and orange symbols on appendix plots. For the linear correlation of k_{OFF} and N_{Det}, we also excluded undersampled values as explained before (Herdly et al. 2021b), which are also shown in hollow/orange symbols in Figure 50/appendix.

The metrics are shown for all buffer conditions in colour coded tables (Figure 51).
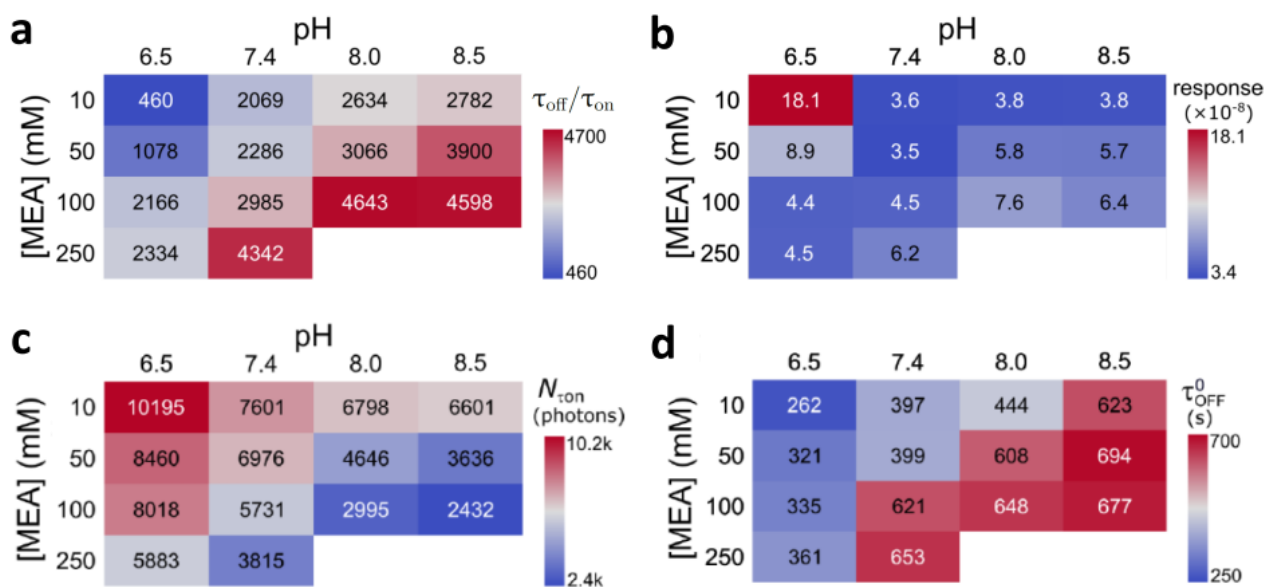
Figure 51 Summary tables of the calculated switching metrics for all measured buffer conditions. (a) The ratio τ_{OFF}/τ_{ON} must be as high as possible to avoid overlap of emitter in one frame. (b) The response of k_{ON} to variations in the illumination are an indicator of the need for flat illumination. (c) The photon budget $N_{\tau_{ON}}$ must be as high as possible to get the best localisation precision. (d) The thermal dark state lifetime τ_{OFF}^0 should be as long as possible to avoid overlapping emitters. Reprinted with permission (CC BY 4.0) from "Benchmarking Thiolate-Driven Photoswitching of Cyanine Dyes", J. Phys. Chem. B 2023, 127, 732-741". Copyright 2021, The Authors. Published By the American Chemical Society" (Herdly et al., 2023)

We can see how the buffer conditions influence the selected metrics. We observe that the metrics change in the same direction with increasing pH and MEA concentration.

The photon budget decreases with the pH and MEA concentration while τ_{OFF}^0 and τ_{OFF}/τ_{ON} increase with the pH and MEA concentration. The effect on the thermal OFF time agrees with the proton-assisted elimination of thiol mechanism demonstrated by Gidi et al (Gidi et al. 2020).

The response of k_{ON} was highest for low pH and MEA concentration and becomes relatively constant for other conditions.

τ_{OFF}/τ_{ON} is an important parameter for SMLM and it must be finely controlled to ensure that most of the fluorophores are in the dark state at any time during the imaging. This ensured that single emitters can be localised without overlap of their PSFs. High values are the goal for resolving densely labelled complex structures smaller than the diffraction limit. τ_{OFF}/τ_{ON} can be used to evaluate the maximum achievable resolution (Van De Linde et al. 2011; Cordes et al. 2010; Herdly et al. 2021b).

The duty cycle $\frac{\tau_{ON}}{\tau_{ON}+\tau_{OFF}}$ is almost equal to the inverse of the previous ratio and has been shown to be a good indicator of photoswitching quality (Dempsey et al. 2011).

τ_{OFF}/τ_{ON} is influenced by two competing mechanisms when the illumination intensity increases. An increase of the laser intensity will shorten the τ_{ON} as we can see in the centre of the field of view in Figure 49 column 1, benefiting the τ_{OFF}/τ_{ON} ratio. Conversely, an increase of the laser intensity will shorten $\tau_{OFF} = \frac{1}{k_{ON}}$ as we can see on Figure 49 column 2.

To resolve which effect affects the ratio, we look at Figure 49 column 3. The first effect has a stronger influence on the ratio and the higher laser intensity favours higher values for τ_{OFF}/τ_{ON}. At the same illumination intensity, we see an increase of τ_{OFF}/τ_{ON} for higher MEA concentration and pH.

5.4.3. Thiolate concentration as a metric simplifies the control of photoswitching in dSTORM

We observed that photoswitching metrics are influenced by pH and MEA concentration but previous studies showed that the influences of MEA is mediated by its anionic form, i.e. thiolate, and that its concentration is the proper metric to study photoswitching instead of the total MEA concentration (Heilemann et al. 2009; van de Linde et al. 2011; Gidi et al. 2020). Hence, we studied the previous results regarding the influence of the thiolate concentration as the main driving force.

To determine the thiolate concentration in each buffer, we can use the Henderson Hasselbach equation (Burner and Obinger 1997):

$$[RS^-] = \frac{[MEA]_0}{1 + 10^{pK_a - pH}} \tag{27}$$

Where $[RS^-]$ is the thiolate concentration ($mol \cdot L^{-1}$)

$[MEA]_0$ is the initial concentration of MEA in the buffer ($mol \cdot L^{-1}$). It corresponds to the sum of concentrations of the thiol and thiolate.

pK_a is a constant for an acid/base pair and it corresponds to the pH at which half of the molecules are deprotonated (here, the thiolate form).

To calculate the equation, we need the value of the pK_a. Several different values have been reported in the literature (8.19 (Serjeant and Dempsey 1979), 8.27 (Lide 2003), 8.31 (Avdeef and Brown 1984), 8.35 (Benesch and Benesch Reinhold 1955), 8.4 (Suwandaratne et al. 2016), 8.6 (Lundbald and Macdonald 2018), so MEA was titrated in switching buffer conditions by PWT and the pK_a value was measured at 8.353 $\pm$ 0.004 (Herdly et al. 2023). We calculated the dissociated base fraction of MEA at 1.4, 10.0, 30.7 and 58.4 % for pH 6.5, 7.4, 8.0 and 8.5, respectively. This in turn allowed the calculation of final thiolate

concentration in the 14 buffer conditions ranging from 0.14 to 58.38 mM (Table 7).

Table 7 pH dependant thiolate concentrations were calculated using equation (27)

pH- dependant Thiolate concentration (mM)		pH			
		6.5	7.4	8	8.5
[MEA](mM)	10	0.14	1.00	3.07	5.84
	50	0.69	5.01	15.36	29.19
	100	1.38	10.03	30.73	58.38
	250	3.46	25.06		

We then plotted the previous metrics in function of the thiolate concentration (Figure 52). By using a logarithmic scale on the thiolate concentration, we see a strong dependency of the metrics with thiolate concentration. The photon budget $N_{\tau_{ON}}$ decreased with the increased thiolate concentration following the mechanism of singlet quenching and increased dark state formation described before (Heilemann et al. 2009; Gidi et al. 2020).

The thermal OFF time τ_{OFF}^0 increased slowly with thiolate concentration up to 5 mM then increased sharply and reached a saturation above 20 mM. As demonstrated before, decreasing pH shortened the thermal OFF time because the thiol moiety can be released from the dark state in the presence of H^+ (Gidi et al. 2020). Independently of the pH, increasing thiolate concentrations lengthened the thermal OFF time. Further investigation is needed to understand this effect. The response of k_{ON} to illumination intensity was extracted from the linear fits for all conditions as shown in the plots in the Appendix. Figure 52(c) shows that for low concentration of thiolate, the fluorescence recovery rate is very sensitive to the illumination intensity independent of the pH. We see a 4-fold higher sensitivity for the buffer with 0.14 mM RS^- compared to 1.38 mM RS^- even though the pH is 6.5 in both cases.

Further research needs to investigate the underlying causes, but this encourages the use of
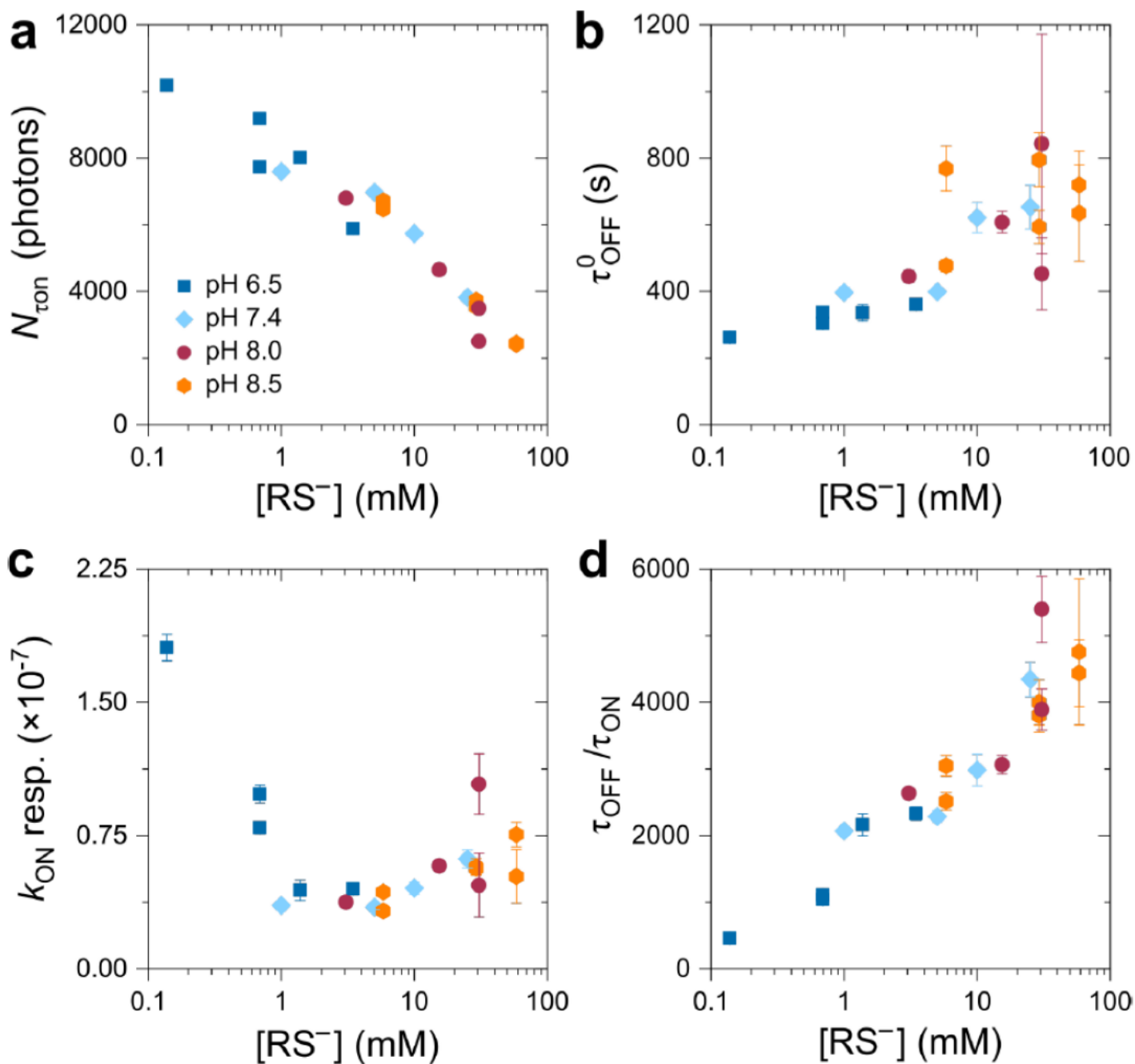
Figure 52 Switching metrics vary with the thiolate concentration in the switching buffer. (a) Photon budget $N_{\tau ON}$, (b) Thermal recovery time τ_{OFF}^0, (c) ON-switching rate response and τ_{OFF}/τ_{ON} as a function of thiolate concentrations. Reprinted with permission (CC BY 4.0) from "Benchmarking Thiolate-Driven Photoswitching of Cyanine Dyes", J. Phys. Chem. B 2023, 127, 732-741". Copyright 2021, The Authors. Published By the American Chemical Society" (Herdly et al., 2023)

at least 1 mM thiolate in the switching buffer to stabilize the OFF state and it supports the

use of homogeneous illumination for consistent photoswitching across the field of view. Above 1 mM thiolate, we cannot observe more effect of more thiolate on the recovery rate response to illumination intensity.

τ_{OFF}/τ_{ON} increased with the concentration of thiolate, following the model of thiolate directly promoting the formation of the dark state.

$N_{\tau_{ON}}$ and τ_{OFF}/τ_{ON} seem to be mostly influenced by the thiolate concentration, independently of the pH used to obtain the respective thiolate concentration, for example 250 mM MEA at pH 6.5 and 10 mM MEA at pH 8.0 contained 3.5 and 3.1 mM thiolate, respectively, and showed very close values for $N_{\tau_{ON}}$ and τ_{OFF}/τ_{ON}.

In SMLM, both the number of photons detected in each frame and the ratio of lifetimes τ_{OFF}/τ_{ON} are important parameters to optimize the image quality.

5.4.4. The trade-off between N_Det and τ_{OFF}/τ_{ON}

High N_Det contribute to better localisation precision (H. Li and Vaughan 2018; Shen et al. 2017) while τ_{OFF}/τ_{ON} must be high enough to limit the number of active fluorophores at any time, i.e. to statistically minimise PSF overlap (Van De Linde et al. 2011; Cordes et al. 2010). τ_{OFF}/τ_{ON} values must be even higher when samples are densely labelled to limit the pointillist artefacts that can be observed when labelling is too sparse.

Higher values for both metrics are synonymous with better SMLM results but because the trends are opposite with increasing thiolate concentrations (Figure 53(a)), an intermediate condition must be chosen. From experience, N_{Det} should be at the minimum 4000 photons and τ_{OFF}/τ_{ON} should be more than 2000.

To choose the ideal switching buffer on more precise conditions, we compared the resolution improvement for both metrics with regards to thiolate concentration.
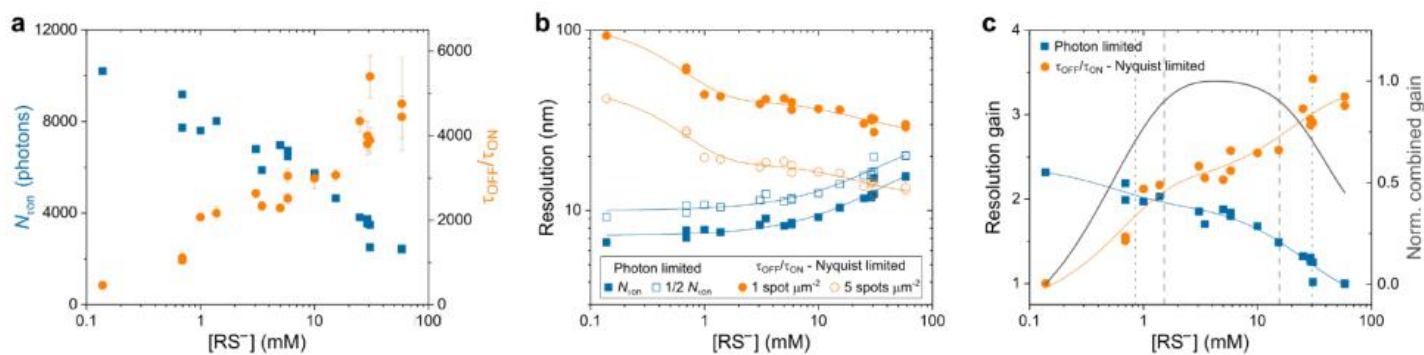
Figure 53 The resolution trade-off. (a) the photon budget decreases and τ_{OFF}/τ_{ON} increases with increasing thiolate concentrations. (b) Low thiolate concentrations alter the Nyquist structural resolution while high thiolate concentrations affect the localisation precision. (c) A trade-of can be found at thiolate concentrations of 1.5-15.6 mM in our experiments where the resolution is optimized. Reprinted with permission (CC BY 4.0) from "Benchmarking Thiolate-Driven Photoswitching of Cyanine Dyes", J. Phys. Chem. B 2023, 127, 732-741". Copyright 2021, The Authors. Published By the American Chemical Society" (Herdly et al., 2023)

For τ_{OFF}/τ_{ON}, the theoretical resolution was calculated from the highest tolerable active emitter density at one time. This is based of the Nyquist criterion that says that the sampling interval must be twice as fine as the desired resolution (Shroff et al. 2008). Previous studies report that most localisations software can manage an active emitter density of 1 $spot \cdot \mu m^{-2}$ and localisation software that have been optimized for high density can handle 5 $spot \cdot \mu m^{-2}$ (Sage et al. 2019). We use those two values here for the maximum tolerable active label density. On the other hand, the Nyquist criterion for 2D states that the structural resolution is $d_{2D} = \frac{2}{\sqrt{n}}$,with *n*, the label density. Here, we will calculate the effective label density by multiplying the active emitter density limits (1 and 5 respectively) by the τ_{OFF}/τ_{ON} ratio that describes the average proportion of active emitters at any time. We plot two curves (Figure 53(b), blue) to account for two active emitter density thresholds. On the other hand, the theoretical resolution that can be expected for N_{Det} photons is calculated according to equation (24) (Mortensen et al. 2010). The need for localisation algorithms that can work with high emitter densities is

189

highlighted here. For example, if we choose a target Nyquist resolution of 40 nm, this corresponds to a label density of 2500 μm^{-2}. To meet the localisation density thresholds, τ_{OFF}/τ_{ON} must be at least 2500 and 500 for standard and high-density localisation algorithms, respectively. This gives more room for buffer adjustments or resolution improvements if high-density localisation algorithms are available (Sage et al. 2019).

Recent developments (Helmerich et al. 2022) bring a new limit to resolution as it has been shown that in very densely labelled samples, fluorophores closer than 10 nm can participate in resonance energy transfers to dark state fluorophores, increasing the reactivation rate and reducing τ_{OFF} and, consequently, τ_{OFF}/τ_{ON}.

We observe in Figure 53(b) that photon limited resolution is smaller than the Nyquist resolution for thiolate concentrations below 30 mM. The photon limited resolution is also not influenced by low thiolate concentrations up to 20 mM where thiolate quenching of the singlet state impacts the photon emitting rate and N_{Det}. The Nyquist resolution is an order of magnitude larger for low thiolate concentration and improves sharply when small amounts of thiolate in the mM concentration range are added. The resolution was still improved for higher thiolate concentrations, though the impact was smaller.

We can use the Nyquist resolution and photon number resolution to define lower and upper bounds for the optimal buffer conditions.

We combined the resolution improvements for both resolutions in Figure 53(c). Double exponential functions were fitted to the data and the normalized sum of the fit show the combined gain of resolution. We place the limits of optimal buffer conditions within 90 % combined resolution improvement. This corresponds to thiolate concentrations of 1.5-15.6 mM. We note that it excludes the respective regions of strong adverse effects of the buffer conditions for each resolution calculations.

We propose this range of thiolate concentrations as a reference frame for buffer conditions

with Alexa 647.

Table 8 shows the conditions within the chosen boundaries among the conditions tested. We can see that the pH can be chosen over a wide range, allowing to adapt the buffer to target specific requirements of many research projects.

The choice of the exact buffer composition will also vary depending on the target structural parameters. On targets with dense structural details, a high label density is required to achieve the best resolution. Here, the τ_{OFF}/τ_{ON} will be the limiting factor and the switching buffer will be chosen towards the higher thiolate concentration limit.

Table 8 Summary of optimal (+), acceptable (o) and poor (-) buffer conditions regarding the photoswitching of Alexa647. We propose 6 combinations of MEA concentration and pH that correspond to the best resolutions in our experiments, they correspond to thiolate concentrations in the range 1.5-15.6 mM.

		pH			
		6.5	7.4	8	8.5
[MEA](mM)	10	-	o	+	+
	50	-	+	+	o
	100	o	+	-	-
	250	+	o		

+	Very good switching, more than 90% resolution gain
o	Usable switching, 70-90% resolution gain
-	Unsufficient switching quality

On the other hand, if the target is known to have a lower structural complexity, reduced thiolate concentrations could ensure shorter acquisition times and high localisation precision. Finally, low thiolate buffers would benefit the imaging of complex structures with super-resolution methods that study intensity fluctuations over time like SOFI (Dertinger et al. 2009) and SRRF (N. Gustafsson et al. 2016).

5.4.5. The role of the enzymatic oxygen scavenger system

Continuing this project, Peter Tinning studied the role of the enzymatic oxygen scavenger system used widely in dSTORM. His work was also presented in the same paper as the author's work presented in the current chapter.

5.4.6. Application to biological samples

The final validation of our study of photoswitching consisted of comparing two switching buffers on the imaging of biological samples.

We imaged the glucose transporter GLUT-4 in adipocyte cells located at the plasma membrane. The switching buffer contained 100 mM MEA and pH 7.4 and 8.0 respectively. According to the Henderson-Hasselbach equations, this corresponds to thiolate concentration of 10 and 31 mM respectively (Table 7).
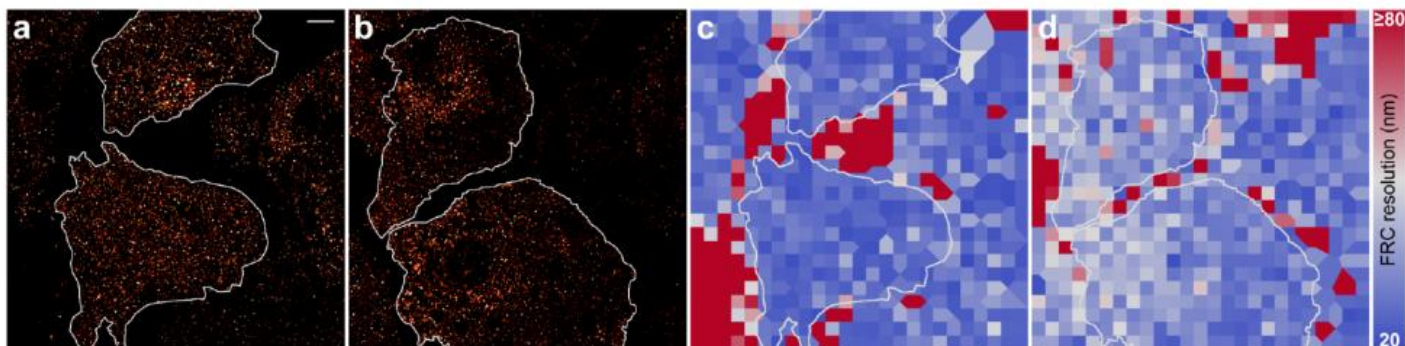
Figure 54 Application to biological samples Super resolution reconstructed image and the corresponding FRC resolution Map for (a,c) 100 mM MEA pH 7.4 and (b,d) 100 mM MEA pH 8.0. A small change in the pH can significatively modify the switching and alter the resolution. The average FRC resolution was 26.1 ± 3.1 and 26.4 ± 2.8 nm (median ± MAD) for the top and bottom cell in (a,c) and 35.1 ± 4.3 and 32.8 ± 5.0 nm for the top and bottom cell in (b,d). Reprinted with permission (CC BY 4.0) from "Benchmarking Thiolate-Driven Photoswitching of Cyanine Dyes", J. Phys. Chem. B 2023, 127, 732-741". Copyright 2021, The Authors. Published By the American Chemical Society" (Herdly et al., 2023)

To assess the real-life resolution of the imaging of the sample in both buffers (Figure 54), we calculated the FRC resolution and obtained average resolutions of 26 ± 3 and 34 ± 5 nm (median ± MAD) for pH 7.4 and 8.0, respectively. The better resolution at pH 7.4 corresponds to thiolate concentrations within the optimal range described above whereas a 0.6 point increase of the pH leads to a 3-fold increases of the thiolate concentration and shows the degradation of the photoswitching and consequently the resolution when the switching buffer is outside of the proposed optimal thiolate concentrations (1.5-15.6 mM).

5.5 Conclusion

The ultimate goal of SMLM methods development is to provide optimized tools to investigate biological questions with the best accuracy. To do so, we must understand how the multiple parameters of SMLM affect the results of imaging and investigate the boundaries of optimal parameters. We contributed to this effort in this project to better understand how the photoswitching buffer composition impacts on photoswitching and consequently on the final image quality.

We used a MEMS mirror originally introduced in our setup for homogeneous illumination (see chapter 4) and repurposed it to create a tuneable illumination intensity gradient in our sample. Thus, allowing the recording of switching at different illumination intensities in a single acquisition.

We studied 14 combinations of pH and MEA concentrations to investigate their respective impact on photoswitching. Their impact appears to be summarised by the thiolate concentration as a one-dimension parameter that is dependent on the two other parameters.

We demonstrated that small changes to thiolate concentration can strongly penalize the

resolution of SMLM. Low concentrations lead to small τ_{OFF}/τ_{ON} and limit the resolution according to the sampling analysis based on Nyquist's criterion. High concentrations reduce N_{Det} and alter the localisation precision, and consequently the maximum achievable resolution as determined by the localisation precision. We propose the use of a range of thiolate concentrations of 1.5-15.6 mM for which we observed >90% of the resolution improvement. Within this range of thiolate concentrations, the MEA concentration and pH can be varied to accommodate other imperatives of experiments such as the combination of cyanine dyes with other pH sensitive dyes or pH sensitive samples.

The acidification of the buffer by the GGC system during experiments can have adverse effects on the thiolate concentration and consequently on resolution. We quantified the acidification of our buffer and the impact on photoswitching and theoretical resolution. We propose the systematic sealing of completely filled buffer chambers as a standard for the preparation of SMLM samples as it limits the loss of resolution to acceptable levels for 20 h compared to the rapid deterioration of resolution in an open sample chamber within 4 h.

Finally, the buffer should be adjusted to the sample that is imaged as structure complexity, time constraints and other factors might demand buffer optimisation. Hence, the opportunity to change the buffer after starting the imaging could be beneficial for on-the-fly buffer tuning (Almada et al. 2019).

Conclusion

This thesis work described the building and optimisation of a multipurpose microscopy setup primarily designed for dSTORM but capable of adapting to other future microscopy projects. This project covers several components of the microscopy process such as buffer chemistry, microscopy hardware and data analysis. Modularity was a central idea of the project. Each component was thought as a module that could be improved independently and could be used or removed in future projects.

This project started with the development of a microscopy platform to meet the requirements of a wide range of microscopy experiments with its TIRF ability, 3D capability and improved stability of the nosepiece. 3D SMLM was demonstrated on the setup and lenses allowing 3D as well as data analysis were optimised to improve the performance of 3D-SMLM. The adaptability of this microscopy setup will allow several microscopy projects to share a single platform that cares to the specific requirements of each method. Future improvements could include more complex PSF engineering methods to improve 3D axial resolution and range. Controlling the use of one or another module by computer (widefield, Hilo or TIRF illumination for example) would be beneficial if multiple projects must use the microscope with different requirements. Combining this platform with other super-resolution methods would allow even more flexibility in future microscopy projects. Integrating microfluidics for sample treatment or switching buffer adjustment during the acquisition would be a major improvement in terms of possible experiments for biology research applications. Finally, computer-driven live correction of drift and focus would allow longer acquisition times and more reproducible imaging performance.

Multi-channel dSTORM usually rests on the use of fluorophores of different emission wavelength which leads to chromatic aberrations that need to be corrected. In this work, we presented a novel approach to separate channels according to the emission intensity of fluorophores at the same wavelength. We demonstrated quenching in our probe in spectroscopic measurements but could not separate channels in single molecule imaging experiments. This lack of separation was attributed to a lack of illumination uniformity and limited control of the quencher switching. Future developments could study other dark quenchers and how they behave in the switching buffer. Other quenching methods should also be studied such as Metal Induced Energy Transfer (MIET). Modifying or exploring alternatives to the DNA scaffold could also stabilise the relative orientation and distance between donor and acceptor in our probe which would narrow the intensity distributions and ameliorate the channel separation. Fluorescence Lifetime Imaging Microscopy (FLIM) could be an alternative for separating channels in our FRET based approach as FRET and other energy transfers also affect the fluorescence lifetime of the donor fluorophore.

A prominent issue of microscopy in general and SMLM in particular is the homogeneous illumination of wide fields of view. Gaussian illumination that is often used generates missed localisations in the corners of the field of view, variations of the photoswitching kinetics and achievable resolution across the field of view. We described the use of a single MEMS mirror to effectively and easily establish a homogeneous illumination across the field of view that matched the performance of a commercially available optical beam shaping device, the piShaper. Our MEMS approach had the advantage to produce a squarish illumination pattern that better matched the FOV shape than the circular pishaper pattern. Additionally, the MEMS features a higher adaptability as it can be switched

between flat-illumination, Gaussian illumination or an intermediate intensity gradient by changing the driving electrical signal. Future work on this project will aim at improving the reflectivity of the MEMS by adding a metal or dielectric coating. A live control of the MEMS resonance frequencies would improve the quality of the flat illumination for different laser powers. Until now, changing the laser power required individual calibration to measure resonance frequencies that change with the laser induced heating of the MEMS. Adding other lasers of a different wavelengths would increase the flexibility of the microscopy platform. The small footprint and low control requirements of the MEMS make it a good candidate to provide flat illumination in "black-box" microscopy systems that provide easy-access to microscopy for researchers that are not microscopy experts.

Cyanine photoswitching in dSTORM is controlled by thiols reducing agents and oxygen in the switching buffer and the illumination. We systematically studied 14 combinations of pH and thiopl concentrations to better understand Alexa 647 photswitching. Thiolate concentration which depends on both pH and thiol concentration was shown to be the main parameter controlling the ON and OFF switching kinetics. We also confirmed the relation between photoswitching kinetics, the number of detected photons per localisation and resolution. This work can help improve switching buffer and serve as an example to benchmark buffer compositions with established metrics that directly translate super resolution performance.

Future developments should explore microfluidics to allow providing fresh buffer during long acquisition sessions to ensure constant switching kinetics. On-the-fly adjustments of the buffer composition would help to adapt the photoswitching kinetics to the sample's density and complexity for optimal active emitter density. The benchmarking protocol with its analysis routines could be applied to other fluorophores and other photoswitching

buffer systems. Benchmarking the dark quenchers used in ou multi-channel probes could help better understand their interaction with the switching buffer that is necessary for Alexa 647 switching. This could lead to a better choice of quencher to improve the performance of our multi-channel approach.

This work demonstrated that many factors contribute to super-resolution microscopy performance from hardware to buffer condition and data analysis. We provided various approaches to benchmark several of those factor to incrementaly improve our SMLM platform.

Future work on the platform will include the validation of the microscope on reference biological samples such as nuclear pore complexes or microtubules of the cytoskeleton. Combining SMLM with other super-resolution methods such as SIM or STED would improve the adaptability of our microscopy platform to the requirements of application projects as each method has advantages and limitations. Further, we could develop protocols to combine SMLM with electronic microscopy to combine information from the two methods to explore complex systems.

Our understanding of the many factors influencing the performance of SMLM could drive a project to design a portable SMLM microscope that could be used for specific observation in clinical or in-the-field context.

To conclude, this work was a project involving several fields of science to better understand and improve how we design and use SMLM microscopes. Several improvements were described and they open many new improvements opportunities.

Bibliography

Almada, Pedro, Pedro M. Pereira, Siân Culley, Ghislaine Caillol, Fanny Boroni-Rueda, Christina L. Dix, Guillaume Charras, et al. 2019. 'Automating Multimodal Microscopy with NanoJ-Fluidics'. *Nature Communications* 10 (1). Nature Publishing Group. doi:10.1038/s41467-019-09231-9.

Andor, Oxford Instruments. n.d. 'EMCCDs for Low-Light Spectroscopy'. https://andor.oxinst.com/learning/view/article/emccd-technology-in-spectroscopy.

Andronov, Leonid, Rachel Genthial, Didier Hentsch, and Bruno P Klaholz. 2022. 'SplitSMLM, a Spectral Demixing Method for High-Precision Multi-Color Localization Microscopy Applied to Nuclear Pore Complexes'. *Communications Biology* 5 (1). Springer US. doi:10.1038/s42003-022-04040-1.

Arganda-Carreras, Ignacio, Carlos O S Sorzano, Roberto Marabini, José María Carazo, Carlos Ortiz-De-Solorzano, and Jan Kybic. 2006. 'Consistent and Elastic Registration of Histological Sections Using Vector-Spline Regularization'. In *Computer Vision Approaches to Medical Image Analysis. CVAMIA*. Springer. doi:https://doi.org/10.1007/11889762_8.

Avdeef, Alex, and Jessica A Brown. 1984. 'Cadmium Binding by Biological Ligands. 2 [1]. Formation of Protonated and Polynuclear Complexes between Cadmium and 2-Mercaptoethylamine'. *Inorganica Chimica Acta* 91: 61–74.

Bakas, Spyridon, Deepak Uttamchandani, Hiroshi Toshiyoshi, and Ralf Bauer. 2021. 'MEMS Enabled Miniaturized Light-Sheet Microscopy with All Optical Control'. *Scientific Reports* 11 (1). Nature Research. doi:10.1038/s41598-021-93454-8.

Balzarotti, Francisco, Yvan Eilers, Klaus C Gwosch, Arvid H Gynnå, Volker Westphal, Fernando D Stefani, Johan Elf, and Stefan W Hell. 2017. 'Nanometer Resolution Imaging and Tracking of Fluorescent Molecules with Minimal Photon Fluxes'. *Science* 355: 606–12. doi:10.1126/science.aak9913.

Banterle, Niccolò, Khanh Huy Bui, Edward A Lemke, and Martin Beck. 2013. 'Fourier Ring Correlation as a Resolution Criterion for Super-Resolution Microscopy'. *Journal of Structural Biology* 183 (3): 363–67. doi:10.1016/j.jsb.2013.05.004.

Bates, Mark, Timothy R Blosser, and Xiaowei Zhuang. 2005. 'Short-Range Spectroscopic Ruler Based on a Single-Molecule Optical Switch'. *Phys Rev Lett* 94 (10): 108101.

Bates, Mark, Bo Huang, Graham T. Dempsey, and Xiaowei Zhuang. 2007. 'Multicolor Super-Resolution Imaging with Photo-Switchable Fluorescent Probes'. *Science* 317 (5845): 1749–53. doi:10.1126/science.1146598.

Bauer, Ralf, Alan Paterson, Caspar Clark, Deepak Uttamchandani, and Walter Lubeigt. 2015. 'Output Characteristics of Q-Switched Solid-State Lasers Using Intracavity MEMS Micromirrors'. *IEEE Journal of Selected Topics in Quantum Electronics* 21 (1). doi:10.1109/JSTQE.2014.2345700.

Becker, Wolfgang, and Axel Bergmann. 2023. *A Common Mistake in Lifetime-Based FRET Measurement.*

Benesch, Ruth E., and Benesch Reinhold. 1955. 'The Acid Strength of the -SH Group in Cysteine and Related Compounds'. *J. Am. Chem. Soc.* 77.

Betzig, Eric, George H Patterson, Rachid Sougrat, O Wolf Lindwasser, Scott Olenych, Juan S Bonifacino, Michael W Davidson, Jennifer Lippincott-Schwartz, and Harald F Hess. 2006. 'Imaging Intracellular Fluorescent Proteins at Nanometer Resolution'. *Science* 313 (5793): 1642–45. doi:10.1126/science.1127344.

Bossi, Mariano, Jonas Föiling, Vladimir N Belov, Vadim P Boyarskiy, Rebecca Medda, Alexander Egner, Christian Eggeling, Andreas Schönle, and Stefan W Hell. 2008. 'Multicolor Far-Field Fluorescence Nanoscopy through Isolated Detection of Distinct Molecular Species'. *Nano Letters* 8 (8): 2463–68. doi:10.1021/nl801471d.

'Broadband Polarizing Beamsplitter Cubes in 30 Mm Cage Cubes'. n.d. https://www.thorlabs.com/newgrouppage9.cfm?objectgroup_id=4137&pn=CCM1-PBS251/M.

Brochon, J-C. 1999. 'Pulse 6 Brochon'.

Broeken, Jordi, Hannah Johnson, Diane S. Lidke, Sheng Liu, Robert P.J. Nieuwenhuizen, Sjoerd Stallinga, Keith A. Lidke, and Bernd Rieger. 2015. 'Resolution Improvement by 3D Particle Averaging in Localization Microscopy'. *Methods and Applications in Fluorescence* 3 (1). IOP Publishing Ltd. doi:10.1088/2050-6120/3/1/014003.

Burner, U., and C. Obinger. 1997. 'Transient-State and Steady-State Kinetics of the Oxidation of Aliphatic and Aromatic Thiols by Horseradish Peroxidase'. *FEBS Letters* 411 (2–3): 269–74. doi:10.1016/S0014-5793(97)00713-8.

Cabriel, Clément, Nicolas Bourg, Pierre Jouchet, Guillaume Dupuis, Christophe Leterrier, Aurélie Baron, Marie Ange Badet-Denisot, Boris Vauzeilles, Emmanuel Fort, and Sandrine Lévêque-Fort. 2019. 'Combining 3D Single Molecule Localization Strategies

for Reproducible Bioimaging'. *Nature Communications* 10 (1). Springer US: 1–10. doi:10.1038/s41467-019-09901-8.

Cella Zanacchi, Francesca, Zeno Lavagnino, Michela Perrone Donnorso, Alessio Del Bue, Laura Furia, Mario Faretta, and Alberto Diaspro. 2011. 'Live-Cell 3D Super-Resolution Imaging in Thick Biological Samples'. *Nature Methods* 8 (12): 1047–50. doi:10.1038/nmeth.1744.

Chen, Shih-Ya, Felix Bestvater, Wladimir Schaufler, Rainer Heintzmann, and Christoph Cremer. 2018. 'Patterned Illumination Single Molecule Localization Microscopy (PiSMLM): User Defined Blinking Regions of Interest'. *Optics Express* 26 (23). The Optical Society: 30009. doi:10.1364/oe.26.030009.

Chen, Sung Liang, Zhixing Xie, L. Jay Guo, and Xueding Wang. 2013. 'A Fiber-Optic System for Dual-Modality Photoacoustic Microscopy and Confocal Fluorescence Microscopy Using Miniature Components'. *Photoacoustics* 1 (2): 30–35. doi:10.1016/j.pacs.2013.07.001.

Chung, Jinkyoung, Uidon Jeong, Dokyung Jeong, Seokran Go, and Doory Kim. 2021. 'Development of a New Approach for Low-Laser-Power Super-Resolution Fluorescence Imaging'. *Analytical Chemistry*. doi:10.1021/acs.analchem.1c01047.

Clegg, Robert M, Alastair I H Murchiet, Annelies Zechel, and David M J Lilleyt. 1993. *Observing the Helical Geometry of Double-Stranded DNA in Solution by Fluorescence Resonance Energy Transfer. Proc. Natl. Acad. Sci. USA*. Vol. 90. https://www.pnas.org.

Cnossen, Jelmer, Tao Ju Cui, Chirlmin Joo, and Carlas Smith. 2021. 'Drift Correction in Localization Microscopy Using Entropy Minimization'. *Optics Express* 29 (18): 27961. doi:10.1364/oe.426620.

Cnossen, Jelmer, Taylor Hinsdale, Rasmus Thorsen, Marijn Siemons, Florian Schueder, Ralf Jungmann, Carlas S. Smith, Bernd Rieger, and Sjoerd Stallinga. 2020. 'Localization Microscopy at Doubled Precision with Patterned Illumination'. *Nature Methods* 17 (1). Nature Research: 59–63. doi:10.1038/s41592-019-0657-7.

Coltharp, Carla, Xinxing Yang, and Jie Xiao. 2014. 'Quantitative Analysis of Single-Molecule Superresolution Images'. *Current Opinion in Structural Biology*. doi:10.1016/j.sbi.2014.08.008.

Cordes, Thorben, Mathias Strackharn, Stefan W. Stahl, Wolfram Summerer, Christian Steinhauer, Carsten Forthmann, Elias M. Puchner, Jan Vogelsang, Hermann E. Gaub, and Philip Tinnefeld. 2010. 'Resolving Single-Molecule Assembled Patterns with

Superresolution Blink-Microscopy'. *Nano Letters* 10 (2): 645–51. doi:10.1021/nl903730r.

Cowen, Allen, Greg Hames, Konstantin Glukh, and Busbee Hardy. 2014. *PiezoMUMPs ™ Design Handbook a MUMPs® Process*.

Culley, Siân, David Albrecht, Caron Jacobs, Pedro Matos Pereira, Christophe Leterrier, Jason Mercer, and Ricardo Henriques. 2018a. 'Quantitative Mapping and Minimization of Super-Resolution Optical Imaging Artifacts'. *Nature Methods* 15 (4). Nature Publishing Group: 263–66. doi:10.1038/nmeth.4605.

———. 2018b. 'Quantitative Mapping and Minimization of Super-Resolution Optical Imaging Artifacts Supp Inf'. *Nature Methods* 15 (4). Nature Publishing Group: 263–66. doi:10.1038/nmeth.4605.

Culley, Siân, Kalina L. Tosheva, Pedro Matos Pereira, and Ricardo Henriques. 2018. 'SRRF: Universal Live-Cell Super-Resolution Microscopy'. *The International Journal of Biochemistry & Cell Biology* 101 (August). Pergamon: 74–79. doi:10.1016/J.BIOCEL.2018.05.014.

Dani, Adish, Bo Huang, Joseph Bergan, Catherine Dulac, and Xiaowei Zhuang. 2010. 'Superresolution Imaging of Chemical Synapses in the Brain'. *Neuron* 68 (5): 843–56. doi:10.1016/j.neuron.2010.11.021.

Dempsey, Graham T, Mark Bates, Walter E Kowtoniuk, David R Liu, Roger Y Tsien, and Xiaowei Zhuang. 2009. 'Photoswitching Mechanism of Cyanine Dyes'. *Journal of the American Chemical Society* 131 (51): 18192–93. doi:10.1021/ja904588g.

Dempsey, Graham T., Joshua C. Vaughan, Kok Hao Chen, Mark Bates, and Xiaowei Zhuang. 2011. 'Evaluation of Fluorophores for Optimal Performance in Localization-Based Super-Resolution Imaging'. *Nature Methods* 8 (12): 1027–40. doi:10.1038/nmeth.1768.

Dertinger, T, R Colyer, G Iyer, S Weiss, and J Enderlein. 2009. 'Fast, Background-Free, 3D Super-Resolution Optical Fluctuation Imaging (SOFI)'. *PNAS* 106 (52): 22287–92. doi:10.1073/pnas.0907866106.

Deschamps, Joran, Andreas Rowald, and Jonas Ries. 2016. 'Efficient Homogeneous Illumination and Optical Sectioning for Quantitative Single-Molecule Localization Microscopy'. *Optics Express* 24 (24): 28080. doi:10.1364/oe.24.028080.

Diekmann, Robin, Maurice Kahnwald, Andreas Schoenit, Joran Deschamps, Ulf Matti, and Jonas Ries. 2020. 'Optimizing Imaging Speed and Excitation Intensity for Single

Molecule Localization Microscopy'. *Nature Methods* 17 (9): 909–12. doi:10.1038/s41592-020-0918-5.Optimizing.

Dittrich, P.S., and P. Schwille. 2001. 'Photobleaching and Stabilization of Fluorophores Used for Single-Molecule Analysis with One- and Two-Photon Excitation'. *Applied Physics B* 73 (8): 829–37. doi:10.1007/s003400100737.

Dominic, Helmerich. 2017. *Intensity-Based Multi-Colour Localisation Microscopy*.

Douglass, Kyle M., Christian Sieben, Anna Archetti, Ambroise Lambert, and Suliana Manley. 2016. 'Super-Resolution Imaging of Multiple Cells by Optimized Flat-Field Epi-Illumination'. *Nature Photonics* 10 (11). Nature Publishing Group: 705–8. doi:10.1038/nphoton.2016.200.

Eggeling, C., J. Widengren, R. Rigler, and C. A. M. Seidel. 1998. 'Photobleaching of Fluorescent Dyes under Conditions Used for Single-Molecule Detection: Evidence of Two-Step Photolysis'. *Analytical Chemistry* 70 (13): 2651–59. doi:10.1021/ac980027p.

Ehmann, Nadine, Sebastian van de Linde, Amit Alon, Dmitrij Ljaschenko, Xi Zhen Keung, Thorge Holm, Annika Rings, et al. 2014. 'Quantitative Super-Resolution Imaging of Bruchpilot Distinguishes Active Zone States'. *Nature Communications* 5. Nature Publishing Group: 1–12. doi:10.1038/ncomms5650.

Endesfelder, Ulrike, Kieran Finan, Seamus J. Holden, Peter R. Cook, Achillefs N. Kapanidis, and Mike Heilemann. 2013. 'Multiscale Spatial Organization of RNA Polymerase in Escherichia Coli'. *Biophysical Journal* 105 (1): 172–81. doi:10.1016/j.bpj.2013.05.048.

Ernst Abbe. 1874. 'A Contribution to the Theory of the Microscope, and the Nature of Microscopic Vision'. Translated by H. E. Fripp. *Proceedings of the Bristol Naturalists' Society* 1: 200–261.

Fazekas, Frank J, Thomas R Shaw, Sumin Kim, Ryan A Bogucki, and Sarah L Veatch. 2021. 'A Mean Shift Algorithm for Drift Correction in Localization Microscopy'. *Biophysical Reports* 1 (1). Elsevier. doi:10.1016/j.bpr.2021.100008.

Förster, Th. 1948. 'Zwischenmolekulare Energiewanderung Und Fluoreszenz'. *Annalen Der Physik* 437 (1–2): 55–75. doi:https://doi.org/10.1002/andp.19484370105.

Förster, Theodor. 2012. 'Energy Migration and Fluorescence'. *Journal of Biomedical Optics* 17 (1). SPIE-Intl Soc Optical Eng: 011002. doi:10.1117/1.jbo.17.1.011002.

Frahm, Lars. 2016. 'Stochastic Modeling of Photoswitchable Fluorophores for Quantitative Superresolution Microscopy'. Gottingen Graduate School for Neurosciences,

Biophysics, and Molecular Biosciences. https://pdfs.semanticscholar.org/b598/ed21a0e318dc02cc9a4e8c312ee110f889e4.pdf.

Franke, Christian, Tomáš Chum, Zuzana Kvíčalová, Daniela Glatzová, Gregor Jörg Gentsch, Alvaro Rodriguez, Dominic A Helmerich, et al. 2022. 'Approach to Map Nanotopography of Cell Surface Receptors'. *Communications Biology* 5 (1): 1–16. doi:10.1038/s42003-022-03152-y.

Franke, Christian, Markus Sauer, and Sebastian van de Linde. 2017. 'Photometry Unlocks 3D Information from 2D Localization Microscopy Data'. *Nature Methods* 14 (1): 41–44. doi:10.1038/nmeth.4073.

Franke, Christian, Markus Sauer, and Sebastian Van De Linde. 2017. 'Photometry Unlocks 3D Information from 2D Localization Microscopy Data'. *Nature Methods* 14 (1). Nature Publishing Group: 41–44. doi:10.1038/nmeth.4073.

Funatsu, Takashi, Yoshie Harada, Makio Tokunaga, Kiwamu Saito, and Toshio Yanagida. 1995. 'Imaging of Single Fluorescent Molecules and Individual ATP Turnovers by Single Myosin Molecules in Aqueous Solution'. *Nature* 374: 555–59. doi:10.1038/374555a0.

Gao, Lan, Junling Chen, Jing Gao, Hongda Wang, and Wenyong Xiong. 2017. 'Super-Resolution Microscopy Reveals the Insulin-Resistanceregulated Reorganization of GLUT4 on Plasma Membranes'. *Journal of Cell Science* 130 (2). Company of Biologists Ltd: 396–405. doi:10.1242/jcs.192450.

Gidi, Yasser, Liam Payne, Viktorija Glembockyte, Megan S. Michie, Martin J. Schnermann, and Gonzalo Cosa. 2020. 'Unifying Mechanism for Thiol-Induced Photoswitching and Photostability of Cyanine Dyes'. *Journal of the American Chemical Society* 142 (29). American Chemical Society: 12681–89. doi:10.1021/jacs.0c03786.

Granger, Brian E., and Fernando Perez. 2021. 'Jupyter: Thinking and Storytelling with Code and Data'. *Computing in Science and Engineering* 23 (2). IEEE Computer Society: 7–14. doi:10.1109/MCSE.2021.3059263.

Grimm, Jonathan B., Brian P. English, Jiji Chen, Joel P. Slaughter, Zhengjian Zhang, Andrey Revyakin, Ronak Patel, et al. 2015. 'A General Method to Improve Fluorophores for Live-Cell and Single-Molecule Microscopy'. *Nature Methods* 12 (3). Nature Publishing Group: 244–50. doi:10.1038/nmeth.3256.

Grimm, Jonathan B, Brian P English, Heejun Choi, Anand K Muthusamy, Brian P Mehl, Peng

Dong, Timothy A Brown, et al. 2016. 'Bright Photoactivatable Fluorophores for Single-Molecule Imaging'. *Nature Methods* 13 (12): 985–88. doi:10.1038/nmeth.4034.

Gu, Lusheng, Yuanyuan Li, Shuwen Zhang, Yanhong Xue, Weixing Li, Dong Li, Tao Xu, and Wei Ji. 2019. 'Molecular Resolution Imaging by Repetitive Optical Selective Exposure'. *Nature Methods* 16 (11). Nature Publishing Group: 1114–18. doi:10.1038/s41592-019-0544-2.

Gustafsson, Mats G.L., Lin Shao, Peter M. Carlton, C. J.Rachel Wang, Inna N. Golubovskaya, W. Zacheus Cande, David A. Agard, and John W. Sedat. 2008. 'Three-Dimensional Resolution Doubling in Wide-Field Fluorescence Microscopy by Structured Illumination'. *Biophysical Journal* 94 (12). Biophysical Society: 4957–70. doi:10.1529/biophysj.107.120345.

Gustafsson, Nils, Siân Culley, George Ashdown, Dylan M. Owen, Pedro Matos Pereira, and Ricardo Henriques. 2016. 'Fast Live-Cell Conventional Fluorophore Nanoscopy with ImageJ through Super-Resolution Radial Fluctuations'. *Nature Communications* 7 (August). Nature Publishing Group. doi:10.1038/ncomms12471.

Gyongy, Istvan, Amy Davies, Neale A W Dutton, Rory R Duncan, Colin Rickman, Robert K Henderson, and Paul A Dalgarno. 2016. 'Smart-Aggregation Imaging for Single Molecule Localisation with SPAD Cameras'. *Scientific Reports* 6. Nature Publishing Group. doi:10.1038/srep37349.

Gyongy, Istvan, Amy Davies, Benjamin Gallinet, Neale A W Dutton, Rory R Duncan, Colin Rickman, Robert K Henderson, and Paul A Dalgarno. 2018. 'Cylindrical Microlensing for Enhanced Collection Efficiency of Small Pixel SPAD Arrays in Single-Molecule Localisation Microscopy'. *Optics Express* 26 (3): 2280. doi:10.1364/oe.26.002280.

Ha, Taekjip, and Philip Tinnefeld. 2012. 'Photophysics of Fluorescent Probes for Single-Molecule Biophysics and Super-Resolution Imaging'. *Annual Review of Physical Chemistry*. Annual Reviews Inc. doi:10.1146/annurev-physchem-032210-103340.

Harley, Iain James. 2020. 'Optimisation of Single-Molecule Localisation Microscopy Submitted in Partial Fulfilment for the Degree of Msc Nanoscience'.

Hebisch, E, E Wagner, V Westphal, J J Sieber, and S E Lehnart. 2017. 'A Protocol for Registration and Correction of Multicolour STED Superresolution Images'. *Journal of Microscopy* 267 (2): 160–75. doi:10.1111/jmi.12556.

Heilemann, Mike, Sebastian van de Linde, Anindita Mukherjee, and Markus Sauer. 2009. 'Super-Resolution Imaging with Small Organic Fluorophores'. *Angewandte Chemie -*

International Edition 48 (37): 6903–8. doi:10.1002/anie.200902073.

Heilemann, Mike, Sebastian van de Linde, Mark Schüttpelz, Robert Kasper, Britta Seefeldt, Anindita Mukherjee, Philip Tinnefeld, and Markus Sauer. 2008. 'Subdiffraction-Resolution Fluorescence Imaging with Conventional Fluorescent Probes'. *Angewandte Chemie - International Edition* 47 (33): 6172–76. doi:10.1002/anie.200802376.

Heilemann, Mike, Sebastian Van De Linde, Mark Schüttpelz, Robert Kasper, Britta Seefeldt, Anindita Mukherjee, Philip Tinnefeld, and Markus Sauer. 2008. 'Subdiffraction-Resolution Fluorescence Imaging with Conventional Fluorescent Probes'. *Angewandte Chemie - International Edition* 47 (33): 6172–76. doi:10.1002/anie.200802376.

Heilemann, Mike, Emmanuel Margeat, Robert Kasper, Markus Sauer, and Philip Tinnefeld. 2005. 'Carbocyanine Dyes as Efficient Reversible Single-Molecule Optical Switch'. *Journal of the American Chemical Society* 127 (11): 3801–6. doi:10.1021/ja044686x.

Hell, Stefan, and Ernst H K Stelzer. 1992. 'Properties of a 4Pi Confocal Fluorescence Microscope'. *Journal of the Optical Society of America A* 9 (12): 2159. doi:10.1364/josaa.9.002159.

Helmerich, Dominic A., Gerti Beliu, Danush Taban, Mara Meub, Marcel Streit, Alexander Kuhlemann, Sören Doose, and Markus Sauer. 2022. 'Photoswitching Fingerprint Analysis Bypasses the 10-Nm Resolution Barrier'. *Nature Methods* 19 (8). Nature Research: 986–94. doi:10.1038/s41592-022-01548-6.

Henriques, Ricardo, Mickael Lelek, Eugenio F. Fornasiero, Flavia Valtorta, Christophe Zimmer, and Musa M. Mhlanga. 2010. 'QuickPALM: 3D Real-Time Photoactivation Nanoscopy Image Processing in ImageJ'. *Nature Methods*. doi:10.1038/nmeth0510-339.

Herdly, Lucas, Paul Janin, Ralf Bauer, and Sebastian van de Linde. 2021a. 'Tuneable Wide-Field Illumination and Single-Molecule Photoswitching with a Single MEMS Mirror', June. doi:10.1101/2021.06.08.447519.

———. 2021b. 'Tunable Wide-Field Illumination and Single-Molecule Photoswitching with a Single MEMS Mirror'. *ACS Photonics* 8 (9). American Chemical Society: 2728–36. doi:https://doi.org/10.1021/acsphotonics.1c00843.

Herdly, Lucas, Peter W. Tinning, Angéline Geiser, Holly Taylor, Gwyn W. Gould, and Sebastian van de Linde. 2022. 'Benchmarking Thiolate-Driven Photoswitching of Cyanine Dyes'. *BioRxiv*. doi:https://doi.org/10.1101/2022.09.15.507984.

Herdly, Lucas, Peter W Tinning, Angéline Geiser, Holly Taylor, Gwyn W Gould, and

Sebastian van de Linde. 2023. 'Benchmarking Thiolate-Driven Photoswitching of Cyanine Dyes'. *Journal of Physical Chemistry B* 127 (3): 732–41. doi:10.1021/acs.jpcb.2c06872.

Hess, Samuel T, Thanu P K Girirajan, and Michael D Mason. 2006. 'Ultra-High Resolution Imaging by Fluorescence Photoactivation Localization Microscopy'. *Biophysical Journal* 91 (11): 4258–72. doi:10.1529/biophysj.106.091116.

Holden, Seamus J., Stephan Uphoff, Johannes Hohlbein, David Yadin, Ludovic Le Reste, Oliver J. Britton, and Achillefs N. Kapanidis. 2010. 'Defining the Limits of Single-Molecule FRET Resolution in TIRF Microscopy'. *Biophysical Journal* 99 (9). Biophysical Society: 3102–11. doi:10.1016/j.bpj.2010.09.005.

Holzmeister, Phil, Andreas Gietl, and Philip Tinnefeld. 2014. 'Geminate Recombination as a Photoprotection Mechanism for Fluorescent Dyes'. *Angewandte Chemie - International Edition* 53 (22). Wiley-VCH Verlag: 5685–88. doi:10.1002/anie.201310300.

Hong, Sung-Hye, and Wolfgang Maret. 2003. 'A Fluorescence Resonance Energy Transfer Sensor for the β-Domain of Metallothionein'. *Proceedings of the National Academy of Sciences* 100 (5): 2255–60. doi:10.1073/pnas.0438005100.

Horiba Scientific. n.d. 'Horiba DAS6 User Guide 6.7'.

'Https://Www.Originlab.Com/Origin'. n.d. *Https://Www.Originlab.Com/Origin*.

Huang, Bo, Wenqin Wang, Mark Bates, and Xiaowei Zhuang. 2008. 'Three-Dimensional Super-Resolution Imaging by Stochastic Optical Reconstruction Microscopy'. *Science* 319 (5864): 810–13. doi:10.1126/science.1153529.

Ibrahim, Khalid A., Dora Mahecic, and Suliana Manley. 2020. 'Characterization of Flat-Fielding Systems for Quantitative Microscopy'. *Optics Express* 28 (15). Optica Publishing Group: 22036. doi:10.1364/oe.395900.

Jablonski, A. 1933. 'Efficiency of Anti-Stokes Fluorescence in Dyes'. *Nature*, 839–40.

Janin, Paul, Ralf Bauer, Paul Griffin, Erling Riis, and Deepak Uttamchandani. 2019. 'Fast Piezoelectric Scanning MEMS Mirror for 1D Ion Addressing'. In *2019 International Conference on Optical MEMS and Nanophotonics (OMN), Daejeon, Korea (South)*, 220–21.

Jiang, Quanbo, Benoît Rogez, Jean Benoît Claude, Guillaume Baffou, and Jérôme Wenger. 2019. 'Temperature Measurement in Plasmonic Nanoapertures Used for Optical Trapping'. *ACS Photonics* 6 (7). American Chemical Society: 1763–73. doi:10.1021/acsphotonics.9b00519.

Jimoyiannis, Athanassios, and Vassilis Komis. 2001. 'Computer Simulations in Physics Teaching and Learning: A Case Study on Students' Understanding of Trajectory Motion'. *Computers and Education* 36 (2): 183–204. doi:10.1016/S0360-1315(00)00059-2.

Jordan, Brian. 2018. 'An Investigation into Three-Dimensional Single Molecule Localization Microscopy'.

Jordan McEwen. 2024. 'Jablonski Diagram'. *Https://Chem.Libretexts.Org/Bookshelves/Physical_and_Theoretical_Chemistry_Textbook_Maps/Supplemental_Modules_(Physical_and_Theoretical_Chemistry)/Spectroscopy/Electronic_Spectroscopy/Jablonski_diagram*.

Juette, Manuel F, Travis J Gould, Mark D Lessard, Michael J Mlodzianoski, Bhupendra S Nagpure, Brian T Bennett, Samuel T Hess, and Joerg Bewersdorf. 2008. 'Three-Dimensional Sub-100 Nm Resolution Fluorescence Microscopy of Thick Samples'. *Nature Methods* 5 (6): 527–29. doi:10.1038/nmeth.1211.

Jungmann, Ralf, Maier S. Avendaño, Mingjie Dai, Johannes B. Woehrstein, Sarit S. Agasti, Zachary Feiger, Avital Rodal, and Peng Yin. 2016. 'Quantitative Super-Resolution Imaging with QPAINT'. *Nature Methods* 13 (5). Nature Publishing Group: 439–42. doi:10.1038/nmeth.3804.

Keenan, Alan. 2019. *Characterisation of Novel FRET Pairs for Future Design Chromatic Aberration Free Super-Resolution Single-Molecule Microscopy - PH952 MSc Project Report*.

Khaw, Ian, Benjamin Croop, Jialei Tang, Anna Möhl, Ulrike Fuchs, and Kyu Young Han. 2018. 'Flat-Field Illumination for Quantitative Fluorescence Imaging' 26 (12): 15276–88. doi:10.1364/OE.26.015276.

Klar, T A, S Jakobs, M Dyba, A Egner, and S W Hell. 2000. 'Fluorescence Microscopy with Diffraction Resolution Barrier Broken by Stimulated Emission'. *Proceedings of the National Academy of Sciences* 97 (15): 8206–10. doi:10.1073/pnas.97.15.8206.

Kluyver, Thomas, Benjamin Ragan-Kelley, Fernando Pérez, Brian Granger, Matthias Bussonnier, Jonathan Frederic, Kyle Kelley, et al. 2016. 'Jupyter Notebooks—a Publishing Format for Reproducible Computational Workflows'. In *Positioning and Power in Academic Publishing: Players, Agents and Agendas - Proceedings of the 20th International Conference on Electronic Publishing, ELPUB 2016*, 87–90. IOS Press BV. doi:10.3233/978-1-61499-649-1-87.

Koester, Anna M., Angéline Geiser, Peter R.T. Bowman, Sebastian van de Linde, Nikolaj Gadegaard, Nia J. Bryant, and Gwyn W. Gould. 2022. 'GLUT4 Translocation and Dispersal Operate in Multiple Cell Types and Are Negatively Correlated with Cell Size in Adipocytes'. *Scientific Reports* 12 (1). Nature Research. doi:10.1038/s41598-022-24736-y.

Koester, Anna M., Angéline Geiser, Kamilla M.E. Laidlaw, Silke Morris, Marie F.A. Cutiongco, Laura Stirrat, Nikolaj Gadegaard, et al. 2022. 'EFR3 and Phosphatidylinositol 4-Kinase IIIα Regulate Insulin-Stimulated Glucose Transport and GLUT4 Dispersal in 3T3-L1 Adipocytes'. *Bioscience Reports* 42 (7). Portland Press Ltd. doi:10.1042/BSR20221181.

Laine, Romain F, Anna Albecka, Sebastian van de Linde, Eric J Rees, Colin M Crump, and Clemens F Kaminski. 2015. 'Structural Analysis of Herpes Simplex Virus by Optical Super-Resolution Imaging'. *Nature Communications* 6. Nature Publishing Group: 1–10. doi:10.1038/ncomms6980.

Laine, Romain F, Kalina L Tosheva, Nils Gustafsson, Robert D M Gray, Pedro Almada, David Albrecht, Gabriel T Risa, et al. 2019. 'NanoJ: A High-Performance Open-Source Super-Resolution Microscopy Toolbox'. *Journal of Physics D: Applied Physics* 52 (16). doi:10.1088/1361-6463/ab0261.

Lakowicz, Joseph R. 2006. *Principles of Fluorescence Spectroscopy*. Edited by Springer Science+Business Media. 3rd ed.

Lampe, André, Volker Haucke, Stephan J. Sigrist, Mike Heilemann, and Jan Schmoranzer. 2012. 'Multi-Colour Direct STORM with Red Emitting Carbocyanines'. *Biology of the Cell* 104 (4): 229–37. doi:10.1111/boc.201100011.

Lampe, André, Georgi Tadeus, and Jan Schmoranzer. 2015. 'Spectral Demixing Avoids Registration Errors and Reduces Noise in Multicolor Localization-Based Super-Resolution Microscopy'. *Methods and Applications in Fluorescence* 3 (3). IOP Publishing. doi:10.1088/2050-6120/3/3/034006.

Landry, Joseph, Stephen Hamann, and Olav Solgaard. 2020. 'High-Speed Axially Swept Light Sheet Microscopy Using a Linear MEMS Phased Array for Isotropic Resolution'. *Journal of Biomedical Optics* 25 (10). SPIE-Intl Soc Optical Eng. doi:10.1117/1.jbo.25.10.106504.

Lelek, Mickaël, Melina T Gyparaki, Gerti Beliu, Florian Schueder, Juliette Griffié, Suliana Manley, Ralf Jungmann, Markus Sauer, Melike Lakadamyali, and Christophe Zimmer.

2021. 'Single-Molecule Localization Microscopy'. *Nature Reviews Methods Primers* 1 (39). doi:10.1038/s43586-021-00038-x.

Li, Honglin, and Joshua C. Vaughan. 2018. 'Switchable Fluorophores for Single-Molecule Localization Microscopy'. *Chemical Reviews*. American Chemical Society. doi:10.1021/acs.chemrev.7b00767.

Li, Siwei, Jingjing Wu, Heng Li, Danying Lin, Bin Yu, and Junle Qu. 2018. 'Rapid 3D Image Scanning Microscopy with Multi-Spot Excitation and Double-Helix Point Spread Function Detection'. *Optics Express* 26 (18). Optica Publishing Group: 23585. doi:10.1364/oe.26.023585.

Li, Wei, Gabriele S. Kaminski Schierle, Bingfu Lei, Yingliang Liu, and Clemens F. Kaminski. 2022. 'Fluorescent Nanoparticles for Super-Resolution Imaging'. *Chemical Reviews*. American Chemical Society. doi:10.1021/acs.chemrev.2c00050.

Li, Yiming, Markus Mund, Philipp Hoess, Joran Deschamps, Ulf Matti, Bianca Nijmeijer, Vilma Jimenez Sabinina, Jan Ellenberg, Ingmar Schoen, and Jonas Ries. 2018. 'Real-Time 3D Single-Molecule Localization Using Experimental Point Spread Functions'. *Nature Methods* 15 (5). Nature Publishing Group: 367–69. doi:10.1038/nmeth.4661.

Lide, D.R. 2003. *Handbook of Chemistry and Physics*. 84th ed. CRC Press.

Linde, Sebastian van de. 2019. 'Single-Molecule Localization Microscopy Analysis with ImageJ'. *Journal of Physics D: Applied Physics* 52. IOP Publishing. doi:10.1088/1361-6463/ab092f.

Linde, Sebastian Van De. 2019. 'Single-Molecule Localization Microscopy Analysis with ImageJ'. *Journal of Physics D: Applied Physics*. Institute of Physics Publishing. doi:10.1088/1361-6463/ab092f.

Linde, Sebastian Van De, Sarah Aufmkolk, Christian Franke, Thorge Holm, Teresa Klein, Anna Löschberger, Sven Proppert, Steve Wolter, and Markus Sauer. 2013. 'Investigating Cellular Structures at the Nanoscale with Organic Fluorophores'. *Chemistry and Biology*. doi:10.1016/j.chembiol.2012.11.004.

Linde, Sebastian van de, Ivan Krstić, Thomas Prisner, Sören Doose, Mike Heilemann, and Markus Sauer. 2011. 'Photoinduced Formation of Reversible Dye Radicals and Their Impact on Super-Resolution Imaging'. *Photochemical and Photobiological Sciences* 10 (4): 499–506. doi:10.1039/c0pp00317d.

Linde, Sebastian Van De, Anna Löschberger, Teresa Klein, Meike Heidbreder, Steve Wolter, Mike Heilemann, and Markus Sauer. 2011. 'Direct Stochastic Optical Reconstruction

Microscopy with Standard Fluorescent Probes'. *Nature Protocols* 6 (7): 991–1009. doi:10.1038/nprot.2011.336.

Linde, Sebastian Van De, and Markus Sauer. 2014. 'How to Switch a Fluorophore: From Undesired Blinking to Controlled Photoswitching'. *Chemical Society Reviews*. Royal Society of Chemistry. doi:10.1039/c3cs60195a.

Linde, Sebastian van de, Markus Sauer, and Mike Heilemann. 2008. 'Subdiffraction-Resolution Fluorescence Imaging of Proteins in the Mitochondrial Inner Membrane with Photoswitchable Fluorophores'. *Journal of Structural Biology* 164 (3). Elsevier Inc.: 250–54. doi:10.1016/j.jsb.2008.08.002.

Linde, Sebastian Van De, Steve Wolter, and Markus Sauer. 2011. 'Single-Molecule Photoswitching and Localization'. In *Australian Journal of Chemistry*, 64:503–11. doi:10.1071/CH10284.

Löschberger, Anna, Sebastian van de Linde, Marie Christine Dabauvalle, Bernd Rieger, Mike Heilemann, Georg Krohne, and Markus Sauer. 2012. 'Super-Resolution Imaging Visualizes the Eightfold Symmetry of Gp210 Proteins around the Nuclear Pore Complex and Resolves the Central Channel with Nanometer Resolution'. *Journal of Cell Science* 125 (3): 570–75. doi:10.1242/jcs.098822.

Lundbald, Roger L., and Fiona M. Macdonald. 2018. *Handbook of BIOCHEMISTRY and MOLECULAR BIOLOGY Fifth Edition*. 5th ed. CRC Press.

Mahecic, Dora, Davide Gambarotto, Kyle M Douglass, Denis Fortun, Niccoló Banterle, Khalid A Ibrahim, Maeva Le Guennec, et al. 2020. 'Homogeneous Multifocal Excitation for High-Throughput Super-Resolution Imaging'. *Nature Methods* 17 (7). Springer US: 726–33. doi:10.1038/s41592-020-0859-z.

Malus, Etienne Louis. 1809. 'Sur Une Propriété Des Forces Répulsives Qui Agissent Sur La Lumière.' *Mémoires de Physique et de Chimie de La Société d'Arcueil* 2: 2254–67.

Marenda, Mattia, Elena Lazarova, Sebastian van de Linde, Nick Gilbert, and Davide Michieletto. 2021. 'Parameter-Free Molecular Super-Structures Quantification in Single-Molecule Localization Microscopy'. *Journal of Cell Biology* 220 (5). Rockefeller University Press. doi:10.1083/jcb.202010003.

Markham, Nicholas R., and Michael Zuker. 2005. 'DINAMelt Web Server for Nucleic Acid Melting Prediction'. *Nucleic Acids Research* 33 (SUPPL. 2). doi:10.1093/nar/gki591.

Mau, Adrien, Karoline Friedl, Christophe Leterrier, Nicolas Bourg, and Sandrine Lévêque-Fort. 2021. 'Fast Widefield Scan Provides Tunable and Uniform Illumination

Optimizing Super-Resolution Microscopy on Large Fields'. *Nature Communications* 12 (1). Nature Research. doi:10.1038/s41467-021-23405-4.

Meadowlark Optics. 2003. 'Basic Polarization Techniques and Devices'. https://www.jlab.org/accel/inj_group/laserparts/Basic_Polarization_Techniques.pdf.

Moerner, W. E. 2012. 'Microscopy beyond the Diffraction Limit Using Actively Controlled Single Molecules'. *Journal of Microscopy* 246 (3): 213–20. doi:10.1111/j.1365-2818.2012.03600.x.

Moerner, W E. 2015. 'Nobel Lecture: Single-Molecule Spectroscopy, Imaging, and Photocontrol: Foundations for Super-Resolution Microscopy'. *Reviews of Modern Physics* 87 (4): 1183–1212. doi:10.1103/RevModPhys.87.1183.

Mortensen, Kim I., L. Stirling Churchman, James A. Spudich, and Henrik Flyvbjerg. 2010. 'Optimized Localization Analysis for Single-Molecule Tracking and Super-Resolution Microscopy'. *Nature Methods* 7 (5): 377–81. doi:10.1038/nmeth.1447.

Mullan, Alan. n.d. 'Camera Pixel Size and Photon Collection'. https://andor.oxinst.com/learning/view/article/when-bigger-pixels-rule-pixel-size-and-photon-collection-efficiency.

Nicovich, Philip R., Dylan M. Owen, and Katharina Gaus. 2017. 'Turning Single-Molecule Localization Microscopy into a Quantitative Bioanalytical Tool'. *Nature Protocols*. Nature Publishing Group. doi:10.1038/nprot.2016.166.

Nieuwenhuizen, Robert P.J., Keith A. Lidke, Mark Bates, Daniela Leyton Puig, David Grünwald, Sjoerd Stallinga, and Bernd Rieger. 2013. 'Measuring Image Resolution in Optical Nanoscopy'. *Nature Methods* 10 (6): 557–62. doi:10.1038/nmeth.2448.

Nwokeoji, Alison O., Peter M. Kilby, David E. Portwood, and Mark J. Dickman. 2017. 'Accurate Quantification of Nucleic Acids Using Hypochromicity Measurements in Conjunction with UV Spectrophotometry'. *Analytical Chemistry* 89 (24). American Chemical Society: 13567–74. doi:10.1021/acs.analchem.7b04000.

Ober, Raimund J, Sripad Ram, and E Sally Ward. 2004. 'Localization Accuracy in Single-Molecule Microscopy'. *Biophysical Journal* 86: 1185–1200.

'OptoSplit II'. 2023. Accessed April 24. https://www.cairn-research.co.uk/product/optosplit-ii/.

Ovesný, Martin, Pavel Křížek, Josef Borkovec, Zdeněk Švindrych, and Guy M. Hagen. 2014. 'ThunderSTORM: A Comprehensive ImageJ Plug-in for PALM and STORM Data Analysis and Super-Resolution Imaging'. *Bioinformatics* 30 (16). Oxford University

Press: 2389–90. doi:10.1093/bioinformatics/btu202.

Pavani, Sri Rama Prasanna, Michael A Thompson, Julie S Biteen, Samuel J Lord, Na Liu, Robert J Twieg, Rafael Piestun, and W E Moerner. 2009. 'Three-Dimensional, Single-Molecule Fluorescence Imaging beyond the Diffraction Limit by Using a Double-Helix Point Spread Function'. *Proceedings of the National Academy of Sciences of the United States of America* 106 (9): 2995–99. doi:10.1073/pnas.0900245106.

Phillips, Ross. 2019. *Three-Dimensional Single-Molecule Based Super-Resolution Imaging*.

———. 2020. *Characterising DNA Probes for Multi-Channel Single Molecule Localisation Microscopy - Lab Project Report*.

Proppert, Sven Martin. 2014. 'Design , Implementation and Characterization of a Microscope Capable of Three-Dimensional Two Color Super-Resolution Fluorescence Imaging Dissertation Zur Erlangung Des Bayerischen Julius-Maximilians-Universität Würzburg Sven Martin Proppert'.

Qiu, Zhen, and Wibool Piyawattanametha. 2019. 'MEMS Actuators for Optical Microendoscopy'. *Micromachines*. MDPI AG. doi:10.3390/mi10020085.

Rayleigh, Lord. 1903. 'On the Theory of Optical Images, with Special Reference to the Microscope'. *Journal of the Royal Microscopical Society* 23 (4). Wiley: 474–82. doi:10.1111/j.1365-2818.1903.tb04831.x.

Ren, Zhihao, Yuhua Chang, Yiming Ma, Kailing Shih, Bowei Dong, and Chengkuo Lee. 2020. 'Leveraging of MEMS Technologies for Optical Metamaterials Applications'. *Advanced Optical Materials*. Wiley-VCH Verlag. doi:10.1002/adom.201900653.

Reste, Ludovic Le, Johannes Hohlbein, Kristofer Gryte, and Achillefs N. Kapanidis. 2012. 'Characterization of Dark Quencher Chromophores as Nonfluorescent Acceptors for Single-Molecule FRET'. *Biophysical Journal* 102 (11): 2658–68. doi:10.1016/j.bpj.2012.04.028.

Rimoli, Caio Vaz, Cesar Augusto Valades-Cruz, Valentina Curcio, Manos Mavrakis, and Sophie Brasselet. 2022. '4polar-STORM Polarized Super-Resolution Imaging of Actin Filament Organization in Cells'. *Nature Communications* 13. Springer US: 301. doi:10.1038/s41467-022-27966-w.

Rowlands, Christopher J, Florian Ströhl, Pedro P.Vallejo Ramirez, Katharina M Scherer, and Clemens F Kaminski. 2018. 'Flat-Field Super-Resolution Localization Microscopy with a Low-Cost Refractive Beam-Shaping Element'. *Scientific Reports* 8 (1): 1–8. doi:10.1038/s41598-018-24052-4.

Roy, Rahul, Sungchul Hohng, and Taekjip Ha. 2008. 'A Practical Guide to Single-Molecule FRET'. *Nature Methods*. doi:10.1038/nmeth.1208.

Rust, Michael J., Mark Bates, and Xiaowei Zhuang. 2006. 'Sub-Diffraction-Limit Imaging by Stochastic Optical Reconstruction Microscopy (STORM)'. *Nature Methods* 3 (10): 793–95. doi:10.1038/nmeth929.

Sage, Daniel, Thanh An Pham, Hazen Babcock, Tomas Lukes, Thomas Pengo, Jerry Chao, Ramraj Velmurugan, et al. 2019. 'Super-Resolution Fight Club: Assessment of 2D and 3D Single-Molecule Localization Microscopy Software'. *Nature Methods* 16 (5). Nature Publishing Group: 387–95. doi:10.1038/s41592-019-0364-4.

Sahl, Steffen J., Stefan W. Hell, and Stefan Jakobs. 2017. 'Fluorescence Nanoscopy in Cell Biology'. *Nature Reviews Molecular Cell Biology*. Nature Publishing Group. doi:10.1038/nrm.2017.71.

Sauer, Markus, and Mike Heilemann. 2017. 'Single-Molecule Localization Microscopy in Eukaryotes'. *Chemical Reviews*. American Chemical Society. doi:10.1021/acs.chemrev.6b00667.

Schäfer, Philip, Sebastian Van De Linde, Julian Lehmann, Markus Sauer, and Sören Doose. 2013. 'Methylene Blue- and Thiol-Based Oxygen Depletion for Super-Resolution Imaging'. *Analytical Chemistry* 85 (6): 3393–3400. doi:10.1021/ac400035k.

Schermelleh, Lothar, Peter M. Carlton, Sebastian Haase, Lin Shao, Lukman Winoto, Peter Kner, Brian Burke, et al. 2008. 'Subdiffraction Multicolor Imaging of the Nuclear Periphery with 3D Structured Illumination Microscopy'. *Science* 320 (5881): 1332–36. doi:10.1126/science.1156947.

Schermelleh, Lothar, Alexia Ferrand, Thomas Huser, Christian Eggeling, Markus Sauer, Oliver Biehlmaier, and Gregor P.C. Drummen. 2019. 'Super-Resolution Microscopy Demystified'. *Nature Cell Biology*. Nature Publishing Group. doi:10.1038/s41556-018-0251-8.

Schindelin, Johannes, Ignacio Arganda-Carreras, Erwin Frise, Verena Kaynig, Mark Longair, Tobias Pietzsch, Stephan Preibisch, et al. 2012. 'Fiji: An Open-Source Platform for Biological-Image Analysis'. *Nature Methods* 9 (7): 676–82. doi:10.1038/nmeth.2019.

Schlichthaerle, Thomas, Maximilian T Strauss, Florian Schueder, Alexander Auer, Bianca Nijmeijer, Moritz Kueblbeck, Vilma Jimenez Sabinina, et al. 2019. 'Direct Visualization of Single Nuclear Pore Complex Proteins Using Genetically-Encoded Probes for DNA-PAINT'. *Angewandte Chemie - International Edition* 58 (37): 13004–8.

doi:10.1002/anie.201905685.

Schmied, Jürgen J., Carsten Forthmann, Enrico Pibiri, Birka Lalkens, Philipp Nickels, Tim Liedl, and Philip Tinnefeld. 2013. 'DNA Origami Nanopillars as Standards for Three-Dimensional Superresolution Microscopy'. *Nano Letters* 13 (2): 781–85. doi:10.1021/nl304492y.

Schnitzbauer, Joerg, Maximilian T. Strauss, Thomas Schlichthaerle, Florian Schueder, and Ralf Jungmann. 2017. 'Super-Resolution Microscopy with DNA-PAINT'. *Nature Protocols* 12 (6). Nature Publishing Group: 1198–1228. doi:10.1038/nprot.2017.024.

Schulz, Olaf, Christoph Pieper, Michaela Clever, Janine Pfaff, Aike Ruhlandt, Ralph H. Kehlenbach, Fred S. Wouters, Jörg Großhans, Gertrude Bunt, and Jörg Enderlein. 2013. 'Resolution Doubling in Fluorescence Microscopy with Confocal Spinning-Disk Image Scanning Microscopy'. *Proceedings of the National Academy of Sciences of the United States of America* 110 (52): 21000–5. doi:10.1073/pnas.1315858110.

Serjeant, E P, and B Dempsey. 1979. *Ionisation Constants of Organic Acids in Aqueous Solution. International Union of Pure and Applied Chemistry (IUPAC). IUPAC Chemical Data Series No. 23. IUPAC Chemical Data Series*.

Sharonov, Alexey, and Robin M Hochstrasser. 2006. *Wide-Field Subdiffraction Imaging by Accumulated Binding of Diffusing Probes*. www.pnas.orgcgidoi10.1073pnas.0609643104.

Shcherbakova, Daria M., Prabuddha Sengupta, Jennifer Lippincott-Schwartz, and Vladislav V. Verkhusha. 2014. 'Photocontrollable Fluorescent Proteins for Superresolution Imaging'. *Annual Review of Biophysics* 43 (1). Annual Reviews Inc.: 303–29. doi:10.1146/annurev-biophys-051013-022836.

Shen, Hao, Lawrence J. Tauzin, Rashad Baiyasi, Wenxiao Wang, Nicholas Moringo, Bo Shuang, and Christy F. Landes. 2017. 'Single Particle Tracking: From Theory to Biophysical Applications'. *Chemical Reviews*. American Chemical Society. doi:10.1021/acs.chemrev.6b00815.

Shroff, Hari, Catherine G. Galbraith, James A. Galbraith, and Eric Betzig. 2008. 'Live-Cell Photoactivated Localization Microscopy of Nanoscale Adhesion Dynamics'. *Nature Methods* 5 (5): 417–23. doi:10.1038/nmeth.1202.

Shtengel, Gleb, James A Galbraith, Catherine G Galbraith, Jennifer Lippincott-Schwartz, Jennifer M Gillette, Suliana Manley, Rachid Sougrat, et al. 2009. 'Interferometric Fluorescent Super-Resolution Microscopy Resolves 3D Cellular Ultrastructure'.

Proceedings of the National Academy of Sciences 106 (9): 3125–30.

Sochacki, Kem A, Gleb Shtengel, Schuyler B Van Engelenburg, Harald F Hess, and Justin W Taraska. 2014. *Correlative Super-Resolution Fluorescence and Metal Replica Transmission Electron Microscopy*. *Nat Methods*. Vol. 11. http://www.nature.com/authors/editorial_policies/license.html#terms‡.

Spodniakova Pfefferova, Miriam. 2015. 'The Development of Scientific Thinking of Students Using Simulations'. *Journal of Technology and Information* 7 (1). Palacky University Olomouc: 81–89. doi:10.5507/jtie.2015.006.

Stehr, Florian, Petra Schwille, and Ralf Jungmann. 2019. 'Flat-Top TIRF Illumination Boosts DNA-PAINT Imaging and Quantification'. *Nature Communications*. Springer US, 1–8. doi:10.1038/s41467-019-09064-6.

Stennett, Elana M S, Monika A Ciuba, and Marcia Levitus. 2014. 'Photophysical Processes in Single Molecule Organic Fluorescent Probes'. *Chemical Society Reviews* 43 (4): 1057–75. doi:10.1039/c3cs60211g.

Suwandaratne, Nuwanthi, Juan Hu, Kumudu Siriwardana, Manuel Gadogbe, and Dongmao Zhang. 2016. 'Evaluation of Thiol Raman Activities and PKa Values Using Internally Referenced Raman-Based PH Titration'. *Analytical Chemistry* 88 (7). American Chemical Society: 3624–31. doi:10.1021/acs.analchem.5b04241.

Szalai, Alan M., Bruno Siarry, Jerónimo Lukin, David J. Williamson, Nicolás Unsain, Alfredo Cáceres, Mauricio Pilo-Pais, et al. 2021. 'Three-Dimensional Total-Internal Reflection Fluorescence Nanoscopy with Nanometric Axial Resolution by Photometric Localization of Single Molecules'. *Nature Communications* 12 (1). Nature Research. doi:10.1038/s41467-020-20863-0.

Szymborska, Anna, Alex De Marco, Nathalie Daigle, Volker C Cordes, John A G Briggs, and Jan Ellenberg. 2013. 'Nuclear Pore Scaffold Structure Analyzed by Super-Resolution Microscopy and Particle Averaging'. *Science* 341 (6146): 655–58. doi:10.1126/science.1240672.

Tam, Johnny, Guillaume Alan Cordier, Joseph Steven Borbely, Ángel Sandoval Álvarez, and Melike Lakadamyali. 2014. 'Cross-Talk-Free Multi-Color Storm Imaging Using a Single Fluorophore'. *PLoS ONE* 9 (7). doi:10.1371/journal.pone.0101772.

Tang, Y, X Wang, X Zhang, J Li, and L Dai. 2014. 'Sub-Nanometer Drift Correction for Super-Resolution Imaging'. *Optics Letters* 39 (19): 5685. doi:10.1364/ol.39.005685.

Tanguy, Quentin A. A., Olivier Gaiffe, Nicolas Passilly, Jean-Marc Cote, Gonzalo Cabodevila,

Sylwester Bargiel, Philippe Lutz, Huikai Xie, and Christophe Gorecki. 2020. 'Real-Time Lissajous Imaging with a Low-Voltage 2-Axis MEMS Scanner Based on Electrothermal Actuation'. *Optics Express* 28 (6). Optica Publishing Group: 8512. doi:10.1364/oe.380690.

Thatipamala, R, G A Hill, and S Rohani. 1993. 'Absorption of Radiation by Substances at "High" Concentrations: A New Equation and Process Monitoring Applications'. *The Canadian Journal of Chemical Engineering* 71.

'The Nobel Prize in Chemistry 2014. NobelPrize.Org'. 2024. *<https://Www.Nobelprize.Org/Prizes/Chemistry/2014/Summary/>*. December 14.

ThermoFisher Scientific. 2022. *Analysis of DNA Melting through UV-Visible Absorption Spectroscopy Effect of Base-Pair Mismatch and Solvent Environment.*

Thevathasan, Jervis Vermal, Maurice Kahnwald, Konstanty Cieśliński, Philipp Hoess, Sudheer Kumar Peneti, Manuel Reitberger, Daniel Heid, et al. 2019. 'Nuclear Pores as Versatile Reference Standards for Quantitative Superresolution Microscopy'. *Nature Methods* 16 (10). Nature Publishing Group: 1045–53. doi:10.1038/s41592-019-0574-9.

Thompson, Russell E., Daniel R. Larson, and Watt W. Webb. 2002. 'Precise Nanometer Localization Analysis for Individual Fluorescent Probes'. *Biophysical Journal* 82 (5). Biophysical Society: 2775–83. doi:10.1016/S0006-3495(02)75618-X.

Tokunaga, Makio, Naoko Imamoto, and Kumiko Sakata-Sogawa. 2008. 'Highly Inclined Thin Illumination Enables Clear Single-Molecule Imaging in Cells'. *Nature Methods* 5 (2): 159. doi:10.1038/NMETH.1171.

Truong, Kevin, and Mitsuhiko Ikure. 2001. 'The Use of FRET Imaging Microscopy to Detect Protein–Protein Interactions and Protein Conformational Changes in Vivo'. *Current Opinions in Structural Biology*, no. 11: 573–78.

Turkowyd, Bartosz, David Virant, and Ulrike Endesfelder. 2016. 'From Single Molecules to Life: Microscopy at the Nanoscale'. *Analytical and Bioanalytical Chemistry*. Springer Verlag. doi:10.1007/s00216-016-9781-8.

Uphoff, Stephan, Seamus J. Holden, Ludovic Le Reste, Javier Periz, Sebastian Van De Linde, Mike Heilemann, and Achillefs N. Kapanidis. 2010. 'Monitoring Multiple Distances within a Single Molecule Using Switchable FRET'. *Nature Methods* 7 (10): 831–36. doi:10.1038/nmeth.1502.

Valeur, Bernard, and Mário N. Berberan-Santos. 2011. 'A Brief History of Fluorescence and

Phosphorescence before the Emergence of Quantum Theory'. *Journal of Chemical Education*. doi:10.1021/ed100182h.

Valley, Christopher C, Sheng Liu, Diane S Lidke, and Keith A Lidke. 2015. 'Sequential Superresolution Imaging of Multiple Targets Using a Single Fluorophore'. *PLoS ONE* 10 (4): 1–22. doi:10.1371/journal.pone.0123941.

Valli, Jessica, Adrian Garcia-Burgos, Liam M. Rooney, Beatriz Vale de Melo e Oliveira, Rory R. Duncan, and Colin Rickman. 2021. 'Seeing beyond the Limit: A Guide to Choosing the Right Super-Resolution Microscopy Technique'. *Journal of Biological Chemistry*. American Society for Biochemistry and Molecular Biology Inc. doi:10.1016/j.jbc.2021.100791.

Vangindertael, J., R. Camacho, W. Sempels, H. Mizuno, P. Dedecker, and K. P.F. Janssen. 2018. 'An Introduction to Optical Super-Resolution Microscopy for the Adventurous Biologist'. *Methods and Applications in Fluorescence*. IOP Publishing Ltd. doi:10.1088/2050-6120/aaae0c.

Wahl, Michael. 2014. *The Principle of Time-Correlated Single Photon Counting*.

Waldchen, Sina, Julian Lehmann, Teresa Klein, Sebastian Van De Linde, and Markus Sauer. 2015. 'Light-Induced Cell Damage in Live-Cell Super-Resolution Microscopy'. *Scientific Reports* 5 (October). Nature Publishing Group. doi:10.1038/srep15348.

Wegel, Eva, Antonia Göhler, B. Christoffer Lagerholm, Alan Wainman, Stephan Uphoff, Rainer Kaufmann, and Ian M. Dobbie. 2016. 'Imaging Cellular Structures in Super-Resolution with SIM, STED and Localisation Microscopy: A Practical Comparison'. *Scientific Reports* 6 (June). Nature Publishing Group. doi:10.1038/srep27290.

Welchman, Andrew E. 2016. 'The Human Brain in Depth: How We See in 3D'. *Annual Review of Vision Science*. doi:10.1146/annurev-vision-111815-114605.

Wolter, Steve, Ulrike Endesfelder, Sebastian van de Linde, Mike Heilemann, and Markus Sauer. 2011. 'Measuring Localization Performance of Super-Resolution Algorithms on Very Active Samples'. *Optics Express* 19 (8): 7020–33. doi:10.1364/OA_License_v1#VOR.

Wolter, Steve, Anna Löschberger, Thorge Holm, Sarah Aufmkolk, Marie Christine Dabauvalle, Sebastian van de Linde, and Markus Sauer. 2012. 'RapidSTORM: Accurate, Fast Open-Source Software for Localization Microscopy'. *Nature Methods* 9 (11). Nature Publishing Group: 1040–41. doi:10.1038/nmeth.2224.

Wolter, Steve, Anna Löschberger, Thorge Holm, Sarah Aufmkolk, Marie Christine

Dabauvalle, Sebastian Van De Linde, and Markus Sauer. 2012. 'RapidSTORM: Accurate, Fast Open-Source Software for Localization Microscopy'. *Nature Methods*. doi:10.1038/nmeth.2224.

Xu, Ke, Guisheng Zhong, and Xiaowei Zhuang. 2013. 'Actin, Spectrin, and Associated Proteins Form a Periodic Cytoskeletal Structure in Axons'. *Science* 339 (6118): 452–56. doi:10.1126/science.1232251.

Zhao, Zeyu, Bo Xin, Luchang Li, and Zhen-Li Huang. 2017. 'High-Power Homogeneous Illumination for Super-Resolution Localization Microscopy with Large Field-of-View'. *Optics Express* 25 (12). Optica Publishing Group: 13382. doi:10.1364/oe.25.013382.

Zhou, Yongzhuang, Michael Handley, Guillem Carles, and Andrew R Harvey. 2019. 'Advances in 3D Single Particle Localization Microscopy'. *APL Photonics* 4 (6). doi:10.1063/1.5093310.

Appendix

Oligonucleotides and probes sequences

M2-s-33bp-16- AF647
5'   GAT TGA CCC TAG ACC **X**TG ATT CGC ATT GAC TAC 3'

M2-as-33bp-5'Bio
3'   CTA ACT GGG ATC TGG AAC TAA GCG TAA CTG ATG - Biotin 5'

M2-as-33bp-5'Bio-28-DyQ700
3'   CTA AC**X** GGG ATC TGG AAC TAA GCG TAA CTG ATG - Biotin 5'

M3-s-30bp-8-AF647
5'   GCC TGA T**X**A TAT TAC TTG ATT CGC ATT CCC 3'

M3-s-30bp-10-AF647
5'   GCC TGA TTA **X**AT TAC TTG ATT CGC ATT CCC 3'

M3-s-30bp-12-AF647
5'   GCC TGA TTA TA**X** TAC TTG ATT CGC ATT CCC 3'

M3-as-30bp-5'Bio-3'DyQ700
3' **DyQ700** -   CGG ACT AAT ATA ATG AAC TAA GCG TAA GGG - Biotin 5'

M3-as-30bp-5'Bio
3'   CGG ACT AAT ATA ATG AAC TAA GCG TAA GGG - Biotin 5'

dsDNA Probes
M2-16-N = M2-s-33bp-16- AF647 + M2-as-33bp-5'Bio
5'   GAT TGA CCC TAG ACC **X**TG ATT CGC ATT GAC TAC 3'
3'   CTA ACT GGG ATC TGG AAC TAA GCG TAA CTG ATG - Biotin 5'

M2-16-Q = M2-s-33bp-16- AF647 + M2-as-33bp-5'Bio-28-DyQ700
5'   GAT TGA CCC TAG ACC **X**TG ATT CGC ATT GAC TAC 3'
3'   CTA AC**X** GGG ATC TGG AAC TAA GCG TAA CTG ATG – Biotin

M3-8-N = M3-s-30bp-8-AF647 + M3-as-30bp-5'Bio
5'   GCC TGA T**X**A TAT TAC TTG ATT CGC ATT CCC 3'
3'   CGG ACT AAT ATA ATG AAC TAA GCG TAA GGG - Biotin 5'

M3-8-Q = M3-s-30bp-8-AF647 + M3-as-30bp-5'Bio-3'DyQ700
5'   GCC TGA T**X**A TAT TAC TTG ATT CGC ATT CCC 3'
3' **DyQ700** -   CGG ACT AAT ATA ATG AAC TAA GCG TAA GGG - Biotin 5'

M3-10-N = M3-s-30bp-10-AF647 + M3-as-30bp-5'Bio
5'   GCC TGA TTA **X**AT TAC TTG ATT CGC ATT CCC 3'
3'   CGG ACT AAT ATA ATG AAC TAA GCG TAA GGG - Biotin 5'

M3-10-Q = M3-s-30bp-10-AF647 + M3-as-30bp-5'Bio-3'DyQ700
5'   GCC TGA TTA **X**AT TAC TTG ATT CGC ATT CCC 3'
3' **DyQ700** -   CGG ACT AAT ATA ATG AAC TAA GCG TAA GGG - Biotin 5'

M3-12-N = M3-s-30bp-12-AF647 + M3-as-30bp-5'Bio

5'   GCC TGA TTA TA**X** TAC TTG ATT CGC ATT CCC 3'
3'   CGG ACT AAT ATA ATG AAC TAA GCG TAA GGG - Biotin 5'

M3-12-Q = M3-s-30bp-12-AF647 + M3-as-30bp-5'Bio-3'DyQ700
5'   GCC TGA TTA TA**X** TAC TTG ATT CGC ATT CCC 3'
3' **DyQ700** -   CGG ACT AAT ATA ATG AAC TAA GCG TAA GGG - Biotin 5'

Linear correlation of k_{ON} and N_{Det}
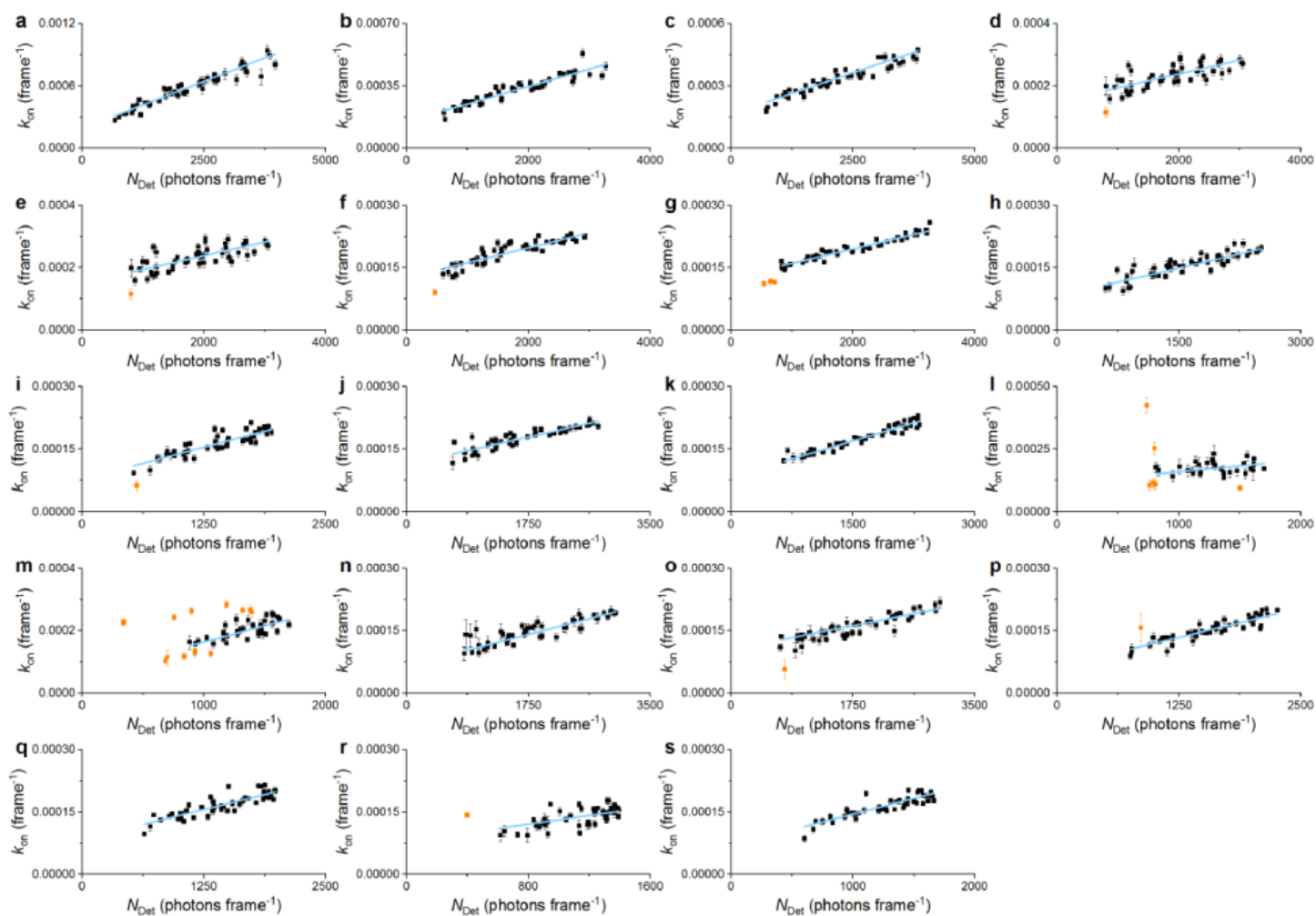
Figure App.55 Linear fits (blue lines) of k_{ON} as a function of N_{Det}. For all studied conditions, the enzymatic oxygen scavenger system was present as described in Methods. (a) 10 mM MEA, pH 6.5, (b,c) 50 mM MEA, pH 6.5, (d) 100 mM MEA, pH 6.5, (e) 250 mM MEA, pH 6.5, (f) 10 mM MEA, pH 7.4, (g) 50 mM MEA, pH 7.4, (h) 100 mM MEA, pH 7.4, (i) 250 mM MEA, pH 7.4, (j) 10 mM MEA, pH 8.0, (k) 50 mM MEA, pH 8.0, (l,m) 100 mM MEA, pH 8.0, (n,o) 10 mM MEA, pH 8.5, (p,q) 50 mM MEA, pH 8.5, (r,s) 100 mM MEA, pH 8.5. Some buffer conditions are duplicated because visual inspection of the raw data during the acquisition lead to replicate recordings when the low switching quality was recognized. Orange datapoints are excluded as extreme outliers.

Linear correlation of k_{OFF} and N$_{Det}$
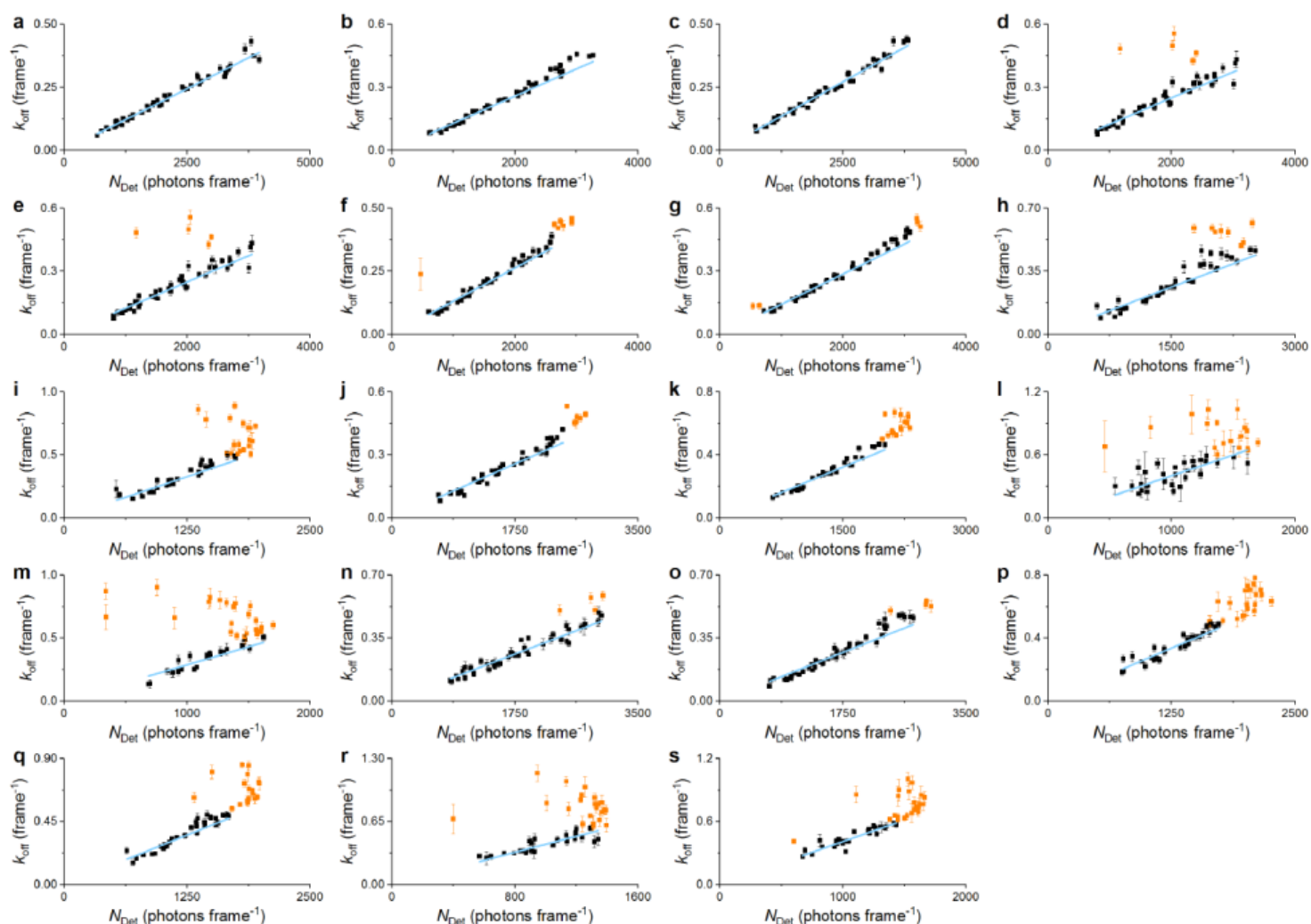
Figure App.2 Linear fits (blue lines) of k_{OFF} as a function of N_{Det}. For all studied conditions, the enzymatic oxygen scavenger system was present as described in Methods. (a) 10 mM MEA, pH 6.5, (b,c) 50 mM MEA, pH 6.5, (d) 100 mM MEA, pH 6.5, (e) 250 mM MEA, pH 6.5, (f) 10 mM MEA, pH 7.4, (g) 50 mM MEA, pH 7.4, (h) 100 mM MEA, pH 7.4, (i) 250 mM MEA, pH 7.4, (j) 10 mM MEA, pH 8.0, (k) 50 mM MEA, pH 8.0, (l,m) 100 mM MEA, pH 8.0, (n,o) 10 mM MEA, pH 8.5, (p,q) 50 mM MEA, pH 8.5, (r,s) 100 mM MEA, pH 8.5. Some buffer conditions are duplicated because visual inspection of the raw data during the acquisition lead to replicate recordings when the low switching quality was recognized. Orange datapoints are excluded as extreme outliers or unaccurate due to undersampling.